A

PhD Thesis

entitled

Synthesis and photocatalytic study of NbC-C nanocomposites

Submitted in the partial fulfillment of the requirement
for the award of degree of

Doctor of Philosophy (Ph.D.)

under the guidance of

Dr. O.P. Pandey
(Senior Professor)

by

Aayush Gupta
(Reg. no.: 901512001)

School of Physics and Materials Science

**Thapar Institute of Engineering and Technology,
Patiala (Punjab), INDIA – 147004**

(July 2019)

DECLARATION

I hereby certify that the present work in thesis ***'Synthesis and photocatalytic study of NbC-C nanocomposites'*** in the partial fulfilment of the requirement for the award of the degree of **DOCTOR OF PHILOSOPHY (Ph.D.)** in School of Physics and Materials Science, Thapar Institute of Engineering and Technology, Patiala is an authentic record of my own work carried out under the supervision of **Dr. O.P. Pandey**. The matter embodied in this thesis has not been submitted in part or full to any other institute/university for the award of any degree.

Aayush Gupta

This is to certify that the above statement made by the candidate is true to the best of my knowledge.

Dr. O.P. Pandey
(Senior Professor and Head)
School of Physics and Materials Science
Thapar Institute of Engineering and Technology
Patiala (Punjab)- 147004

CONTENT

ACKNOWLEDGMENT

This thesis has been kept on track and been seen through to completion with the support and encouragement of numerous people including my supervisor, colleagues, friends and various institutions. It is my pleasure to express my deep sense of thanks to several individuals who journeyed with me and helped me to reach my destination. My first and foremost offering of thanks goes to my supervisor **Dr. O.P. Pandey** for his excellent guidance, constant encouragement, valuable suggestions, blessings, extreme care and providing me with an excellent atmosphere for academic and personal growth. I especially thank him for keeping faith in me when I lost all of mine. It is my privilege to thank **Prof. Prakash Gopalan** (Director) Thapar Institute of Engineering and Technology, Patiala for providing me resources in the institution and needful help during the various stages of my work.

I also like to express my thanks to current and previous Head, SPMS for their continuous support and encouragement. I would like to express my whole-hearted thanks to the members of my doctoral committee for their constant encouragement, insightful comments and fruitful criticisms. My special thanks to all my teachers (**Dr. Kulvir Singh, Dr. Puneet Sharma, Dr. B.N. Chudasama, Dr. B.C. Mohanty and Dr. L.K. Brar**) at SPMS who always supported and encouraged me. I would also like to thank **Mr. Indermani Mishra, Mr. Purshottam Singh, Mr. Jant Singh** and **Mr. Lal Ji** for their timely help at various times. I was fortunate to share my journey with **Savidh Khan**, **Varun Singhal, Mohd. Abuzar Saeed**, **Ghanshyam Mourya**, **Sachin Jaidka** and **Ratandeep Pandey** (*BABU*).

I would like to thank my seniors (**Dr. Ranvir S. Panwar, Dr. Jagdeep Kaur, Dr. Manish Mittal, Dr. Deepak Kumar, Dr. Suresh Kumar, Dr. Gourav Singla and Dr. Paramjyot K. Jha**) and all current lab mates (PhD and M.Sc. students) at Functional Materials Lab. This journey would have been very boring and joyless w/o you all. The encouraging and helpful atmosphere made my time in the lab a very interesting learning experience. I would also like to thank **Dr. Akshay Kumar** (SGGSWU, Fatehgarh) for timely encouragement and **Mr. Nazrehayat** (IIT Roopnagar), **Ms. Deepika** (IIT Roorkee) for making me comfortable in new techniques (MS and TOC) related to my work. The new techniques and fields to which I was introduced which helped me to master for the analysis of the work done. I find this is a good time to acknowledge all my friends for keeping my life full of joy and positivity.

I really cannot find words which can express my love, regard and thanks to my family (specially **Shriya**, **Vibhor**, **Animesh**, **Samarth** and **Mishika**) for standing by me in this long journey. I would especially like to thank **Mahesh K. Singh**, **Maniraj Singh** and **P. Rajagopalan** for keeping me grounded and focused on important things in life: good food/drinks, PUBG/DOTA and laughter with family. Above all I would like to acknowledge the ***Almighty*** for blessings and positive energy which sustained me during all stages of this work. I am especially grateful for the gift of all the special people that surround me.

Aayush Gupta

LIST OF PUBLICATIONS

From Ph.D. work:

1. **Aayush Gupta** and O.P. Pandey, Visible irradiation induced photodegradation by NbC/C nanocomposite derived from smoked cigarette litter (filters), *Solar Energy 163, 167–176 (2018).*
2. **Aayush Gupta**, M. Mittal, M.K. Singh, S.L. Suib and O.P. Pandey, Visible light induced photocatalytic degradation characteristics of NbC/C nano-composite synthesized at low temperature, *Scientific Reports 8:13597 (2018).*
3. **Aayush Gupta** and O.P. Pandey, NbC/C heterojunction for efficient photodegradation of methylene blue under visible irradiation, *Solar Energy 183, 398-409 (2019).*
4. **Aayush Gupta**, L.K. Brar and O.P. Pandey, Influence of laboratory and waste grade cellulose acetate on photo and electrocatalytic properties of NbC_xO_y/C and NbC/C nanocomposites, *Solar energy (Accepted; 18/07/2019).*

Other publications:

5. **Aayush Gupta**, G. Singla and O.P. Pandey, Effect of synthesis parameters on structural and thermal properties of NbC/C nano composite synthesized via in-situ carburization reduction route at low temperature, *Ceramics International 42(11) 13024-13034 (2016).*
6. S. Garg, S. Thakur, **Aayush Gupta**, G. Kaur and O.P. Pandey, Antibacterial and anticancerous drug loading kinetics for (10-x)CuO-xZnO-20CaO-60SiO_2-10P_2O_5 ($2 \leq x \leq 8$) mesoporous bioactive glasses, *J. Mater. Sci.: Mater. Med. 28:11 (2017).*
7. D. Basandrai, R.K. Bedi, A. Dhami, J. Sharma, S.B. Narang, K. Pubby, **Aayush Gupta** and A.K. Srivastav, Aluminum and chromium substituted Z-type hexaferrite for antenna and microwave absorber applications, *J. Sol-Gel Sci. Technology, 85, 59-65 (2017).*
8. **Aayush Gupta**, V. Singhal and O.P. Pandey, Facile in-situ synthesis of NbB_2 nanoparticles at low temperature, *Journal of Alloys and Compounds, 736, 306*-313 *(2018).*
9. M. Mittal, **Aayush Gupta** and O.P. Pandey, Role of oxygen vacancies in Ag/Au doped CeO_2 nanoparticles for fast photocatalysis, *Solar Energy 165, 206-216* (*2018*).
10. Amit Singh Vig, **Aayush Gupta**, O.P. Pandey, Efficient photodegradation of methylene blue (MB) under solar radiation by ZrC nanoparticles, *Advanced Powder Technology 29(9), 2231-2242 (2018).*
11. L.K Brar, **Aayush Gupta** and O.P. Pandey, Influence of carbon content of nano-TaC powders on the electrocatalytic and photocatalytic properties, *Catalysis Today 325, 98-108 (2018).*
12. J. Kaur, **Aayush Gupta** and O.P. Pandey, Photocatalytic study of ZnS-Ag_2S nanocomposites-effect of thioglycerol, *Solar Energy 176, 678-687 (2018).*
13. V. Vivekananthan, N.R. Alluri, A. Chandrasekhar, Y. Purusothaman, **Aayush Gupta** and S.J. Kim, Zero-power consumed intruder identification system by enhanced piezoelectricity of $K_{0.5}Na_{0.5}NbO_3$ using substitutional doping of BTO NPs, *Journal of*

Materials Chemistry C 7, 7563-7571 (2019).

14. K. Rajrana, **Aayush Gupta**, R.A. Mir and O.P. Pandey, Facile sono-chemical synthesis of nanocrystalline MnO_2 for catalytic and capacitive applications, *Physica B: Condensed Matter 564, 179–185 (2019).*

15. J. Sharma, **Aayush Gupta** and O.P. Pandey, Effect of Zr doping and aging on optical and photocatalytic properties of ZnS nanopowder, *Ceramics International 45(11), 13671-13678 (2019).*

16. A.S. Vig, N. Rani, **Aayush Gupta** and O.P. Pandey, Influence of Ca-doped $NaNbO_3$ and its heterojunction with g-C_3N_4 on the photoredox performance, *Solar Energy 185, 469-479 (2019).*

17. **Aayush Gupta**, R. Kour and L.K. Brar, Facile synthesis of carbon nanospheres from saccharides for photocatalytic applications, *SN Applied Science (Communicated).*

LIST OF CONFERENCES

1. R. Mir, **Aayush Gupta** and O.P. Pandey*, Study on reduction of MoO_3 to Mo_2C via carburization*, 2nd Conference on Microscopy in Materials Science (AMST-2016) held at Thapar University, Patiala on Feb. 25-27th, 2016.
2. R. Mir, **Aayush Gupta** and O.P. Pandey, *Study on reduction-carburization of MoO_3 to nano Mo_2C*, *Proc. of International conference on nanotechnology for better living*, 3(1) (2016) 149 (doi:10.3850/978-981-09-7519-77nbl16-rps-149).
3. **Aayush Gupta** and O.P. Pandey, *Optimization of synthesis parameters to obtain Nano Niobium Carbide (NbC) from Nb_2O_5 through carbo-thermal route at low temperature*, International Conference on role of microscopy and allied techniques in the development of multifunctional nanomaterials (ICMAMN 2016) held at Fakir Mohan University, Balasore (Orissa) on November 25-27th, 2016.
4. **Aayush Gupta** and O.P. Pandey, *Effect of synthesis parameters on photocatalytic properties of Nano Niobium Carbide (NbC)*, National seminar on Advances of Functional Materials held at All Saints College, Trivandrum on September 19-20th, 2017.
5. **Aayush Gupta**, R. Mir and O.P. Pandey, *Synthesis and photo-catalytic behavior of NbC/C nanocomposite*, 9th International Symposium on Group Five Elements held at Vivanta by Taj, New Delhi on November 22-24th, 2017.
6. **Aayush Gupta** and O.P. Pandey, *Carrot grass derived NbC/g-C heterojunction: an efficient photocatalyst for degradation of methylene blue dye under house-hold CFL radiation*, 9th International Colloids Conference held at Hotel Melia Sitges, Sitges, Barcelona (Spain) on June 16-19th, 2019.

LIST OF FIGURES

Chapter 5

LIST OF TABLES

PREFACE

Transition metal carbides (TMCs) are considered as excellent compounds for cutting tool and tribological applications with extremely high hardness and thermal stability. Among all TMCs, niobium carbide (NbC) exhibits better toughness than other carbides such as TiC, ZrC and WC and is extensively used in steel industries for better mechanical properties. The present work describes the versatility of NbC as a photocatalyst for the degradation of methylene blue as an organic pollutant. In this work, the synthesis of nano NbC using different carbon precursors and its photocatalytic behavior is reported. The entire work is presented in 8 chapters which are as follows:

Chapter 1 presents the current status of water pollution and the treatment of polluted water using different techniques. Among all the available processes, the role of photocatalysis to treat organic pollutants has been described in this chapter. Moreover, some of the real-time limitations of semiconductors as photocatalyst has also been discussed. Apart from this, basic introduction of TMCs along with their various applications is presented. A detailed discussion of NbC is done considering its nature of bonding and solubility dependent phase transition (NbC_x, α- Nb_2C, β- Nb_2C and γ- Nb_2C). Further, the need of nano scaled NbC for some specific applications are also discussed.

Chapter 2 gives details of the available literature pertaining to the synthesis and characterization of nano-scale NbC. This chapter includes the different synthesis methods where synthesis conditions such as precursors, temperature, pressure and environment are different to get defined morphologies of nano NbC. It also describes the effect of synthesis conditions on the composition of NbC_x and its mechanical, electrochemical and capacitive characteristics. Thereafter, utilization of organic waste/discarded materials as carbon source in order to obtain NbC has also been discussed. One of the most common daily life utilities i.e. smoked cigarette filters and a hazardous agricultural weed i.e. parthenium hysterophorous are discussed on the basis of their adverse environmental effects and their utilization to develop an engineering material. Based on literature, the work plan for this thesis is also proposed.

Chapter 3 presents the path for designing different experiments which include the synthesis and characterization of nano NbC using different carbon precursors. The adopted methodology along with a brief introduction of characterizations techniques (XRD, TEM, Raman, XPS, UV-visible spectroscopy and BET) are also presented in this chapter. Moreover, the detailed methodology of photocatalytic experiments is described at the end of this chapter. Considering the available literature, the methodology has been designed

into two sections in which organic waste materials (smoked cigarette filters and parthenium hysterophorous) and the associated laboratory grade chemicals (cellulose acetate and activated charcoal) were used as carbon precursors as has been presented in subsequent chapters.

Chapter 4 describes a brief introduction of cigarette usage, compositional and morphological features of smoked cigarette filters (CFs). The optimization of synthesis parameters using smoked cigarette filters as carbon source (temperature, holding time and CF content) is done to obtain nano NbC. In terms of lattice distortion and carbon content (x) in NbC_x, the effect of temperature and holding time on the formation of NbC has been discussed in detail. TEM results revealed the formation of NbC-C nanocomposite in which NbC nanoparticles are embedded in graphitic carbon network. BET analysis has been done to understand the nature of pore distribution and specific surface area of the synthesized nanocomposite sample. Further, Raman and XP spectroscopy were carried out to understand the nature of carbon network and elemental composition on the surface of optimized sample. Since, absorption of visible radiation has been observed from UV-visible spectroscopy, detailed photocatalytic experiments were carried out to optimize the concentration of dye (methylene blue; MB) and catalyst (NbC-C nanocomposite) under the illumination of household CFL lamp. The degradation of MB molecule associated to decreased absorption of dye solution has been confirmed with the help of mass spectrometry (MS) and scavenger tests. Further, a detailed mechanism associated to photocatalytic activity of optimized NbC-C nanocomposite has been proposed at the end of the chapter.

Chapter 5 describes the allelopathic and other adverse effects of parthenium hysterophorous (PH) on crop production and livestock health. The idea of the transformation of agricultural weed to get an engineering product for the treatment of pollutants is presented in this chapter. The optimization of synthesis parameters has been discussed to obtain single phase NbC-C nanocomposite sample. Different characterization techniques suggest that the synthesis of NbC involves the simultaneous reduction-carburization process with the incorporation of NbC_xO_y or NbO_z centers inside the NbC nanoparticles. Moreover, the effect of nature of carbon network and composition of NbC_x on the photocatalytic performance has been discussed in this chapter. Further, with the help of MS, total organic carbon (TOC) and scavenger tests, a detailed degradation mechanism of MB dye under household CFL illumination with the help of optimized NbC-C nanocomposite sample has also been discussed at the end of the chapter.

Chapter 6 describes the optimization of synthesis parameters (temperature and holding time) to obtain NbC from cellulose acetate which is a major component of cigarette filter. This study was undertaken to understand the effect of processing parameters for the synthesis of NbC using a chemical grade cellulose acetate. This chapter explains the effect of carbon precursor and its morphology for achieving reduction and carburization at relatively lower temperature. Due to the solid-state carburization reaction, composition of NbC_x and nature of carbon were modified as compared to those obtained using cigarette filters. Hence, the modification in the surface chemistry has also been observed affecting the photocatalytic performance of synthesized nano NbC-C nanocomposite. Further, the involved degradation parameters with degradation kinetics and responsible mechanism.

Chapter 7 describes the synthesis of NbC-C nanocomposite using activated charcoal as carbon source. This work was undertaken to probe the pathway of reduction-carburization of Nb_2O_5 yielding NbC-C nanocomposite. The influence of amorphous carbon source as compared to polymeric carbon sources as studied in earlier chapters is described. This chapter also provides the carbon source dependent structural features such as particle size, composition of NbC_x (distribution of oxygen centers inside the NbC inducing NbC_xO_y or NbO_z) and specific surface area of the synthesized NbC-C nanocomposite sample. Moreover, Raman spectroscopy suggested the amorphous nature of *in-situ* produced carbon network engulfing the NbC nanoparticles in it. With the help of thermodynamic calculations (Gibb's free energy; ΔG), a detailed discussion related to synthesis mechanism of NbC nanoparticles has been done. Higher specific surface area and smaller particle size of NbC-C nanocomposite sample enhanced the adsorption of MB dye on the surface of the nanocomposite. Further, the photodegradation efficiency of optimized NbC-C nanocomposite sample to degrade MB dye under similar conditions is discussed and the degradation mechanism is also proposed.

Chapter 8 summarizes the entire work to understand the effect of synthesis parameters and carbon source for the synthesis of NbC-C nanocomposite at relatively low temperature. The influence of different carbon sources, composition and nature of carbon network on the photocatalytic activity of NbC-C nanocomposite is compared. Further, as an effect of carbon source it has been observed that direct conversion of waste product resulted efficient NbC-C nanocomposite as photocatalyst as compared to laboratory grade chemicals. At the end of this chapter, possible future work based on the present work is also given.

CHAPTER 1 INTRODUCTION

Overview

The extensive discharge of industrial waste into water bodies has polluted most of the natural resources. This has led to depletion of pure water for our livelihood. In order to make them reusable, many techniques have been developed to treat wastewater. Among these, photocatalysis is considered as better treatment process as no external chemical reagent (except catalyst) is required in this process. Many photocatalysts including semiconductors have been developed and studied to degrade or mineralize organic effluents. Transition metal carbides (TMCs), being thermally and chemically stable compounds, are being explored for the same purpose. However, the associated pathway of photochemical reactions for TMCs is still untraced problem.

In this chapter, a brief description of above-mentioned problems and the role of different photocatalysts and the corresponding mechanisms to degrade the effluents have been described. Moreover, the effect of carbon deficiency in NbC_x on the optical and mechanical properties of NbC has also been discussed.

1.1. Background

According to a joint report of *United Nations* and *Asian Institute of Technology*, South Asian (SA) countries contribute 25% of global population and only 4% of global water resources. While, 90% of available water resources are utilized in agriculture sector i.e. higher than average global use in agriculture (~70%) [1]. Ganges-Brahmaputra-Meghna basin endorses almost 40% of the SA population which is being polluted by discharging 270-450 billion kg (approximately) of domestic and industrial wastes (toxic sludge and heavy metals) annually [2]. Pharmaceuticals, pulp-paper and textile are some of the major industries which dispose the respective byproducts into the natural water resources. Water pollution affects the aquatic flora-fauna by reducing the dissolved oxygen, penetration of solar radiation and inducing human mutation [3,4]. A variety of processes are available to treat such contaminated water resources. The stepwise treatments followed are shown in figure 1.1 [5]. Such a frightful situation of polluted natural resources induces the demand of potable water and clean energy for social survival. Considering these facts different catalysts have been used to catalyze the wastewater treatment process. However, the efficiency of these catalysts depends upon surface characteristics.

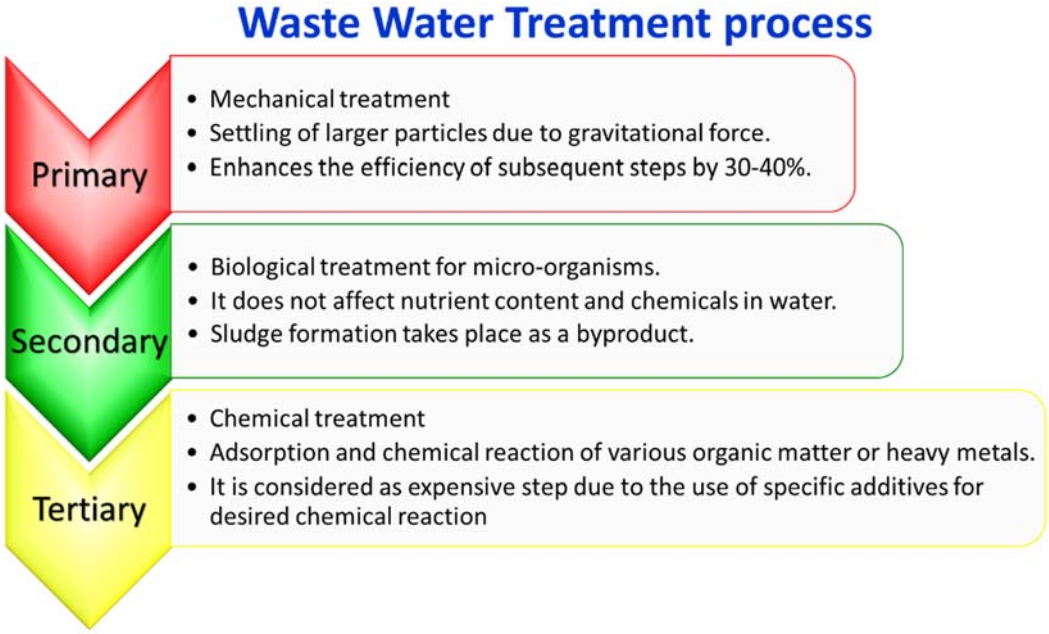

Figure 1.1: Wastewater treatment process chart.

1.2. Photocatalysis – Need of the hour

In order to reduce the scarcity of potable water, research groups have developed various technologies to treat wastewater such as ozonation [6,7], reverse osmosis [8], flocculation [9], electrochemical [10] and adsorption [11–13] etc. Among these, photocatalysis is considered as green advanced oxidative approach with quick, efficient results without any

toxic byproducts (CO_2, H_2O and mineral acids) and with flexibility of variety of pollutants [14]. For a typical photocatalytic process, a schematic representation of photon-matter interaction is shown in figure 1.2 where a semiconducting compound generates e^--h^+ pair during UV-visible exposure. The photogenerated charge carriers further participate in the chemical reactions to produce different oxidative radicals as represented in eq. (1.1-1.8). These photochemical reactions illustrate the formation of hydroxyl ($\dot{O}H$) and superoxide anion radical ($\dot{O_2^-}$), known as strong oxidizing agents. These radicals oxidize the organic/inorganic pollutant molecule resulting decomposition or mineralization of pollutant in wastewater [15,16].

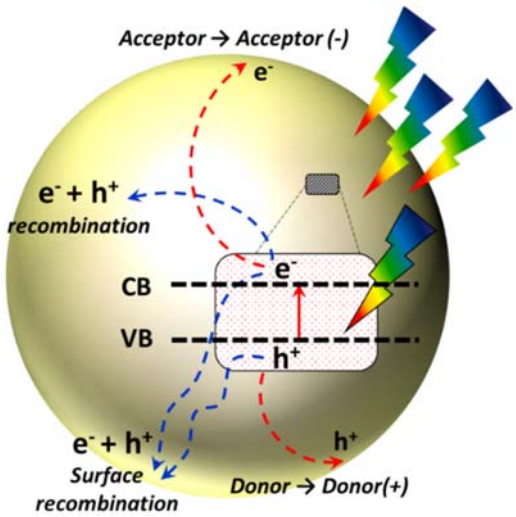

Figure 1.2: Schematic representation of different steps occurring during the photocatalytic process.

$$\text{photocatalyst} + h\nu \rightarrow \text{photocatalyst} + h^+_{VB} + e^-_{CB} \quad (1.1)$$
$$H_2O \rightarrow H^+ + OH^- \quad (1.2)$$
$$H_2O + h^+_{VB} \rightarrow H^+ + OH^{\cdot} \quad (1.3)$$
$$OH^- + h^+_{VB} \rightarrow OH^{\cdot} \quad (1.4)$$
$$O_2 + e^- \rightarrow \dot{O_2^-} \quad (1.5)$$
$$\dot{O_2^-} + e^- + 2H^+ \rightarrow H_2O_2 \quad (1.6)$$
$$2\dot{O_2^-} + 2H^+ \rightarrow O_2 + H_2O_2 \quad (1.7)$$
$$H_2O_2 + e^- \rightarrow OH^- + OH^{\cdot} \quad (1.8)$$

Further, generation and propagation of charge carriers can be modified by adding an external element in host lattice (referred as doping) and by using the combination of two or more different classes of materials (metal-metal or metal-semiconductor or semiconductor-semiconductor), referred as composite or heterojunctions. Conceptually, heterojunctions contain two different components exhibiting the reaction potentials that are required for the photochemical reaction. The required exciton gets promoted to desired potential from one component to another one to accomplish the formation of radicals. For

example, in Z-scheme, two different semiconductors are combined together, and both get excited upon irradiation. But e^- of first component combines with hole of other component so that e^- of second component can participate in possible reduction reaction occurring at conduction band edge (CBE) of second component. Some of the configurations of composites along with their photoexcitation and charge transfer mechanisms are shown in figure 1.3 [17–21]. The formation of interface between the constituents controls the effective performance of the system as catalyst which influences the charge transfer or recombination of charge carriers [22,23]. Moreover, such synergistic contact can also alter the optical characteristics of the system by quenching specific electronic transition responsible for optical emission [21,24–26].

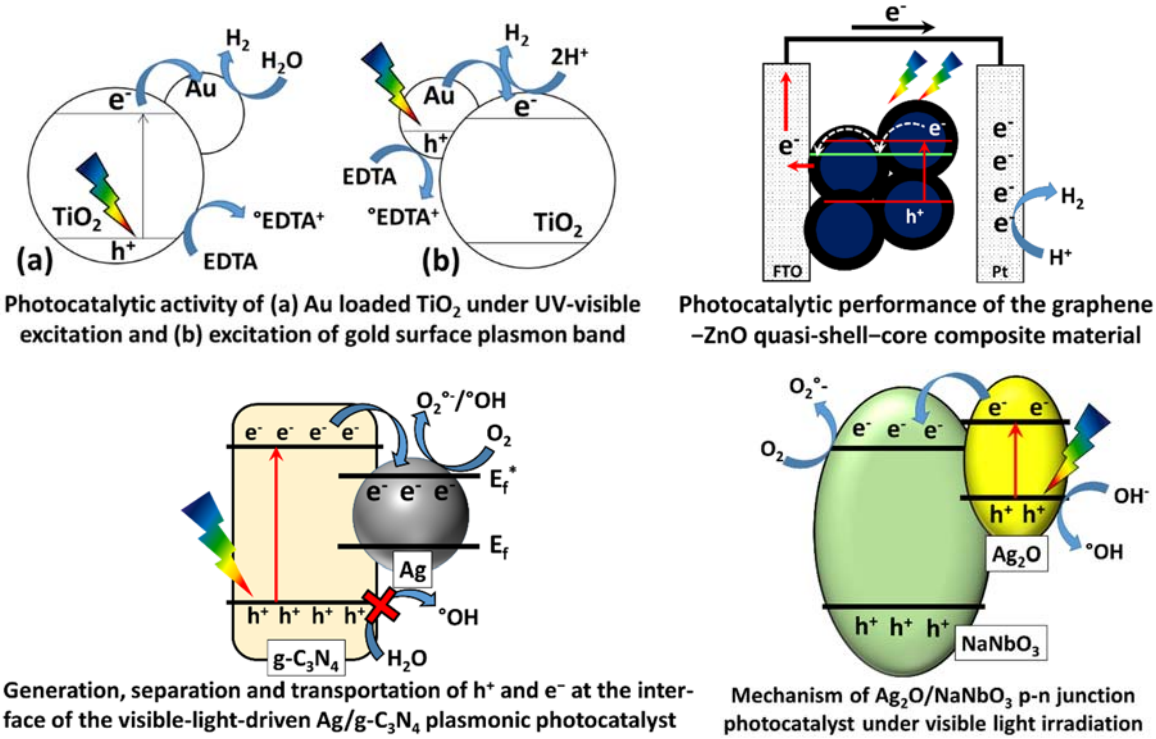

Figure 1.3: Schematic schemes of different configuration of photocatalysts: loading of gold nanoparticle on TiO_2 [19], core shell morphology [18], decoration of photocatalyst nanoparticles on semiconducting g-C_3N_4/graphene oxide sheets [20] and combination of Ag_2O-$NaNbO_3$ as p-n junctions [21].

1.3. Limitations of semiconductors as photocatalyst

Despite of such incredible photochemical characteristics, semiconducting compounds do exhibit some limitations. Some of the major features that hinder their practical applicability are as follows:

(i) Excitation source: Optical band gap (higher than 3.1 eV) of semiconductors limits their usage under UV irradiation e.g. TiO_2, SiO_2 and ZrO_2 etc.

Moreover, nanosized semiconductors also exhibit blue shift of absorption edge as compared to respective bulk form due to their size (comparable to Bohr radius of excitons).

(ii) Temperature: To accomplish successful photochemical reaction, temperature plays a critical role by maneuvering the rate of reaction through thermal energy. Along with the rate of reaction, thermal stability is also very important factor to be considered at the time of selection for a catalyst. For example, non-oxide catalysts such as sulfides and phosphates exhibit temperature sensitive profile up to 450 °C while, zeolites show various structural transitions beyond 150 °C [27–30]. Further, TiO_2 (most studied compound as photocatalyst) shows different polymorphic transitions upon heating which alters its photochemical response [31].

(iii) Stability: The most critical parameter to be considered for selection of catalyst is its stability in the required chemical conditions. Majority of catalysts diminish their catalytic response during repetitive runs due to the leakage of surface charge (pH) and active sites [32–35]. In photocatalytic reactions, catalysts are activated thermally prior to use in subsequent run.

Based on above discussion, it would be advantageous to utilize transition metal carbide (TMC) as a catalyst which would fulfill all these ambiguities due to its thermal stability and dual electronic character i.e. semiconductor (generation of excitons) and conductor (charge transfer) at nano scale.

1.4. Transition metal carbides

Transition metal carbides (TMCs) is a specific class of materials in which carbon is bonded with equivalent or less electronegative element. Large difference of electronegativity and size (metal-carbon) is responsible for the occupancy of sp^3 hybridized carbon in the interstices of host metallic lattice [36]. TMCs are popular compounds due to their high melting temperatures (T_m >2500 °C) along with excellent thermal and electrical conductivities (comparable to metals). They also exhibit high elastic modulus and hardness which are comparable to ceramics. TMCs also find technological applications in various engineering fields such as cutting tools, bearings, grain-growth inhibitor in steels, optical coatings, biosensors for pesticide detection, H_2 evolution, CO_2 reduction and catalysts for fuel cell applications [24,37–42].

1.5. Properties of TMCs

As a result of occupancy of carbon atoms in interstices of host transition metal lattice, a crystallographic transformation is observed. BCC or HCP unit cell of host metal

gets transformed to FCC or hexagonal unit cell of TMC. Such transformation of crystal structure is a function of size ratio of carbon (R_c) and metal (R_m) atom with $R_c/R_m = 0.59$. For $R_c/R_m<0.59$, FCC/HCP and hexagonal are the two possible lattices with octahedral ($R_c/R_m \leq 0.59$) and tetragonal voids ($0.53<R_c/R_m<0.59$), respectively. Further, $R_c/R_m>0.59$ distorts the lattice to a more extent which stimulates complex structures (e.g. Cr_3C_2). Further, the occupancy of sp^3 hybridized C induces multiple bonding character in TMCs. Table 1.1 represents a comparative physical property of different TMCs. Physical and electronic properties of TMCs are governed by metal-metal (M-M) and metal-carbon (M-C) bonds present in it. Due to the M-M bonds, TMCs possess finite density of states at Fermi level to behave like metals. While, partial occupancy of d-electrons in metals and M-C interaction contribute to partial covalent character (M-M bond) and ionic character to TMCs, respectively. Therefore, physical properties of TMCs match with that of ceramic materials while, electronic properties with metals.

Table 1.1: Details of different physical properties of various TMCs. [36]

	Ti (TiC)	**Zr (ZrC)**	**Hf (HfC)**	**V (VC)**	**Nb (NbC)**	**Ta (TaC)**	**Cr (Cr_3C_2)**	**Mo (Mo_2C)**	**W (WC)**
Electronegativity difference	1.0	1.1	1.2	0.9	0.9	1.0	0.9	0.7	0.8
Metal lattice	HCP BCC	HCP BCC	HCP BCC	BCC	BCC	BCC	BCC	BCC	BCC
Carbide lattice	FCC	FCC	FCC	FCC	FCC	FCC	Orth.	Hex	Hex
R_c/R_m	0.526	0.483	0.486	0.576	0.530	0.529	0.609	0.556	0.553
Density change (%)	+8.1	+1.2	-5.1	-7.5	-9.0	-12.6	-7.2	-11.3	-18.1
Melt. point (MP, °C)	3067	3420	3928	2830	3600	3950	1810	2520	2870
MP_{MC}/MP_M	1.9	1.9	1.77	1.5	1.46	1.32	0.97	0.96	0.84
Hardness (GPa)	28-35	25.9	26.1	27.2	19.6	16.7	10-18	16-24	22
Modulus of elasticity (GPa)	410-510	350-440	350-510	430-430	338-580	285-560	344-400	535-535	620-720

It is well studied fact that TMCs (especially WC and Mo_2C) are suitable candidate for various fuel cell applications such as hydrogen evolution reaction (HER) and oxygen reduction reaction (ORR). Specifically, TMCs are more useful as catalyst support due to their good stability in acidic media and resistance to poisoning due to their electronic configuration which is similar to noble metals (Pt and Pd etc.) with better efficiency and reduced cost [43–45]. As far as electronic structure is concerned, such a good catalytic activity of TMCs is induced by the occupancy of metallic d-orbitals (near Fermi level) by carbon [46].

Among all the TMCs, WC is the most studied carbide compound which has been proposed to be used as cathodic catalyst for proton exchange membrane (PEM), microbial electrolysis [35,47–51]. In the same sequence, Mo_2C and NbC have been proposed to be active

catalyst support materials after WC for different electrochemical applications such as HER reactions, ORR reactions, MeOH electro-oxidation and supercapacitors [52–56].

1.6. Niobium carbide (NbC) – properties and its applications

The metal carbides with very high melting temperature (>2500 °C) are required for preparing crucibles to handle molten rare metals, heating elements for electric resistance furnaces in reducing or inert atmosphere and coating of dispersion fuel elements [57]. Despite of being used in such supercritical applications, NbC finds its usage in other various mechanical and chemical applications e.g. cutting tools, turbine blades, wear, corrosion resistant coating of steels and biological applications [36,37,57–59]. Due to better toughness, NbC finds its applications as reinforcement in different cermets (combination of metal and ceramic) to induce some ductility into it [38]. Moreover, NbC is also used in aerospace industries as the properties of Nb similar to Ta with lesser density enhancing the strength to weight ratio. Due to wide range of the solubility of carbon in rock salt structure of NbC, excellent electric and superconducting applications are also reported in literature [60]. Further, various physical, mechanical, electrical and thermal properties of NbC has been listed in table 1.2.

Table 1.2: Different properties of niobium carbide (NbC). *[# at 20 °C]*

Property	**Magnitude**
Crystal structure	Rock-salt (B1)
Space group	$Fm\bar{3}m$
Lattice parameter	4.4704 Å
C/Nb atomic radius ratio	0.53
Molecular weight	104.91 g/mole
Composition	$NbC_{0.7}$-$NbC_{1.0}$
Density	7.79 g/cm^3
Melting point	~3600 °C
Bond energy	16.32 eV
Heat of formation (at 298.15 K)	~140.5 kJ/mole
Thermal conductivity[#]	14.2 W/m.K
Electrical resistivity[#]	35 µohm-cm
Coefficient of thermal expansion (CTE)[#]	6.6×10^{-6} /°C
Transition temperature for super-conduction (T_c)	11.2 K
Hardness (VHN)	19.6 GPa
Young's modulus	340-580 GPa
Bulk modulus	296 GPa
Shear modulus	214 GPa
Poisson's ratio	0.21

1.6.1. NbC - phase diagram and crystal structure

Transition metal carbides (TMCs) consist of carbon atom located at the interstices of metal network based on the atomic radius ratio of carbon and metal i.e. C/M<0.59. Based

on the solid solubility of carbon in niobium, NbC pertains variable amount of lattice carbon (0.7-1.0). Figure 1.4 represents the binary phase diagram of Nb-NbC in which 4 different composition of Nb-C has been shown as NbC, zeta phase (Nb_4C_3), α-Nb_2C and β-Nb_2C based on C-content. Moreover, Nb-NbC system shows peritectic and eutectic transitions at 3080 °C ($NbC_{0.52}$) and 2335 °C ($NbC_{0.12}$), respectively [58]. Kempter *et al.* [61] observed that the variation in theoretical density of NbC_x cannot be used to explain unambiguous dependency of lattice constant and C/Nb ratio (as shown in table 1.3).

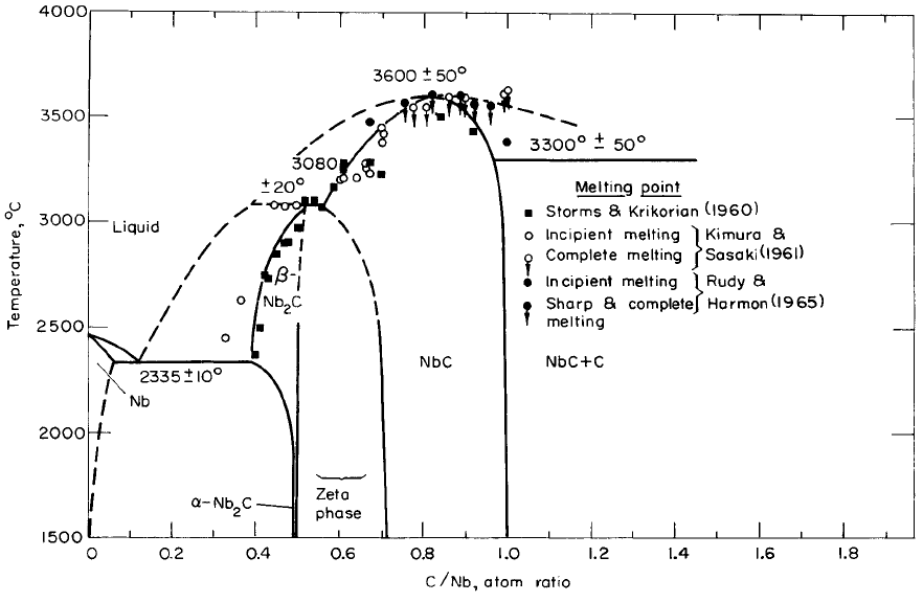

Figure 1.4: Binary phase diagram of Nb-NbC system showing the wide range of solubility (~0.7<C/Nb<1.0) of carbon in Nb lattice to form NbC [58].

Table 1.3: Variation of theoretical densities with respect to C/Nb ratio.

Composition	x = C/Nb	Density (g/cm^3)	Composition	x = C/Nb	Density (g/cm^3)
Nb	0.00	8.53	$NbC_{0.700}$	0.70	7.73
Nb_2C	0.50	7.95	$NbC_{1.0}$ *(extrapolation)*	1.00	7.79
$NbC_{0.788}$	0.78	7.71			

NbC possesses rock-salt structure having space group of Fm3m in which regular site of face centered cubic unit cell and octahedral voids are occupied by Nb and C atom, respectively. Metastable carbon deficient Nb-C system i.e. Nb_2C exhibits a transition from α-Nb_2C (orthogonal) to β-Nb_2C (trigonal) near 1200-1500 °C and β-Nb_2C (trigonal) to γ-Nb_2C (disordered hexagonal) above 2500 °C [62,63]. Still no literature is available for the transition of γ-Nb_2C to α-Nb_2C [62,63].

$$\alpha - Nb_2C \xleftrightarrow{\sim 1200^{\circ}C} \beta - Nb_2C \xleftrightarrow{\sim 2500^{\circ}C} \gamma - Nb_2C$$

Further, variable solubility of C in Nb lattice to execute NbC i.e. C/Nb = 0.7-1.0 resulted to different disordered NbC_x compositions e.g. Nb_8C_7, Nb_6C_5 and Nb_4C_3. Many

research groups have studied their ordered-disordered transition as a function of temperature and carbon content [64–66]. Moreover, Gusev and Rempel [64] proposed the formation of short range ordered trigonal and monoclinic superstructures of Nb_6C_5. They also suggested the degree of long-range ordering (η) as a function of C/Nb (x) ratio which can be expressed as follows;

$$\eta = \begin{cases} 6(1-\mathrm{x}) & \text{if } \mathrm{x} \geq \frac{5}{6} \\ \frac{6}{5}\mathrm{x} & \text{if } \mathrm{x} < \frac{5}{6} \end{cases} \quad (1.9)$$

Storms and Krikorian [66] calculated a general mathematical relationship between lattice constant and C/Nb (x) ratio over a range of NbC_x compositions. They suggested the increase in lattice constant with increasing 'x'. Here, 'x' is independent of temperature at which the heat treatment was employed. Further, Kempter *et al.* [61] described the variation profile of lattice constant with respect to C/Nb ratio with the help of following equation;

$$\mathrm{a(\dot{A})} = 4.09847 + 0.7128\left(\frac{\mathrm{C}}{\mathrm{Nb}}\right) - 0.34570(\mathrm{C/Nb})^2 \quad (1.10)$$

1.6.2. Applications of NbC

Some of the well-known hard metals have gained significant interest on material health and safety issue in which REACH (The European Registration, Evaluation, Authorization and Restriction of Chemical substance program) has listed Co and WC-Co dust as very toxic material for human health [42]. On the contrary for niobium (Nb), due to its excellent biocompatibility, any critical hazard for its carbide and oxides is not reported so far. Moreover, variable stoichiometry of NbC_x does not show any significant effect on biocompatibility of Ti-6Al-4V alloy for human body implantation [42,59,67].

Further, NbC is being widely used as micro-alloying element in steels used for pipelines, high performance cars and structural applications. It can also be used as secondary carbide phase in tool steels and hard-metals to enhance the respective wear resistance, hardness and to restrict the grain growth [68–72]. It also finds its usage in corrosion resistant applications due to excellent stability in chemical environment such as coating of bearing steel AISI52100 [70], AISI D2 steel disks [73] and AISI 1045 steel [74].

For fuel cell applications, NbC has emerged as a potential candidate for electrodes. Recently, Tolosa *et al.* [75] have suggested the use of NbC nanofibers to harvest NbC-CDC (niobium carbide derived carbon) and Nb_2O_5-C mats as high power supercapacitor and electrodes. Various electrochemical reaction with the help of NbC e.g. methanol oxidation [55], alcohol production [76] and H_2 evolution reactions (HERs) [52,53,77–79] is also reported.

1.6.3. Nano-crystalline NbC

Today's engineering world has been revolutionized by reducing the size (few nanometers) of conventional materials due to the modified properties at nano scale (order of 10^{-9} m). There are two major approaches to synthesize nanomaterials; 1) *Top-down* (breaking the larger sized crystal to obtain nanocrystal) and 2) *Bottom-up* approach (attachment of atoms/molecules/ions to achieve nanocrystal). Due to the distinguished surface to volume characteristics at nanoscale, materials possess very interesting optical characteristics with different morphologies. Development and applicability of nano NbC is still a very challenging task to industrialize the use of NbC as a potential candidate for mechanical, fuel cells and human body implantation applications. In the view of above discussion, some of the literature has been reviewed to synthesize nano crystalline NbC and its applicability as catalyst for photodegradation of organic effluents which is described in the next chapter.

References:

1 M. S. Babel and S. M. Wahid, *United Nations Environ. Program. Nairobi, Kenya Asian Inst. Technol. Bangkok, Thail.*, 2010, 1–45.
2 *UNESCO-World Water Assess. Program.*
3 M. A. Meetani, M. A. Rauf, S. Hisaindee, A. Khaleel, A. AlZamly and A. Ahmad, *RSC Adv.*, 2011, **1**, 490–497.
4 C. Zaharia, D. Suteu, A. Muresan, R. Muresan and A. Popescu, *Environ. Eng. Manag. J.*, 2009, **8**, 1359–1369.
5 UNEP, *A Snapshot of the World's Water Quality: Towards a global assessment*, 2016.
6 M. Mehrjouei, S. Müller and D. Möller, *Chem. Eng. J.*, 2015, **263**, 209–219.
7 J. Xiao, Y. Xie and H. Cao, *Chemosphere*, 2015, **121**, 1–17.
8 V. Colla, T. A. Branca, F. Rosito, C. Lucca, B. P. Vivas and V. M. Delmiro, *J. Clean. Prod.*, 2016, **130**, 103–115.
9 C. Y. Teh, P. M. Budiman, K. P. Y. Shak and T. Y. Wu, *Ind. Eng. Chem. Res.*, 2016, **55**, 4363–4389.
10 Y. Feng, L. Yang, J. Liu and B. E. Logan, *Environ. Sci. Water Res. Technol.*, 2016, **2**, 800–831.
11 S. De Gisi, G. Lofrano, M. Grassi and M. Notarnicola, *Sustain. Mater. Technol.*, 2016, **9**, 10–40.
12 L. Ai, C. Zhang and L. Meng, *J. Chem. Eng. Data*, 2011, **56**, 4217–4225.
13 Y. S. Ho, *J. Hazard. Mater.*, 2006, **136**, 681–689.
14 M. N. Chong, B. Jin, C. W. K. Chow and C. Saint, *Water Res.*, 2010, **44**, 2997–3027.
15 C. A. K. Gouvea, F. Wypych, S. G. Moraes, N. Duran, N. Nagata and P. Peralta-Zamora, *Chemosphere*, 2000, **40**, 433–440.
16 A. L. Linsebigler, G. Lu and J. T. Yates, *Chem. Rev.*, 1995, **95**, 735–758.
17 H. Li, Y. Zhou, W. Tu, J. Ye and Z. Zou, *Adv. Funct. Mater.*, 2015, **25**, 998–1013.
18 Y. Bu, Z. Chen, W. Li and B. Hou, *ACS Appl Mater Interfaces*, 2013, **5**, 12361–12368.
19 C. G. Silva, R. Juárez, T. Marino, R. Molinari and H. García, *J. Am. Chem. Soc.*, 2011, **133**, 595–602.
20 Y. Yang, Y. Guo, F. Liu, X. Yuan, Y. Guo, S. Zhang, W. Guo and M. Huo, *Appl. Catal. B Environ.*, 2013, **142**–**143**, 828–837.
21 B. Zhang, D. Zhang, Z. Xi, P. Wang, X. Pu, X. Shao and S. Yao, *Sep. Purif. Technol.*, 2017, **178**, 130–137.
22 M. Mittal, M. Sharma and O. P. Pandey, *Sol. Energy*, 2016, **125**, 51–64.
23 M. Sharma, T. Jain, S. Singh and O. P. Pandey, *Sol. Energy*, 2012, **86**, 626–633.
24 J. Dong, Y. Shi, C. Huang, Q. Wu, T. Zeng and W. Yao, *Appl. Catal. B Environ.*, 2019, **243**, 27–35.
25 Y. Pan, T. Zhou, J. Han, J. Hong, Y. Wang, W. Zhang and R. Xu, *Catal. Sci. Technol.*, 2016, **6**, 2206–2213.
26 H. Shi, G. Chen, C. Zhang and Z. Zou, *ACS Catal.*, 2014, **4**, 3637–3643.
27 J. Osuntokun and P. A. Ajibade, *J. Nanomater.*, , DOI:10.1155/2016/3296071.
28 D. J. Martin, G. Liu, S. J. A. Moniz, Y. Bi, A. M. Beale, J. Ye and J. Tang, *Chem. Soc. Rev.*, 2015, **44**, 7808–7828.
29 M. Banach and A. Makara, *J. Chem. Eng. Data*, 2011, **56**, 3095–3099.
30 G. Cruciani, *J. Phys. Chem. Solids*, 2006, **67**, 1973–1994.
31 A. Sclafani and J. M. Herrmann, *J. Phys. Chem.*, 1996, **100**, 13655–13661.
32 A. Gupta, M. Mittal, M. K. Singh, S. L. Suib and O. P. Pandey, *Sci. Rep.*, 2018, **8**, 13597.
33 Y. C. Kimmel, X. Xu, W. Yu, X. Yang and J. G. Chen, *ACS Catal.*, 2014, **4**, 1558–1562.
34 Z. Chen, D. Higgins, A. Yu and J. Zhang, *Energy Environ. Sci.*, 2011, **4**, 3167–3192.
35 D. V. Esposito, S. T. Hunt, A. L. Stottlemyer, K. D. Dobson, B. E. McCandless, R. W. Birkmire and J. G. Chen, *Angew. Chemie - Int. Ed.*, 2010, **49**, 9859–9862.
36 H. O. Pierson, *Handbook of Refractory Carbides and Nitrides*, Noyes Publications, 369 Fairview Avenue, Westwood, New Jerey, U.S.A., 1996.
37 S. T. Oyama, *The Chemistry of Transition Metal Carbides and Nitrides*, Blackie Academic

& Professional, an imprint of Chapman & Hall, Wester Cleddens Road, Bishopbriggs, Glassgow G64 2NZ, 1996.
38 S. G. Huang, R. L. Liu, L. Li, O. Van Der Biest and J. Vleugels, *Int. J. Refract. Met. Hard Mater.*, 2008, **26**, 389–395.
39 A. Singh, M. H. Modi, A. K. Sinha, R. Dhawan and G. S. Lodha, *Surf. Coatings Technol.*, 2015, **272**, 409–414.
40 S. Wannakao, N. Artrith, J. Limtrakul and A. M. Kolpak, *J. Phys. Chem. C*, 2017, **121**, 20306–20314.
41 L. Zhou, X. Zhang, L. Ma, J. Gao and Y. Jiang, *Biochem. Eng. J.*, 2017, **128**, 243–249.
42 H. Mohrbacher, M. Woydt, J. Vleugels and S. Huang, in *Advances in Materials Science for Environmental and Energy Technologies V*, Joh Wiley & Sons, Inc., Hoboken, New Jersy, 5th edn., 2016.
43 Y. Liu, T. G. Kelly, J. G. Chen and W. E. Mustain, *ACS Catal.*, 2013, **3**, 1184–1194.
44 J. B. Christian, S. P. E. Smith, M. S. Whittingham and H. D. Abruña, *Electrochem. commun.*, 2007, **9**, 2128–2132.
45 R. B. Levy and M. Boudart, *Science (80-.).*, 1973, **181**, 547–549.
46 L. H. Bennett, J. R. Cuthill, A. J. McAlister and N. E. Erickson, *Science (80-.).*, 1975, **187**, 859–859.
47 D. V. Esposito, S. T. Hunt, Y. C. Kimmel and J. G. Chen, *J. Am. Chem. Soc.*, 2012, **134**, 3025–3033.
48 F. Harnisch, G. Sievers and U. Schroder, *Appl. Catal. B Environ.*, 2009, **89**, 455–458.
49 M. Rosenbaum, F. Zhao, M. Quaas, H. Wulff, U. Schröder and F. Scholz, *Appl. Catal. B Environ.*, 2007, **74**, 261–269.
50 F. Harnisch, U. Schröder, M. Quaas and F. Scholz, *Appl. Catal. B Environ.*, 2009, **87**, 63–69.
51 H. Zheng, J. Huang, W. Wang and C. Ma, *Electrochem. commun.*, 2005, **7**, 1045–1049.
52 S. Meyer, A. V Nikiforov, I. M. Petrushina, K. Kohler, E. Christensen, J. O. Jensen and N. J. Bjerrum, *Int. J. Hydrog. Energy*, 2015, **40**, 2905–2911.
53 E. Coy, L. Yate, D. P. Valencia, W. Aperador, K. Siuzdak, P. Torruella, E. Azanza, S. Estrade, I. Iatsunskyi, F. Peiro, X. Zhang, J. Tejada and R. F. Ziolo, *ACS Appl. Mater. Interfaces*, 2017, **9**, 30872–30879.
54 L. Elbaz, C. R. Kreller, N. J. Henson and E. L. Brosha, *J. Electroanal. Chem.*, 2014, **720–721**, 34–40.
55 Z. Qiu, H. Huang, J. Du, T. Feng, W. Zhang, Y. Gan and X. Tao, *J. Phys. Chem. C*, 2013, **117**, 13770–13775.
56 H. Zhang, J. Liu, Z. Tian, Y. Ye, Y. Cai, C. Liang and K. Terabe, *Carbon N. Y.*, 2016, **100**, 590–599.
57 T. V. Kosolapova, *CARBIDES: Properties, Production and Applications*, Plenum Press, New York, London, 1971.
58 E. K. Storms, *The Refractory Carbides*, Academic Press Inc., 111 Fifth Avenue, New York 10003, 1967.
59 M. Braic, V. Braic, M. Balaceanu, A. Vladescu, C. N. Zoita, I. Titorencu, V. Jinga and F. Miculescu, *Thin Solid Films*, 2011, **519**, 4064–4068.
60 Y. Kumashiro, Ed., *Electric Refractory Materials*, CRC Press, 1st edn., 2000.
61 C. P. Kempter, E. K. Storms and R. J. Fries, *J. Chem. Phys.*, 1960, **33**, 1873–1874.
62 B. Vishwanadh, K. V. M. Krishna, A. Upadhyay, R. Banerjee, A. Arya, R. Tewari, H. L. Fraser and G. K. Dey, *Acta Mater.*, 2016, **108**, 186–196.
63 E. Rudy and C. E. Brukl, *J. Am. Ceram. Soc.*, 1967, **50**, 265–268.
64 A. I. Gusev and A. A. Rempel, *Phys. Status Solidi*, 1986, **93**, 71–80.
65 M. G. Kostenko, S. V. Sharf and A. A. Rempel, *Bull. Russ. Acad. Sci. Phys.*, 2017, **81**, 373–376.
66 E. K. Storms and N. H. Krikorian, *J. Phys. Chem.*, 1959, **63**, 1747–1749.
67 L. Yate, L. E. Coy, D. Gregurec, W. Aperador, S. E. Moya and G. Wang, *ACS Appl. Mater. Interfaces*, 2015, **7**, 6351–6358.
68 M. Woydt, H. Mohrbacher, J. Vleugels and S. Huang, *Met. Powder Rep.*, , DOI:10.1016/j.mprp.2015.12.010.

69 S. Qin, B. Liao, F. Xiao and L. Mao, *Mater. Manuf. Process.*, 2015, **30**, 116–121.
70 F. A. P. Fernandes, J. Gallego, C. A. Picon, G. Tremiliosi Filho and L. C. Casteletti, *Surf. Coatings Technol.*, 2015, **279**, 112–117.
71 M. Woydt and H. Mohrbacher, *Wear*, 2013, **306**, 126–130.
72 P. Montenegro, J. Gomes, R. Rego and A. Borille, *Int. J. Refract. Met. Hard Mater.*, 2018, **70**, 116–123.
73 F. E. Castillejo, D. M. Marulanda, J. J. Olaya and J. E. Alfonso, *Surf. Coatings Technol.*, 2014, **254**, 104–111.
74 A. OrjuelaG, R. Rincón and J. J. Olaya, *Surf. Coatings Technol.*, 2014, **259**, 667–675.
75 A. Tolosa, B. Krüner, S. Fleischmann, N. Jäckel, M. Zeiger, M. Aslan, I. Grobelsek and V. Presser, *J. Mater. Chem. A*, 2016, **4**, 16003–16016.
76 J. M. Christensen, L. D. L. Duchstein, J. B. Wagner, P. A. Jensen, B. Temel and A. D. Jensen, *Ind. Eng. Chem. Res.*, 2012, **51**, 4161–4172.
77 B. M. Tackett, Y. C. Kimmel and J. G. Chen, *Int. J. Hydrogen Energy*, 2016, **41**, 5948–5954.
78 W.-F. Chen, J. T. Muckerman and E. Fujita, *Chem. Commun.*, 2013, **49**, 8896.
79 S. Wirth, F. Harnisch, M. Weinmann and U. Schröder, *Appl. Catal. B Environ.*, 2012, **126**, 225–230.

CHAPTER 2 LITERATURE REVIEW

Overview

Synthesis of porous nano NbC is a critical task as far as stability of nano materials is concerned. Several research groups have developed different synthesis processes to obtain nano NbC with reduced efforts and better efficiency. However, the properties of these synthesized nano NbC differs from one synthesis route to other. A detailed review of the synthesis of nano NbC using different precursors and environment has been presented in this chapter.

As a result of critical review, it has been found that the synthesis parameters (temperature, time, precursors, environment and apparatus used) play an important role in achieving particular morphological features of nano NbC. Based on the critical analysis of synthesis parameters, a strategic plan to synthesize nano NbC at relatively low temperature has been outlined. A critical review of the applications of TMCs as a photocatalyst has also been presented.

All the transition metals exhibit lesser affinity towards carbon to form metal carbides (WC, ZrC, TiC, Mo_2C and NbC) than oxygen forming semiconducting metal oxides (Nb_2O_5, WO_3, ZrO_2 etc.). Such high affinity towards oxygen hinders the carburization of transition metals which makes their synthesis a tedious process. Specifically, synthesis of NbC requires very high temperature (>1000 °C) to carburize Nb_2O_5 yielding NbC [1,2]. Apart from Nb_2O_5, many research groups have used other Nb-precursors such as niobium iodide (NbI_4), niobium chloride ($NbCl_5$) and other organic complex precursors of Nb. The use of different reagents at different synthesis conditions has also been investigated to obtain NbC with desired characteristics. An overview of the proposed synthesis methods and their respective outcomes has been discussed in this chapter.

2.1. Synthesis of nano niobium carbide (NbC)

In mid-20th century (1954), NbC was synthesized via carbothermal route in which very high temperature (1600-1700 °C) was adopted and variation of carbon content was studied to establish stoichiometry [3]. In 1987, Smith *et al.* [4] reviewed the temperature-composition relationship of Nb and C to form different phases such as NbC, Nb_6C_5, Nb_4C_3 and Nb_2C. Moreover, they have also proposed the relationship between the enthalpy of formation and composition of NbC_x which can be described as $\Delta_f H\left(298.15\ K; \frac{kJ}{mol\ Nb}\right) = -56.8 - 86.0x$. Gibb's free energy related to $NbC_{0.98}$ has been estimated to follow $\Delta_f G\left(\frac{J}{mol\ Nb}\right) = -138200 + 8.326T - 1.001T\ln T + 5.255 \times 10^{-4}T^2 + 5.145 \times 10^5 T^{-1}$ relationship with respect to temperature which has been considered as a better experimental approach [4]. Further, carbothermal treatment of Nb-oxides was implemented as commercial process to obtain NbC. In the same sequence, some other research groups have developed different processing techniques to obtain NbC which are summarized below:

2.1.1. Carbothermal reaction:

2.1.1.1. Heating under high pressure (Autoclaving)

Kobayashi *et al.* [5] produced a conducting nanowires consisting of NbC encapsulated carbon nanotubes (CNTs) which can tailor the electrical and mechanical properties. They obtained NbC filled CNTs by heating the mixture of $NbCl_5$ and CNTs at 900 °C (3.0 h) under reducing H_2 atmosphere at 10^5 Pa. They confirmed the filling of NbC inside the CNTs through Raman and HRTEM. Further, it has been observed that metallic NbC@CNTs exhibited decreasing relative resistance with respect to decreasing

temperature. While, empty CNTs exhibited semiconductor type relationship with temperature i.e. decreasing resistance with increasing temperature.

To reduce the working temperature, some of the research groups have also obtained NbC powder at relatively low temperature by using autoclave. Chen *et al.* [6] successfully achieved NbC nano particles by using 50 ml stainless steel autoclave under Ar atmosphere at 550 °C with 6.0 h of holding time. They used Nb_2O_5, Mg powder and CH_3COOK (molar ratio = 1.0:8.3:1.3, respectively) as Nb- source, reducing agent and C- source, respectively. According to the report, as-synthesized powder sample required acid leaching by dilute HCl to remove MgO and K_2CO_3 as shown in following reactions;

$$3Nb_2O_5 + 17Mg + 4CH_3COOK \rightarrow 6NbC + 17MgO + 2K_2CO_3 + 6H_2 \quad (2.1)$$

$$K_2CO_3 + 2HCl \rightarrow 2KCl + H_2O + CO_2 \quad (2.2)$$

$$MgO + 2HCl \rightarrow MgCl_2 + H_2O \quad (2.3)$$

Further, they have proposed the applicability of NbC nanoparticles as photocatalyst to degrade rhodamine blue (RhB) dye under the exposure of 300 W Hg lamp. They have demonstrated the effect of irradiation for 12 h after which absorption peak associated to RhB dye was disappeared which might be related to decolorization or photodegradation of dye molecule.

Ma *et al.* [7] have also reported the similar synthesis process by using autoclave at 550 °C for 10 h of holding time under inert (Ar) atmosphere. They have also taken Nb_2O_5, Mg as Nb source and reducing agent (respectively) with $MgCO_3$ as carbon source and reducing agent, both. They confirmed the nano-crystalline phase formation with XRD and TEM results. Further, they studied the thermal stability of the synthesized NbC nanoparticles through thermal gravimetry/differential thermal analysis (TGA/DTA) upto 1000 °C. TGA/DTA results suggested the exothermic oxidation of NbC resulting Nb_2O_5 at 540 °C due to nano-regime and it has also been suggested that the synthesized NbC nanoparticles can be used below 400 °C with excellent oxidation resistance.

2.1.1.2. Heating under normal pressure

In 2015, Chen *et al.* [8] proposed excellent electrocatalytic performance of NbC/TiC aerogels which were prepared at 800 °C under vacuum (~0.67 Pa) in sealed quartz tube. For the preparation of highly porous (79.36 vol%) NbC sample, metallic Nb and iodine were reacted resulting gaseous NbI_4 complex followed by carbonization with the help of carbon aerogel plate as templet within the sealed quartz tube for 6.0 h at 800 °C. As per the proposed mechanism, the formation of Nb-I complex occurred at low temperature (<500

°C). However, the heating above 550 °C led to the decomposition of Nb-complex incorporating the metal particles on the carbon templet resulting the formation of NbC through diffusion-controlled layer growth mechanism. Further, they compared the electrocatalytic activity of TiC, NbC and C aerogels for I_3^-/I^- reduction reaction in dye sensitized solar cells (DSSCs). They observed the better catalytic activity of carbide-carbon aerogels (Tafel slope = 128 mV/dec) due to the synergistic contact between both components as compared to carbide aerogels (Tafel slope = 330 mV/dec). Moreover, TiC counter electrodes exhibited higher power conversion efficiency (PCE) i.e. 6.1% than NbC and carbon aerogels (4.1% and 1.4%, respectively) due to higher current density and lower charge transfer resistance.

Similarly, Atchison *et al.* [9] also proposed a multistep process in which a niobium complex fibers were prepared using niobium n-butoxide (2.47 ml) and acetic anhydride (0.55 ml). These fibers were obtained from the solution of dimethyl formamide (DMF, 25 ml) and PVP (3.0 g) at applied potential of 23 kV. Thereafter, fibers were aged in ambient humidity for 72 h followed by two step heat treatment; (i) at low temperature (400 °C for 3.0 h with 5 °C/min) and (ii) at high temperature (1100, 1300, 1500 and 1700 °C for 4.0 h with 5 °C/min). Such multi-step synthesis route exhibited uniform thickness (65±32 nm) of annealed fibers at 1700 °C. Moreover, the fabricated fibers consisted of adhered NbC nanoparticles.

Similarly, Witkowski *et al.* [10] suggested the formation mechanism of NbC from Nb_2O_5 through temperature programmed reaction (TPR) method in which oxide precursor was heated upto 1100 °C with a heating rate of 1-2 °C/min and kept for 12 h under the flow of CH_4/H_2 mixture (1:10; volume). Thereafter, the heated sample was rapidly cooled to room temperature followed by passivation (O_2/He gaseous mixture). With the help of this experiment, diffusion of oxygen into gaseous state has been found as rate determining step which was responsible for the formation of NbC at nano/micro regime. They suggested that a fine layer of NbC get deposited on the Nb-precursor in the beginning of the chemical reaction which would further reduce the precursor resulting the diffusion of carbon inwards and oxygen outwards. Due to the simultaneous diffusion of carbon and oxygen, various phases of carbon deficient NbC has been obtained such as Nb_2C, Nb_4C_3 and Nb_6C_5.

Medeiros *et al.* [11] have also adopted TPR route to obtain NbC powder through the carburization of Nb precursor i.e. $(NH_4)_3[NbO(C_2O_4)_8].xH_2O$ at 950 °C (@ 5 °C/min) for 2.0 h under CH_4/H_2 atmosphere (gas flow 20 ltr/h). Further, the synthesized product was used to study its effect on the grain growth behavior of Co-WC composite. A comparative

study among bare Co-WC, Co-WC-$NbC_{commercial}$ and Co-WC-$NbC_{prepared}$ has revealed that incorporation of prepared NbC enhanced the hardness (1776 to 1827; HV50) and inhibited the grain growth of WC as compared to commercial NbC.

Shimada *et al.* [12] prepared NbC through solid state reaction method using metal oxide precursor and carbon (charcoal and graphite powder) with variable molar ratios (7, 10 and 12). The mixture of reactants was heated up to different temperatures (1000-1200 °C) for 120 min under Ar or Ar/H_2 atmosphere using different containers (Al_2O_3 boat, graphite boat, graphite crucible and covered graphite crucible). Depending upon the nature of carbon, it was observed that charcoal initiated the formation of NbC at lower temperature i.e. 1000 °C as compared to that with graphite (1150 °C). But, in both the cases, chemical reaction was completed around 1200 °C to get NbC with lesser reaction time i.e. 40 and 70 min (respectively) as compared to lower temperature (~1100 °C).

Similar work was also done by Silva *et al.* [13] in which TPR process was adopted to probe the synthesis mechanism of NbC from Nb_2O_5 under CH_4/H_2 (20% v/v) with variable flow and heating rates. In the different sets of experiments, the evolved gases were charged to mass spectrometer to monitor the reaction byproducts (H_2, CH_4, CO, CO_2 and H_2O). Further, the product at different test conditions were quenched and characterized by XRD for the determination of crystallographic features (phase formation). It has been observed that the complete transformation of Nb_2O_5 to NbC followed two simultaneous steps; i) reduction (formation of NbO_2) and ii) *in-situ* reduction carburization (formation of NbC). They have also proposed the transformation pathway that can be illustrated as follows;

$$Nb_2O_5 \rightarrow NbO_2 \rightarrow [NbC_xO_y] \rightarrow NbC \quad (2.4)$$

Xu *et al.* [14] developed solid cage shaped NbC crystals through heating a multi-component setup to 1020-1520 °C @ 15 °C/min for 0.25-0.5 h under N_2 environment (0.1 MPa). This setup consisted of covered two graphite cubicles (one inside another) separated by activated carbon powder and inner crucible was filled with a mixture of Nb_2O_5, NaF and $C_{12}H_{22}O_{11}$ (1:4:4). They observed that the reaction product consists of NbC_x whiskers with 1.5-15.0 μm (diameter) and 0.25-1.5 μm (thickness).

Fukunaga *et al.* [15] have taken quartz ampoules containing powder mixture (Nb, CNTs and iodine; 10:10:1) filled with Ar gas to obtain NbC nanorods and nanoparticles. These ampoules were heated to different temperatures (620-1000 °C) for 120 h to obtain single phase NbC following the chemical reaction ($C + NbI_5(gas) \rightarrow NbC + 2.5I_2$). With the increase in treatment temperature (620-1000 °C), amount of lattice carbon (x) in NbC_x

(estimated by Vegard's law) increased from 0.8 to 1.02, respectively. They also reported that increasing temperature induced the transformation of NbC nanorods into spheroidal particles of NbC.

Nabil *et al.* [16] suggested the use of NbC/C nanotubes as catalyst support for proton exchange membrane fuel cells as cathode material. For the fabrication of NbC/C nanotubes, a multistep route was adopted in which Nb_2O_5 fibers were prepared by using electrospinning technique and calcined at 600 °C for 3 h and followed by heating under carburizing atmosphere (10% CH_4/H_2) at 1100 °C. With the help of various spectroscopic techniques (XRD, Raman, XPS and BET), graphene coated NbC tubes exhibited intergranular slit shaped porosity (meso- and macro-) with H3-type N_2 sorption isotherm. Electrochemical studies revealed the higher stability (retained 31% of electrochemical surface area; ECSA) of NbC/C supported Pt electrode after 10000 voltage cycles as compared to traditional 50%$_{wt}$ Pt/C (Alfa-Aesar) electrode that retained only 5%. They also observed the participation of oxide layer in enhancing the corrosion resistance of NbC/C supported Pt electrode for ORR reaction in 0.1M $HClO_4$.

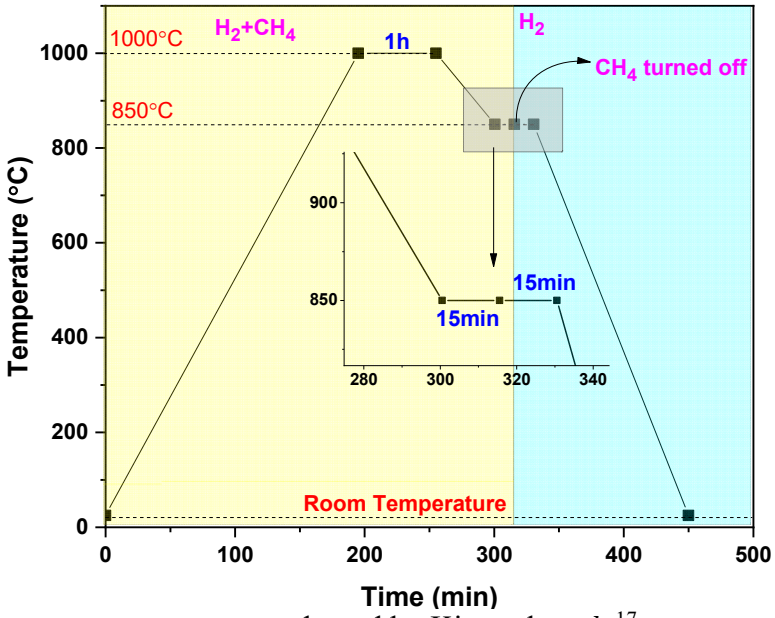

Figure 2.1: Heat treatment program adopted by Kimmel *et al.* [17].

Kimmel *et al.* [17] have synthesized NbC through carburization of Nb foil under H_2/CH_4 environment. The treatment cycle was divided into various sections and shown in figure 2.1. Initially Nb foil (as-procured) was treated with acetone and 0.3M NaOH prior to heat treatment which was subdivided into 2 steps, heating to 1000 °C for 1h followed by 850 °C (@ 3.3 °C/min) for 15 min (for the heat treatment, 122 cm^3/min (H_2) and 32.6 cm^3/min (CH_4)). Thereafter, at this temperature (850 °C), flow of CH_4 was turned off and allowed to cool to room temperature after 15 min. Further, electrocatalytic studies revealed

that synthesized NbC did not exhibit as much stability as TaC, TiC and ZrC (prepared via similar methodology) under acidic (0.5M H_2SO_4) and basic (0.1M KOH) medium, both. Further, Tackett *et al.* [18] studied the catalytic response of as-synthesized NbC thin film for HER reaction with the loading of noble metals (Pt and Ag) in tap water to understand the impurity resistance of electrocatalyst. They observed the reduced HER activity of Pt/NbC film in alkaline medium as compared to that in acidic medium as a function of the thickness of metallic coating. Moreover, excellent impurity resistance has been exhibited by Pt/NbC catalyst in the presence of tap water resembling the HER stability (in acidic and basic medium) in the presence of pure water.

Qiu *et al.* [19] suggested the applicability of NbC nanowires (NWs) supported Pt nanoparticles as efficient catalyst for direct methanol fuel cells (DMFCs). For the considered application, they have used bamboo chips (2.5×0.7×0.2 mm) as templet to grow NbC NWs. In the first step, bamboo chips were immersed in Nb-Ni-F emulsion prepared by dissolving Nb_2O_5, NaF and $Ni(NO_3).6H_2O$ in ethanol. The cured (at 110 °C for 2.0 h) emulsion was heated to 1250 °C for 2.0 h under Ar atmosphere (350 cubic centimeter per minute (sccm)). This prepared catalyst has also compared with conventional Pt/C and Pt/bamboo charcoal catalysts in which Pt/NbC NWs exhibited far superior characteristics with forward current density (766.1 mA/mg Pt) and stability (2.4% current loss after 200 cycles) for electrocatalytic methanol oxidation application (0.1M H_2SO_4 + 1.0M CH_3OH @ 20 mV s^{-1}). While, pure NbC NWs did not exhibit any activity towards electrocatalytic methanol oxidation reaction. The higher ratio of peak currents of forward (I_f) and backward (I_b) scans for NbC NWs supported Pt catalyst illustrated the better poisoning tolerance than other considered catalysts (NbC NWs, Pt/C and Pt/bamboo charcoal).

2.1.2. Synthesis of thin or thick films

Zhang *et al.* [20] proposed an alternate compound i.e. NbC as wear resistant coating by depositing it on Si (100) substrate. They studied the effect of carbon content during the deposition using a pure Nb target in DC reactive magnetron sputtering under Ar and CH_4 atmosphere. During the sputtering experiments, amount of carbon was controlled by varying the flow of CH_4 (4-22 sccm at STP) and prior to deposition, target was pre-sputtered by Ar^+ to remove oxide layer for 10 min. Further, 0.3 A and -60 V were used as applied current and DC bias voltage for Nb target (respectively). The enhanced feasibility of the formation of NbC was observed with the increasing flow of CH_4 to 18.0 sccm. While,

at higher flow rate 22.0 sccm, broadened diffraction peaks of NbC were observed which were associated to increased lattice distortion.

Yate *et al.* [21] have studied the electrical and mechanical properties of NbC thin films deposited on Si (100) using Nb and C target in reactive magnetron sputtering under vacuum (10^{-7} Pa). The effect of composition on above mentioned properties was observed by varying applied power to Nb target (0-230 W) keeping carbon target DC power constant (380 W). Reduced content of free carbon was observed with the increasing applied power and 230 W yielded carbon free NbC polycrystalline film. Further, maximum hardness and elastic recovery of deposited film (at 100 W) was observed as 22.5 GPa and 86%, respectively. While, increased free carbon content at lower power resulted to decrement in crystallite size of NbC inducing lesser hardness. Moreover, film deposited at 100 W (Nb target) exhibited better conductivity (2.1×10^6 S/m) at room temperature (except pure Nb film; 6.2×10^6 S/m) than other samples, thus making its applicability in flexible electronics. Similarly, Coy *et al.* [22] studied the effect of Nb target voltage on the mechanical properties and catalytic activity of NbC thin film electrode for electrochemical hydrogen evolution reaction (HER). Further, the deposited thin film samples consisted C-C graphitic amorphous tissue coatings around NbC nanocrystals enhancing the mechanical and catalytic performance as compared to their bulk and powdered forms. They observed that the deposited film at 100 W (as Nb target voltage) exhibited higher current density as compared to other operating voltages in 0.1M H_2SO_4 as electrolyte. 28 and 35 mV/dec were calculated as Tafel slopes for Pt and NbC (100 W) samples (respectively) suggesting the role of Volmer-Tafel (formation of H_{ads} followed by the recombination of H_{ads} resulting H_2) mechanism for H_2 evolution. As a result of terahertz measurements, electrical conductivity of the samples decreased with increasing amount of free carbon and smaller NbC grains. Further, they have also postulated that high surface area, electrical conductivity and amount of free carbon influenced the electrocatalytic reaction by providing active sites and charge transfer phenomenon (respectively).

Similarly, Liao *et al.* [23] studied the effect of Ar pressure (0.5-2.0 Pa) on NbC thin film deposition on Si (100) using rf magnetic sputtering. It was found that low Ar pressure induced poor crystallinity of NbC and increased amount of free carbon on Si (100). Moreover, decreasing C/Nb ratio (x = 1.51 to 1.25) was also observed with the increase in the Ar pressure from 0.5 to 2.0 Pa. Further, the transformation of NbC film to niobium oxide was observed when oxygen pressure has been increased to 15% of Ar pressure. They

have proposed that the controlled oxygen flow (during deposition) purified and prevented the NbC film from oxidation through oxygen etching mechanism:

$$(NbC_x)C + 2O \rightarrow NbC_x + CO_2 \quad (2.5)$$

Yate *et al.* [24] suggested the biological engineering application of NbC-C nanocomposite films for hard tissue implantation due to its high hardness (22.5 GPa), young's modulus (191.7 GPa), elastic recovery (85%) and excellent biocompatibility. They have adopted non-reactive and reactive magnetron sputtering using Si (100), glass and AISI316LVM steel substrates at 10^{-7} Pa pressure. For the deposition of amorphous carbon and NbC, they used 2.0-inch elemental targets of carbon (purity 99.999%) and Nb (purity 99.95%) in confocal configuration at 0.25 Pa pressure of pure Ar. Prior to the deposition of NbC, fine layer of Nb (~30 nm) was deposited onto substrate to enhance the adhesion. Biocompatibility and bioactivity (in vitro cell experiments with preosteoblasts; MC3T3-E1) of the films suggested that NbC film enhanced the cell adhesion and alkaline phosphate activity of the cultured cells.

Meyer *et al.* [25] studied the medium temperature (~260 °C) catalytic behavior of various TMCs (WC, Mo_2C, NbC and TaC) wires for electrocatalytic HER reactions in molten KH_2PO_4 as electrolyte. For the synthesis of TM-TMC wires, metallic wires (W, Mo, Nb and Ta) were heated to temperatures (700, 600, 450 and 550 °C, respectively) under oxidative environment (20% O_2/Ar) to form their oxides (WO_3, MoO_3, Nb_2O_5 and Ta_2O_5), followed by heating to higher temperatures (900, 750, 900 and 950 °C, respectively) under carburizing atmosphere (25% CH_4/H_2) resulting the transformation of metallic wires into WC, Mo_2C, NbC and TaC on the surface of wires. Further, it was observed that the electrochemical generation of H_2 was controlled by the dissociation of $H_2PO_4^-$ anion in molten KH_2PO_4 through $H_2PO_4^- \leftrightarrow H^+ + HPO_4^{2-} \leftrightarrow 2H^+ + PO_4^{3-}$ and $2H^+ + 2e^- \rightarrow H_2$. They have also observed that electrocatalytic activity of TMCs is different than that has been observed at room temperatures. Even at relatively high temperature (260 °C), WC exhibited better catalytic activity than Pt wire after 3rd cycles and the reduction of onset reduction potential (in terms of HER activity) was observed in following order: $WC > Pt \cong Mo_2C > NbC > TaC$.

2.1.3. Miscellaneous:

Shiri *et al.* [26] have studied the compromised electrical conductivity with enhanced mechanical (hardness and wear resistance) properties for electrical contact application. They have successfully designed the pellet of Cu-NbC nanocomposite with variable

concentration of NbC across thickness. They adopted two-step process in which ball-milled powder (Cu, Nb and graphite for 7.0 h), 5 layers of different concentration of NbC (0, 3.74, 8.96, 12.07, 15%) were stacked and sintered at 900 °C for 1.0 h under Ar atmosphere. They have concluded that functional gradient Cu/NbC structure exhibited excellent wear resistance and electrical conductivity (75.83% IACS; International Annealed Copper Standard) through NbC and Cu network, respectively. Zhang *et al.* [27] proposed a Nb_2O_5/C/NbC hybrid as electrode for charge storage applications. For the preparation, freshly prepared Nb_2AlC was etched with the help of concentrated hydrofluoric acid for 90 h at room temperature and washed several times to attain pH~4. Thereafter, prepared powder sample was oxidized by CO_2 (@150 sccm) at 800 °C for 1 h. The partially oxidized samples exhibited T-Nb_2O_5 (orthorhombic) /carbon/Nb_2CT_x hybrid structure with excellent charge storage capacity of 330 C/g and 660 mF/cm^2 over charging-discharging period of 4 min in 1M $LiClO_4$/EC/DMC as electrolyte. Same sample (partially oxidized Nb_2CT_x) also exhibited significant charge storage capacity of 430 mF/cm^2 even at faster charge-discharge time i.e. 1 min.

Grigor'ev and Sinel'nikova [28] fabricated single crystals of NbC having different carbon concentration in the lattice ($NbC_{0.78}$–$NbC_{0.82}$) as it exhibits wide range of solubility of carbon. They have varied the concentration of carbon by adding the appropriate amount of niobium to $NbC_{0.97}$ via arc-plasma technique using NbC single crystal with <100> orientation as seed. All the considered composition did not exhibit any significant variation in mechanical properties (resistance to crack and hardness) with 10^5 cm^{-2} as average dislocation density. Moreover, it has also been found that the prepared samples exhibited brittle failure through {111} <110> slip system.

Storms and Krikorian [29] studied the variation of lattice constant with respect to the composition of NbC_x; where x represents the carbon content in the NbC unit cell. They prepared the samples by heating the pellet of variable composition of treated C and Nb at 3000 °C for 30 min under vacuum. Thereafter, prepared samples were pulverized before any characterization. Each sample was repeated several times to ensure the results obtained from XRD test and it was found that lattice constant (a) can be related to mole ratio of C and Nb as; $a(\dot{A}) = 4.4704 - 0.02391x - 0.3586x^2$. With respect to these observations, it was observed that lattice constant deceased with decreasing carbon content that was independent of the working temperature for single phase region of phase diagram. While in two phase region, phase composition of NbC has followed the phase boundary with

respect to temperature (under equilibrium) resulting the temperature dependent lattice constant.

Samson *et al.* [30] studied the effect of pulse duration on the structural features of deposited film of NbC on Si (100) under vacuum (1.5×10^{-4} Pa) at 500 °C. For the same objective, pulse laser ablation-deposition method was adopted with two different lasers; (i) Nd:glass laser (527 nm, τ = 250 fs, repetition rate = 10 Hz) and (ii) Nd:YAG laser (532 nm, τ = 10 ns, repetition rate = 10 Hz). It was found that the shorter pulse duration i.e. 250 fs resulted in a compact layer comprising of the coalesced nanoparticles with average size of around 10 nm whereas, pulse duration of 10ns led to the formation of an amorphous film.

Recently, Yang *et al.* [31] proposed the use of NaCl-KCl molten salt as reaction medium to provide carburization pathway. They have heated the mixture of $NbCl_5$, Nb (Nb source) and acetylene black (carbon source) in the presence of molten salt mixture at different temperatures (800 and 900 °C) and holding times (0.5-5.0 h). They observed that higher temperature and $NbCl_5$/Nb ratio supported the formation of NbC following the transformation of Nb (V) to Nb (IV) to NbC on acetylene black as templet.

2.2. Transformation of waste to engineering material

Considering the above discussed literature for the synthesis of NbC at relatively lower inputs with desired properties, it has become very critical to state the current status of the different kinds of waste products in order to utilize it for the development of engineering materials. In today's world, use of cigarettes has become disaster for environment pollution (air pollution and as well as soil pollution). Recently, Lee *et al.* [32] proposed the use of used cigarette filters to develop energy storage material with very high surface area (~1600 m^2/g). They have achieved ultra-high surface area that too with just heat treatment at 900 °C under Ar and NH_3 atmosphere. Heat treatment of cigarettes filters under NH_3 led to the attachment of N to the carbon fibers and Ti resulting pyrrolic, pyridine and TiN (respectively). This N-attached carbon fiber exhibited 153.8 Fg^{-1} (SSA=1634 m^2g^{-1}) which is very high as compared to 125.0 Fg^{-1} (SSA=1989 m^2g^{-1}) with a stability upto 6000 cycles.

Parthenium hysterophorous, commonly known as carrot grass, has been designated as agricultural waste which is an obnoxious weed inducing the soil infertility and diseases to livestock in South Asian countries [33–36]. Various research groups are examining its utilization as an engineering material for different applications such as ethanol production, heavy metal (Hg^{2+}, Cd^{2+}, Fe^{2+} and Cr^{6+}) removal from industrial waste water, oxalic acid

production, organic pollutant treatment (methylene blue, rhodamine B, portion orange, acid violet 17 and malachite green), phenol, p-cresol and producing biochar [37–45].

2.3. Gaps in the study

Based on the literature, synthesis of a refractory compound specifically NbC requires relatively high temperature under inert (Ar) or reducing (CH_4/H_2) atmosphere and specific precursors (Nb_2O_5, Nb powder and Nb foil etc.). Even, some of the research groups have also designed special apparatus to achieve desired characteristics [14,46,47]. *Ma et al.* [7] proposed the single step synthesis of nanocrystalline NbC at 550 °C using stainless autoclave without any discussion on the effect of synthesis parameters on structural and morphological features. As per the available literature of different TMCs (WC, VC and TaC), different hydrocarbons (ethanol, acetone and hexane) induced the fragmentation of oxide precursor due to hydrogen embrittlement under high working vapor pressure of these liquid compounds [48–52]. Moreover, effect of different routes and Nb-precursors has been explored thoroughly but, it lacks in the responsible structural and thermodynamic mechanism to yield nano-sized NbC form micro-sized precursor(s). Apart from above mentioned gaseous and liquid carbon source(s), the formation of NbC by using solid carbon precursor is yet to be explored. Therefore, some laboratory chemicals and organic wastes can be utilized as carbon source to establish a detailed mechanism rendering NbC at nano-scale. Due to the variable solubility of carbon in Nb lattice forming NbC_x, it is essential to optimize the C/Nb ratio to achieve considerable catalytic performance of as-synthesized samples.

As far as photocatalytic activity of TMCs is concerned, a limited number of articles are available [6,53,54]. Chen *et al.* [6,53] explored the photocatalytic performance of NbC and TiC by degrading rhodamine blue (RhB) dye as model organic compound under UV-visible illumination (300 W Hg lamp). Further, they have also observed the better photocatalytic activity of nanosized TiC as compared to micro-sized TiC. The removal of RhB dye might be related to discoloration of aqueous solution due to adsorption of dye molecule on the substrate. The observed trend was reported based on absorbance spectra of dye solution only. They have not provided sufficient and logical explanation of such optical response of synthesized NbC and TiC, both. Further, a detailed discussion on the pathway of photo-chemical reactions were also missing from the respective reports. While, Mashtalir *et al.* [54] have studied the removal of methylene blue (MB) dye with the help of MXene ($Ti_3C_2T_x$) under UV irradiation. They suggested that water is not a good medium to study the

photocatalytic performance of $Ti_3C_2T_x$ due to its instability in water. Further, they have also not given the detailed mechanism responsible for the excellent adsorption and photodegradation efficiency of $Ti_3C_2T_x$. In 2010, Kirihara *et al.* [55] proposed the applicability of NbC/TaC as catalyst for oxidation of sulfides with hydrogen peroxide (H_2O_2) as chemoselective synthesis of sulfones or sulfoxides. They have also found that other organic functionalities such as ketones, alcohols, amines and acetals were inactive in organic reaction medium in the presence of as-purchased catalysts.

From the above discussion, it is apparent that limited work has been carried out to degrade different dyes using TMCs. The literature pertaining to these studies which also include the work of our group is given in table 2.1.

Table 2.1: Comparative photocatalytic performance of TMCs as reported in literature.

Catalyst	Concentration (mg/L)		Illumination source	Time (h)	Efficiency (%)
	Catalyst	Dye			
$Ti_3C_2T_x$ [54]	1000.0	50 (MB)	UV lamp	5.0	81.0
Nano/micro TiC [53]	1000.0	3.1 (RhB)	500W Hg lamp	16.0	-
Nano NbC [6]	1000.0	3.1 (RhB)	300W Hg lamp	12.0	-
ZrC/C [56]	100.0	1.0 (MB)	Solar light	5.0	80.0
TaC/C [57]	500.0	1.0 (MB)	85W CFL lamp	6.0	100.0

The present work is undertaken to obtain nano NbC at relatively low temperature by taking waste material as carbon source (cigarette filter and stems of parthenium hysterophorous, respectively). Further, the results obtained from these sources have been compared with the results by using charcoal (activated carbon) and cellulose acetate (laboratory reagent) which are major constituents of the considered waste materials. Thereafter, effect of composition (phase purity) and type of carbon (lattice; C/Nb and free carbon) have also been studied on catalytic performance of synthesized samples.

2.4. Objective

Considering above discussion, goal of the present study has been designed for the optimization of the synthesis parameters such as temperature, holding time and the content of carbon precursor to obtain single phase NbC. Further, the synthesized samples were used to study the effect of different structural features on catalytic activity of synthesized NbC. Considering these aspects, following objectives have been set for the present study:

1. To synthesize niobium carbide using different carbon sources in an autoclave.
2. To characterize the synthesized product using different techniques.
3. To study the photocatalytic activity of synthesized samples.

Detailed methodology for the adopted set of experiments has been discussed in the next chapter.

References:

1 J. Y. Chan and S. M. Kauzlarich, *Chem. Mater.*, 1997, **9**, 531–534.
2 B. F. Dal, S. G. Hardin, D. G. Hay and T. W. Turney, *J. Mater. Sci.*, 1993, **28**, 6657–6664.
3 V. G. Brauer, H. Renner and J. Wernet, *Zeitschrift für Anorg. und Allg. Chemie*, 1954, **277**, 249–257.
4 J. F. Smith, O. N. Carlson and R. R. de Avillez, *J. Nucl. Mater.*, 1987, **148**, 1–16.
5 K. Kobayashi, R. Kitaura, Q. Wang, I. Wakamori, H. Shinohara, S. Anada, T. Nagase, T. Saito, M. Kiyomiya and H. Yasuda, *Appl. Phys. Express*, 2014, **7**, 5–9.
6 Y. Chen, H. Zhang, J. Zhang, J. Ma, L. Wang, H. Ye and G. Qian, *Adv. Powder Technol.*, 2013, **24**, 207–211.
7 J. Ma, M. Wu, Y. Du, S. Chen, W. Jin, L. Fu, Q. Yang and A. Wen, *J. Alloys Compd.*, 2009, **475**, 415–417.
8 K. Chen, X. Huang, Z. Zhang, A. Du, B. Zhou, Y. Xu, Z. Zhou and Y. Wang, *J. Mater. Chem. A*, 2015, **3**, 11745–11749.
9 J. S. Atchison, M. Zeiger, A. Tolosa, L. M. Funke, N. Jäckel and V. Presser, *RSC Adv.*, 2015, **5**, 35683–35692.
10 S. Witkowski, M. Ruszak, C. Sayag, J. Pielaszek and G. Djéga-Mariadassou, *Appl. Catal. A Gen.*, 2006, **307**, 205–211.
11 F. F. P. Medeiros, A. G. P. Da Silva and C. P. De Souza, *Powder Technol.*, 2002, **126**, 155–160.
12 S. Shimada, T. Koyama, K. Kodaira and T. Mastushita, *J. Mater. Sci.*, 1983, **18**, 1291–1296.
13 V. L. S. Teixeira Da Silva, M. Schmal and S. T. Oyama, *J. Solid State Chem.*, 1996, **123**, 168–182.
14 G. Y. Xu, J. B. Li, Y. Huang, W. Y. Yang and Z. P. Xie, *Mater. Sci. Eng. B*, 1999, **60**, 185–188.
15 A. Fukunaga, S. Chu, M. E. McHenry and M. Nagumo, *Mater. Trans. JIM*, 1999, **40**, 118–122.
16 Y. Nabil, S. Cavaliere, I. A. Harkness, J. D. B. Sharman, D. J. Jones and J. Rozière, *J. Power Sources*, 2017, **363**, 20–26.
17 Y. C. Kimmel, X. Xu, W. Yu, X. Yang and J. G. Chen, *ACS Catal.*, 2014, **4**, 1558–1562.
18 B. M. Tackett, Y. C. Kimmel and J. G. Chen, *Int. J. Hydrogen Energy*, 2016, **41**, 5948–5954.
19 Z. Qiu, H. Huang, J. Du, T. Feng, W. Zhang, Y. Gan and X. Tao, *J. Phys. Chem. C*, 2013, **117**, 13770–13775.
20 K. Zhang, M. Wen, G. Cheng, X. Li, Q. N. Meng, J. S. Lian and W. T. Zheng, *Vacuum*, 2014, **99**, 233–241.
21 L. Yate, L. Emerson Coy, G. Wang, M. Beltrán, E. Díaz-Barriga, E. M. Saucedo, M. A. Ceniceros, K. Załęski, I. Llarena, M. Möller and R. F. Ziolo, *RSC Adv.*, 2014, **4**, 61355–61362.
22 E. Coy, L. Yate, D. P. Valencia, W. Aperador, K. Siuzdak, P. Torruella, E. Azanza, S. Estrade, I. Iatsunskyi, F. Peiro, X. Zhang, J. Tejada and R. F. Ziolo, *ACS Appl. Mater. Interfaces*, 2017, **9**, 30872–30879.
23 M. Y. Liao, Y. Gotoh, H. Tsuji and J. Ishikawa, *J. Vac. Sci. Technol. B Microelectron. Nanom. Struct.*, 2004, **22**, L24.
24 L. Yate, L. E. Coy, D. Gregurec, W. Aperador, S. E. Moya and G. Wang, *ACS Appl. Mater. Interfaces*, 2015, **7**, 6351–6358.
25 S. Meyer, A. V Nikiforov, I. M. Petrushina, K. Kohler, E. Christensen, J. O. Jensen and N. J. Bjerrum, *Int. J. Hydrog. Energy*, 2015, **40**, 2905–2911.
26 S. G. Shiri, P. Abachi, K. Pourazarang and M. M. Rahvard, *Trans. Nonferrous Met. Soc. China (English Ed.*, 2015, **25**, 863–872.
27 C. Zhang, M. Beidaghi, M. Naguib, M. R. Lukatskaya, M. Zhao, B. Dyatkin, K. M. Cook, S. J. Kim, B. Eng, X. Xiao, D. Long, W. Qiao, B. Dunn and Y. Gogotsi, *Chem. Mater.*, 2016, **28**, 3937–3943.

28 O. N. Griegor'ev, *Inst. Mater. Sci. Acad. Sci. Ukranian SSR*, 1981, **12**, 81–86.
29 E. K. Storms and N. H. Krikorian, *J. Phys. Chem.*, 1959, **63**, 1747–1749.
30 M. Sansone, A. De Bonis, A. Santagata, J. V Rau, A. Galasso and R. Teghil, *Appl. Surf. Sci.*, 2016, **374**, 112–116.
31 L. X. Yang, H. L. Zhang, Y. Wang, H. J. Liu and C. L. Zeng, *Ceram. Int.*, 2018, 0–1.
32 M. Lee, G. P. Kim, H. Don Song, S. Park and J. Yi, *Nanotechnology*, , DOI:10.1088/0957-4484/25/34/345601.
33 S. Patel, *3 Biotech*, 2011, **1**, 1–9.
34 R. A. Khan, M. Ahmed, M. R. Khan, M. Yasir, B. Muhammad and R. Khan, *African J. Pharm. Pharmacol.*, 2011, **5**, 2073–2078.
35 M. Kaur, N. K. Aggarwal, V. Kumar and R. Dhiman, *Int. Sch. Res. Not.*, 2014, **2014**, 1–12.
36 A. Javaid and T. Riaz, *Pakistan J. Bot.*, 2012, **44**, 123–126.
37 S. Mondal, K. Aikat and G. Halder, *Ecol. Eng.*, 2016, **92**, 158–172.
38 N. SHubhaneel, S. Ghosh, S. Haldar, A. Ganguly and P. K. Chatterjee, *Int. J. Emerg. Technol. Adv. Eng. Vol.*, 2013, **3**, 167–172.
39 S. Singh, S. Sarma, M. Agarwal, A. Goyal and V. S. Moholkar, *Bioresour. Technol.*, 2015, **188**, 287–294.
40 S. A. Bapat and D. K. Jaspal, *Glob. J. Environ. Sci. Manag.*, 2016, **2**, 135–144.
41 H. Lata, V. K. Garg and R. K. Gupta, *J. Hazard. Mater.*, 2008, **157**, 503–509.
42 M. Ajmal, R. A. K. Rao, R. Ahmad and M. A. Khan, *J. Hazard. Mater.*, 2006, **135**, 242–248.
43 R. S. Singh, P. Kumar and M. K. Mondal, *Int. J. Chem. Environ. Eng.*, 2016, **6**, 15–21.
44 R. K. Singh, S. Kumar, S. Kumar and A. Kumar, *J. Hazard. Mater.*, 2008, **155**, 523–535.
45 Rajeshwarisivaraj and V. Subburam, *Bioresour. Technol.*, 2002, **85**, 205–206.
46 P. A. Clayborne, C. E. Jones, U. Gupta, J. J. Melko, S. N. Khanna and A. W. Castleman, *J. Phys. Chem. A*, 2010, **114**, 1290–1297.
47 F. A. O. Fontes, K. K. P. Gomes, S. A. Oliveira, C. P. Souza and J. F. Sousa, *Brazilian J. Chem. Eng.*, 2004, **21**, 393–403.
48 G. Singla, K. Singh and O. P. Pandey, *Int. J. Hydrogen Energy*, 2015, **40**, 5628–5637.
49 G. Singla, K. Singh and O. P. Pandey, *J. Alloys Compd.*, 2016, **665**, 186–196.
50 M. Mahajan, S. Rajpoot and O. P. Pandey, *Int. J. Refract. Met. Hard Mater.*, 2015, **50**, 113–119.
51 A. Kumar, K. Singh and O. P. Pandey, *Int. J. Refract. Met. Hard Mater.*, 2011, **29**, 555–558.
52 L. K. Brar, G. Singla and O. P. Pandey, *RSC Adv.*, 2016, **6**, 109174–109184.
53 Y. Chen, H. Zhang, D. Ma, J. Ma, H. Ye, G. Qian and Y. Ye, *Mater. Res. Bull.*, 2011, **46**, 1800–1803.
54 O. Mashtalir, K. M. Cook, V. N. Mochalin, M. Crowe, M. W. Barsoum and Y. Gogotsi, *J. Mater. Chem. A*, 2014, **2**, 14334–14338.
55 M. Kirihara, A. Itou, T. Noguchi and J. Yamamoto, *SYNLETT*, 2010, **10**, 1557–1561.
56 A. Singh Vig, A. Gupta and O. P. Pandey, *Adv. Powder Technol.*, 2018, **29**, 2231–2242.
57 L. K. Brar, A. Gupta and O. P. Pandey, *Catal. Today*, 2018, **325**, 98–108.

CHAPTER 3 METHODOLOGY

Overview

The adopted methodology for the synthesis and characterizations of niobium carbide(s) has been discussed in this chapter. Various characterizations such as X-ray diffraction, electron microscopy, surface area measurement, X-ray photoelectron spectroscopy, optical study and catalytic study have been described in this chapter. The required fundamental aspects along with the required test conditions have also been described.

3.1. Precursors

3.1.1. Niobium and Magnesium source

To synthesize NbC nanopowder, niobium pentaoxide (Nb_2O_5; 99.99%, Sigma Aldrich) and metallic Mg (99.0%; Loba Chemie) powder were used as Nb and Mg source without any prior treatment or purification. X-ray diffraction and scanning electron microscopy images along with the particle size distribution are shown in figure 3.1. With the help of histograms, the average particle size of Nb_2O_5 and Mg comes out to be 257 nm and 167 µm, respectively. Further, metallic Mg powder has flake like morphology whereas Nb_2O_5 has spherical, faceted to elongated faceted morphology.

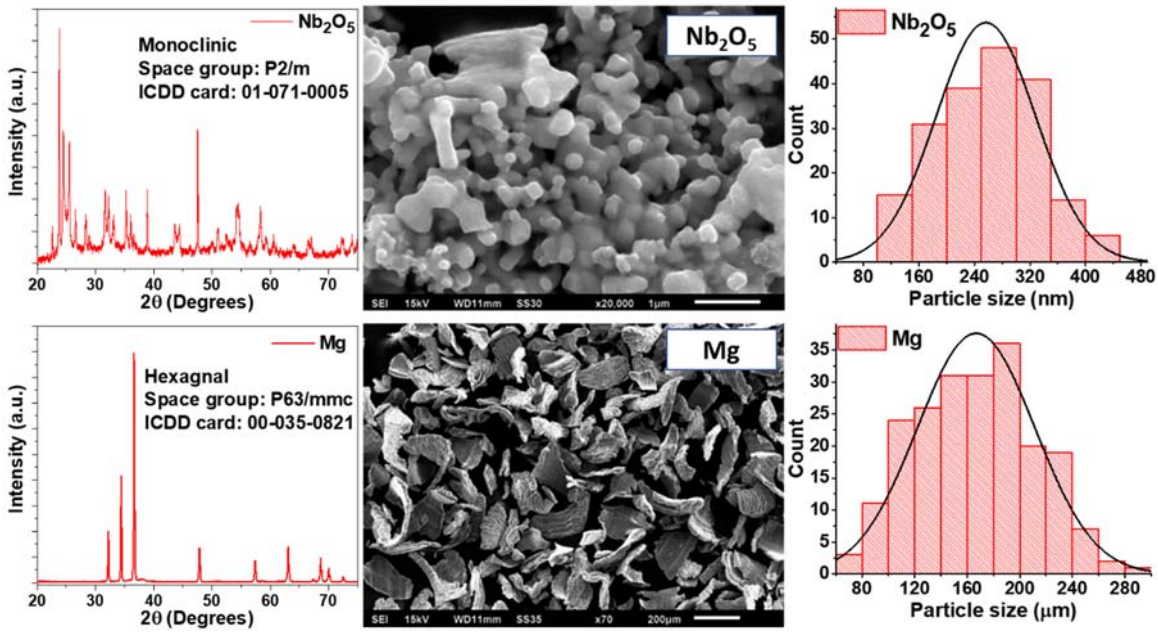

Figure 3.1: XRD, SEM micrograph and histogram of Nb_2O_5 and Mg powder.

3.1.2. Carbon source

As discussed in chapter 2, some natural and synthetic grade waste materials were taken as carbon source in the present investigation. The waste materials taken as carbon source are (1) smoked cigarette filters (CF) and (2) parthenium hysterophorous (PH) to syntheisize nano NbC. Since, CFs consist of tightly packed cellulose acetate fibers to filter tar and exhaled CO_2 from smoked cigarette so, cellulose acetate powder (99.0%, Loba Chemie) was also used as carbon source to compare the results obtained from CFs. To avoid ambiguity, smoked CFs of Gold Flake (small sized), ITC Ltd. were collected. The collected CFs were used without any chemical treatment as shown in figure 3.2a. PH plants (with well grown white flowers) were collected from the institute campus in the month of August, 2017. The stems were separated and washed thoroughly. Thereafter, stems were cut into small pieces (~1cm) and dried under sun light for 6 h followed by vacuum drying

at 60 °C for 48 h. Dried pieces of PH stem were crushed by agate mortar for further use as shown in figure 3.2b.

Figure 3.2: Photographs of (a) Smoked cigarette filters; (b) dried and crushed PH stems.

Since, all the above mentioned carbon sources get decomposed to char around 400 °C, activated charcoal (99.0%, Loba Chemie) was also used for better understanding of synthesis mechanism and other characteristics of nano NbC [1–3].

3.2. Methodology

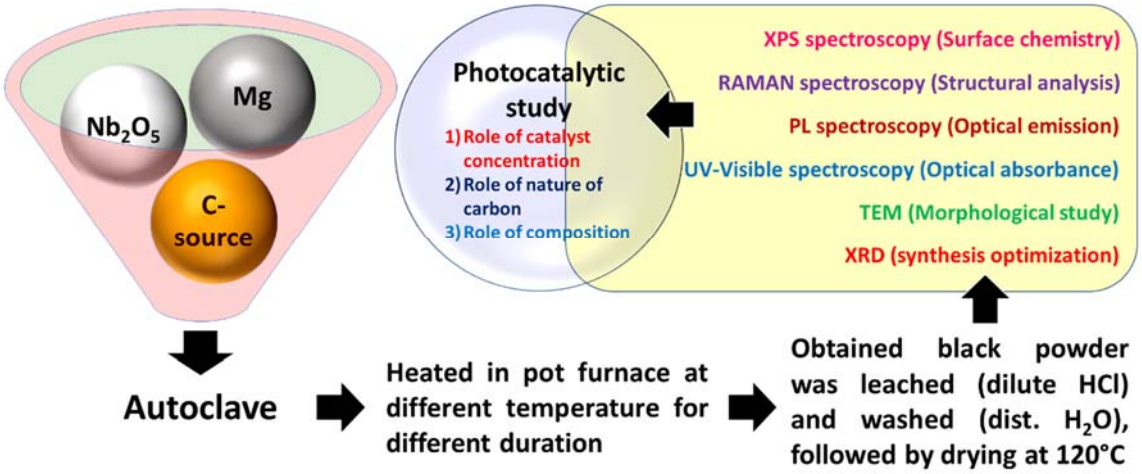

Figure 3.3: Schematic representation of adopted methodology for the optimization to obtain single phase NbC/C nanocomposite powder sample.

The adopted methodology is shown in figure 3.3. The adopted synthesis process includes a specially designed autoclave (volume capacity = 25.0 ml) made of steel in which mixture of precursors was charged. Details of the different precursors with experimental conditions have been given in the respective chapters. Thereafter, charged autoclave was tightened with steel bolts and heated (@ 5 °C/min) at different temperatures and holding times to optimize various parameters such as temperature, holding time, amount of carbon source and reducing agent i.e. Mg by keeping same metal source i.e. Nb_2O_5. After the completion of the reaction, autoclave was allowed to cool within the furnace to room temperature. Then, the obtained black colored powder was leached with acid solution

(HCl:H_2O :: 1:1) to remove MgO and remaining metallic Mg. Thereafter, it was washed with distilled H_2O to remove the traces of unreacted acid. Finally, the washed black powder was dried at 120 °C in vacuum oven.

3.3. Characterization techniques

3.3.1. X-ray diffraction (XRD):

For the identification of phases obtained at different synthesis conditions, XRD of all samples have been recorded. The obtained diffraction peaks were matched with ICDD (International Center of Diffraction Data) cards. The diffraction peaks are generated by constructive interference which follows Bragg's law as given below:

$$n\lambda = 2d_{hkl} \sin \theta_{hkl} \quad (3.1)$$

where, n, λ, θ_{hkl} and d_{hkl} are order of the diffraction, wavelength of X-ray used (Cu-Kα = 0.15406nm), diffraction angle and interplanar spacing of plane (hkl), respectively. For the synthesized powder samples in the present study, XRD pattern has been scanned between 20-80° (2θ) with the step size of 0.013° (2θ) and total scan time = 14 min. Prior to the measurement, the dried powder sample was ground using agate mortar to break the major agglomerates. The details of the ICDD cards which have been used for the phase confirmation are listed in table 3.1.

Table 3.1: Details of the ICDD cards used for the XRD analysis.

Compound	Symbol	ICDD Card	Compound	Symbol	ICDD Card
NbC	•	01-089-3690	NbO_2	β	00-034-0898
Nb	α	01-089-3715	Nb_2O_5	Δ	01-071-0005
NbO	δ	00-042-1125	C	o	01-089-8487

Further, average lattice parameter and carbon content inside the unit cell have been determined by using $a = d\sqrt{h^2 + k^2 + l^2}$ and $a(\dot{A}) = 4.09847 + 0.7128x - 0.3457x^2$ (respectively) where 'a' and 'x' represent the lattice constant and atomic ratio C/Nb [4].

3.3.2. Williamson-Hall analysis:

Based on the XRD patterns of synthesized samples, mathematical peak functions have been designed to estimate various structural features of samples such as crystallite size and lattice distortion. For the fitting of diffraction peaks, Pearson's VII peak function has been used due to the contribution of Gaussian and Lorentzian component in Pearson's VII function with maximum quality of fitting (R^2 ~0.99) and minimum error. Moreover, prior to calculate various parameters from XRD pattern, instrumental error has been deducted using $\beta_{calc} = \sqrt{\beta_{obs}^2 - \beta_{inst}^2}$ for Si standard as (analyzed at same test conditions).

To determine the minimum size of coherent scattering, Scherer method has been considered as versatile criteria ($t_{hkl} = (k\lambda)/(\beta_{hkl}\cos\theta_{hkl})$) providing volume weighted quantity and peak broadening i.e. β_{hkl} is solely associated to crystallite size (t_{hkl}). While, Wilson and Stokes [5] have suggested the contribution of lattice distortion along with crystallite size which can modify the Scherrer's criteria as

USM
$$\beta_{hkl}\cos\theta_{hkl} = \frac{k\lambda}{t} + 4\varepsilon\sin\theta_{hkl} \tag{3.2}$$

The above mathematical relation distinguishes the individual contribution of crystallite size and lattice distortion in peak broadening with homogenous strain representing the uniform strain model (USM) of Williamson-Hall analysis. Further, more realistic approach can be considered as homogeneity of stress and strain energy throughout the lattice as uniform stress deformation model (USDM) and uniform strain energy density model (USEDM) , respectively, as described below [6]:

USDM
$$\beta_{hkl}\cos\theta_{hkl} = \frac{k\lambda}{t} + \frac{4\sigma\sin\theta_{hkl}}{E_{hkl}} \tag{3.3}$$

USEDM
$$\beta_{hkl}\cos\theta_{hkl} = \frac{k\lambda}{t} + 4\sin\theta_{hkl}\left(\frac{2u}{E_{hkl}}\right)^{0.5} \tag{3.4}$$

For cubic systems, elastic modulus (E_{hkl}) is a function of elastic compliances and direction cosines [7] and can be describes as:

$$E_{hkl}^{-1} = s_{11} - 2\left(s_{11} - s_{12} - \frac{s_{44}}{2}\right)(l^2m^2 + m^2n^2 + n^2l^2) \tag{3.5}$$

$s_{12} = -0.3913 \times 10^{-3}\text{GPa}^{-1}$ $s_{11} = 1.7826 \times 10^{-3}\text{GPa}^{-1}$ $s_{44} = 7.1428 \times 10^{-3}\text{GPa}^{-1}$

3.3.3. Transmission electron microscopy (TEM):

After the confirmation of the phase formation, the optimized samples (showing single phase NbC XRD pattern) were further examined under TEM microscope. This helps to analyze the phases present as cluster or independent particles embedded in the matrix of amorphous/crystalline carbon. The high-resolution TEM (HRTEM) helps to confirm the presence of phases along with minor phases which are not observed in XRD patterns. It also provides the lattice defects and interfacial structural features. For TEM study, a small amount of powder sample was dispersed in absolute ethanol and sonicated for 40 min. Thereafter, 1-2 drop of suspension was drop-casted on carbon coated Cu grid (300 mesh) and allowed to dry under ambient conditions for overnight. Further, microstructural features have been recorded on JEOL2100F (at 200 kV) and analyzed by Carl Zeiss Axio Vision 4 software.

3.3.4. Raman spectroscopy:

Raman spectroscopy provides the structural features (molecular functional groups) in the mixture of solids or liquids. This technique is based on the interaction of monochromatic radiation with the matter that provides elastic/inelastic scattering of photon that causes shift of associated energy in terms of wavenumber. In the present study, Raman spectroscopy allows us to determine the nature of structural features of carbon present in the powder sample in the form of disordered or multilayered graphitic carbon at different operating conditions. For the same purpose, specific samples were exposed to 532 nm He-Ne laser on Varian FT-Raman and Varian 600 UMA. To distinguish various bands related to different chemical species, Raman spectrum has been deconvoluted by using Lorentzian function on Origin 13.0 software and analyzed.

3.3.5. X-ray photoelectron spectroscopy (XPS):

To understand the chemical composition upto several nanometers inside the nanoparticles, XPS spectroscopy has been carried out. XPS provides the photoemission that has occurred due to the ejection of an electron from any core energy level of atom. This technique provides all the information about chemical state of desired element. For this technique, Al X-rays (1486.7 eV) are being used on PHI 5000 Versa Prob II, FEI Inc. to eject the core level electron to study the chemical state of an element. Further, all the binding energies have been corrected by considering Ag as calibration standard element. For the deconvolution of high resolution (HR) XPS spectra, XPSPEAK41 software has been used with Gaussian peak profile with doublet separation of 2.74 eV for doublet spin orbital splitting $3d_{5/2}$ and $3d_{3/2}$ of niobium considering same peak width for single oxidation state of Nb.

3.3.6. Optical absorbance spectroscopy (UV-Visible):

Absorbance spectroscopy is also referred as UV-visible spectroscopy in which absorbance of specific wavelength is observed in UV (200-340 nm) and visible (340-800 nm) region of electromagnetic spectrum. The obtained spectrum also provides the energy associated to excite the electron from top of the valence band to bottom of the conduction band, referred as optical band gap of that material. For the determination of optical band gap, intercept on energy axis (from linear portion in $(\alpha h\nu)^{1/n}$ vs. $h\nu$ graph) was calculated using Tauc equation ($\alpha h\nu = A\left(h\nu - E_g\right)^n$) where n = 0.5, 2.0, 1.5 and 3.0 correspond to allowed direct, allowed indirect, forbidden indirect, and forbidden direct transitions

(respectively) [8]. Hitachi double beam UV-Visible Spectrophotometer U-3900H has been used to record absorbance spectra of synthesized samples in solid state.

3.3.7. Optical emission spectroscopy (Photoluminescence; PL):

For the determination of the photoluminescence emission behavior of synthesized samples, PL spectroscopy has been carried out on Perkin Elmer fluorescence spectrometer. PL spectroscopy enables to probe the mechanism of photodegradation by providing the information about entrapment of charge carriers during photoexcitation. The enhanced photo-emission can be correlated to rapid recombination of excitons resulting unavailability of holes/electrons for photochemical reactions along with the participating functional group present on the surface of photocatalyst. To record the PL emission spectra, Cary Eclipse Fluorescence spectrophotometer (G9800A) has been used with excitation wavelength; $\lambda_{exc} = 340$ nm.

3.3.8. N_2 adsorption-desorption

To study the catalytic performance of any compound, its surface features governs the reaction pathway. In these surface features, specific surface area, pore volume, average life size and its distribution maneuvers the absorption behavior of synthesized samples. Based on the IUPAC hysteresis loops of gas adsorption-desorption curve, the texture of the adsorbent can be estimated [9]. Brunauer-Emmett-Teller (BET) criteria has been adopted to calculate the specific surface area (SSA) from ads-des. isotherms. In the present work, Tristar 3000 (Micromeritics) has been used for the N_2 adsorption-desorption analysis with the pretreatment temperature = 150 °C for 2 h.

3.3.9. Photocatalytic study:

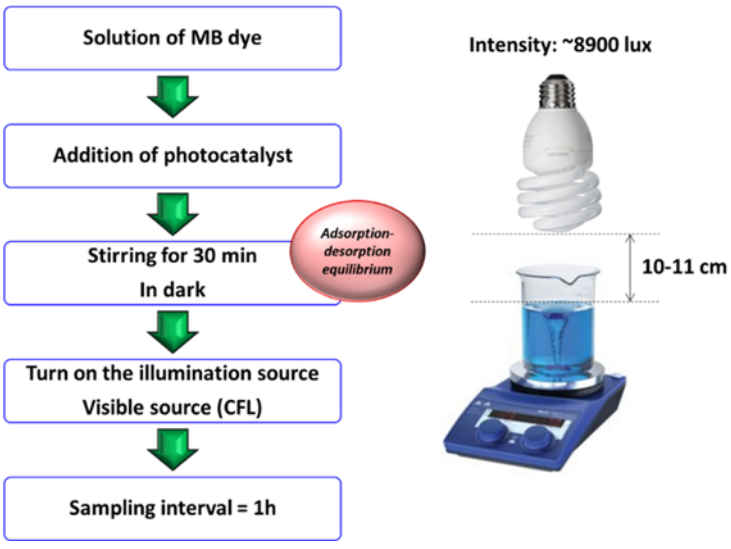

Figure 3.4: Schematic representation of setup for photocatalytic study.

For the photocatalytic performance of synthesized powder samples, a simple experimental design has been adopted (figure 3.4). In this study, optimization of dye concentration (methylene blue; MB dye) and the photocatalyst (carbides) has been done. The optimized concentrations were used for further study. In 100 ml of dye solution of different concentration, appropriate amount of photocatalyst was added and kept under dark chamber to establish adsorption-description equilibrium. Thereafter, house-hold CFL (85 W, ~8900 lux) kept nearly 10-11 cm above the surface of solution was switched on for the illumination. At an interval of 1h, aliquot of 3ml has been extracted, centrifuged (@4000RPM) and charged to UV-visible spectrophotometer to measure the change in the concentration of MB dye which can expressed as follows;

$$\%\text{change in concentration} = \frac{C_0 - C_t}{C_0} \times 100 \tag{3.6}$$

where C_0 and C_t are the concentrations of MB dye at t = '0' and 't' h, respectively. Further, change in concentration during adsorption-description equilibrium represents the amount of adsorbed dye on the surface of photocatalyst. To study the photochemical reaction kinetics for MB dye, pseudo first (rate constant = K_1) and second (rate constant = K_2) order reaction has been employed which can be described as follows:

$$-\ln\left(\frac{C_t}{C_0}\right) = K_1 t \tag{3.7}$$

$$\frac{t}{C_t} = \frac{1}{K_2 C_0^2} + \frac{t}{C_0} \tag{3.8}$$

Based on the above-mentioned kinetics, it can be estimated that the overall photochemical reaction is proceeding through physisorption (pseudo 1st order) or chemisorption (pseudo 2nd order) mechanism.

References:

1 M. da C. C. Lucena, A. E. V. De Alencar, S. E. Mazzeto and S. de A. Soares, *Polym. Degrad. Stab.*, 2003, **80**, 149–155.
2 A. Purai and V. K. Rattan, *Carbon Lett.*, 2010, **11**, 1–8.
3 K. Kadirvelu, P. Senthilkumar, K. Thamaraiselvi and V. Subburam, *Bioresour. Technol.*, 2002, **81**, 87–90.
4 C. P. Kempter, E. K. Storms and R. J. Fries, *J. Chem. Phys.*, 1960, **33**, 1873–1874.
5 S. Vives, E. Gaffet and C. Meunier, *Mater. Sci. Eng. A*, 2004, **366**, 229–238.
6 A. Gupta, G. Singla and O. P. Pandey, *Ceram. Int.*, 2016, **42**, 13024–13034.
7 J. Chen, L. L. Boyer, H. Krakauer and M. J. Mehl, *Phys. Rev. B*, 1988, **37**, 3295–3298.
8 M. Mittal, M. Sharma and O. P. Pandey, *Sol. Energy*, 2014, **110**, 386–397.
9 M. Thommes, *Chemie-Ingenieur-Technik*, 2010, **82**, 1059–1073.
10 L. K. Brar, A. Gupta and O. P. Pandey, *Catal. Today*, 2018, **325**, 98–108.

CHAPTER 4 RESULTS & DISCUSSION-I

Utilization of smoked cigarette filters (CFs; Household waste)

Overview

This chapter presents the synthesis of NbC-C nanocomposite by using smoked cigarette filters (CFs) as carbon source. Based on the XRD results, synthesis parameters (temperature, time and amount of CFs) have been optimized to obtain single phase NbC. Using line profile XRD analysis, lattice distortion and lattice carbon content (x) of NbC were calculated. TEM results revealed the variation in morphological features of the synthesized powder sample at these synthesis conditions. The synthesized pure phase NbC confirmed the presence of NbC and graphitic carbon (g-C) as observed through HR-TEM analysis. Optimized NbC-C nanocomposite sample has been characterized with absorbance spectroscopy to study its optical response enabling it to be used as photocatalyst under visible irradiation. Further, the photocatalytic activity of NbC-C nanocomposite sample was studied by evaluating the degradation of methylene blue dye under visible irradiation.

4.1. Introduction

The organic pollutants, mostly dyes, are the major byproducts of various industries like pharmaceutical, textile and pulp-paper industries which are directly disposed to water that contaminate the natural water. Such polluted water is highly undesired due to the toxic ingredients causing cancer or human mutation [1]. Moreover, the coloration due to dyes can also cause hindrance to the sunlight and oxygen penetration affecting the aquatic living organisms [2]. Apart from water pollution, soil pollution due to the various polymeric litter/garbage also causes severe health hazards to society where degradability of solid waste is a critical issue.

Smokers contribute to air and soil pollution both, by exhaling smoke to air and throwing smoked cigarettes on roadsides, riverbanks and at sea beaches. Cigarette filters (CFs), a major left-over component of smoked cigarette, are being thrown inappropriately at other places also. It is estimated that approximately 9 trillion filtered cigarette would be consumed by 2025 [3,4]. CFs, a fibrous component consisting cellulose acetate as a major constituent, are photodegradable under the exposure of UV radiation in ideal environmental conditions but not biodegradable. Various studies have shown that there is an ambiguity on the biodegradability of cellulose acetate [5]. Cellulose acetate is a very good source of carbon and can be used to develop various engineering materials such as transition metal carbides (TMCs) at relatively low temperature. In the present study, synthesis of nano NbC-C nanocomposite using Nb_2O_5 as precursor of Nb and CFs as carbon source has been done. The obtained carbide is further utilized to degrade organic methylene blue dye. The details of experimental conditions are given in table 4.1.

Table 4.1: Details of experimental conditions to obtain NbC nanopowder.

Precursor (g)			**Sample**	**Temperature**	**Holding time**
Nb_2O_5	**Mg**	**CFs**		**(°C)**	**(h)**
1.329	2.0	1.0	C1	600	5
1.329	2.0	1.0	C2	600	10
1.329	2.0	1.0	C3	600	15
1.329	2.0	1.0	C4	600	20
1.329	2.0	1.0	C5	700	5
1.329	2.0	1.0	C6	700	10
1.329	2.0	1.0	C7	700	15
1.329	2.0	1.0	C8	700	20
1.329	2.0	1.0	C9	800	5
1.329	2.0	1.0	C10	800	10
1.329	2.0	1.0	C11	800	15
1.329	2.0	1.0	C12	800	20
1.329	2.0	0.5	C13	800	20

4.2. Structural and morphological features of smoked CFs:

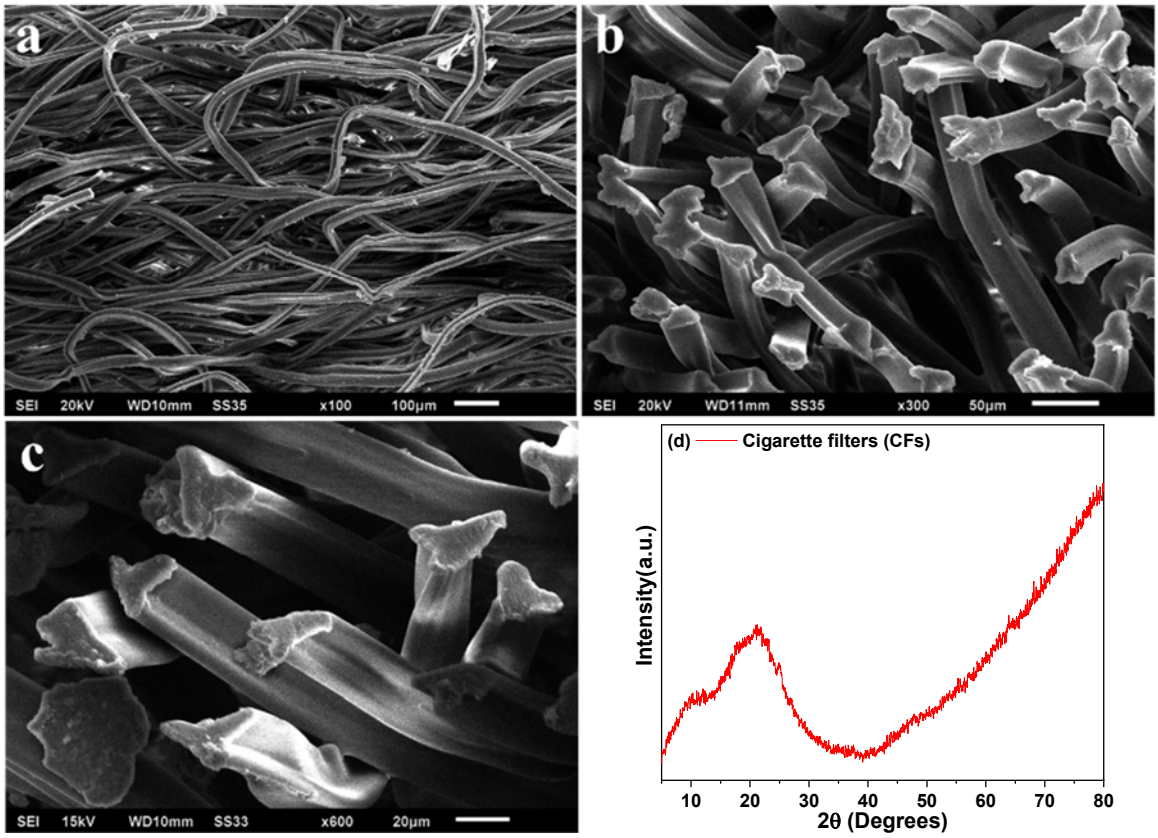

Figure 4.1: SEM micrographs of CFs (a) very long and entangled continuous fibers of cellulose acetate; (b,c) cross-sectional view of CF representing the triangular cross-section of each fiber; (d) XRD pattern of CF showing the amorphous nature of used CFs.

Prior to use CFs as carbon source, it is necessary to understand the structural and morphological features of CF. It is well studied that CF consists of very long organic fibrous structures composed of cellulose acetate (majorly) as shown in figure 4.1. These long continuous and amorphous fibers exhibit triangular cross-section and are entangled among each other to filter the smoke. Moreover, some of the CFs consist of activated charcoal to absorb different toxic constituent of inhaled smoke. XRD pattern of smoked CFs suggests the presence of cellulose acetate [6,7].

4.3. X-ray diffraction (optimization of synthesis parameters):

Figure 4.2 represents the XRD patterns of all the samples synthesized at different temperatures and holding times to obtain single phase NbC. Figure 4.2a represents the XRD patterns of all the samples synthesized at 600 °C with 5 (C1), 10 (C2), 15 (C3) and 20 h (C4) holding in which it can be seen that nucleation of NbC has started at shorter holding time (C1 and C2) while, prolonged holding time (C3 and C4) resulted the formation of NbO. At prolonged holding time, the decarburization of nucleated NbC (obtained in C1

and C2) started. With prolonged holding, the transformation of NbC to NbO is more as observed from XRD pattern in which C4 exhibited the better growth of NbO particles as compared to C3 as indicated by more intense diffraction peak [8]. Broader and less intense diffraction peaks of NbC (marked with dot) suggested the nano regime of NbC crystallites along with metallic Nb and NbO_2 (marked with α and β, respectively). Further to study the effect of temperature, samples were synthesized at 700 °C by keeping same holding time (5, 10, 15 and 20 h) as shown in figure 4.2b. It is evident from XRD pattern that reduction of Nb_2O_5 takes place at lower holding time below 10 h where the formation of NbO_2, NbO, Nb and NbC (minor quantity) can be seen in figure 4.2b. Moreover, beyond 10 h holding time, the decarburization of NbC occurs as can be seen in figure 4.2b. The experiments performed at 700 °C revealed that formation of NbC starts at 700 °C.

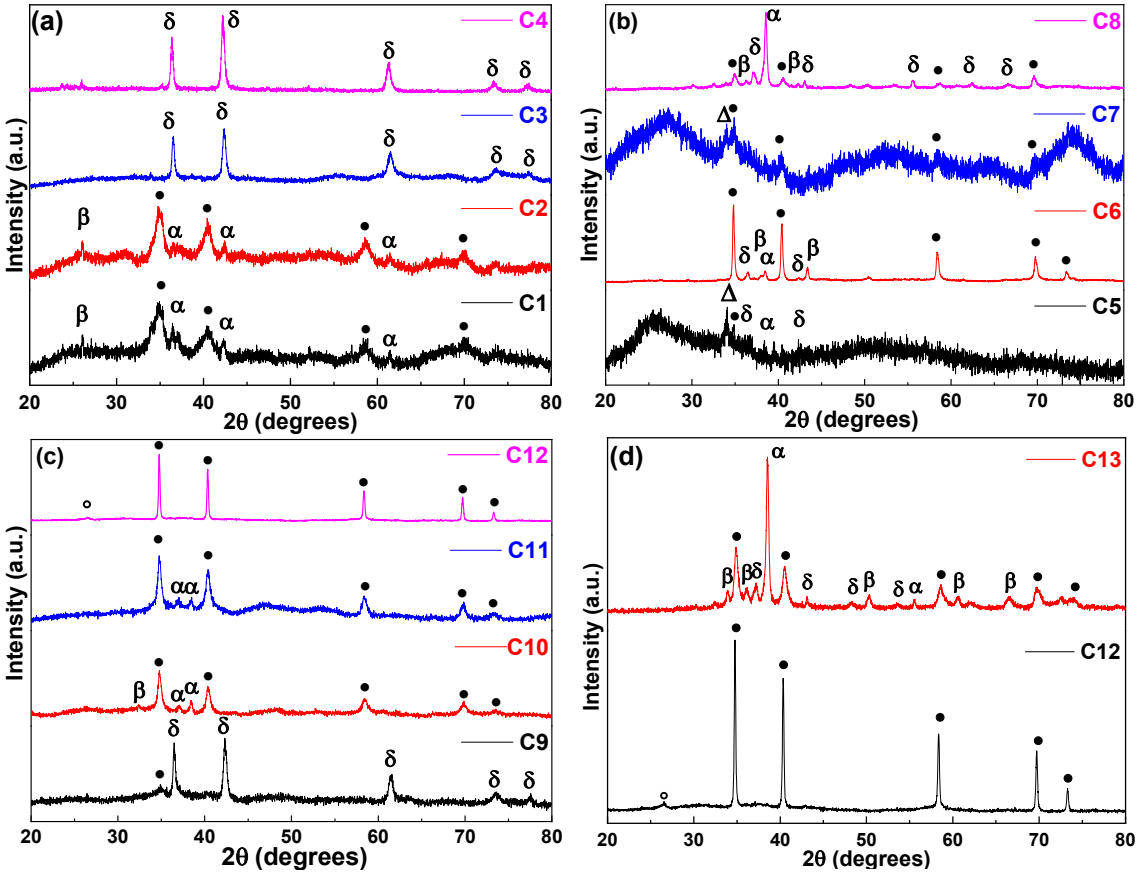

Figure 4.2: XRD patterns of all the samples synthesized at (a) 600 °C (C1 to C4); (b) 700 °C (C5 to C8); (c) 800 °C (C9 to C12) with different holding time and (d) effect of reducing agent i.e. Mg metal powder under optimized conditions (C12). Symbols: • (NbC), α (Nb), δ (NbO), β (NbO_2), Δ (Nb_2O_5) and ° (graphitic carbon).

In order to get pure NbC phase, the temperature was raised to 800 °C to prepare another set of samples in which reduction followed by carburization of Nb_2O_5 has been observed as is evident in figure 4.2c (C9-C12). Sample C9 exhibited single phase NbO

diffraction pattern which got transformed to (NbC+Nb) mixture at 10 h (C10) and 15 h (C11) of holding time at same temperature. Further increment in holding time i.e. 20 h (C12) resulted in the complete carburization of Nb_2O_5 leading to the formation of NbC along with little amount of graphitic C (marked with hollow dot in figure 4.2c).

Further, to optimize the content of carbon source (CFs), its content was reduced to 0.5 g (instead of 1.0 g) as shown in figure 4.2d (C13). It is observed that the reduced content of CFs is not beneficial as it led to the formation of NbC, Nb metal, NbO and NbO_2 which might be associated to the simultaneous reduction and carburization of Nb_2O_5. The insufficient amount of carbon source facilitated the partial reduction-carburization inside the sealed autoclave and hence, mixture of Nb, NbO and NbO_2 has obtained [8].

Based on these XRD results it can be asserted that the transformation of Nb_2O_5 to NbC follows the simultaneous reduction and carburization process as reported by different research groups [8,9] with following intermediate steps;

$$Nb_2O_5 \rightarrow NbO_2 \rightarrow NbO \rightarrow Nb \rightarrow NbC$$

Here, for the better understanding the formation mechanism, amount of lattice carbon content (x; lattice carbon content as mentioned in chapter 3) and lattice distortion have been calculated by using W-H analysis (section 3.3.1.2) from XRD results. Increase in 'x' (0.86–0.94) in NbC lattice also confirmed the increased carburization of Nb with the increased holding time at 800 °C as shown in table 4.2.

Table 4.2: Lattice carbon content (x), lattice constant (a) and W-H postulates of various samples using CFs.

Sample ID	x	a	USM		USDM			USEDM				Scherrer
		Å	ε, $\times10^{-4}$	t, nm	σ, GPa	ε, $\times10^{-4}$	t, nm	u, $\times10^{-5}$, kJm^{-3}	σ, GPa	ε, $\times10^{-4}$	t, nm	t, nm
C10	0.862	4.460	35.4	33.4	1.07	25.4	23.2	197.75	1.30	30.6	27.6	13.3
C11	0.901	4.464	31.6	27.6	1.11	26.5	23.5	184.29	1.25	29.5	25.9	13.3
C12	0.944	4.468	0.84	47.9	0.03	0.703	47.6	0.22	0.03	0.729	47.8	45.6

Moreover, the lattice constant of NbC also increased from 4.460 to 4.468 Å. With respect to holding time at 800 °C, NbC lattice contain variable C-content which may cause the variation in lattice distortion. Among different models of W-H analysis, USM model exhibited better quality of fitting with $R^2 = 0.93$ suggesting uniformity of strain throughout the NbC lattice (as shown in figure 4.3) as compared to other models (USDM and USDEM) with $R^2 = 0.74$ and 0.85, respectively.

Further, with the increased holding time (C10 to C12), amount of crystal distortion and crystallite size tend to decrease and increase, respectively, which also supports the enhanced carburization resulting NbC as carbon is inclined to occupy its equilibrium position in the lattice.

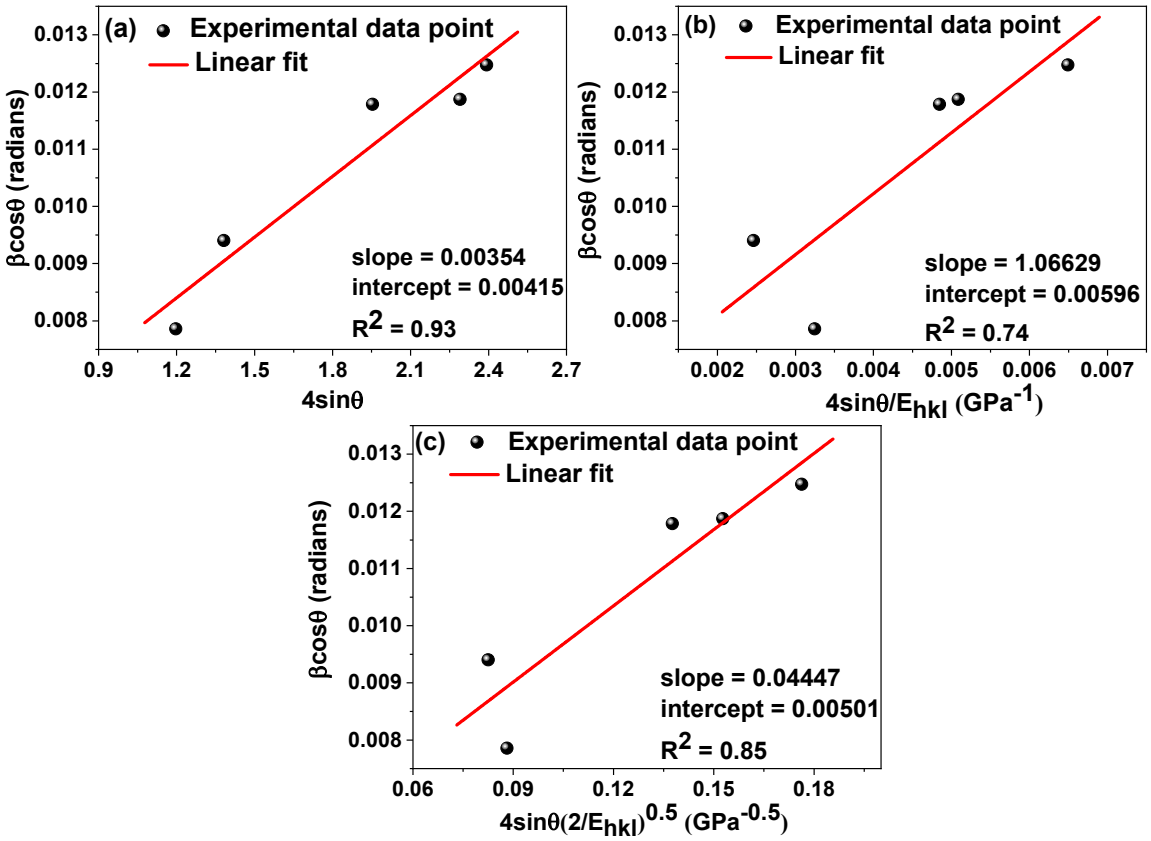

Figure 4.3: Representative graphs of (a) USM, (b) USDM and (c) USDEM models of W-H analysis for sample C10.

4.4. TEM microscopy:

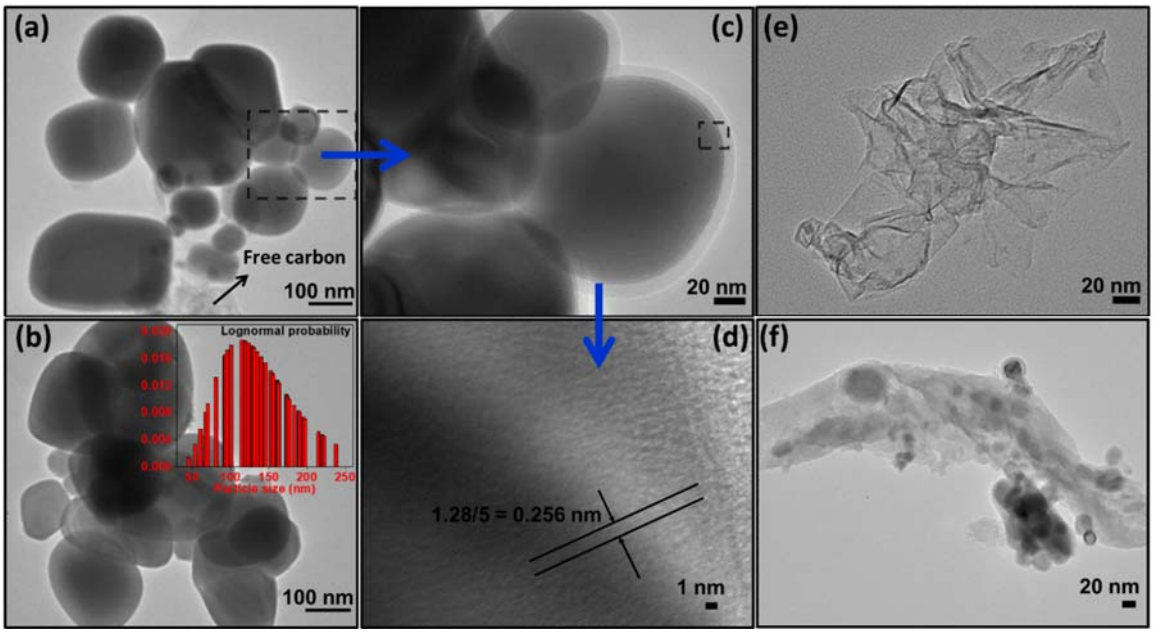

Figure 4.4: (a) General scan of C12 showing the non-faceted morphology of prepared NbC nanoparticles, (b) lognormal distribution of NbC particles having ~120 nm (average particle size), (c) high resolution scan of marked area in (a) suggesting a thin coating on the particles, (d) HR-TEM micrographs representing the lattice fringing of 0.256 nm corresponding to (111) plane, and (e,f) NbC particles are engulfed in sheet like morphology of free carbon.

Figure 4.4 represents TEM micrographs of C12. Agglomeration of the nanoparticles with a wide particle size distribution along with some free carbon (light grey portion in figure 4.4a at bottom) is observed. Inset of figure 4.4b shows the lognormal distribution curve of particle size depicting ~120 nm as average particle size of NbC [8]. At higher magnification, a fine coating on the nanoparticles was also observed which may be associated to carbon as shown in figure 4.4c. Further, high resolution TEM image (figure 4.4d) confirmed the formation of NbC as lattice fringing of 0.256 nm were associated to (111) plane of synthesized NbC, matched with XRD results. Moreover, the presence of free carbon has also been examined and found that it exhibited long graphitic sheets as suggested by diffraction peak at ~26° (figure 4.4e) and NbC particles are engulfed in these graphitic sheets as shown in figure 4.4f.

4.5. Raman spectroscopy:

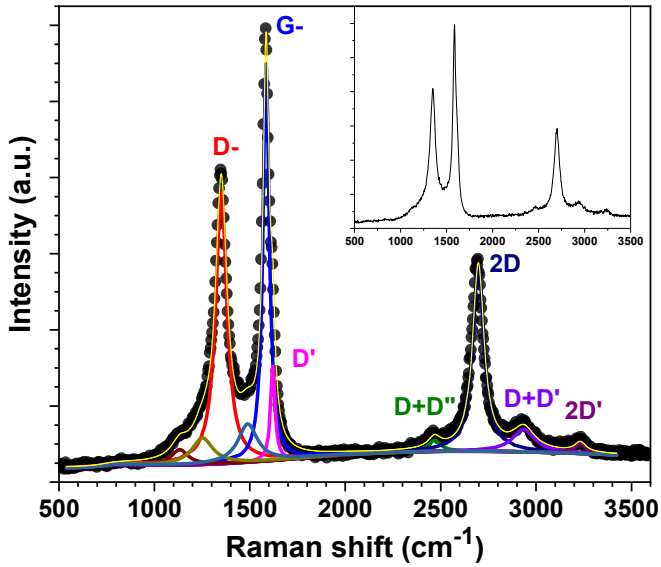

Figure 4.5: Raman spectra of C12 representing the presence of disordered graphitic carbon as multiple layers of graphene.

Figure 4.5 represents the deconvoluted Raman spectra of C12 exhibiting the nature of carbon present in the sample as suggested by XRD results (figure 4.2c). It can be observed that there is no band below 1000 cm^{-1} hence, possibility of any oxide phase (Nb_2O_5, NbO_2 and NbO) can be eliminated. Further, deconvolution suggested the presence of various molecular vibrations related to different modes of carbon. All the details related to position, full width at half maxima (FWHM), intensity ratios are provided in table 4.3.

Table 4.3: List of different bands obtained from deconvolution (Lorentzian peak function) of Raman spectra of C12.

Raman band →	**D-**	**G-**	**D'-**	**2D-**
Position (cm^{-1})	1350.18	1585.25	1620.21	2697.69
FWHM (cm^{-1})	71.05	39.71	28.73	72.34

The presence of characteristic bands (D- and G- band) suggests the formation of disordered and graphitic carbon (positioned at ~1350 cm^{-1} and ~1585 cm^{-1}, respectively) due to disordered scattering and bond stretching of sp^2 carbon atoms [10]. Moreover, presence of Raman band at ~2697 cm^{-1} revealed the presence of 2D graphitic layers i.e. multiple layers of graphene [11]. Further, Raman shift observed at 1620 cm^{-1} and 3232 cm^{-1} associated to D' and 2D' bands which might be originated due to double (DRRS) and triple (TRRS) optical resonance Raman scattering, respectively [12]. Moreover, some other weak vibration modes (D+D" and D+D') are associated to the acoustic branches of intervalley DRRS [12]. Other minor vibration modes between 1100 and 1500 cm^{-1} are associated to different phonon-matter interaction and its various optical-acoustic resonance branches of vibration [12].

Further, the ratio of D- and G- band intensities i.e. I_D/I_G (i.e. 0.71) represents the formation of disordered graphitic carbon. While, the intensity of 2D band is nearly half of G- band (I_{2D}/I_G = 0.46) suggesting the presence of graphite in the form of polycrystalline multilayered graphene. Since, D- and D' are defect induced Raman modes, Eckmann *et al.* [13] suggested that Raman spectroscopy can be used as a powerful tool to identify the nature of defects by using $I_D/I_{D'}$. Considering the linear proportionality of I_D and $I_{D'}$ with the defect concentration and their ratio ($I_D/I_{D'}$) is a function of the physical origin of defect (not the respective concentration), it has been proposed that magnitude of $I_D/I_{D'}$ can be related to sp^3- type defects ($I_D/I_{D'}$ ~13), vacancies ($I_D/I_{D'}$ ~7) and boundaries ($I_D/I_{D'}$ ~3.5). For the C12 sample, $I_D/I_{D'}$ (ratio of I_D/I_G and $I_{D'}/I_G$) came out to be 3.08 suggesting the presence of smaller graphitic grains.

4.6. BET analysis

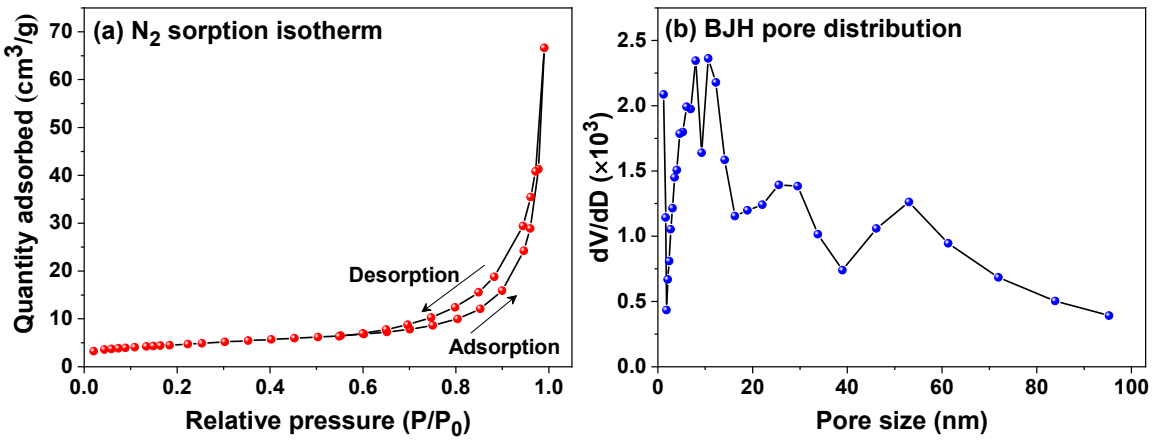

Figure 4.6: (a) N_2 adsorption-desorption isotherm representing the hysteresis loop between 0.6-1.0 (P/P_0), and (b) BJH desorption (dV/dD) plot to determine pore distribution of C12.

Figure 4.6a represents N_2 adsorption-desorption curve for C12 showing type IV isotherm with hysteresis loop ranging P/P_0 between 0.6-1.0 [14]. Such isothermal behavior represents the presence of mesopores on the surface of synthesized nanocomposite sample (C12). BJH (Barrett, Joyner, and Halenda) pore size distribution also confirmed the presence of mesopores having wide distribution which might be associated to the evolution of gases as a result of solid-state reactions between CF fibers and Nb-oxides as shown in figure 4.6b. With the help of BET analysis, specific surface area and total pore volume of C12 came out to be 17.7 m^2/g and 0.0917 cm^3/g (respectively) with average pore diameter 20.7 nm.

4.7. UV-visible spectroscopy

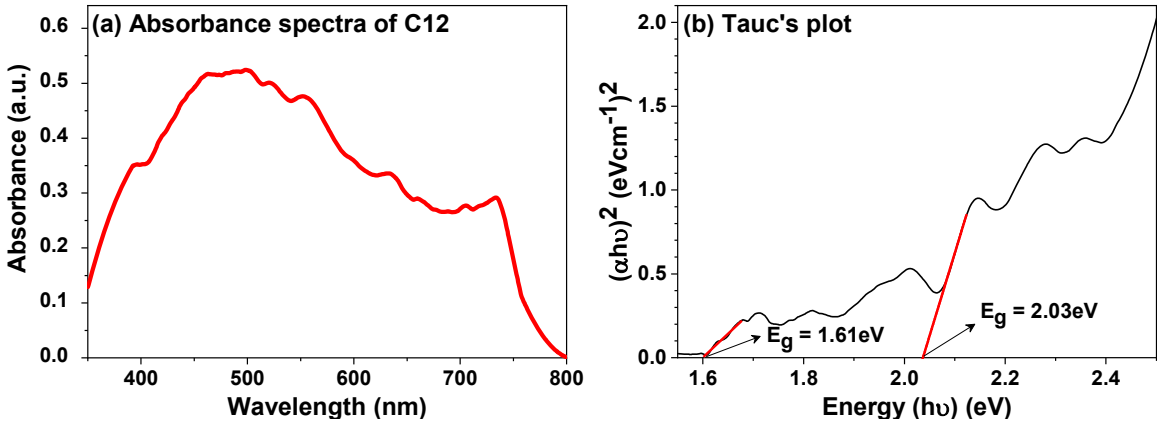

Figure 4.7: (a) UV–visible absorbance spectra of C12, and (b) Tauc's plot depicting multiple bandgaps of 1.61 and 2.03 eV.

UV-visible absorption spectroscopy of C12 has been carried out to observe the optical absorption characteristics of the samples as shown in figure 4.7. Figure 4.7a suggested a broad multiple absorption in the visible region associated with the presence of multiple phases (NbC, carbon as coating and free carbon) in the synthesized nanocomposite samples. Figure 4.7b represents the Tauc's plot of C12 from which multiple bandgap values of 1.61 eV and 2.03 eV can be estimated. The observed absorbance in visible region might be associated to the presence of oxygen centers inside the NbC nanoparticles in the form of Nb-(CO) or Nb-O which is discussed in the subsequent chapter [15,16]. Therefore, C12 is suitable for the generation of electron-hole pair responsible for photocatalytic study under visible irradiation.

4.8. XPS spectroscopy

Further, to study the photocatalytic behavior of synthesized photocatalyst (C12), determination of surface chemical composition is very essential to understand the chemical reactions responsible for photocatalytic activity. Therefore, figure 4.8a shows the survey

spectrum of C12 confirming the presence of Nb3d, C1s and O1s on the surface. High resolution XPS spectra of Nb3d, C1s and O1s are shown in figure 4.8b-d, respectively in which various chemical (oxidation) states of these elements have been illustrated and listed in table 4.4. The convoluted HR-XPS spectra of Nb3d consisting doublet of spin orbital splitting of $3d_{5/2}$ and $3d_{3/2}$ has been shown in figure 4.8b. It has been confirmed that Nb possessed multiple oxidation states (2+, 3+ and 4+). During the synthesis process, it achieves these states where single oxidation state in which 4+ has higher volume fraction dominates than 3+ and 2+ (Table 4.4) [17–19].

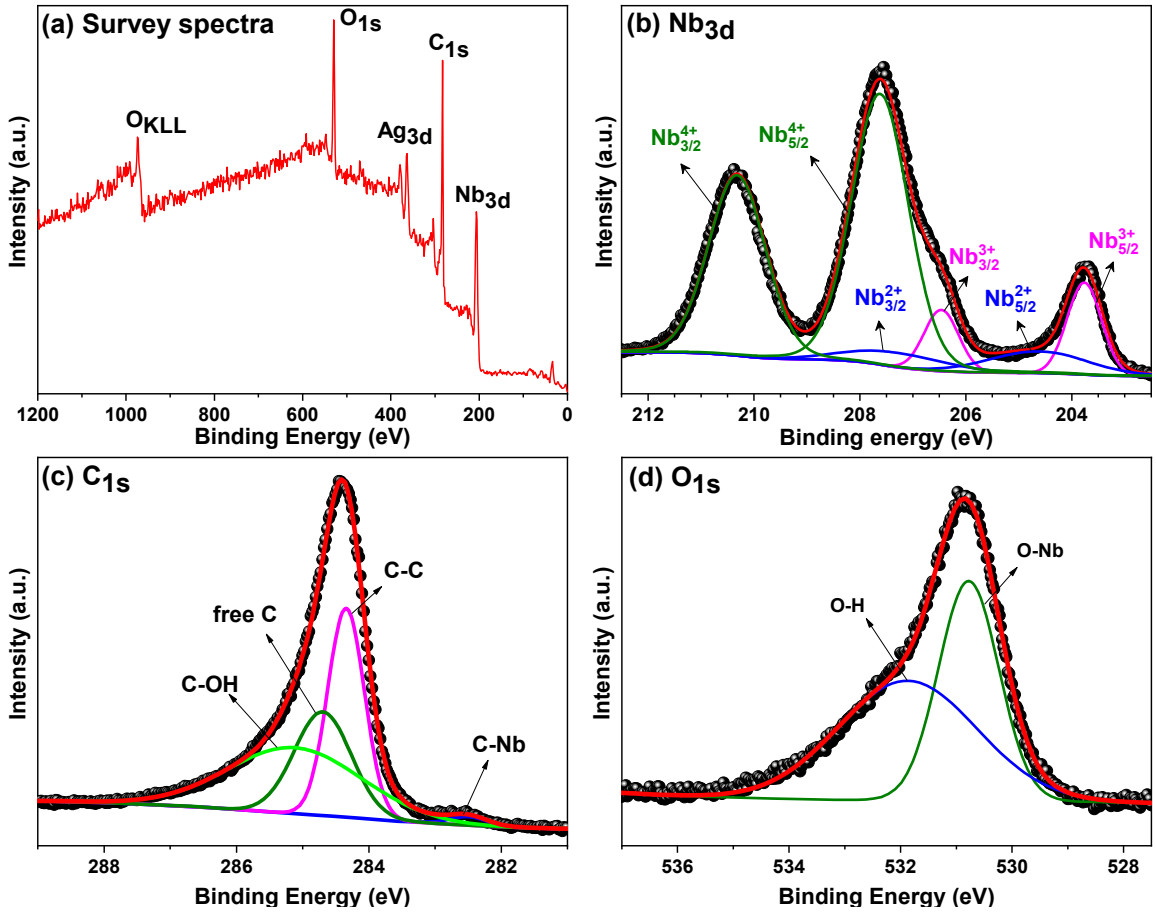

Figure 4.8: XPS spectroscopy of C12 showing the surface composition of the synthesized photocatalyst (a) survey spectra; (b) HR-XPS spectra of Nb3d; (c) HR-XPS spectra of C1s and (d) HR- XPS spectra of O1s.

Table 4.4: Results obtained from HR-XPS spectra of Nb3d, C1s and O1s of C12.

Nb3d			C1s			O1s		
Group	**B.E. (eV)**	**Volume (%)**	**Group**	**B.E. (eV)**	**Volume (%)**	**Group**	**B.E. (eV)**	**Volume (%)**
NbC	203.7, 206.4	14.72	C-Nb	282.5	1.40	O-Nb	530.7	42.77
NbC_xO_y	204.6, 207.3	9.99	C sp^2	284.3	33.79	O-H	531.9	57.23
Nb_2O_5	207.6, 210.3	75.29	C sp^3	284.7	26.03	-	-	-
-	-	-	C-OH	285.2	38.77	-	-	-

HR-XPS of C1s (figure 4.8c) also confirmed the formation of NbC but, the presence of peak on 284.3 and 284.7 eV may be associated to the carbon coating and free carbon present in the powder sample. Further, the peak at 285.2 eV is associated to the adsorbed water molecules on the surface of the C12 [20,21]. Moreover, HR-XPS spectra (figure 4.8d) of O1s supported the *in-situ* reduction-carburization of Nb_2O_5 during the synthesis of C12 as both the peaks at 530.7 and 531.9 eV correspond to O-Nb and adsorbed H_2O, respectively.

4.9. Photocatalytic analysis:

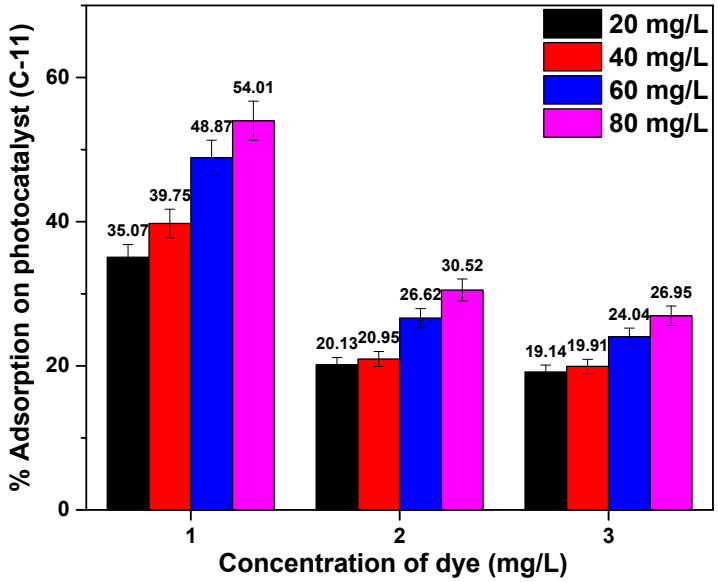

Figure 4.9: Percent adsorption of MB dye on the surface of photocatalyst C12.

Photocatalytic activity of single phase NbC-C nanocomposite sample (C12) was observed with the help of MB dye, a cationic dye acquiring electrons from various donor sites of photocatalyst. Figure 4.9 shows the percent adsorption of MB dye on the surface of C12 under the dark chamber suggesting that the adsorption of dye is a strong function of concentration of photocatalyst and adsorbate (MB dye). As a function of the concentration of photocatalyst, adsorption was increased due to the high surface area for adhesion. The adsorption of the dye got reduced with the increase in concentration of MB dye which might be associated to the repulsive force among adsorbate molecules that are already adsorbed on the surface.

Hereafter, the illumination of visible light was executed for 8.0 h to observe the degradation of MB dye for which the decrement in the concentration of dye with respect to irradiation time has been shown in figure 4.10a-c. With the help of these results, it can be illustrated that as an effect of increased concentration of dye, the degradation of dye has retarded significantly because the less adsorption of dye on the surface of photocatalyst

diminishes the penetration of photon through solution to interact on the surface of photocatalyst.

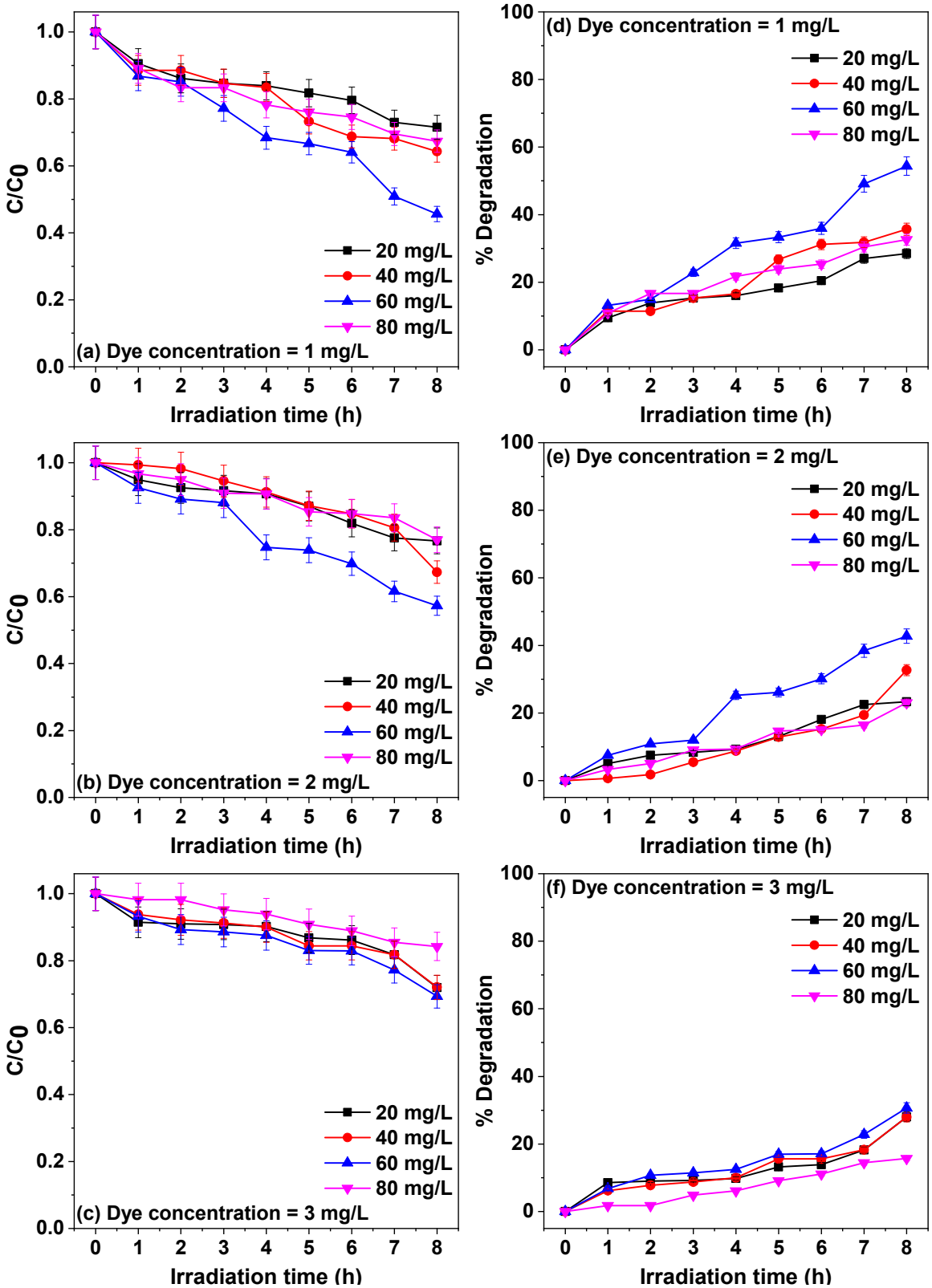

Figure 4.10: Fractional change ((a) 1.0, (b) 2.0, (c) 3.0 mg/L) and percent degradation ((d) 1.0, (e) 2.0, (f) 3.0 mg/L) of MB dye in 8.0 h visible irradiation with the presence of C12.

Similar effect of initial dye concentration on photodegradation has also been studied by Khan and Fulekar [22] which was supported by the availability of adsorbed dye molecules for the degradation with same amount of photocatalyst and catalyst deactivation at higher dye concentration [23]. However, for each concentration of dye, the degradation of dye has increased upto 60.0 mg/L concentration of C12 which got quenched at 80.0 mg/L. Such quenching behavior of degradation can be asserted with the hindrance to the penetration of the visible light by photocatalyst resulting lesser excitation of photocatalyst even at higher adsorption of dye. Further, degradation efficiency has been shown in figure 4.10d-f suggesting the 54% degradation of 1.0 mg/L MB dye with the help of 60 mg/L of photocatalyst which is higher than other experiments.

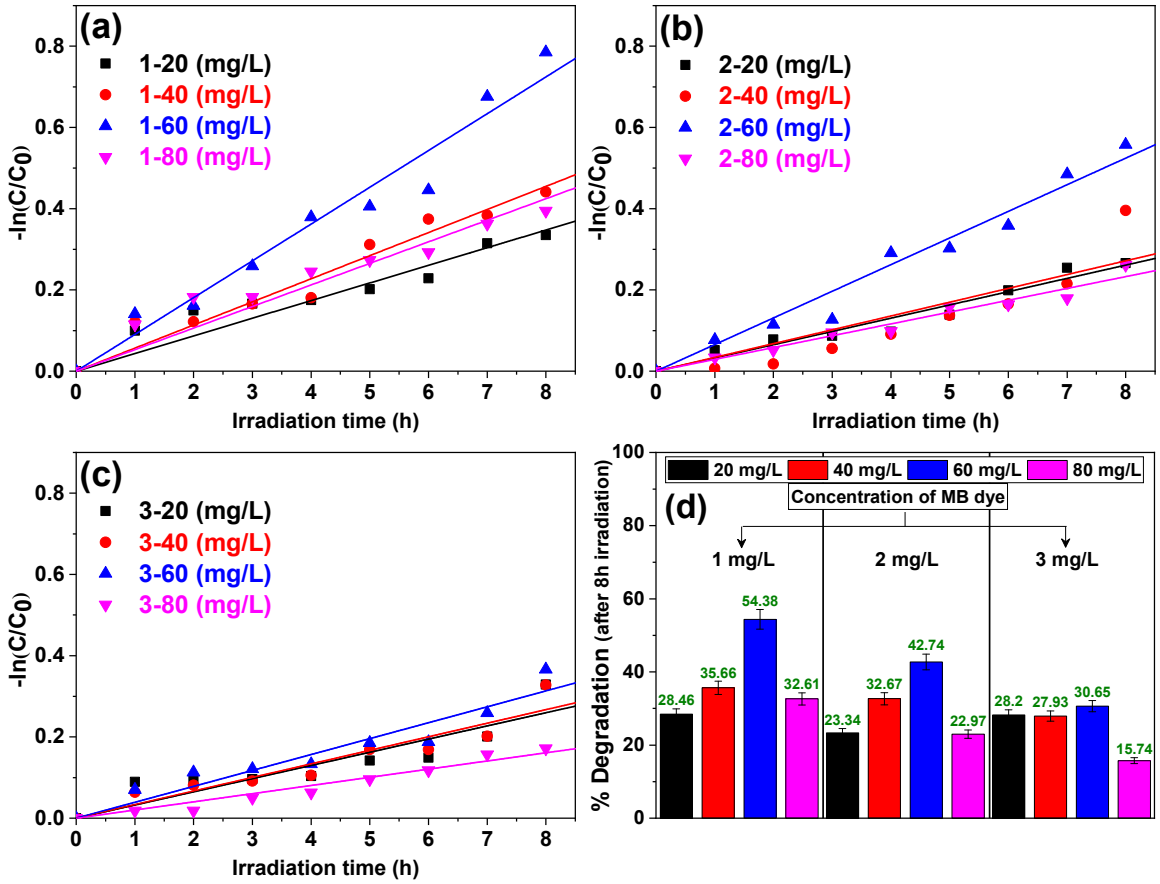

Figure 4.11: First order kinetics of decolorization/degradation of MB dye with C12 (a) 1.0, (b) 2.0, (c) 3.0 mg/L as MB concentration, and (d) comparative bar chart of the final efficiency of C12 at different conditions.

Table 4.5 and figure 4.11a-c show the fitting quality and values of rate constant for various reactions carried out under visible irradiation. Among all the photoreactions, 60.0 mg/L photocatalyst has degraded the 1.0 mg/L MB dye with the highest rate constant 0.0905 h^{-1}. While, all other configurations possess lesser rate constant due to various reasons which have been already discussed. Further, a comparative bar chart has been

shown in figure 4.11d depicting the degradation efficiency after 8.0 h irradiation. It is very much clear that with the increase in the concentration of dye the photocatalytic efficiency of C12 has been decreased but, catalytic performance of C12 was quenched beyond 60.0 mg/L in all dye concentrations.

Table 4.5: Details of photochemical reaction kinetics of MB dye with the help of C12.

Concentration (mg/L)		Catalyst	Efficiency (%)	Rate constant K (h^{-1})	R^2
Dye	Catalyst				
1.0	20.0	C12	28.46	0.0434	0.97
1.0	40.0	C12	35.66	0.0568	0.98
1.0	60.0	C12	54.38	0.0905	0.98
1.0	80.0	C12	32.61	0.0531	0.97
2.0	20.0	C12	23.34	0.0326	0.98
2.0	40.0	C12	32.67	0.0339	0.90
2.0	60.0	C12	42.74	0.0656	0.98
2.0	80.0	C12	22.97	0.0291	0.97
3.0	20.0	C12	28.20	0.0324	0.94
3.0	40.0	C12	27.93	0.0334	0.96
3.0	60.0	C12	30.65	0.0392	0.97
3.0	80.0	C12	15.75	0.0201	0.98

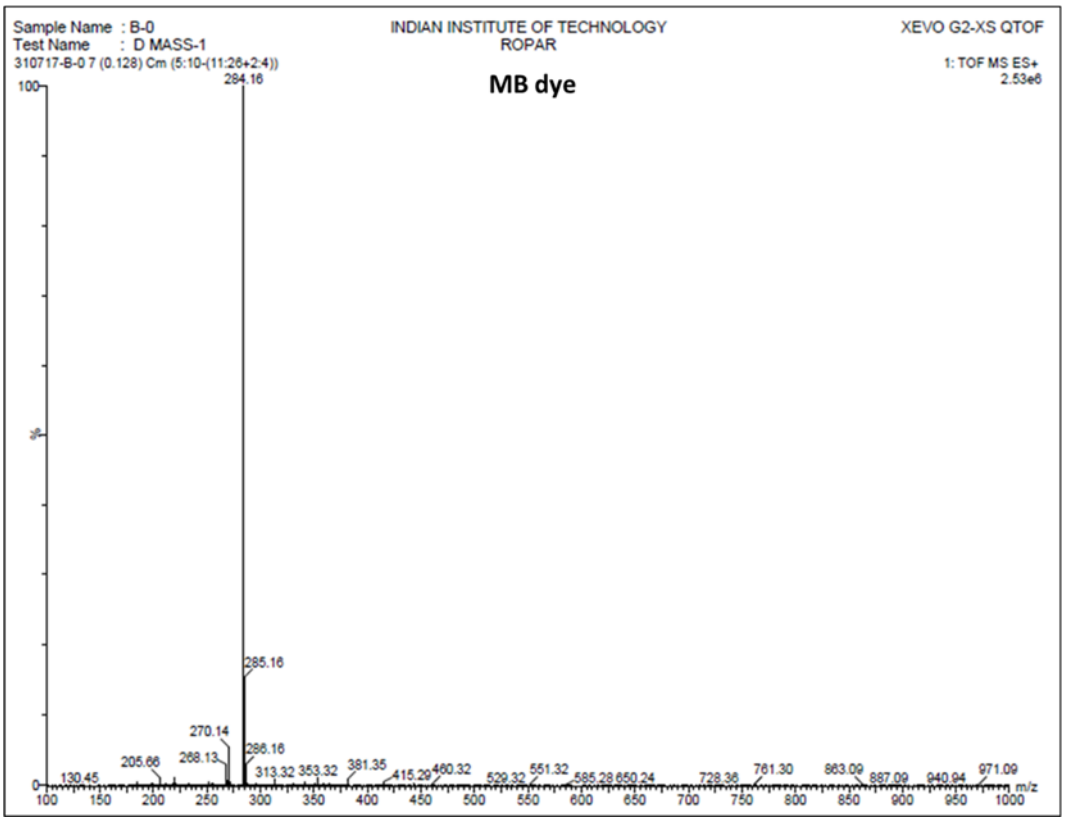

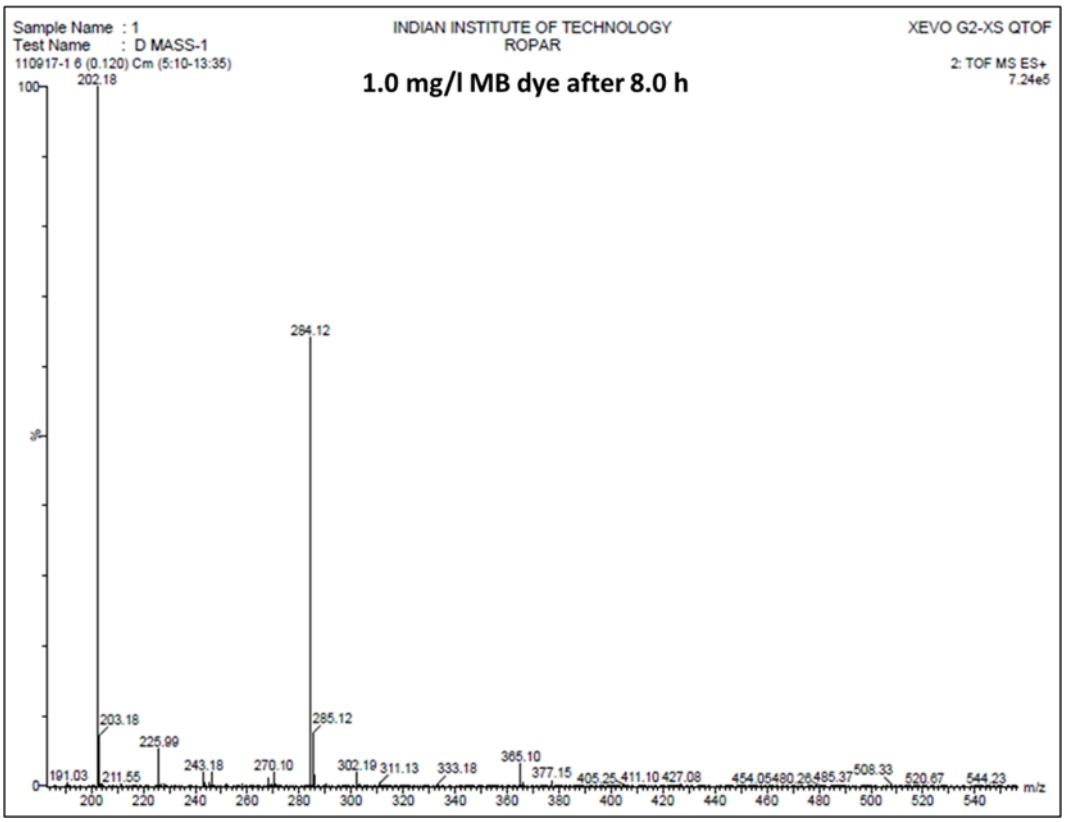
Sample Name : 1
Test Name : D MASS-1
110917-1 6 (0.120) Cm (5:10-13:35)
INDIAN INSTITUTE OF TECHNOLOGY
ROPAR
XEVO G2-XS QTOF
2: TOF MS ES+
7.24e5
1.0 mg/l MB dye after 8.0 h
202.18
284.12
203.18
285.12
225.99
365.10
191.03
211.55
243.18
270.10
302.19
311.13
333.18
377.15
405.25
411.10
427.08
454.05
480.26
485.37
508.33
520.67
544.23
%
m/z

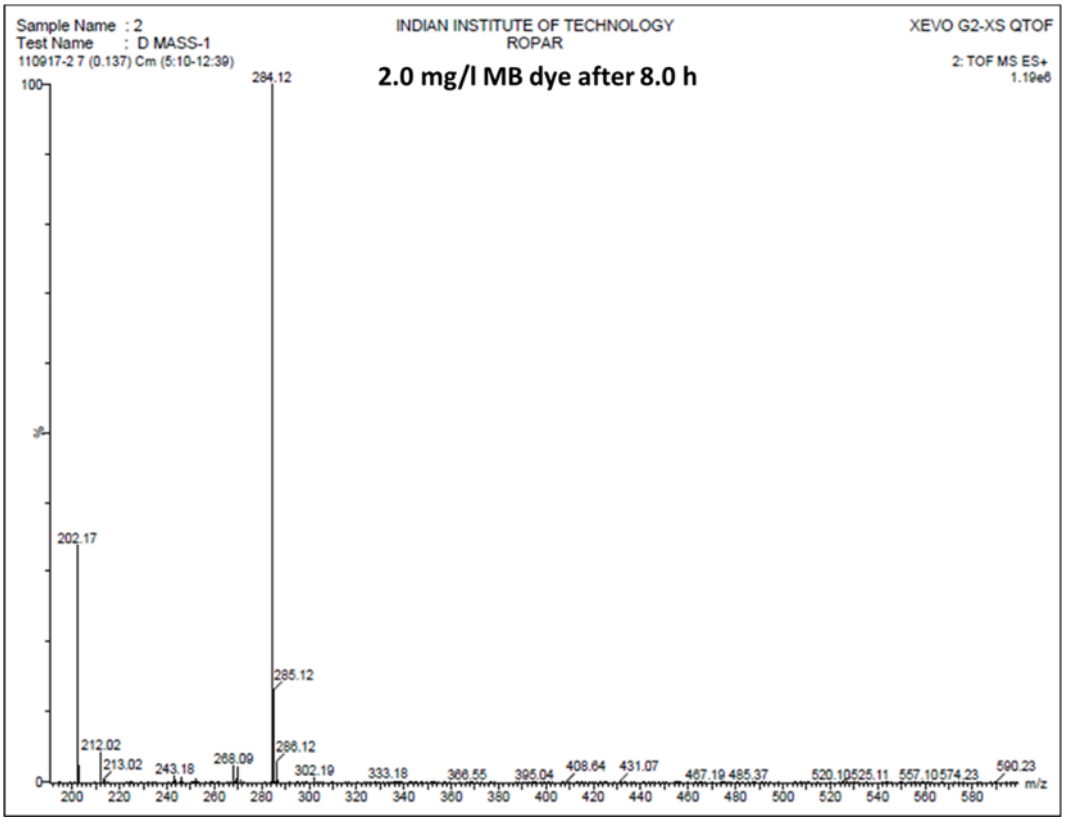
Sample Name : 2
Test Name : D MASS-1
110917-2 7 (0.137) Cm (5:10-12:39)
INDIAN INSTITUTE OF TECHNOLOGY
ROPAR
XEVO G2-XS QTOF
2: TOF MS ES+
1.19e6
2.0 mg/l MB dye after 8.0 h
284.12
202.17
285.12
212.02
213.02
243.18
268.09
286.12
302.19
333.18
366.55
395.04
408.64
431.07
467.19
485.37
520.10
525.11
557.10
574.23
590.23
%
m/z

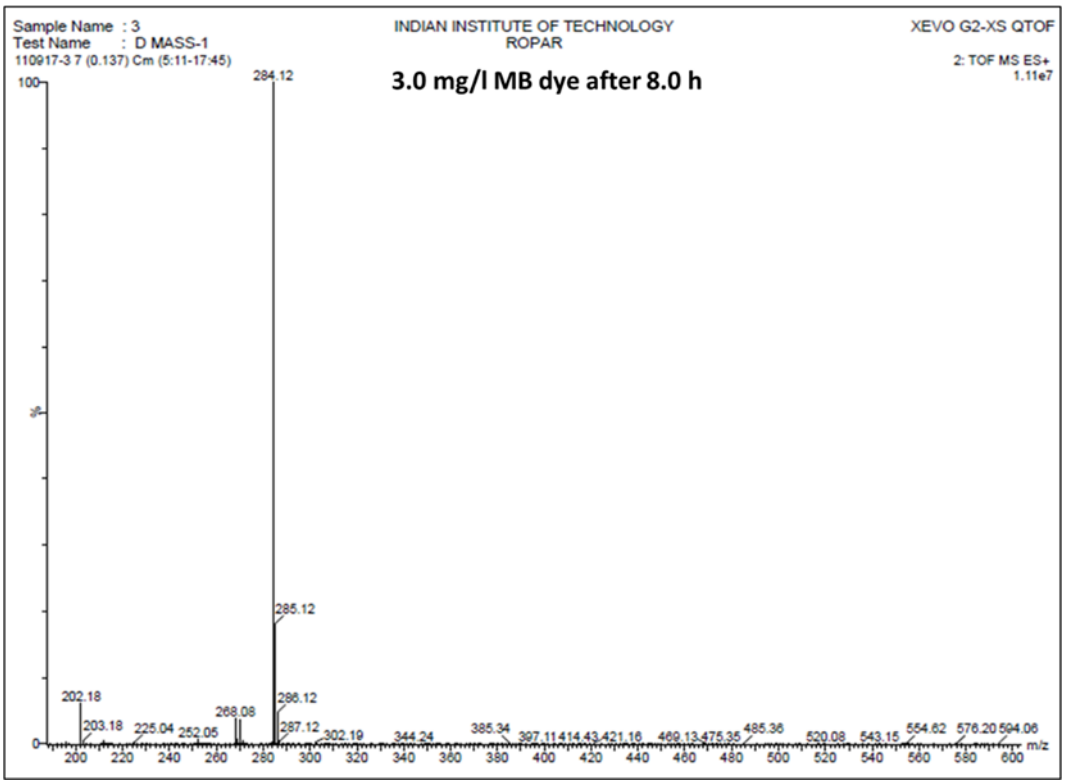

Figure 4.12: Direct mass spectrometry of initial MB dye solution and 1.0, 2.0 and 3.0 mg/L dye solution degraded with the help of C12 under solar irradiations for 8.0 h, respectively. With the increase in the concentration of dye solution, the intensity of m/z = 202.18 tends to decrease which confirmed the decrement in the degradation of MB dye. Here, m/z = 284.12 associated to the MB molecule (excluded Cl^- ion).

To confirm the diminishing absorbance spectrum is related to decolorization or photodegradation of MB dye, direct mass spectrometry (MS) was carried out in which m/z = 284.12 is associated with the parent MB dye molecule which got transformed to the combination of two major peaks (m/z = 202.18 and 284.12) in degraded solutions confirming the degradation of dye as shown in figure 4.12.

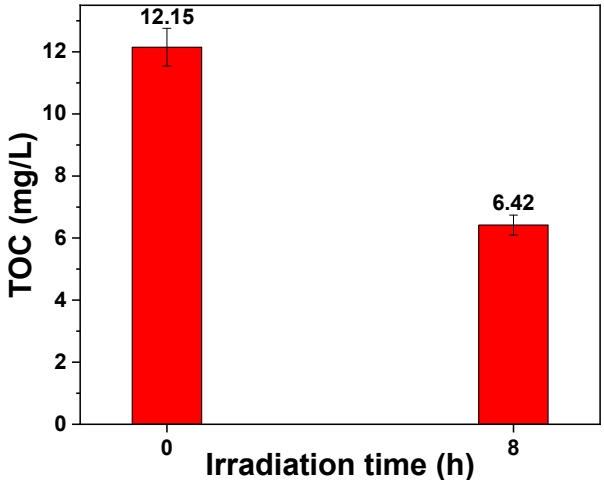

Figure 4.13: TOC analysis confirmed the degradation of MB dye under the exposure of visible radiations after 8.0 h visible exposure with C12.

Further, total organic carbon (TOC) confirmed the photodegradation of MB dye suggesting 47.1% decrement of organic carbon present in the dye solution as shown in figure 4.13. Moreover, 47% removal of organic carbon is slightly less than 54% (absorbance spectra) suggesting that the degradation is slightly delayed process than decolorization.

Further, to establish the mechanism responsible for the photodegradation of MB dye, detection of reactive oxidative species was successfully carried out by adding various scavengers in the reaction solution before the irradiation. Figure 4.14a represents the degradation trend of the 1.0 mg/L MB dye with 60.0 mg/L photocatalyst in the presence of different scavengers. In comparison to the initial degradation efficiency (54.3%) (in the absence of any scavenger), addition of AO (h^+), IPA ($OH^{\cdot}$), NS (e^-) and AA ($O_2^{\cdot-}$) resulted 39.8, 38.9, 35.3 and 15.1% degradation of dye, respectively. These results asserted the generation of reactive oxidative species in the following order; $O_2^{\cdot-} > e^- > OH^{\cdot} \cong h^+$. Therefore, the photodegradation reaction is majorly dominated by the superoxide anion radical which is responsible for the half reduction reaction occurred at conduction band of the photocatalyst.

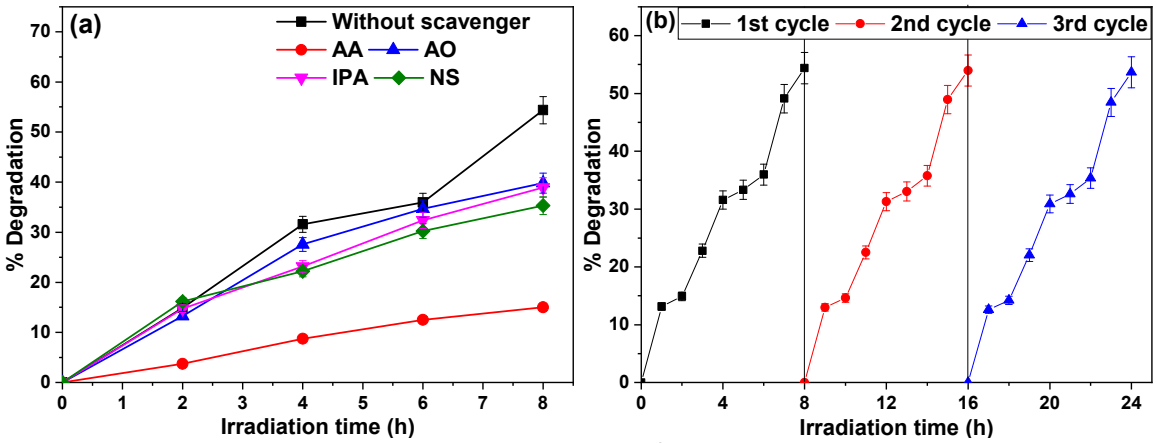

Figure 4.14: (a) Effect of different scavengers (h^+; e^-, $OH^{\cdot}$ and $O_2^{\cdot-}$ scavenger), and (b) Recyclability for the degradation of MB dye with the help of C12 as photocatalyst for 3 cycles.

Further, the applicability of as synthesized photocatalyst can be decided on the basis of its reusability/recyclability. To check the recyclability of C12, three continuous cycles of same experiment (1.0 mg/L dye with 60.0 mg/L C12) were carried out after extracting the photocatalyst by centrifugation (4500 rpm) followed by washing (with distilled water) and drying (45 °C) with same concentration of solution under same illumination. An excellent recyclability of photodegradation for 3 cycles has been observed as shown in figure 4.14b.

4.10. Proposed mechanism

Based on the results obtained from various steps of photocatalytic studies, it became very essential to obtain the contribution of photocatalyst and transformation of reactive oxidative species involved in the photocatalysis. Figure 4.15a represents the valence band spectrum of C12 from where multiple valence band edge (VBE) are clearly obtained i.e. -2.01 eV and 1.56 eV as an intercept on energy axis of extrapolated curve. Further, with the help of optical absorbance spectrum of C12 (figure 4.7) the position of conduction band edge (CBE) were calculated and shown in figure 4.15b.

The reduction potential edge of $O_2/O_2^{\cdot-}$ is -0.046 eV vs. NHE, comparable to the calculated CBE i.e. -0.041 eV leading to easy generation of super oxide anion radical as shown in figure 4.15b [24]. Figure 4.16 represents the mechanism for the photodegradation of MB dye with the help of C12 in which the holes and electron were generated with the illumination of visible light on valence and conduction bands, respectively, can be described as following equations;

$$NbC + C + photon \rightarrow NbC + C + h^+ + e^- \quad (4.1)$$

$$O_2 + e^- \rightarrow O_2^{\cdot-} \quad (4.2)$$

$$O_2^{\cdot-} + H_2O \rightarrow OH^{\cdot} + OH^- \quad (4.3)$$

$$OH^- + h^+ \rightarrow OH^{\cdot} \quad (4.4)$$

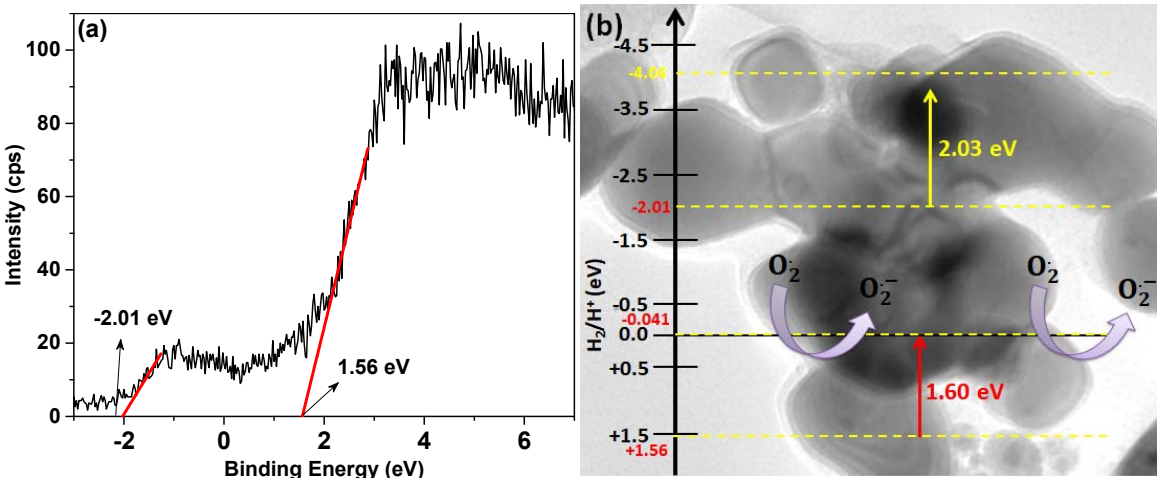

Figure 4.15: (a) Valence band spectra and (b) band diagram of synthesized C12 confirming the absorption corresponding to multiple phases showing generation of $O_2^{\cdot-}$.

It is very well-known fact that NbC has electronic structure similar to noble metals and shows conducting behavior which might be a good support as photocatalyst to degrade organic pollutants. Here, the synthesized photocatalyst (C12) has wide particle size distribution having 120 nm as average particle size with very less specific surface area (17.7 m^2/g). Moreover, the illumination of visible light to the dye and photocatalyst solution, Nb

element is present in 3 oxidation states 2+, 3+ and 4+, simultaneously which may attribute to the photodegradation reaction as follows;

$$Nb^{3+} \leftrightarrow Nb^{4+} + e^{-} \quad (4.5)$$

$$Nb^{2+} \leftrightarrow Nb^{3+} + e^{-} \quad (4.6)$$

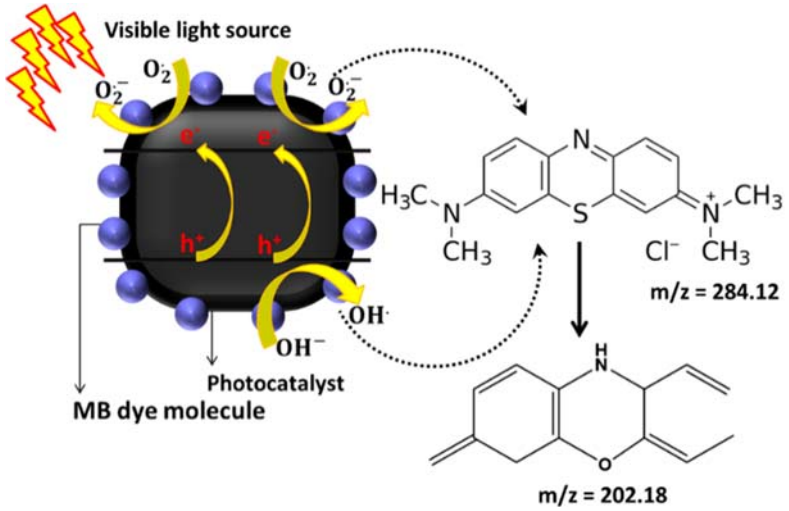

Figure 4.16: Proposed mechanism of the degradation of MB dye with the help of C12 under visible irradiation.

Further, valence band potentials obtained from valence band spectra of C12 also confirmed the chemical reactions governing the generation of $O_2^{\cdot-}$, responsible for the photodegradation of MB dye molecule resulting a probable lighter organic molecule with m/z = 202.18 as shown in figure 4.16.

References:

1 C. Zaharia, D. Suteu, A. Muresan, R. Muresan and A. Popescu, *Environ. Eng. Manag. J.*, 2009, **8**, 1359–1369.
2 M. A. Meetani, M. A. Rauf, S. Hisaindee, A. Khaleel, A. AlZamly and A. Ahmad, *RSC Adv.*, 2011, **1**, 490–497.
3 T. E. Novotny, K. Lum, E. Smith, V. Wang and R. Barnes, *Int. J. Environ. Res. Public Health*, 2009, **6**, 1691–1705.
4 O. Shafey, M. Eriksen, H. Ross and J. Mackay, *The Tobacco Atlas*, The American Cancer Society, Atlanta, eorgia (USA), 3rd Editio., 2009.
5 J. Puls, S. A. Wilson and D. Holter, *J. Polym. Environ.*, 2011, **19**, 152–165.
6 T. Kamal, I. Ahmad, S. B. Khan and A. M. Asiri, *Carbohydr. Polym.*, 2017, **157**, 294–302.
7 M. Mohiuddin, K. K. Sadasivuni, S. Mun and J. Kim, *RSC Adv.*, 2015, **5**, 34432–34438.
8 A. Gupta, G. Singla and O. P. Pandey, *Ceram. Int.*, 2016, **42**, 13024–13034.
9 F. A. O. Fontes, J. F. de Sousa, C. P. Souza, M. Benachour and M. B. D. Bezerra, *Chem. Eng. J.*, 2012, **184**, 303–307.
10 A. C. Ferrari and J. Robertson, *Phys. Rev. B*, 2000, **61**, 14095–14107.
11 A. C. Ferrari, J. C. Meyer, V. Scardaci, C. Casiraghi, M. Lazzeri, F. Mauri, S. Piscanec, D. Jiang, K. S. Novoselov, S. Roth and A. K. Geim, *Phys. Rev. Lett.*, 2006, **97**, 1–4.
12 J.-B. Wu, M.-L. Lin, X. Cong, H.-N. Liu and P.-H. Tan, *Chem. Soc. Rev.*, 2018, **47**, 1822–1873.
13 A. Eckmann, A. Felten, A. Mishchenko, L. Britnell, R. Krupke, K. S. Novoselov and C. Casiraghi, *Nano Lett.*, 2012, **12**, 3925–3930.
14 M. Thommes, *Chemie Ing. Tech.*, 2010, **82**, 1059–1073.
15 Z. Weibin, W. Weidong, W. Xueming, C. Xinlu, Y. Dawei, S. Changle, P. Liping, W. Yuying and B. Li, *Surf. Interface Anal.*, 2013, **45**, 1206–1210.
16 P. Yu, X. Wen, Y.-R. Toh, Y.-C. Lee, K.-Y. Huang, S. Huang, S. Shrestha, G. Conibeer and J. Tang, *J. Mater. Chem. C*, 2014, **2**, 2894–2901.
17 M. Aufray, S. Menuel, Y. Fort, J. Eschbach, D. Rouxel, B. Vincent and N. Université, *J. Nanosci. Nanotechnol.*, 2009, **9**, 4780–4785.
18 H. Lin, S. Gao, C. Dai, Y. Chen and J. Shi, *J. Am. Chem. Soc.*, 2017, **139**, 16235–16247.
19 L. Yate, L. Emerson Coy, G. Wang, M. Beltrán, E. Díaz-Barriga, E. M. Saucedo, M. A. Ceniceros, K. Załęski, I. Llarena, M. Möller and R. F. Ziolo, *RSC Adv.*, 2014, **4**, 61355–61362.
20 C. Zhang, M. Beidaghi, M. Naguib, M. R. Lukatskaya, M. Zhao, B. Dyatkin, K. M. Cook, S. J. Kim, B. Eng, X. Xiao, D. Long, W. Qiao, B. Dunn and Y. Gogotsi, *Chem. Mater.*, 2016, **28**, 3937–3943.
21 J. Halim, K. M. Cook, M. Naquib, P. Eklund, Y. Gogotsi, J. Rosen and M. W. Barsoum, *Appl. Surf. Sci.*, 2016, **362**, 406–417.
22 R. Khan and M. H. Fulekar, *Desalin. Water Treat.*, 2014, **56**, 2438–2446.
23 I. U. Gaya and H. A. Abdullah, *J. Photochem. Photobiol. C Photochem. Rev.*, 2008, **9**, 1–12.
24 Y. Yang, Y. Guo, F. Liu, X. Yuan, Y. Guo, S. Zhang, W. Guo and M. Huo, *Appl. Catal. B Environ.*, 2013, **142**–**143**, 828–837.

CHAPTER 5 RESULTS & DISCUSSION-II

Utilization of parthenium hysterophorous stems (PH; Agricultural waste)

Overview

This chapter describes the synthesis of NbC-C nanocomposite by using stems of parthenium hysterophorous (PH) a weed as carbon source. Optimization of synthesis parameters (temperature, time, reducing agent i.e. Mg and PH content) have been carried out to obtain single phase NbC. Optical and photocatalytic response of single phase NbC samples (based on XRD results) are also discussed with the help of lattice distortion, lattice carbon content (x in NbC_x), absorbance spectroscopy and photodegradation experiments considering similar conditions discussed in previous chapter. Further, details of mechanism associated with degradation of dye has been discussed based on structural features (TEM and Raman results), chemical composition (XPS results) and different photodegradation experiments (scavenger, TOC analysis).

5.1. Introduction

Parthenium hysterophorous (PH, rag weed parthenium in USA and carrot grass in India) is a globally defamed weed to human and animals due to its toxic and allergic characteristics. It invades and adapts new habitats by reducing indigenous cultivation. Moreover, it also causes hay fever, dermatitis, bronchitis and asthma to human and livestock. In order to understand the effect of carbon source and type of carbon (A/G/graphene), stems of parthenium hysterophorous (PH; carrot grass) has been taken as carbon source to synthesize NbC-C heterostructure. The use of PH contains dual approach; (i) utilization of agricultural hazardous weed [1–7] and (ii) development of efficient photocatalyst (alternate to existing compounds). Moreover, previous chapter has explained the effect of composition and other structural parameters (particle size and surface area) on the photocatalytic activity to degrade MB dye. But, type of carbon (A: amorphous, G: graphitic and graphene) in as-synthesized samples also govern the catalytic performance of the synthesized compounds [8–11]. Presence of A- and G- carbon exhibited additional surface area and electronic bridge between carbide particles to facilitate charge transfer, respectively [12,13]. Both of these parameters are very important for the photo and electro- catalytic reactions. The details of the synthesis parameters are given in table 5.1.

Table 5.1: Details of experimental conditions to obtain NbC nanopowder.

Precursor (g)			Sample	Temperature (°C)	Holding time (h)
Nb_2O_5	Mg	C			
1.329	3.5	2.0	G1	600	1
1.329	3.5	2.0	G2	600	3
1.329	3.5	2.0	G3	600	5
1.329	3.5	2.0	G4	700	0
1.329	3.5	2.0	G5	700	1
1.329	3.5	2.0	G6	700	3
1.329	3.5	2.0	G7	800	0
1.329	3.5	2.0	G8	800	1
1.329	3.5	2.0	G9	800	3
1.329	3.5	2.0	G10	800	5
1.329	3.5	1.5	G11	800	0
1.329	3.5	1.0	G12	800	0
1.329	2.0	2.0	G13	800	0

5.2. Structural and morphological features of smoked CFs:

Prior to use the PH stems for the reactions, its XRD and SEM analysis were carried out as shown in figure 5.1. It suggested the amorphous structure along with some minor diffraction peaks associated to cellulose (~15°, 16.5°, 22.8° and 28.3°; ICDD: 00-050-2241 and 00-003-0223) while, figure 5.1b depicts the presence of flaky structures on the surface

along with the tubular structure of around 50µm (diameter) which might help for water transportation.

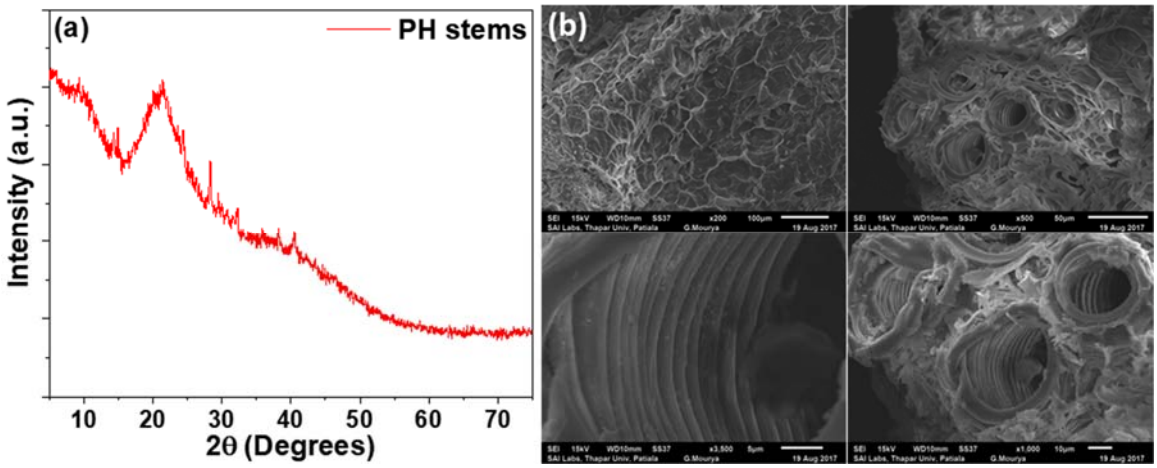

Figure 5.1: (a) XRD pattern and (b) SEM micrographs of crushed PH stems suggesting the presence of organic components cellulose, hemicellulose and flaky, tubular morphologies.

5.3. X-ray diffraction (XRD):

Figure 5.2 represents the XRD patterns of all the synthesized samples at different synthesis parameters (temperature, holding time and amount of PH). From the XRD patterns, the formation of different phases at different synthesis conditions were determined by matching the position of diffraction peaks with the ICDD cards as listed in table 3.2 (chapter 3). Sample G1-G3 consist of a mixture of NbO_2 and Nb_2O_5 (monoclinic and hexagonal) as shown in figure 5.2a suggesting the partial reduction of Nb_2O_5 (monoclinic) to NbO_2 at 600 °C. Moreover, at 600 °C, formation of NbO_2 supersede the Nb_2O_5 phase transformation (monoclinic and hexagonal) with increasing holding time (1.0 - 5.0 h). In order to obtain NbC as a result of reduction and carburization of Nb_2O_5, temperature was raised to 700 °C (0.0 h holding time) which led to the complete phase transformation (monoclinic to hexagonal) of Nb_2O_5 (sample G4) as shown in figure 5.2b. However, increasing holding time (1.0 and 3.0 h) at 700 °C resulted the mixture of NbC+C (G5, G6), respectively (figure 5.2b). Formation of NbC along with graphitic carbon as minor phase (figure 5.2b) may be associated to in-situ reduction followed by carburization of Nb_2O_5 at 700 °C [14]. To understand the effect of synthesis temperature and holding time, experiments were performed at 800 °C with different holding times (0.0, 1.0, 3.0 and 5.0 h) as shown in figure 5.2c (G7-G10).

All these samples contain single phase NbC pattern having small content of graphitic carbon with almost equal volume fraction of NbC and carbon which is shown in table 5.2. Since, with 0.0 h of holding time at 800 °C, single phase NbC has been obtained,

so the other parameters such as amount of PH and Mg powder needs to be optimized at same conditions.

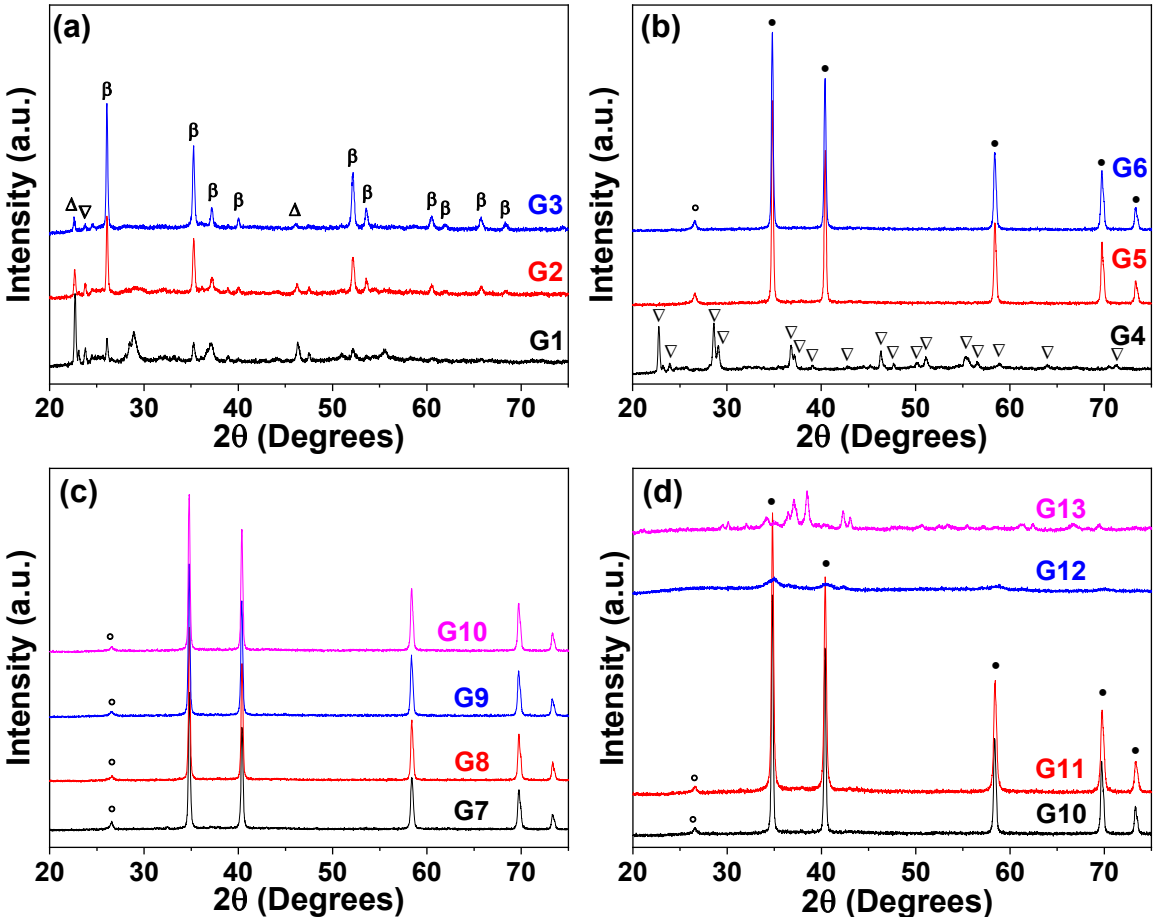

Figure 5.2: XRD diffraction patterns showing the influence of different synthesis parameters; temperature (a) 600 °C (1.0, 3.0 and 5.0 h), (b) 700 °C (0.0, 1.0 and 3.0 h), (c) 800 °C (0.0, 1.0, 3.0 and 5.0 h) and (d) amount of PH (2.0, 1.5 and 1.0 g), reducing agent (Mg; 2.0 g) at 800 °C (0.0 h holding time) on phase formation. Symbols: • (NbC), α (Nb), β (NbO_2), Δ (Nb_2O_5) and ° (graphitic carbon).

To optimize the amount of PH, 2.0, 1.5 and 1.0 g were also used at 800 °C with 0.0 h holding time which are shown in figure 5.2d as G10, G11 and G18 respectively. As an effect of variation in amount of PH, G11 contained lesser amount of graphitic carbon (1.91%) than G10 along with higher NbC content as listed in table 5.2. While, G18 showed less intense diffraction peaks than G10 and G11 which can be attributed to the insufficient amount of carbon present in the autoclave to form NbC (figure 5.2d). Further, amount of reducing agent was also reduced (2.0 g) to understand the role of reducing agent (Mg) which showed the partial reduction-carburization of Nb_2O_5 associated to insufficient amount of Mg metal powder to reduce Nb_2O_5 as represented by G13 in figure 5.2d. XRD pattern of G13 represents the mixed phase consisting Nb metal (most intense diffraction

peak) and NbO (matched with 2 different ICDD cards; 01-074-1709, 00-042-1125) depicting the insufficient reduction of Nb_2O_5.

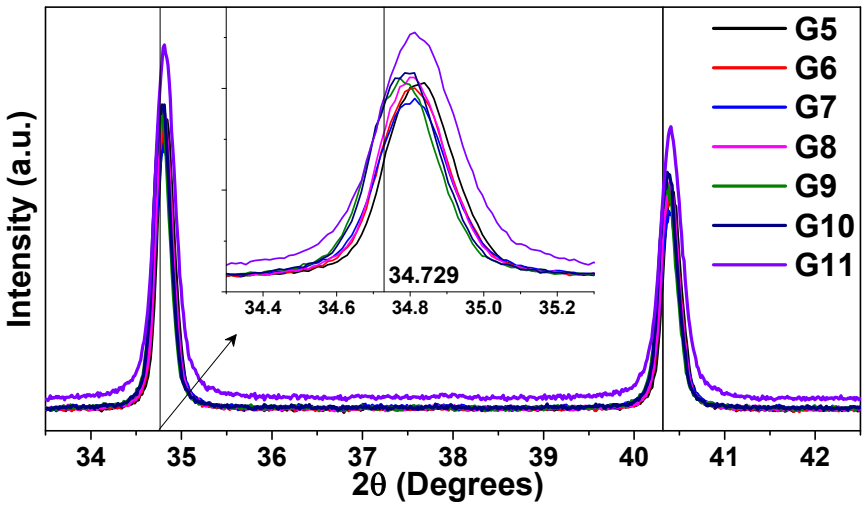

Figure 5.3: XRD patterns of all single phase NbC samples showing the higher angle shifting of diffraction peaks of (111) and (200) planes. Inset shows the magnified (111) peak with the marked standard position of (111) plane of ICDD 01-089-3690.

During the reduction-carburization of the Nb_2O_5, the transportation of C and O resulted the evolution of CO/CO_2 as byproducts inducing the distortion of the NbC lattice and porosity on the surface [9]. With the help of XRD patterns of NbC, it was observed that diffraction peaks were shifted to higher diffraction angle leading to compressive strain in lattice as shown in figure 5.3.

Table 5.2: Volume fractions of NbC and graphitic carbon in different samples (G10-G11) at different synthesis conditions.

	Volume fraction (%)		SSA	Pore volume	Avg. Pore size
	Carbon	NbC	(m^2/g)	(cm^3/g)	(nm)
G10	6.33	93.67	5.21	0.063	1.26
G6	8.29	91.71	13.39	0.071	1.25
G7	5.34	94.66	8.29	0.049	1.31
G8	5.18	94.82	4.21	0.052	1.24
G7	3.43	96.57	5.75	0.048	1.27
G10	5.38	94.62	9.23	0.061	1.26
G11	1.91	98.09	49.47	0.121	4.58

5.4. Williamson-Hall (W-H) analysis:

The XRD results of single phase NbC obtained at different synthesis conditions show higher angle shifting in all the samples. The nature of distortion was estimated with the help of W-H analysis by assuming the homogeneity of (i) strain, (ii) stress and (iii) strain energy density as three different models USM, USDM and USEDM, respectively [15,16]. Among all the W-H models, uniform strain model (USM) provided the better results (R^2=0.99) depicting the homogeneity of strain throughout the NbC lattice as compared to

other model (USDM and USEDM) as shown in figure 5.4. Various postulates of W-H analysis have been listed in table 5.3. It is observed that there is not much variation of lattice strain in all the single phase NbC samples (G5-G11) whereas, the variation in crystallite size calculated from W-H models can be associated to the underestimation of contribution of strain in the peak broadening in Scherrer's method. Therefore, Crystallite size of NbC was estimated by W-H models and Scherrer's criteria suggesting ~80 nm and ~30 nm, respectively.

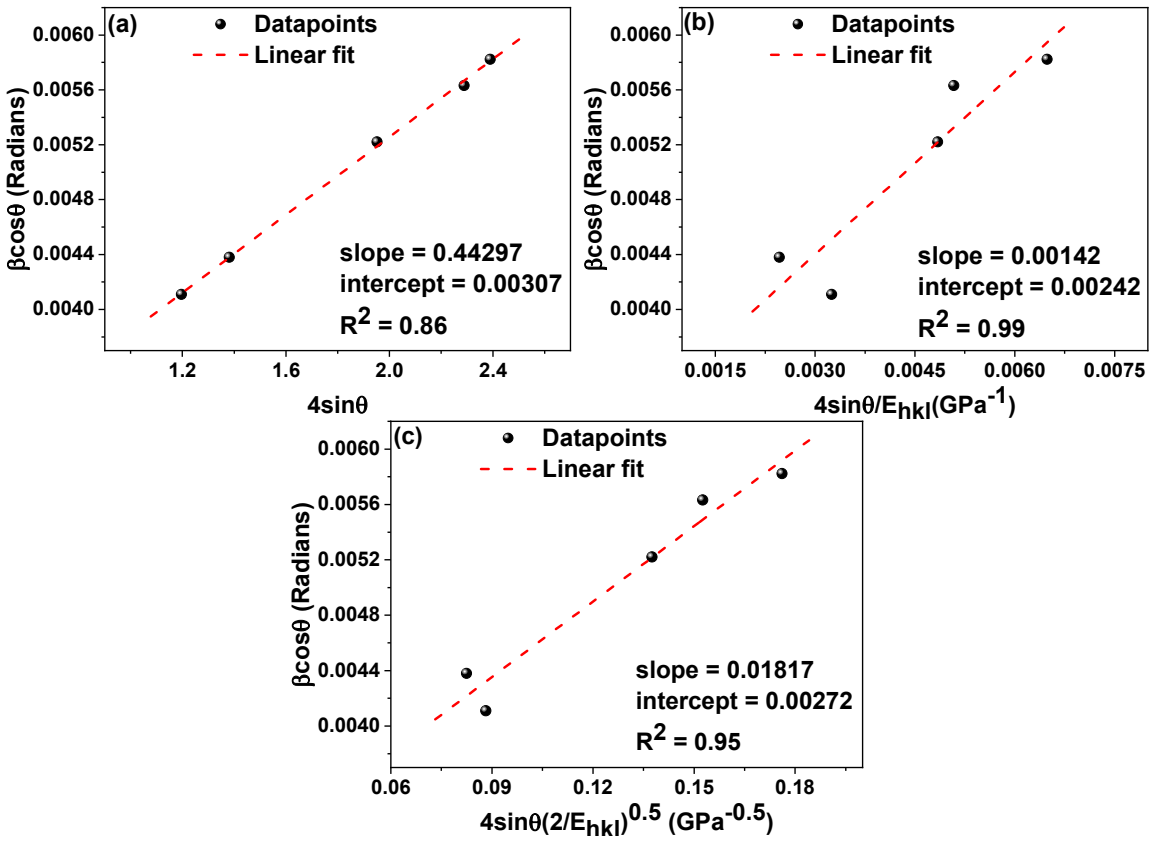

Figure 5.4: Representative graphs of (a) USM, (b) USDM and (c) USDEM models of W-H analysis for sample G11.

Table 5.3: Lattice carbon content (x), lattice constant (a) and W-H postulates of various samples using PH stems.

Sample ID	x	a	USM		USDM			USEDM				Scherrer
		Å	ε, $\times10^{-4}$	t, nm	σ, GPa	ε, $\times10^{-4}$	t, nm	u, $\times10^{-5}$, kJm^{-3}	σ, GPa	ε, $\times10^{-4}$	t, nm	t, nm
G5	0.875	4.462	16.7	83.0	0.44	10.6	59.5	33.30	0.53	12.6	70.0	33.1
G6	0.888	4.463	15.4	89.4	0.49	11.6	62.4	39.32	0.58	13.6	74.9	32.6
G7	0.890	4.463	15.0	79.2	0.47	11.2	57.1	37.01	0.56	13.2	67.3	31.5
G8	0.890	4.463	13.8	81.5	0.42	9.9	58.0	30.41	0.51	12.0	68.3	33.4
G9	0.912	4.465	14.4	80.1	0.45	10.7	58.2	33.96	0.54	12.7	68.6	32.5
G10	0.904	4.465	14.4	82.5	0.49	10.7	59.2	33.82	0.54	12.7	70.0	32.9
G11	0.881	4.462	14.2	57.3	0.44	10.6	45.2	33.01	0.53	12.5	50.9	28.1

5.5. Transmission electron microscopy (TEM):

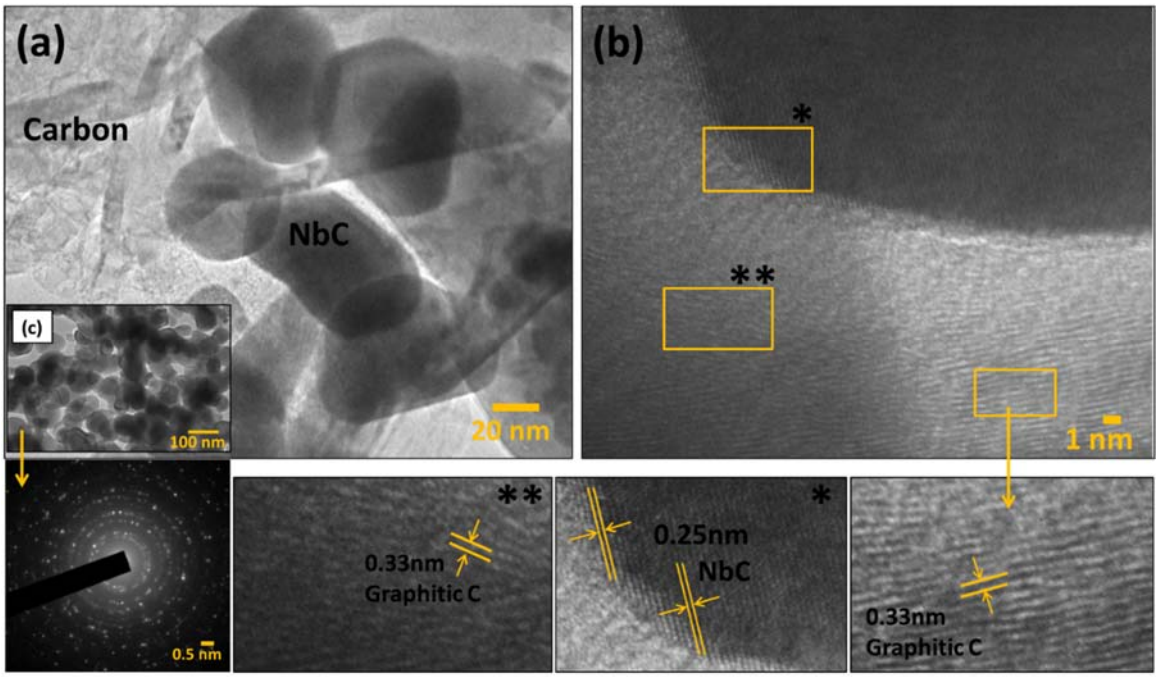

Figure 5.5: TEM micrographs of G11 showing (a) NbC NPs encapsulated in carbon (graphitic) network, (b) HRTEM (lattice fringing) corresponding to NbC (0.25 nm, (111) plane) and g-carbon (0.33 nm, (002) plane) and (c) TEM and SAED pattern depicting the polycrystalline agglomerated NbC NPs.

Morphology of the synthesized nano powder samples was studied by TEM analysis as shown in figure 5.5 for G11. As observed from XRD results, the presence of graphitic carbon can be interpreted as a continuous network in which NbC NPs are embedded as shown in figure 5.5a. HRTEM micrograph of G11 is shown in figure 5.5b in which lattice fringing confirmed the presence of NbC NPs (dark region) and graphitic carbon (magnified structures are shown in insets marked with * and **). Further, figure 5.5c shows the NbC aggregate and the corresponding SAED pattern, shown below, suggesting the nanocrystalline nature of synthesized NbC NPs. Moreover, TEM micrographs of other single-phase samples (G5, G7 and G10) (as shown in figure 5.6) confirmed the presence of NbC NPs embedded in graphitic carbon network. TEM micrographs suggested the formation of the irregular spherical shape of NbC nanoparticles with non-faceted growth. Figure 5.5 represented the homogenous distribution of NbC nanoparticles as compared to other samples as shown in figure 5.6.

The lognormal distribution of particle size of NbC NPs suggested the narrower distribution of NPs in G11 with ~66 nm (mean diameter) whereas for other samples (G5, G7 and G10), it exhibits wider distribution as shown in figure 5.7, further supporting the average crystallite size calculated by W-H models.

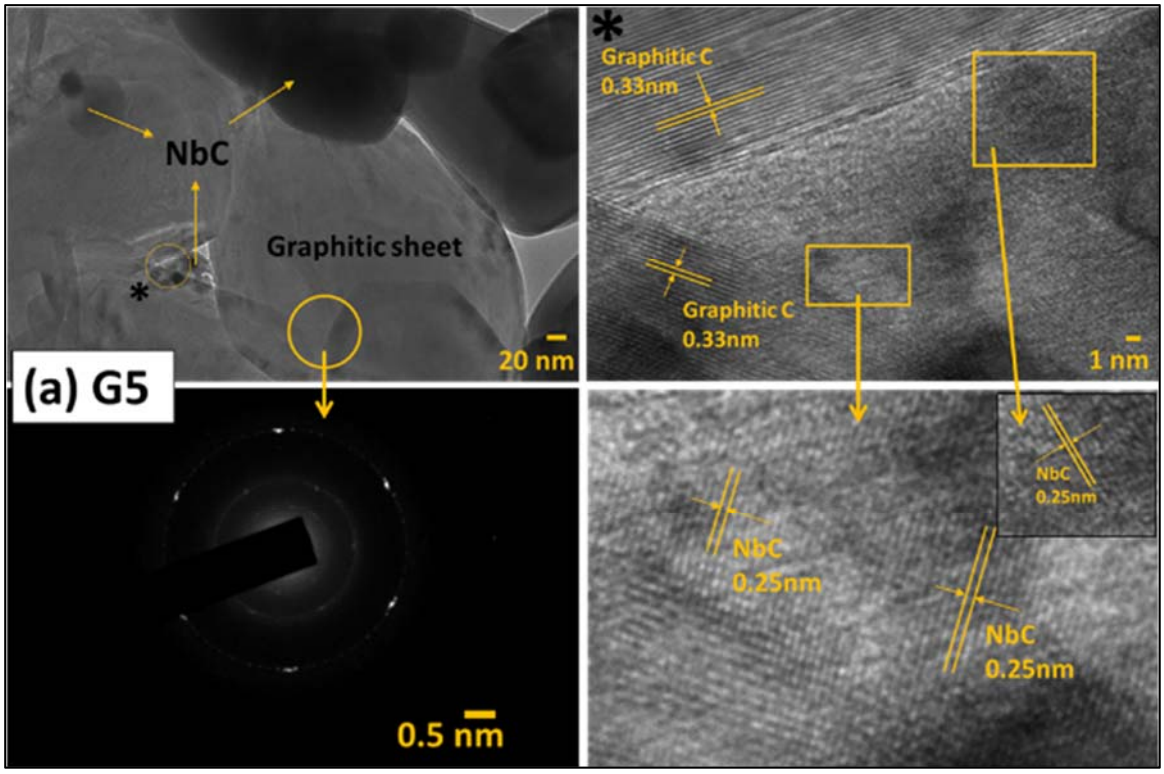
NbC
Graphitic sheet
*
20 nm
(a) G5
0.5 nm
*
Graphitic C
0.33nm
Graphitic C
0.33nm
1 nm
NbC
0.25nm
NbC
0.25nm
NbC
0.25nm

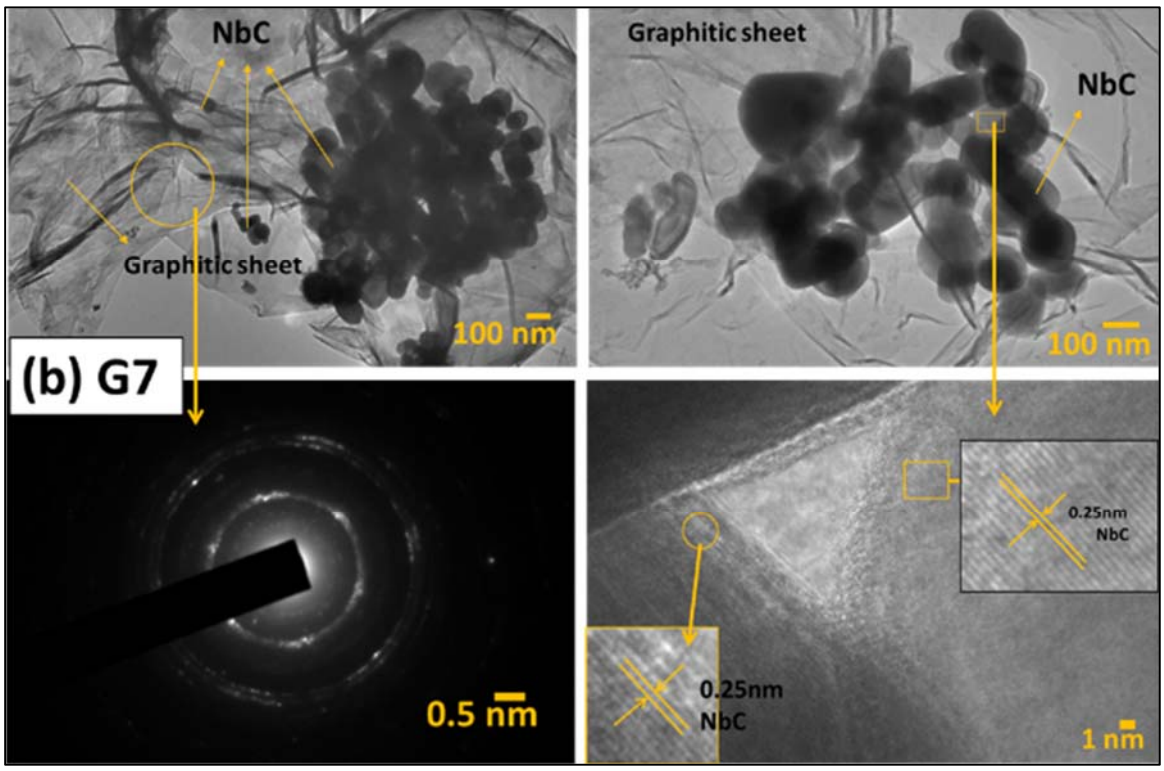
NbC
Graphitic sheet
100 nm
(b) G7
0.5 nm
Graphitic sheet
NbC
100 nm
0.25nm
NbC
0.25nm
NbC
1 nm

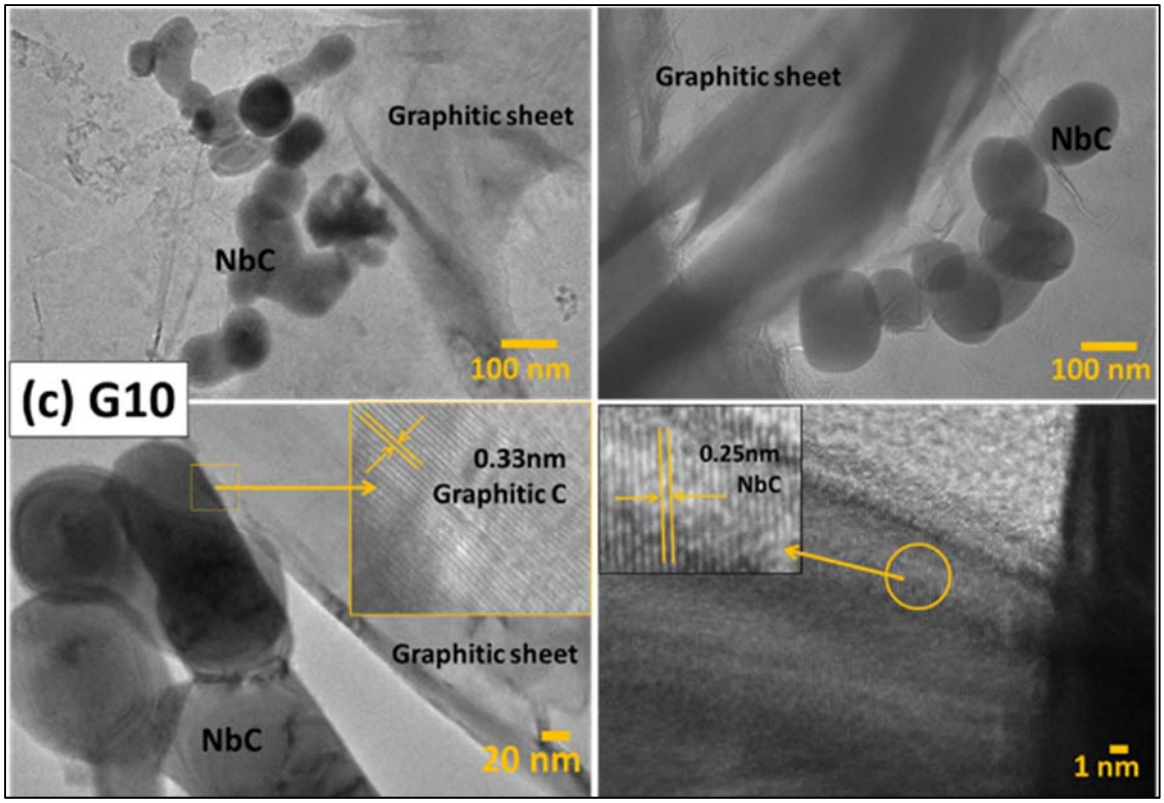

Figure 5.6: TEM micrographs of (a) G5, (b) G7 and (c) G10 showing the presence of NbC nano particles along with the graphitic carbon.

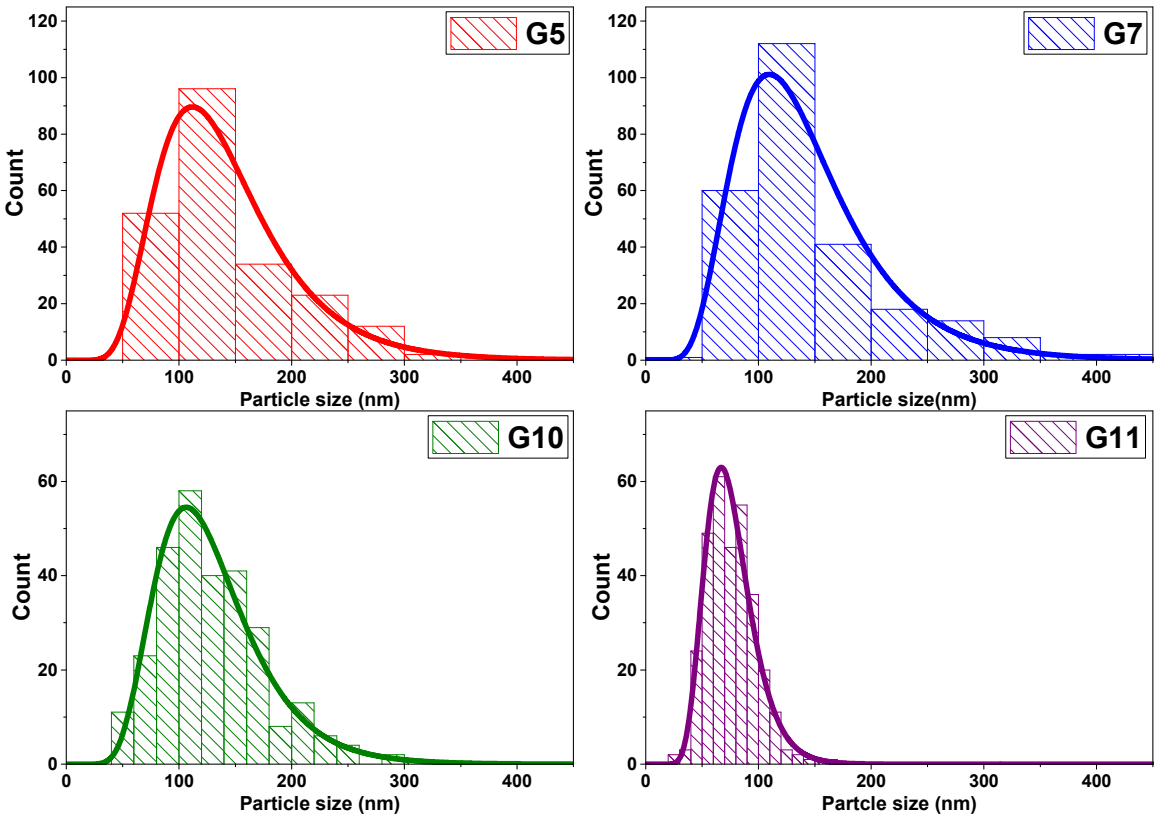

Figure 5.7: Particle size distribution of G5, G7, G10 and G11 sample obtained from TEM micrographs showing a very narrow size distribution in G11 as compared to other samples. In case of samples G5, G7 and G10, the average particle size was calculated to be 112, 108 and 106 nm, respectively.

The presence of different elements (Nb, C and O) throughout the particle has been confirmed with the help of energy dispersive spectroscopy (EDS) pattern and elemental line/area profile as shown in figure 5.8. Figure 5.8a represents the TEM micrograph of the selected area for EDS analysis in which presence of Nb, C and O is shown in figure 5.8c*. Moreover, unmarked peak around 8-9 keV is associated to Cu which may be observed due to the loading of powder sample on Cu grid for TEM analysis. Elemental distribution profile has also been observed to understand the transformation pathway of Nb_2O_5 to NbC as shown in figure 5.8b confirming the presence of NbC NPs along with the homogeneous distribution of oxygen inside the particle and also the presence of rolled graphene sheet marked in figure 5.8b. Further, the presence of oxygen throughout the NPs was also monitored by elemental line profile, estimating the concentration of Nb, C and O along a straight arrow marked in figure 5.8c. Figure 5.8c** represents the concentration profile of the linear region corresponding to magnified area shown below it in which the presence of Nb and C has been confirmed with increased concentration profile on the black region. Moreover, the content of oxygen is very less as compared to carbon inside the NPs (figure 5.8c**) which also has a decreased profile near the periphery of the NPs. The presence of oxygen inside the NbC lattice might be contributing to the lattice distortion (section 5.4) and hence, harvesting NbC_xO_y or NbO_z centers inside the particles [17,18]. These NbC_xO_y or NbO_z centers may contribute to the absorption of light stimulating the generation of e^--h^+ pairs.

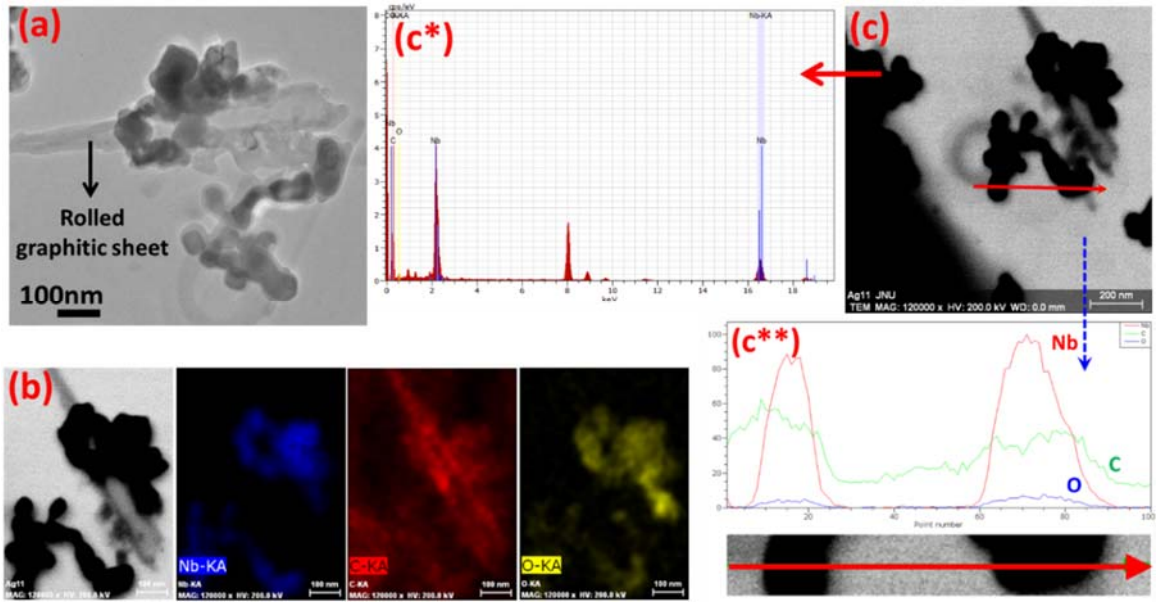

Figure 5.8: (a) TEM micrograph of G11 sample, (b) elemental distribution of Nb, C and O depicting the presence of oxygen within the NbC NPs. (c) elemental line profile suggests the low concentration of O inside the NbC nanoparticle.

5.6. BET analysis:

As an effect of synthesis parameters (temperature, holding time and amount of PH) on specific surface area (SSA) and pore distribution, BET/BJH analysis was carried out for all the single phase NbC samples (based on XRD results) which is shown in figure 5.9 and table 5.2. Figure 5.9a represents the closed adsorption-desorption isotherms for different samples (G5-G11) indicating the type IV hysteresis loop in the range of $0.3<P/P_0<1.0$. Moreover, as a result of reduction-carburization of Nb_2O_5 particles, evolution of CO/CO_2 led to induce mesoporous surface of synthesized nanocomposite samples with a wide pore distribution as shown in figure 5.9b [16]. Among all the synthesized samples, G11 possessed highest SSA i.e. ~49.5 m^2/g with larger pore volume (~0.12 cm^3/g) and wider pores (~4.6 nm) which could stimulate better adhesion of dye molecules on the surface of photocatalyst. As far as synthesis temperature and holding time are concerned, significant variation was not observed in SSA and pore distribution except G11. While, reduced amount of PH (G11) enhanced the surface area along with the pore volume as compared to other samples.

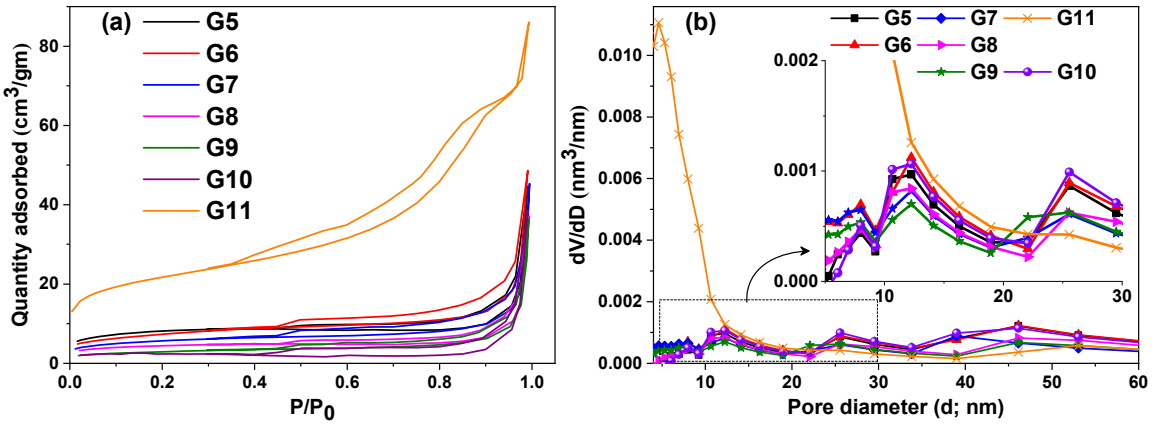

Figure 5.9: (a) Adsorption-desorption curve (BET) and (b) pore size distribution (dV/dD) curve for all the single phase NbC samples (G10-G11).

5.7. X-ray photoelectron spectroscopy (XPS):

Figure 5.10 and 5.11 represent the chemical composition on the surface of photocatalyst for which XPS analysis was carried out for G5, G7, G10 and G11. Figure 5.10 confirmed the presence of Nb, C and O on the surface of the synthesized photocatalysts from survey spectrums. Deconvoluted HR-XPS spectra of all the elements are shown in figure 5.11. Various oxidation states (corresponding to different compounds) of Nb, C and O have been listed in table 5.4 along with their respective volume fractions. All the samples possess mixture of NbC, NbC_xO_y, NbO_2 and Nb_2O_5 on the surface of the NPs while XRD results suggested single phase NbC pattern. The observed XPS peaks of Nb_2O_5/NbO_2 along with NbC_xO_y might be associated to the entrapped oxygen (Nb-O) near the surface of the

NPs during the reduction process. G5, G7 and G10 have almost similar amount NbC and NbC_xO_y on the surface whereas higher content of NbC and NbC_xO_y (22.9 and 23.7%, respectively) was observed in G11.

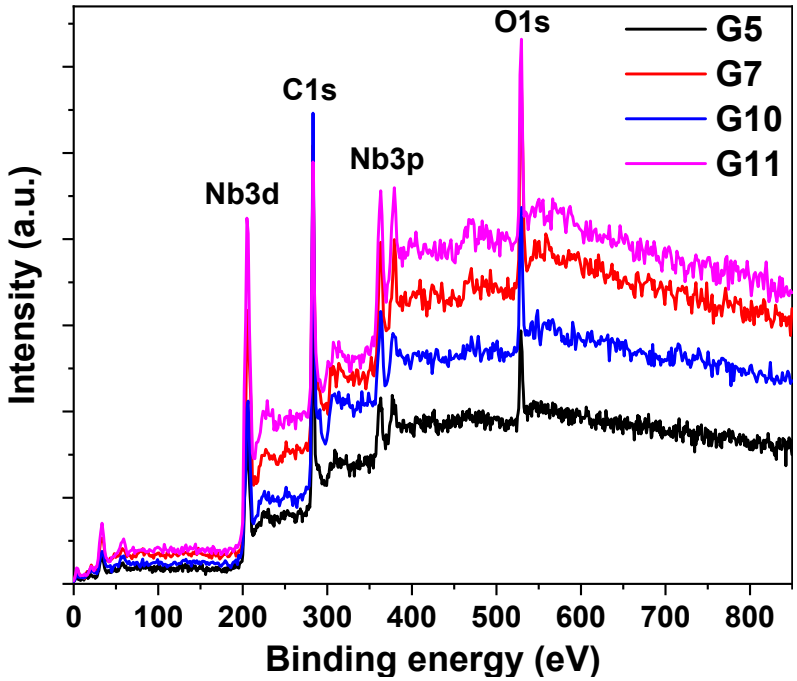

Figure 5.10: Survey spectrum of G5, G7, G10 and G11 confirming the pressence of Nb, C and O on the surface of synthesized photocatalyst.

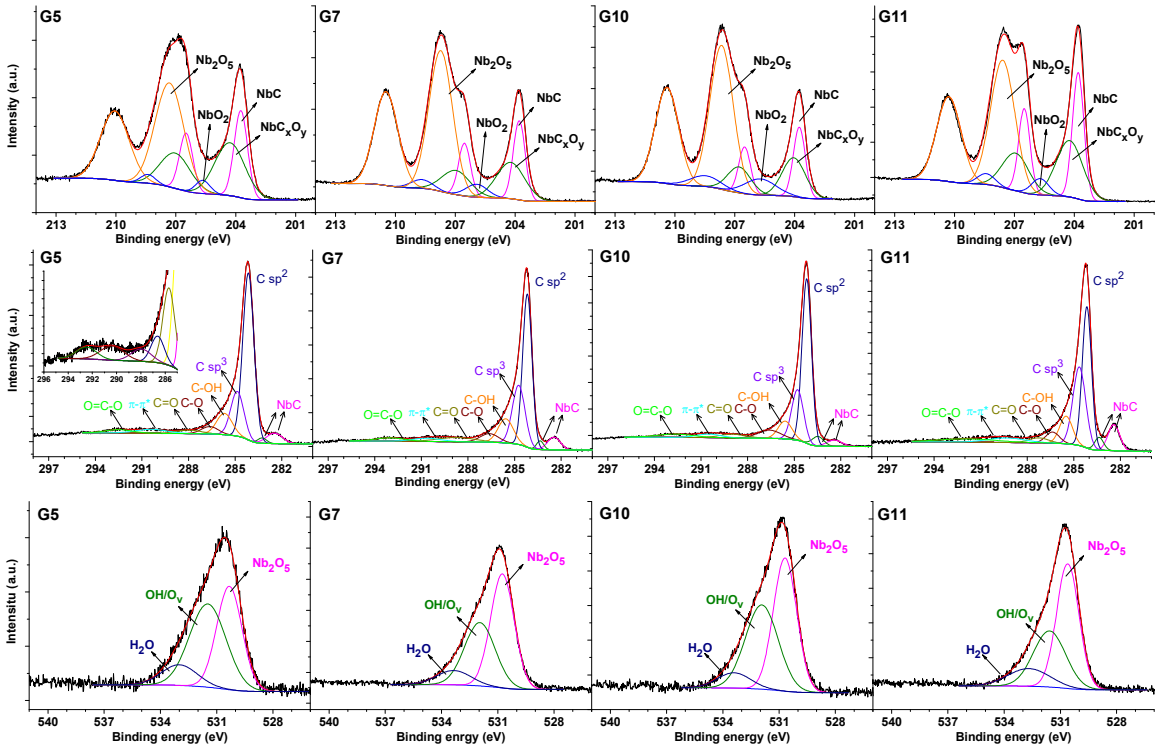

Figure 5.11: HRXPS spectra of G5 to G11 of Nb3d, C1s and O1s (top to down) showing the presence of various functional groups.

Table 5.4: Results obtained from HR-XPS spectra of Nb3d, C1s and O1s of G5, G7, G10 and G11.

Group	G5		G7		G10		G11		
	B.E. (eV)	Volume (%)	B.E. (eV)	Volume (%)	B.E. (eV)	Volume (%)	B.E. (eV)	Volume (%)	
NbC	203.7 206.4	17.8	203.7 206.5	16.9	203.7 206.5	14.8	203.8 206.5	22.9	[19–21]
NbC_xO_y	204.2 207.1	19.8	204.2 206.9	18.3	204.0 206.7	16.1	204.2 206.9	23.7	
NbO_2	205.6 208.3	3.6	205.9 208.6	5.2	205.7 208.4	8.9	205.7 208.4	4.5	
Nb_2O_5	207.3 210.1	58.8	207.7 210.4	59.6	207.6 210.4	60.2	207.5 210.2	48.9	
NbC	282.4	4.9	282.4	5.1	282.4	3.2	282.4	8.3	[21,22]
NbC	283.2	1.4	283.3	1.8	283.4	3.5	283.3	6.1	[23,24]
C sp^2	284.4	54.6	284.4	43.6	284.4	50.4	284.4	35.3	[19,25]
C sp^3	284.8	17.3	284.7	23.2	284.7	19.3	284.6	24.4	[25,26]
C-OH	285.6	9.6	285.5	11.2	285.5	7.9	285.4	9.6	[25,26]
C-O	286.6	3.6	286.6	4.7	286.5	6.2	286.3	4.2	[26,27]
C=O	287.9	2.6	288.7	4.8	288.9	3.1	287.2	2.6	[25–27]
π-π*	290.3	3.5	290.6	2.7	290.5	2.8	289.3	4.4	[28]
O=C-O	292.4	2.5	293.0	2.9	292.6	3.6	291.8	5.1	[27]
Nb_2O_5	530.3	43.8	530.7	47.5	530.6	48.8	530.6	50.2	[29]
OH/O_v	531.4	47.6	531.9	42.9	531.9	43.3	531.5	33.9	[30]
H_2O/C=O	532.9	8.6	533.3	9.6	533.4	7.9	532.6	15.8	[31]

Moreover, due to the decomposition of PH stem, several organic compounds might have formed which may further produce carbon above 400 °C which is responsible for the carburization of Nb resulting NbC [6,32,33]. As a result of carburization reaction, several organic functional groups were found on the surface of the photocatalysts as shown in figure 5.11. Binding energies of 284.1 and 284.8 eV were associated to the sp^2 and sp^3 hybridized carbon present in the samples (respectively) with higher volume fraction of C (sp^2). Moreover, 282.4 [21,22] and 283.2 eV [23,24] can be related to NbC. Further, the presence of C-OH, C-O, C=O, π-π* and O=C-O may be affirmed with peaks at 285.6, 286.6, 287.9, 290.3 and 292.4 eV, respectively [25–27]. The presence of such organic functional groups might alter the photocatalytic activity of synthesized sample which is discussed in subsequent sections.

The HRXPS spectra of oxygen revealed that the binding energies near 530.3, 531.4 and 532.9 eV may be associated to Nb oxide, oxygen vacancies (O_v) and adsorbed H_2O/carbonyl (C=O) group, respectively [29,31,34]. The presence of O_v and Nb oxide near the surface of as-synthesized photocatalysts can be attributed to the reduction-carburization reactions responsible for the formation of NbC. The highlight of the O1s spectra of studied samples is the decreased O_v content in G11 as compared to other samples which would surely harvest the photocatalytic characteristic of the synthesized samples.

5.8. Absorbance and photoluminescence (PL) spectroscopy:

In order to use the synthesized nanocomposite samples as photocatalyst, the optical properties have been studied to observe absorbance and emission spectra. Figure 5.12a shows the absorbance spectra of G5, G7, G10 and G11 depicting the high absorbance of visible radiations (400-800 nm). The decrement in absorbance between 240 and 320 nm may be associated to graphitic carbon as graphene which has also been supported by various research groups [35–37]. Moreover, all four samples show slight increment in absorbance in visible region (430-750 nm) which might be associated to the presence of NbC_xO_y centers in NPs as observed from line profile of STEM microstructures [38,39].

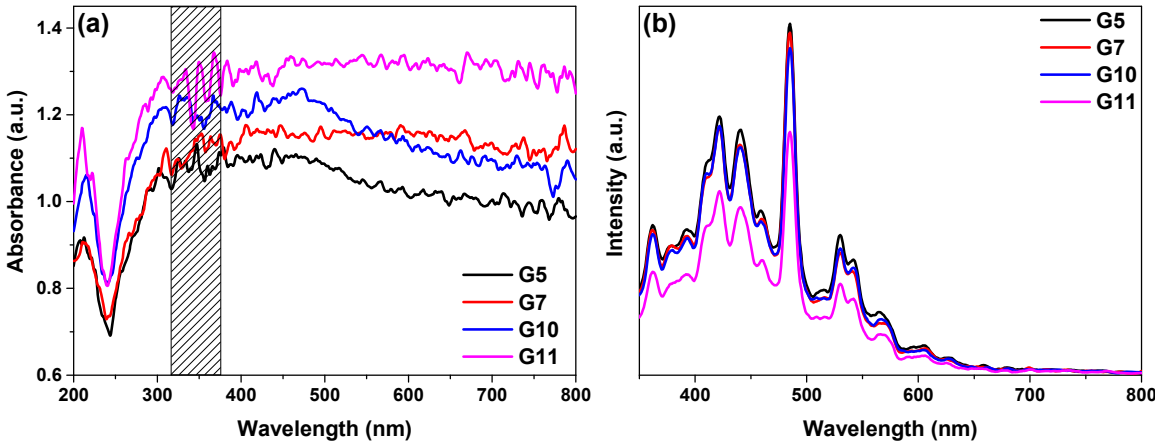

Figure 5.12: (a) UV-visible absorption spectra in which shaded region depicts the fluctuated absorbance due to switching of WI lamp (visible) to D2 lamp (UV) and (b) PL emission spectra of single phase NbC samples (G10-G11).

The photoluminescence (PL) emission spectra (λ_{exc}=340 nm) of same samples from 350 to 800 nm was also taken to observe the rate of recombination in the sample as shown in figure 5.12b. A broad emission spectra (upto 650 nm) of the synthesized samples can be attributed to the disordered graphitic carbon consisting of various organic functional groups along with π-π* transitions (observed from XPS results) and attachment of oxygen atoms to graphitic sheet providing some optical signature of graphene oxide (GO) [40–42]. Emission peaks around 500 nm (~435-450, ~490 and ~540 nm) can be attributed to the transfer of electron from carbon to oxygen in GO, due to the shifting of highest occupies molecular orbital (HOMO) downward as opening of band gaps [41,43].

5.9. Raman spectroscopy:

Figure 5.13a shows the Raman spectra of synthesized nanocomposite samples consisting 3 major bands around 1350, 1580 and 2700 cm^{-1} representing the presence of disordered (D- band), graphitic (G- band) and 2D graphitic carbon, respectively [44,45].

Raman spectra of all the considered samples do not exhibit any signature of Nb-O vibration (around 550-750 cm^{-1}) suggesting the absence of Nb oxide(s) (which has been observed from XPS spectroscopy). Moreover, figure 5.13b suggested the slight shifting of D- and 2D- band towards lower frequency which might be associated to the inhomogeneous self-doping of electrons and holes in graphitic network [44]. Figure 5.13c represents the convoluted spectrum of G7 in which Lorentzian peak function was used to de-convolute to locate the position, FWHM and intensity of various bands has been shown in table 5.5. The presence of second order D- band (2D) suggested the loss of 3D ordering and the presence of turbostratic graphite with c-axis ordering. $FWHM_{2D}$ is higher than 50 cm^{-1} which might be associated to the presence of defects in graphitic carbon [44,46].

Table 5.5: List of different bands obtained from deconvolution (Lorentzian peak function) of Raman spectra of G5, G7, G10 and G11.

Sample ↓	**Raman band →**	**D-**	**G-**	**D'-**	**2D-**
G5	**Position (cm^{-1})**	1345.94	1578.92	1612.80	2698.70
	FWHM (cm^{-1})	48.88	22.77	20.88	69.03
G7	**Position (cm^{-1})**	1344.55	1573.01	1608.89	2692.36
	FWHM (cm^{-1})	47.96	22.41	14.02	94.61
G10	**Position (cm^{-1})**	1339.52	1575.93	1607.66	2694.27
	FWHM (cm^{-1})	45.89	23.67	23.06	86.10
G11	**Position (cm^{-1})**	1343.06	1578.86	1605.74	2698.12
	FWHM (cm^{-1})	49.20	23.25	32.46	76.74

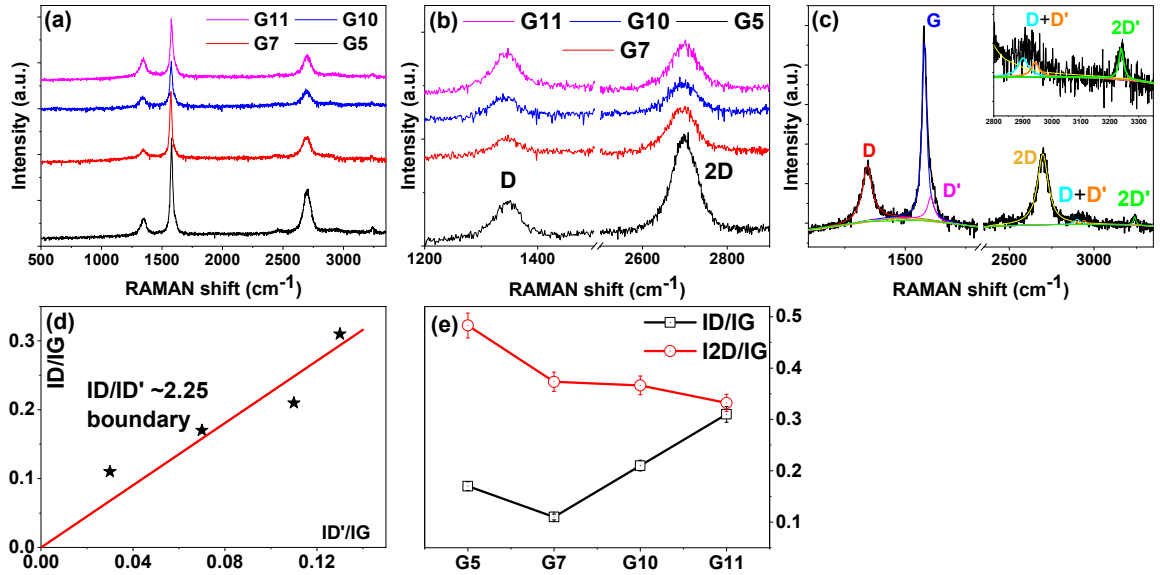

Figure 5.13: (a) Raman spectroscopy of G5-G11 confirming the presence of graphene as D, G and 2D bands, (b) Variation in the D and 2D bands of different samples consisting broadened 2D band due to the presence of multilayered graphene [47], (c) de-convoluted Raman spectrum of G7 showing the contribution of disordered graphitic carbon (D- band), graphitic carbon (G- band) and 2 dimensional graphitic carbon (graphene; 2D- band), (d) I_D/I_G vs. $I_{D'}/I_G$ representing the nature of defect as boundaries [48], and (e) Variation of I_D/I_G and I_D/I_{2D} with respect to different samples.

Eckmann *et al.* [48] suggested that D- and D'- band can provide the nature of defects which are present in the sample as shown in figure 5.13d. It clearly represented the trend of $I_D/I_{D'}$ ratio for all the samples, came out to be ~2.25 (<3.5), can be correlated to the nature of defects i.e. grain boundaries. Figure 5.13e represents the I_D/I_G and I_D/I_{2D} for all four samples in which increasing I_D/I_G from G7 to G11 can be interpreted as smaller graphitic grain with higher disordered surface and high sp^3-like defects [44,47]. Decrement of I_{2D}/I_G from G5 to G11 indicated the increment in graphitic character than graphene [49]. Considering all the observed structural features of carbon which are present in the samples, photocatalytic study has been carried out which is discussed in the following section.

Based on XRD, TEM, XPS and Raman spectroscopy, it can be formulated that as synthesized nanopowder samples exhibited a mixture of NbC and graphitic carbon (disordered and multilayered). While, elemental profile (TEM; figure 5.8) and XPS (figure 5.11) suggested the presence of oxygen inside the NbC lattice in the form of Nb oxide(s) or Nb oxy-carbide which has not been observed in XRD and Raman analysis (figure 5.2 and 5.13). Figure 5.14 symbolizes the schematic representation of NbC nanoparticle in which carbon forms a layer on the Nb_2O_5 particle and formation of NbC occurs as a result of simultaneous reduction-carburization i.e. temperature and time dependent process [16,50]. Due to the diffusion of carbon from periphery to the core of particle, there might be a possibility of entrapment of oxygen inside the particle resulting NbC_xO_y (near periphery) or Nb oxides (at the core) as observed from XPS analysis. These oxygen centers induced the optical active sites in NbC nanoparticles which would be helpful to tailor the photocatalytic reactions.

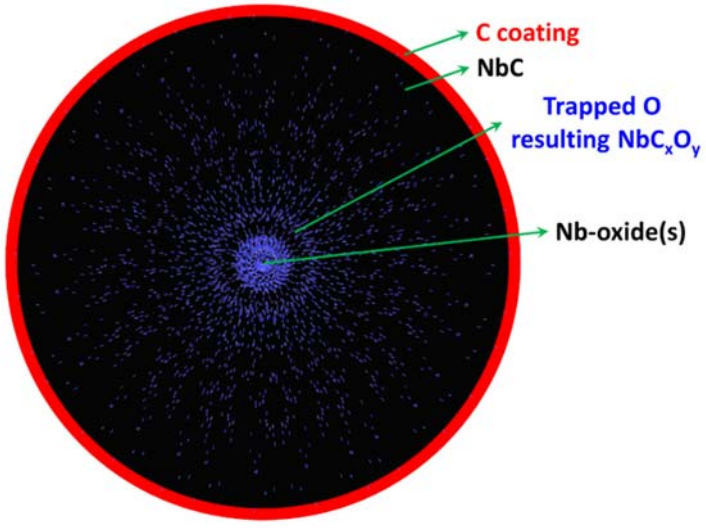

Figure 5.14: Schematic representation of the presence of oxygen centers leading to NbC_xO_y or NbO_z inside the synthesized NbC nanoparticles embedded in graphitic carbon network.

5.10. Photocatalysis study:

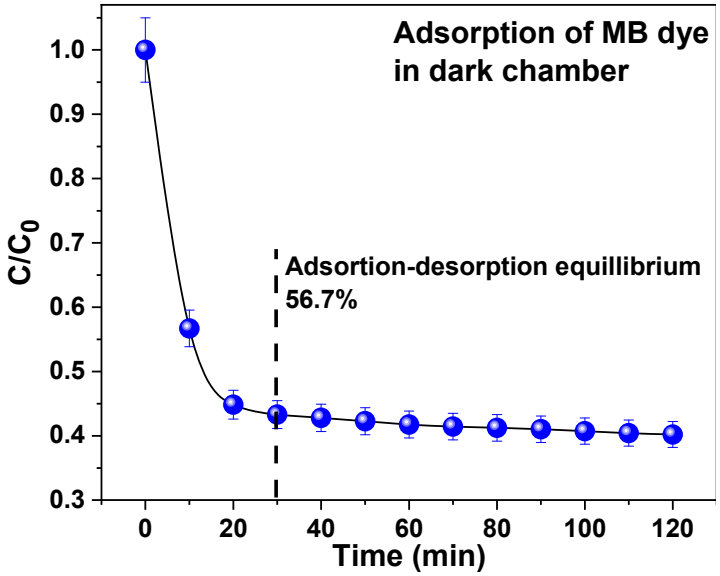

Figure 5.15: Relative change in the concentration of MB dye without irradiation in the presence of G11. Adsorption curve represents the adsorption saturation of MB dye beyond 30 min which has been adopted to establish adsorption-desorption equilibrium for photocatalytic experiments.

For the photocatalytic study, single phase NbC samples were chosen to understand the effect of composition and carbon present in the sample. MB dye (a cationic dye, also known as an electron receptor) was used as a model organic compound. Prior to photodegradation of MB dye under visible irradiation, adsorption behavior of the dye molecule on the surface of G11 revealed the establishment of adsorption-desorption equilibrium within 30 min as shown in figure 5.15.

Figure 5.16a represents the adsorption of dye molecule on the surface of the different photocatalysts in 30 min under dark chamber. Among all the considered samples, G11 showed the highest adsorption of MB dye which may be associated to its smaller particle size, more SSA and pore volume than other samples (G10-G11). Figure 5.16b shows the discoloration/degradation efficiency of the all the photocatalysts under visible irradiation in which G11 has shown almost 100% efficiency. The photochemical reaction kinetics was estimated with the help of pseudo first order law which can be described as $-\ln(C/C_0)$=Kt; where C_0, C, t and K are the initial dye concentration (at t=0), concentration of dye at time 't' and rate constant, respectively. Rate constant and quality of fitting has been shown in figure 5.16c and table 5.6 where G11 showed the highest rate of photochemical reaction (0.553 h^{-1}) with $R^2 = 0.98$ among all the studied samples. Moreover, all the considered samples followed pseudo first order law as $R^2 > 0.96$.

Table 5.6: Details of photochemical reaction kinetics of MB dye with the help of G5-G11.

Concentration (mg/L)		Catalyst	Efficiency (%)	Rate constant K (h^{-1})	R^2
Dye	Catalyst				
1.0	60.0	G5	72.04	0.1603	0.99
1.0	60.0	G7	72.91	0.1716	0.99
1.0	60.0	G10	42.03	0.0791	0.96
1.0	60.0	G11	100.0	0.5537	0.98

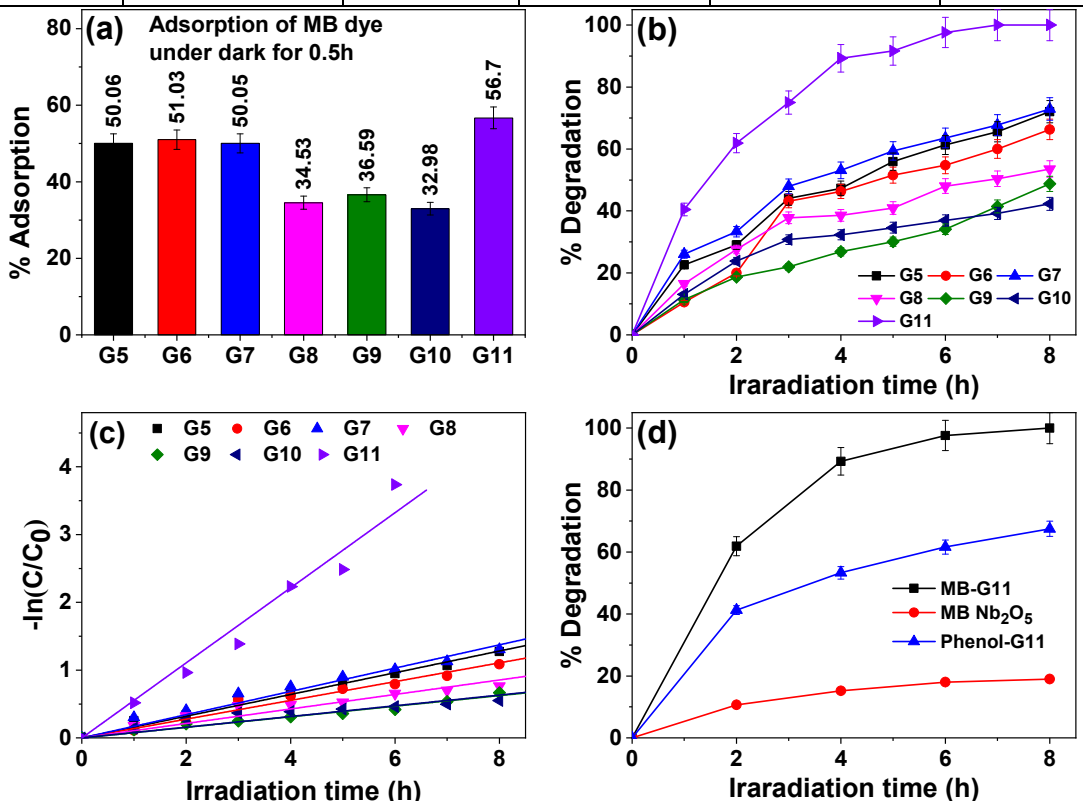

Figure 5.16: (a) Adsorption of MB dye on the surface of photocatalyst during adsorption-desorption equilibrium under dark, (b) percent degradation of MB dye under visible irradiation, (c) -ln(C/C_0) vs. time to determine the rate constant of degradation using pseudo first order reaction method, and (d) comparative degradation profile of MB dye and N-phenol in the presence of G11 and precursor (Nb_2O_5).

Since, MB dye is a visible active compound and the presence of unreacted Nb_2O_5 in the powder sample, another set of experiments were planned to confirm the photodegradation of MB dye where photodegradation of N-phenol and MB dye (G11 and Nb_2O_5, respectively) were observed with respect to MB dye in the presence of G11. Figure 5.16d represents the comparative removal profile of N-phenol and MB dye in the presence of G11 and Nb_2O_5. It has been found that the synthesized G11 participates in photodegradation reactions as catalyst and the removal of MB dye includes simultaneous photodegradation and photosensitization process resulting better efficiency than that of N-phenol and Nb_2O_5. In order to confirm the decreased absorption is attributed to the photodegradation of MB dye, the scavenger test and total organic carbon analysis (TOC)

as shown in figure 5.17 was done. The most efficient photocatalyst i.e. G5 was used for scavenging tests in which the contribution of reactive oxidative species (ROS) were detected by trapping various ROS such as electron (e^-), hole (h^+), hydroxyl radical ($\cdot$ OH) and superoxide anion radical ($\dot{O_2^-}$) with the help of different reagent. Figure 5.17a shows a comparative degradation efficiency in the absence and presence of different scavengers in which a significant decrement of efficiency was observed with the addition of scavengers. Among all the ROS, $\dot{O_2^-}$ (G11+AA) showed the most dominant contribution (~80% reduction) to the photodegradation of MB dye as least efficiency was observed after 8h of visible irradiation. Moreover, rest of the scavengers also reduced the photocatalytic efficiency of G11 by almost 35%. Further, TOC results also supported the photodegradation of MB dye, instead of photo-adsorption, by showing 83.1% reduction of organic carbon (after the illumination) for G11 sample while, absorbance spectroscopy suggested complete removal of MB dye. Such photochemical phenomenon might be associated to the delayed dissociation of organic carbon present in the solution than the discoloration process which is observed in TOC results as shown in figure 5.17b.

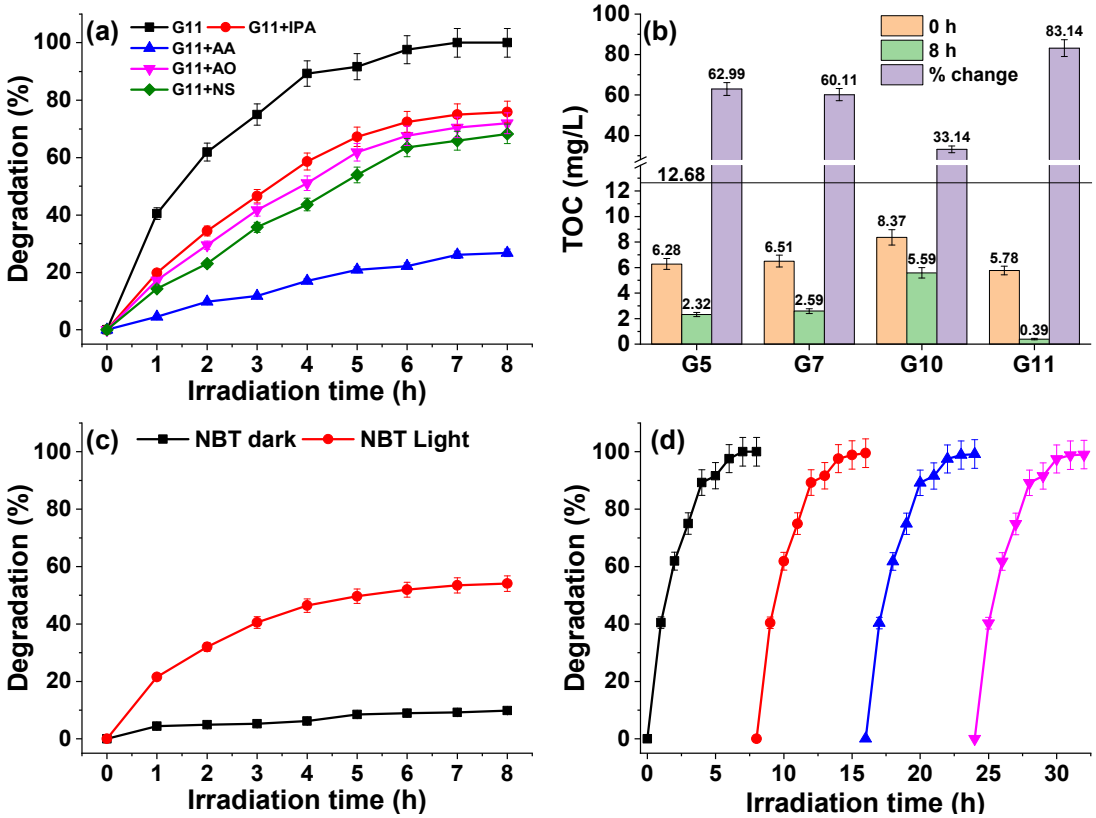

Figure 5.17: (a) Detection of ROS species during the photodegradation of MB dye using G11, (b) total organic carbon (TOC) in different studied photocatalysts, (c) generation of superoxide anion radical using NBT in the presence of G11 in 8.0 h visible irradiations and (d) reusability of same photocatalyst (G11) for 4 cycles under same conditions of photodegradation test.

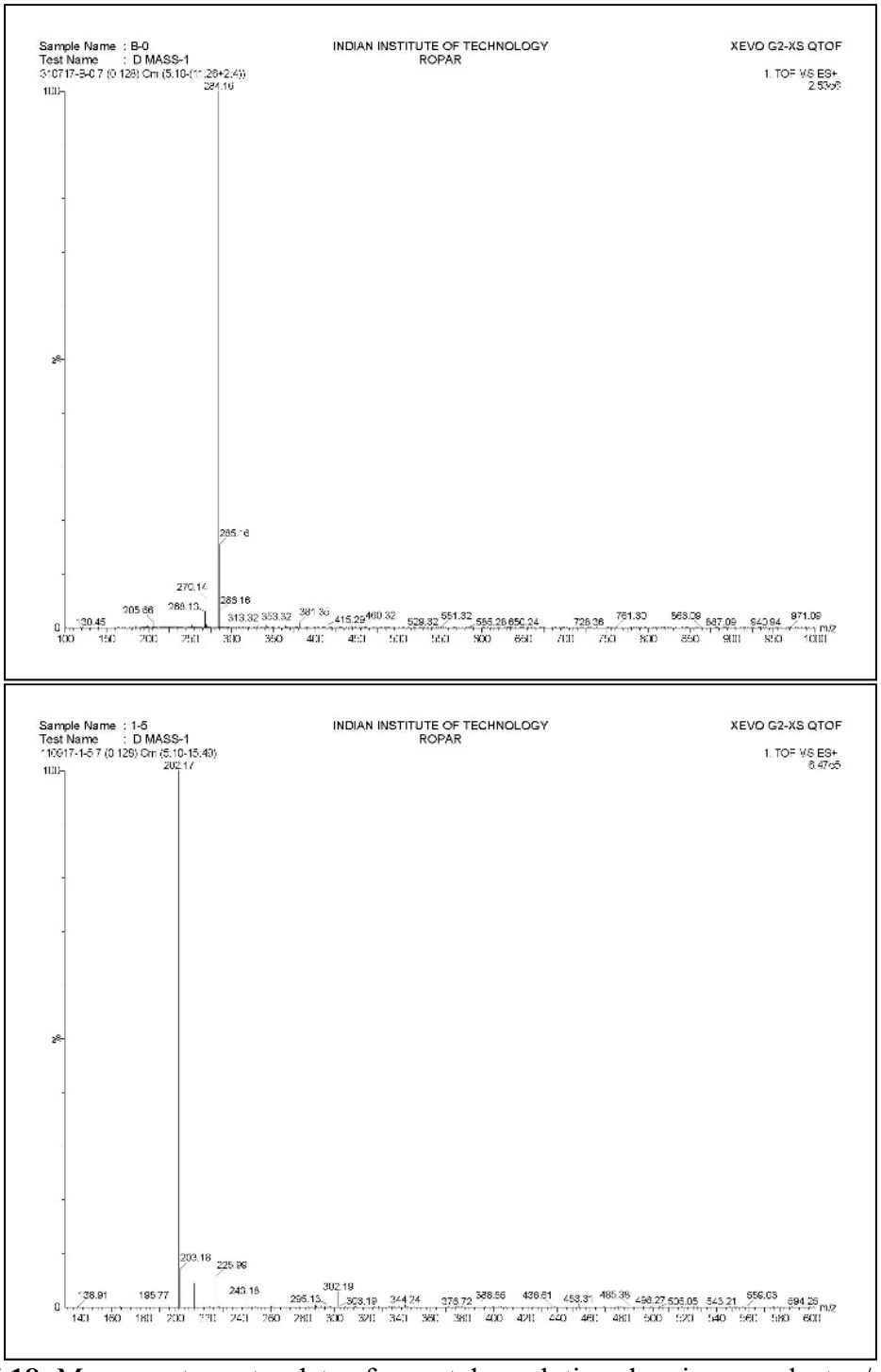

Figure 5.18: Mass spectrometry data of parent dye solution showing a peak at m/z=284.16 which got converted to m/z=202.17 after photodegradation under visible radiations for 8h with the help of G11 confirming the decreasing absorbance (obtained from UV-visible spectroscopy) is associated to the decomposition of MB molecule.

Further, mass spectrometric results also supported the photodegradation of MB dye as m/z=284.16 got converted to m/z=202.17 as shown in figure 5.18. In order to confirm further, the generation of superoxide anion radical, UV-visible spectroscopy using nitro blue tetrazolium (NBT, 50 ml solution of NBT; 0.04 g/L with 0.01 g of G-11; maximum

absorbance ~259 nm) was adopted as shown in figure 5.17c. It is already reported that as a result of reaction of NBT with $O_2^{\bullet-}$ radical, NBT gets transformed to formazan (mono and di) and hence, the absorbance got reduced [51].

Recyclability/reusability of the synthesized sample expresses its applicability as photocatalyst for industrial purposes. For such test, used photo-catalyst (G11) was again charged for photodegradation reaction under same conditions after extracting it (centrifugation @4500 rpm, followed by washing with distilled water and drying at 45 °C). Figure 5.17d represents the excellent recyclability of G11 for 4 continuous cycles under visible irradiations.

5.11. Proposed degradation mechanism:

Based on the above discussed results, detailed mechanism responsible for such remarkable photocatalytic efficiency of synthesized powder was formulated. Due to the presence of NbC_xO_y or NbO_z inside the NbC NPs and trapped oxygen in graphitic sheets, significant absorption of visible radiations was observed [52,53]. Valence band potential (VBE) and conduction band potential (CBE) were calculated with the help of valence band spectra and optical band gap, respectively as shown in figure 5.19 and table 5.7.

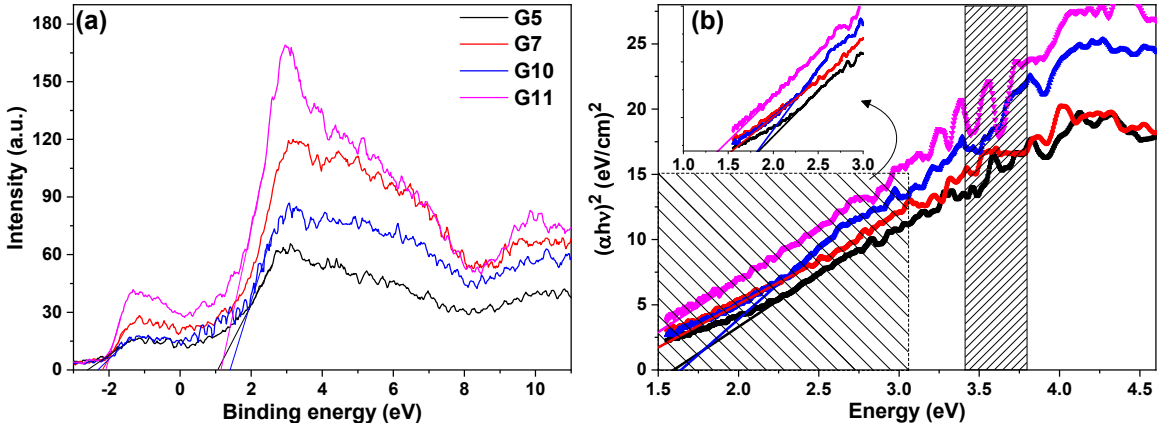

Figure 5.19: (a) Valence band spectra used for photocatalytic study and (b) Tauc plot to estimate the optical band gaps of G5-G11 samples.

Table 5.7: List of valence band position and optical band gaps.

Sample	VB_1 (eV)	VB_2 (eV)	E_g (eV)	Sample	VB_1 (eV)	VB_2 (eV)	E_g (eV)
G5	-2.66	1.03	1.59	**G10**	-2.33	1.24	1.19
G7	-2.24	1.44	1.64	**G11**	-2.10	1.15	1.28

With the help of Raman spectroscopy, it can also be observed that increased defects with smaller graphitic grains enhanced the photon absorption ability of synthesized photocatalyst. Here, the photo-generated electron-hole pair will be transferred towards the surface through NbC/g-C heterojunction (observed emission corresponding to charge

transfer between C and O, figure 5.12b). Further, the photo-generated charge carriers will participate in various photochemical reactions on the surface which are as follows:

$$NbC + C \xrightarrow{photon} NbC + C + h^+ + e^- \quad (5.1)$$

$$OH^- + h^+ \rightarrow OH^{\cdot} \quad (5.2)$$

$$O_2 + e^-(\text{graphene}) \rightarrow \dot{O_2^-} \quad (5.3)$$

-0.041 eV vs. NHE is considered as the reduction potential edge of $O_2/\dot{O_2^-}$ which is slightly lower than the position of CBE of G11 i.e. -0.19 eV vs NHE resulting to an easy generation of superoxide anion radical responsible for the degradation of MB molecule under visible irradiations [54]. Our previous study has elucidated that heterostructure of NbC_x and carbon led to efficient photo-absorption ability [50]. Figure 5.20 represents the photodegradation mechanism of MB dye with the help of G11 under visible irradiations. Although, all the considered samples showed single phase NbC XRD pattern, Nb did not possess its single oxidation state corresponding to NbC but, it is existing with variable oxidation states (3+, 4+ and 5+ associated with NbC, NbC_xO_y, NbO_2 and Nb_2O_5) on the surface of NPs. These variable valence states would participate in photochemical reactions by providing electrons for the generation of superoxide anion radicals which can be described as follows:

$$Nb^{3+} \leftrightarrow Nb^{4+} + e^-; \qquad Nb^{4+} \leftrightarrow Nb^{5+} + e^- \quad (5.4)$$

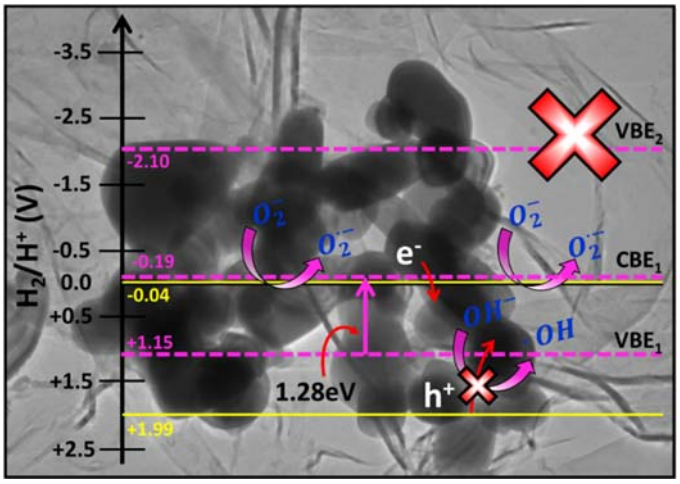

Figure 5.20: Proposed photodegradation mechanism under visible irradiations.

In lieu of various structural features (particle size, SSA and pore volume), the presence of NbC_xO_y/NbO_z centers induced the photo-active sites while, NbC_x/g-C enhanced the charge transfer phenomenon on the surface. Therefore, G11 possessed superior photocatalytic performance than other samples (G5, G7 and G10) despite of exhibiting single phase NbC XRD patterns.

References:

1 S. Mondal, K. Aikat and G. Halder, *Ecol. Eng.*, 2016, **92**, 158–172.
2 S. Patel, *3 Biotech*, 2011, **1**, 1–9.
3 S. A. Bapat and D. K. Jaspal, *Glob. J. Environ. Sci. Manag.*, 2016, **2**, 135–144.
4 S. Chatterjee, A. Kumar, S. Basu and S. Dutta, *Chem. Eng. J.*, 2012, **181**–**182**, 289–299.
5 M. Mulugeta and B. Lelisa, *Mod. Chem. Appl.*, , DOI:10.4172/2329-6798.1000146.
6 A. Purai and V. K. Rattan, *Carbon Lett.*, 2010, **11**, 1–8.
7 V. S. Shrivastava, *Desalin. Water Treat.*, 2010, **22**, 146–155.
8 G. Singla, K. Singh and O. P. Pandey, *J. Alloys Compd.*, 2016, **665**, 186–196.
9 G. Singla, K. Singh and O. P. Pandey, *Int. J. Hydrogen Energy*, 2015, **40**, 5628–5637.
10 L. K. Brar, A. Gupta and O. P. Pandey, *Catal. Today*, 2018, **325**, 98–108.
11 R. A. Mir and O. P. Pandey, *Chem. Eng. J.*, 2018, **348**, 1037–1048.
12 N. S. Alhajri, D. H. Anjum and K. Takanabe, *J. Mater. Chem. A*, 2014, **2**, 10548–10556.
13 K. Zhang, C. Li, Y. Zhao, X. Yu and Y. Chen, *Phys. Chem. Chem. Phys.*, 2015, **17**, 16609–16614.
14 A. Gupta and O. P. Pandey, *Sol. Energy*, 2018, **163**, 167–176.
15 A. Gupta, V. Singhal and O. P. Pandey, *J. Alloys Compd.*, 2018, **736**, 306–313.
16 A. Gupta, G. Singla and O. P. Pandey, *Ceram. Int.*, 2016, **42**, 13024–13034.
17 D. N. Miller, A. K. Azad, H. Delpouve, L. Quazuguel, J. Zhou, A. Sinha, P. Wormald and J. T. S. Irvine, *J. Mater. Chem. A*, 2016, **4**, 5730–5736.
18 J. David, G. Trolliard, C. Volkringer, T. Loiseau and A. Maître, *RSC Adv.*, 2015, **5**, 51650–51661.
19 J. Halim, K. M. Cook, M. Naquib, P. Eklund, Y. Gogotsi, J. Rosen and M. W. Barsoum, *Appl. Surf. Sci.*, 2016, **362**, 406–417.
20 M. T. Marques, A. M. Ferraria, J. B. Correia, A. M. B. do Rego and R. Vilar, *Mater. Chem. Phys.*, 2008, **109**, 174–180.
21 C. Zhang, M. Beidaghi, M. Naguib, M. R. Lukatskaya, M. Zhao, B. Dyatkin, K. M. Cook, S. J. Kim, B. Eng, X. Xiao, D. Long, W. Qiao, B. Dunn and Y. Gogotsi, *Chem. Mater.*, 2016, **28**, 3937–3943.
22 N. Nedfors, O. Tengstrand, E. Lewin, A. Furlan, P. Eklund, L. Hultman and U. Jansson, *Surf. Coat. Technol.*, 2011, **206**, 354–359.
23 L. Ramqvist, K. Hamrin, G. Johansson, A. Fahlman and C. Nordling, *J. Phys. Chem. Solids*, 1969, **30**, 1835–1847.
24 J. A. Klug, T. Proslier, J. W. Elam, R. E. Cook, J. M. Hiller, H. Claus, N. G. Becker and M. J. Pellin, *J. Phys. Chem. C*, 2011, **115**, 25063–25071.
25 S. Muralikrishna, K. Sureshkumar, T. S. Varley, D. H. Nagaraju and T. Ramakrishnappa, *Anal. Methods*, 2014, **6**, 8698–8705.
26 F. Zhao, A. Vrajitoarea, Q. Jiang, X. Han, A. Chaudhary, J. O. Welch and R. B. Jackman, *Sci. Rep.*, 2015, **5**, 17–19.
27 H. Yan, C. Tian, L. Sun, B. Wang, L. Wang, J. Yin, A. Wu and H. Fu, *Energy Environmetal Sci.*, 2014, **7**, 1939–1949.
28 D. Chen, H. Feng and J. Li, *Chem. Rev.*, 2012, **112**, 6027–6053.
29 X. Ma, Y. Chen, H. Li, X. Cui and Y. Lin, *Mater. Res. Bull.*, 2015, **66**, 51–58.
30 M. Zhang, J. Xu, R. Zong and Y. Zhu, *Appl. Catal. B Environ.*, 2014, **147**, 229–235.
31 F. E. Castillejo, D. M. Marulanda, J. J. Olaya and J. E. Alfonso, *Surf. Coatings Technol.*, 2014, **254**, 104–111.
32 H. Lata, V. K. Garg and R. K. Gupta, *J. Hazard. Mater.*, 2008, **157**, 503–509.
33 R. K. Singh, S. Kumar, S. Kumar and A. Kumar, *J. Hazard. Mater.*, 2008, **155**, 523–535.
34 X. Zhang, J. Qin, Y. Xue, P. Yu, B. Zhang, L. Wang and R. Liu, *Sci. Rep.*, 2014, **4**, 4–11.
35 M. E. Khan, M. M. Khan and M. H. Cho, *Sci. Rep.*, 2017, **7**, 5928.
36 X. Wei and M. Chen, *J. Chil. Chem. Soc.*, 2015, **60**, 2988–2997.
37 M. E. Khan, M. M. Khan and M. H. Cho, *New J. Chem.*, 2015, **39**, 8121–8129.
38 E. Pehlivan, F. Z. Tepehan and G. G. Tepehan, *Sol. Energy Mater. Sol. Cells*, 2005, **87**, 317–

322.
39 Z. Weibin, W. Weidong, W. Xueming, C. Xinlu, Y. Dawei, S. Changle, P. Liping, W. Yuying and B. Li, *Surf. Interface Anal.*, 2013, **45**, 1206–1210.
40 Y. Chen, B. Wang, S. Lin, Y. Zhang and X. Wang, *J. Phys. Chem. C*, 2014, **118**, 29981–29989.
41 J. R. Rani, J. Lim, J. Oh, D. Kim, D. Lee, J.-W. Kim, H. S. Shin, J. H. Kim and S. C. Jun, *RSC Adv.*, 2013, **3**, 5926.
42 X. Ding, *J. Mater. Chem. C*, 2014, **2**, 3717–3722.
43 H. K. Jeong, C. Yang, B. S. Kim and K.-J. Kim, *Europhys. Lett.*, 2010, **92**, 37005.
44 A. C. Ferrari, *Solid State Commun.*, 2007, **143**, 47–57.
45 A. C. Ferrari and J. Robertson, *Phys. Rev. B*, 2000, **61**, 14095–14107.
46 P. Lespade, A. Marchand, M. Couzi and F. Cruege, *Carbon N. Y.*, 1984, **22**, 375–385.
47 J.-B. Wu, M.-L. Lin, X. Cong, H.-N. Liu and P.-H. Tan, *Chem. Soc. Rev.*, 2018, **47**, 1822–1873.
48 A. Eckmann, A. Felten, A. Mishchenko, L. Britnell, R. Krupke, K. S. Novoselov and C. Casiraghi, *Nano Lett.*, 2012, **12**, 3925–3930.
49 D. Yang, A. Velamakanni, G. Bozoklu, S. Park, M. Stoller, R. D. Piner, S. Stankovich, I. Jung, D. A. Field, C. A. Ventrice and R. S. Ruoff, *Carbon N. Y.*, 2009, **47**, 145–152.
50 A. Gupta, M. Mittal, M. K. Singh, S. L. Suib and O. P. Pandey, *Sci. Rep.*, 2018, **8**, 13597.
51 V. Lakshmi Prasanna and R. Vijayaraghavan, *Langmuir*, 2015, **31**, 9155–9162.
52 Y. Ohgi, A. Ishihara, K. Matsuzawa, S. Mitsushima, K. I. Ota, M. Matsumoto and H. Imai, *Electrochim. Acta*, 2012, **68**, 192–197.
53 A. Ishihara, M. Tamura, Y. Ohgi, M. Matsumoto, K. Matsuzawa, S. Mitsushima, H. Imai and K. I. Ota, *J. Phys. Chem. C*, 2013, **117**, 18837–18844.
54 Y. Yang, Y. Guo, F. Liu, X. Yuan, Y. Guo, S. Zhang, W. Guo and M. Huo, *Appl. Catal. B Environ.*, 2013, **142**–**143**, 828–837.

CHAPTER 6 RESULTS & DISCUSSION-III

Utilization of cellulose acetate (CA; major component of CFs)

Overview

In this chapter, the formation of NbC-C nanopowder by using chemical grade cellulose acetate (CA) has been discussed. Being a major component of cigarette filters (CFs), CA has been selected as carbon source to understand and compare the effect of both reagents (CA and CF) for obtaining nano NbC. Optimization of parameters (temperature and time) has been carried out with the help of XRD results. Using CA, single phase NbC samples were synthesized at different temperatures (700 and 800 °C). The structural and optical properties of these synthesized samples are compared as the synthesis conditions used here are different. Based on XRD, TEM and Raman results, temperature dependent growth of nanoparticles and the nature of carbon coating on the surface of nanoparticles have been discussed in this chapter.

Further, optical and photocatalytic response of single phase NbC-C samples (based on XRD results) are also compared and associated photocatalytic mechanism has also been discussed in this chapter.

6.1. Introduction:

Smoked cigarette filters mainly consist of cellulose acetate (CA). Considering its very good carburization property as described in chapter 4, the present work is undertaken to synthesize NbC from CA. CA is an industrial raw material for many applications like frame materials eyeglasses, playing cards, photographic films, apparels and diapers etc. The use of CA as carbon source can provide sufficient comparative data to understand the effect of laboratory grade chemical and waste material i.e. smoked cigarette filters. Here, the optimization of synthesis parameters has been discussed by using laboratory grade CA to obtain single phase NbC nanopowder. Table 6.1 represents the details of experimental conditions at which chemical reactions were carried out.

Table 6.1: Details of experimental conditions to obtain NbC nanopowder.

Precursor (g)			Sample	Temperature (°C)	Holding time (h)
Nb_2O_5	Mg	CA			
1.329	2.0	1.0	CA1	800	0
1.329	2.0	1.0	CA2	800	2
1.329	2.0	1.0	CA3	800	5
1.329	2.0	1.0	CA4	800	10
1.329	2.0	1.0	CA5	800	15
1.329	2.0	1.0	CA6	700	0
1.329	2.0	1.0	CA7	700	2
1.329	2.0	1.0	CA8	700	5
1.329	2.0	1.0	CA9	700	10
1.329	2.0	1.0	CA10	700	15
1.329	2.0	1.0	CA11	600	0
1.329	2.0	1.0	CA12	600	2
1.329	2.0	1.0	CA13	600	5
1.329	2.0	1.0	CA14	600	10
1.329	2.0	1.0	CA15	600	15

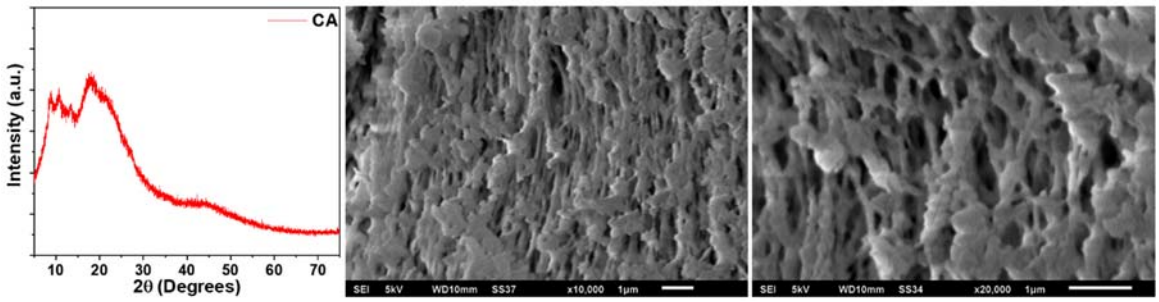

Figure 6.1: XRD and SEM of cellulose acetate (CA) used for the synthesis of NbC nanopowder.

Figure 6.1 represents the XRD pattern of cellulose acetate which is in support with cigarette filters (as shown in figure 4.1) and SEM micrographs depicted the porous and fibrous morphology of the cellulose acetate. The average thickness of CA fibers is around

~0.2 µm which is very thin as compared to CF fibers (figure 4.1; ~20 µm). The reduced thickness along with network like morphology will provide high surface area for the reduction and carburization. It will further help to reduce the synthesis temperature and holding time.

6.2. X-ray diffraction (XRD):

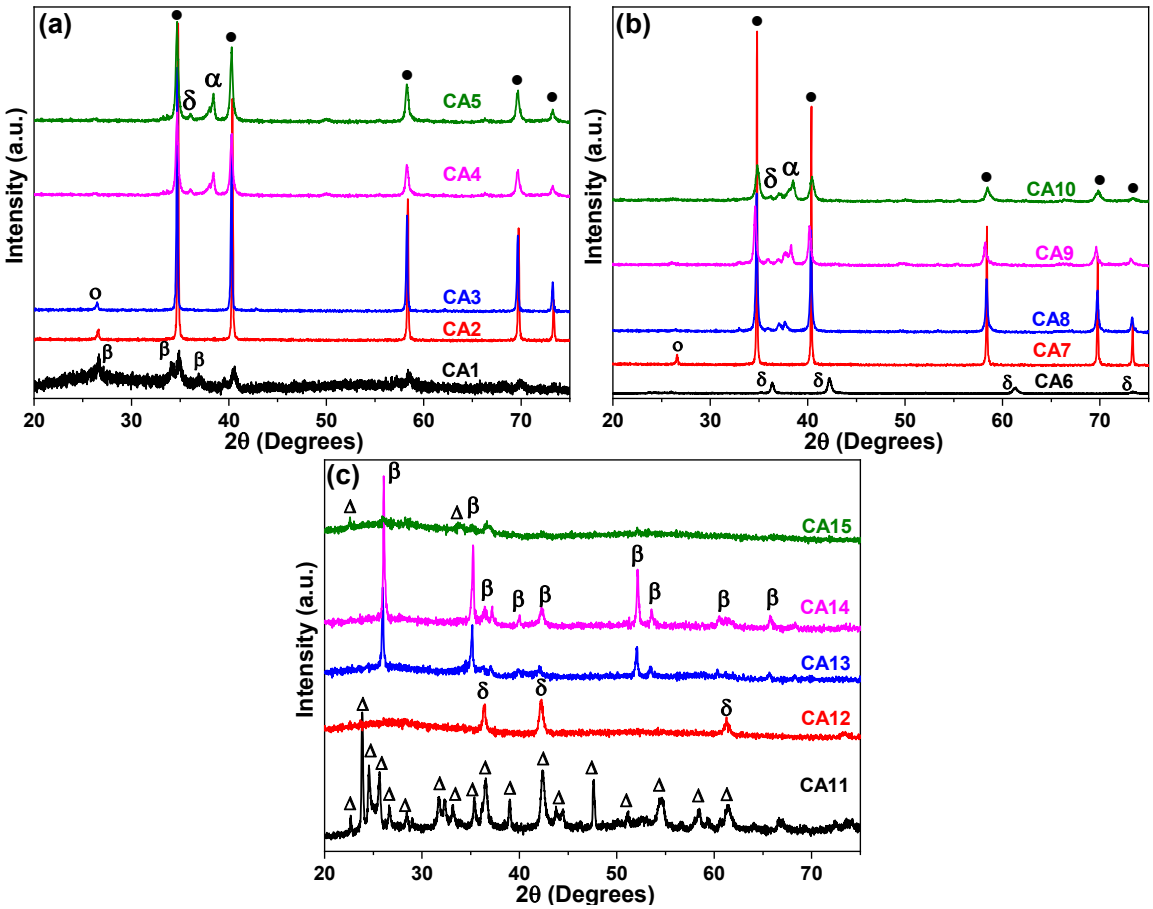

Figure 6.2: XRD patterns of all the synthesized samples for the optimization of synthesis parameters at (a) 800 °C; (b) 700 °C and (c) 600 °C to obtain single phase NbC. Symbols: • (NbC), α (Nb), δ (NbO), β (NbO_2), Δ (Nb_2O_5) and ° (graphitic carbon).

Figure 6.2 represents the XRD patterns of the samples prepared at different conditions to optimize the synthesis temperature and holding time. Keeping the optimized synthesis parameters (mentioned in chapter 4 for CF) as reference, samples were prepared at 800 °C with different holding time, represented as CA1-CA5 in figure 6.2a. It can be observed that CA1 exhibited a mixture of NbC and NbO_2 while, CA2 and CA3 exhibited single phase NbC in XRD pattern with a minor content of graphitic carbon (g-C). The observed phase transformation (NbO_2 to NbC at longer holding; 2 h (CA2) and 5 h (CA3)) is associated to the time dependent carburization of reduced Nb_2O_5 i.e. NbO_2 obtained in CA1 [1]. Further, CA4 and CA5 exhibited decarburization of NbC providing NbO as minor

phase which was increased with increasing holding time (10 h (CA4) → 15 h (CA5)) as shown in figure 6.2a [1]. Thereafter, lower temperature i.e. 700 °C was employed to study the effect of synthesis temperature as shown in figure 6.2b in which CA7 (2 h of holding at 700 °C) exhibited single phase NbC XRD pattern with minor content of g-C similar to CA2 and CA3. Beyond 2 h of holding (CA8 -CA10), samples contained a mixture of NbC and NbO as obtained at 800 °C (CA4 and CA5). The important feature observed was that CA6 (0 h at 700 °C) consisted single phase NbO while, CA1 (0 h at 800 °C) exhibited mixture of NbC and NbO_2 due to insufficient thermal energy responsible for carburization at 700 °C [1].

In the similar lines, lower temperature i.e. 600 °C was employed in order to obtain NbC as shown in figure 6.2c. The adopted holding time at 600 °C resulted in the reduction of Nb_2O_5 exhibiting NbO_2 and NbO at different holding times. Sample C11 (0 h at 600 °C) represents XRD pattern similar to Nb- precursor i.e. Nb_2O_5 suggesting the unreacted Nb_2O_5 with slight broadening of diffraction peaks. At 600 °C, increasing holding time resulted the formation of NbO at 2 h (CA12), mixture of (NbO+NbO_2) at 5 h (CA13) and NbO at 10 h (CA14). Further, increment of holding time to 15 h (CA15) has induced lattice distortion resulting amorphous phase along with some diffraction peaks (less intense) associated to Nb_2O_5 and NbO_2.

6.3. Williamson-Hall (W-H) analysis:

Table 6.2: Lattice carbon content (x), lattice constant (a) and W-H postulates of various samples using CA.

Sample ID	x	a	USM		USDM			USEDM				Scherrer
		Å	ε, $\times 10^{-4}$	t, nm	σ, GPa	ε, $\times 10^{-4}$	t, nm		Å	ε, $\times 10^{-4}$	t, nm	σ, GPa
CA2	0.923	4.466	2.5	73.3	0.08	1.8	76.2	0.11	0.09	2.2	73.3	94.8
CA3	0.978	4.470	1.6	82.0	0.05	1.3	79.2	0.49	0.06	1.5	80.6	69.5
CA7	0.906	4.465	0.6	155.7	0.02	0.021	151.7	0.08	0.02	0.6	151.7	136.9

As discussed in the previous section, sample CA2, CA3 and CA7 exhibited single phase NbC XRD patterns. As an effect of temperature and holding time, all these sample were analyzed with W-H analysis for which different models were adopted as shown in figure 6.3. Among all the models, USEDM model provided better quality of fitting i.e. R^2 = 0.99 suggesting the homogeneity of strain energy density inside the NbC lattice. Moreover, various results of W-H analysis are listed in table 6.2. As an effect of synthesis temperature, CA2 and CA7 exhibited almost equal lattice constant. While, slight reduction in lattice carbon (x = C/Nb) has induced higher distortion in NbC lattice for CA7 as compared to CA2. CA3 composed of reduced lattice distortion than CA2 with increased

lattice carbon and lattice constant at longer holding time (5 h) at 800 °C which is an indication of the time dependent diffusion of carbon resulting NbC.

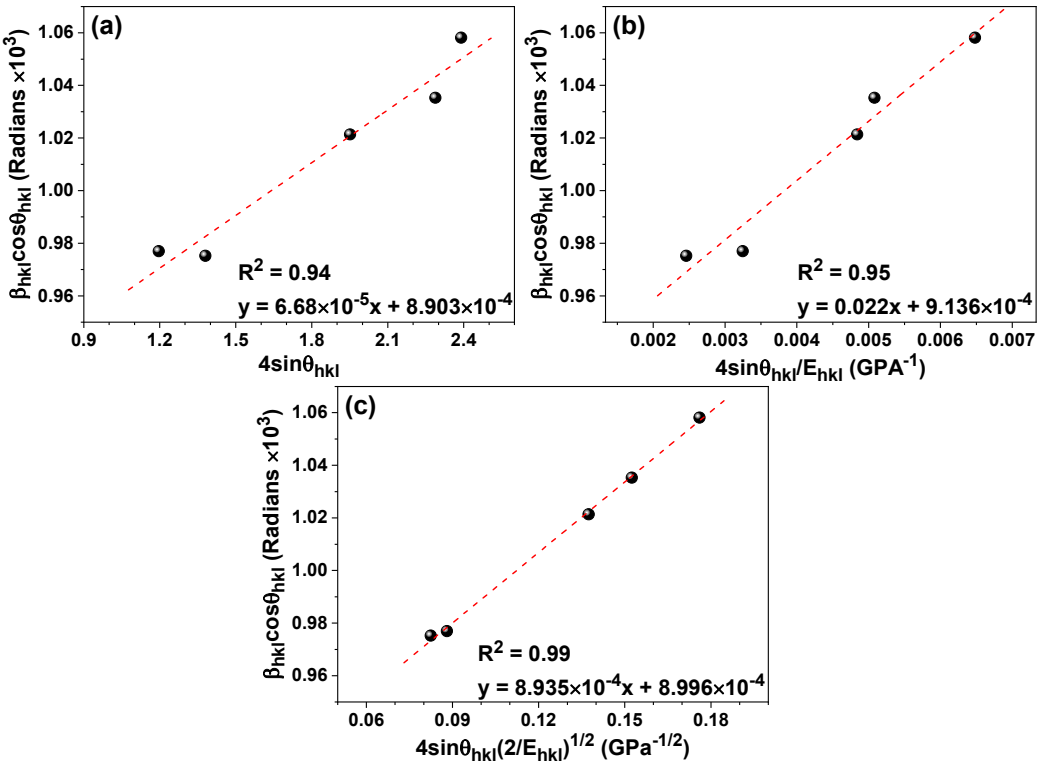

Figure 6.3: Representative graphs of (a) USM, (b) USDM and (c) USEDM models of W-H analysis for sample CA7.

6.4. Transmission electron microscopy (TEM):

Morphology of all the single phase NbC-C nanocomposite samples was examined with the help of TEM as shown in figure 6.4-6.6 (CA2, CA3 and CA7, respectively). It has been observed that all the samples exhibited agglomeration of NbC nanoparticles along with a thin coating of carbon. High resolution TEM (HR-TEM) images confirmed the formation of NbC particles with the observed lattice fringing of 0.257 and 0.158 nm associated to (111) and (220) planes, respectively. Moreover, the presence of graphitic carbon (as observed from XRD results; figure 6.2) has also been confirmed with the lattice fringing corresponding to (002) plane i.e. 0.337 nm. The carbon coating exhibits graphitic and disordered graphitic nature as suggested by discontinuous lattice fringing shown in figure 6.4 and 6.6. Further, elemental profile (STEM images) of CA2 and CA3 represented the distribution of Nb, C and O throughout the agglomerate in which presence of oxygen has been observed inside the NbC nanoparticle (figure 6.4; blue color and 6.5; green color) which might be associated to the oxygen centers in the form of NbC_xO_y or NbO_z [2]. Moreover, the presence of diffraction spots in SAED pattern of CA7 depicted the formation of bigger crystallites as shown in figure 6.6.

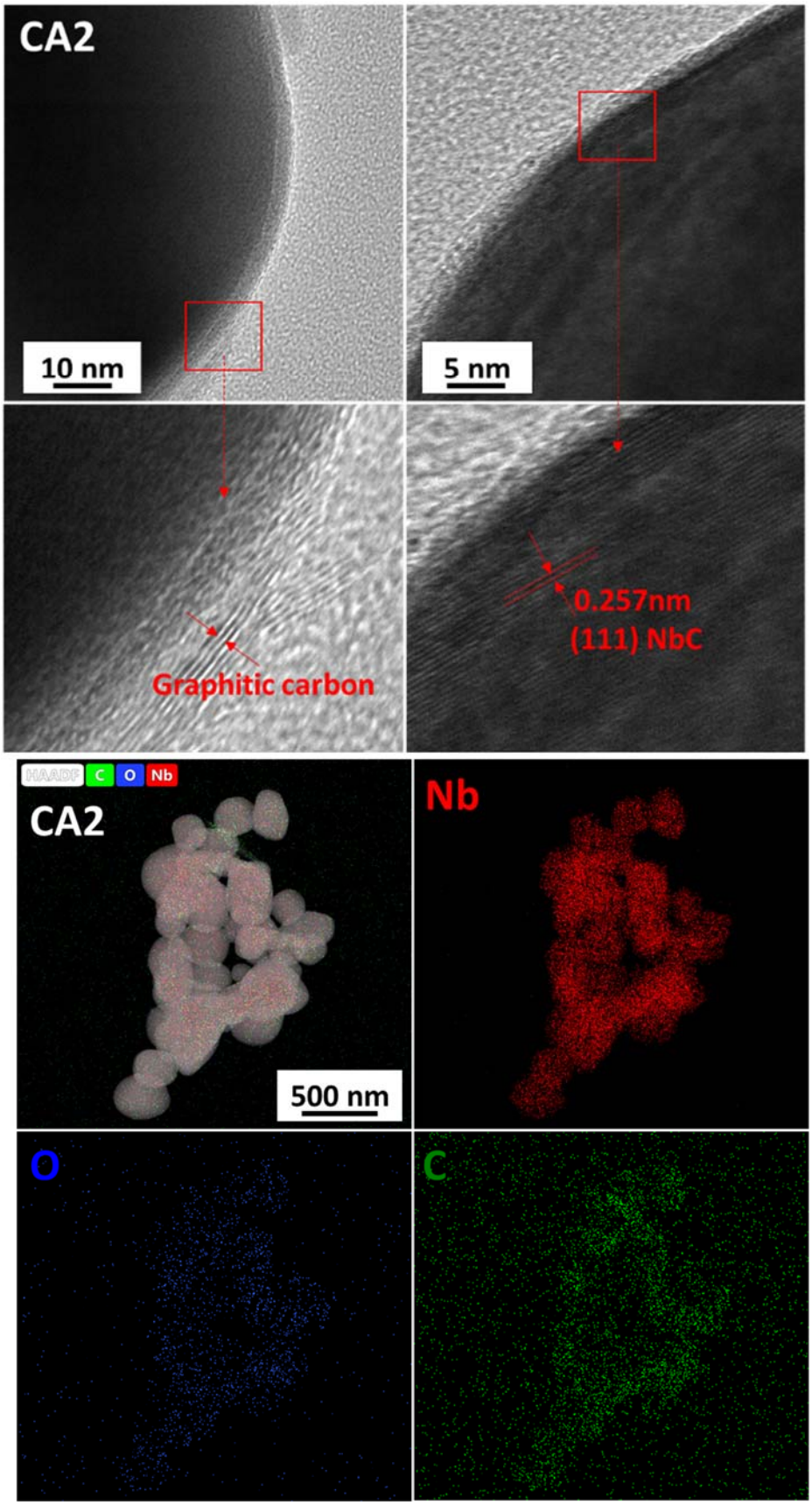

Figure 6.4: High resolution (HR) TEM of CA2 confirming the formation of NbC nanoparticles encapsulated by graphitic carbon and STEM images for elemental (Nb, C and O) distribution across NbC nanoparticles.

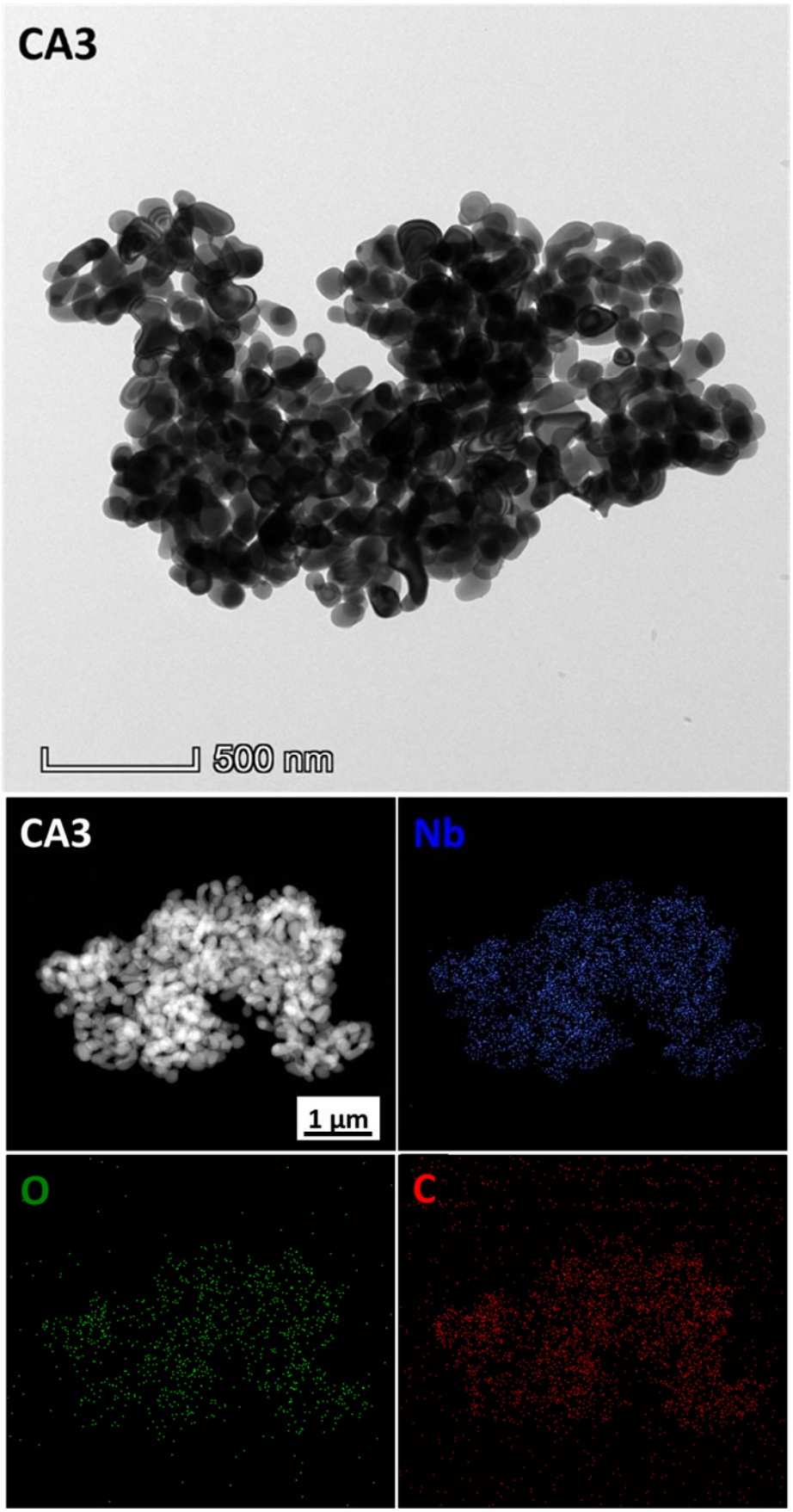

Figure 6.5: TEM and STEM images of CA3 showing the formation of homogeneous distribution of NbC nanoparticles with the presence of oxygen centers (green color) inside nanoparticles.

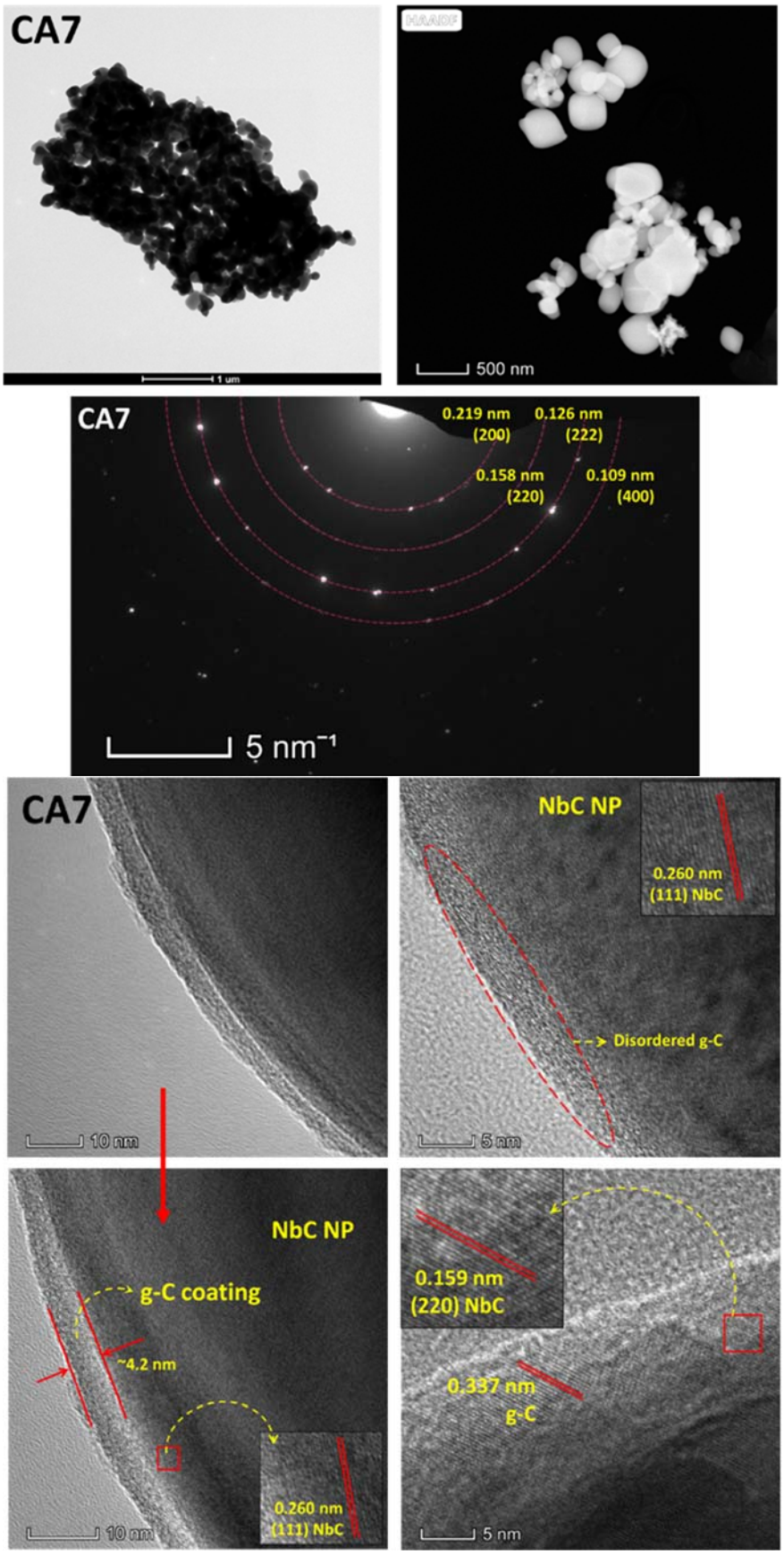

Figure 6.6: High resolution (HR) TEM of CA7 confirming the presence of NbC nanoparticles encapsulated by graphitic carbon and STEM images for elemental (Nb, C and O) distribution across NbC nanoparticles.

It can also be observed that CA3 constituted smaller with homogeneous distribution of NbC nanoparticles as compared to CA2 (~230 nm) and CA7 (~170 nm) having average particle size of ~80 nm.

6.5. Raman spectroscopy:

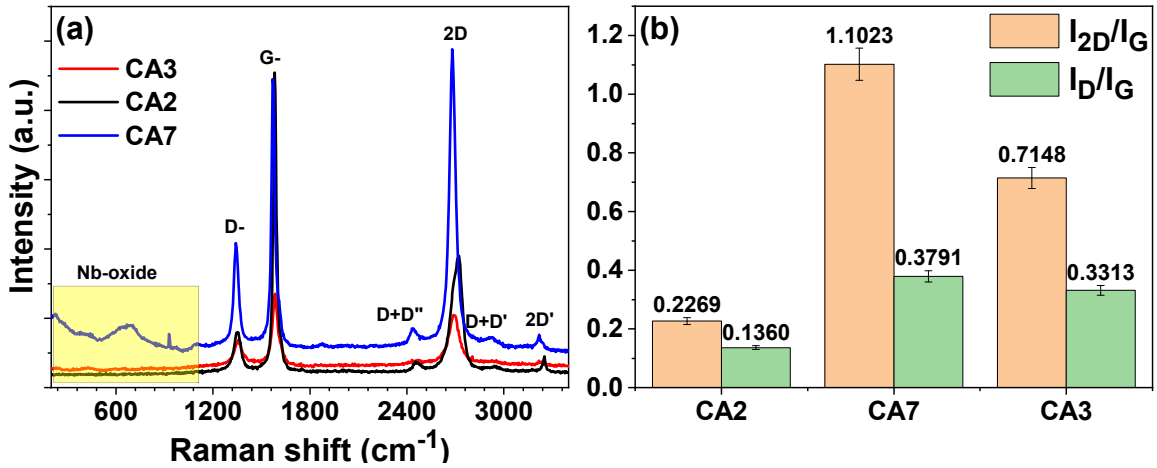

Figure 6.7: (a) Raman spectra; (b) graphitization or 2D growth in CA2, CA3 and CA7.

As observed from the XRD patterns of all the samples, there is a low intensity peak around ~26° associated with graphitic carbon. Raman spectroscopy was carried out in order to understand the nature of carbon present in the sample (figure 6.7a). Positions and FWHM of different Raman bands are listed in table 6.3. All the samples exhibited three major Raman bands around 1350, 1580 and 2690 cm^{-1} suggesting the presence of disordered, graphitic and 2D graphitic carbon (respectively) due to disordered scattering and bond stretching of sp^2 carbon atoms [3]. Weak vibration modes (D+D") and (D+D') are associated to the acoustic branches of intervalley double optical resonance Raman scattering (DRRS) [4].

Table 6.3: List of different bands obtained from deconvolution (Lorentzian peak function) of Raman spectra of CA2, CA3 and CA7.

Sample ↓	Raman band →	D-	G-	D'-	2D-
CA2	Position (cm^{-1})	1351.38	1583.24	1609.07	2690.02
	FWHM (cm^{-1})	49.72	21.11	36.77	61.41
CA3	Position (cm^{-1})	1357.22	1583.88	1621.83	2691.27
	FWHM (cm^{-1})	60.34	37.69	32.26	72.82
CA7	Position (cm^{-1})	1343.95	1572.39	1608.82	2681.66
	FWHM (cm^{-1})	33.26	22.95	23.23	42.94

Moreover, the observed Raman shift below 1000 cm^{-1} is associated to the Nb-O bonds suggesting the presence of Nb-oxide in CA7 sample which was not observed in XRD pattern. Figure 6.7b represents the nature of carbon with the help of I_D/I_G and I_{2D}/I_G. I_D/I_G for CA2 (0.136) is least suggesting the least content of disordered graphitic carbon as compared to other CA3 (0.3313) and CA7 (0.3791) samples. I_{2D}/I_G, which reveals the 2D

growth of graphite in the form of graphene, is quite high in the case of CA7 (1.10) indicating the formation of disordered 2D graphene sheets at lower temperature i.e. 700 °C (CA7) while, CA2 consists multilayered graphitic whiskers [4]. Values obtained for CA3 sample are intermediatery indicating that an increase in holding time at 800 °C (from 2 to 5 h) results in enhanced disorder and 2D graphene growth. $I_D/I_{D'}$ (ratio of I_D/I_G and $I_{D'}/I_G$) represents the physical origin of the defects (not the concentration). For all the samples, it came out to be 3.25, 3.43 and 5.28 (respectively) suggesting the presence of small graphitic grains [4].

6.6. BET analysis:

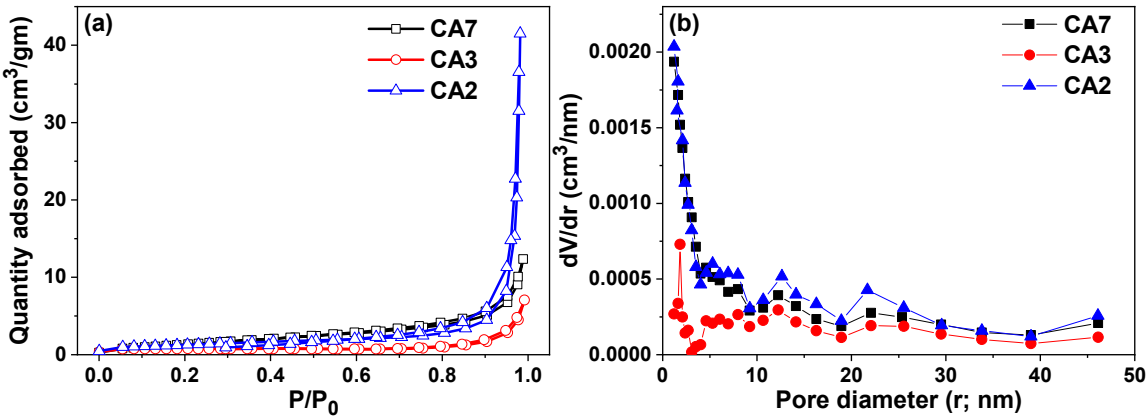

Figure 6.8: BET adsorption-desorption isotherms (inset) and BJH pore size distribution curves of CA2, CA3 and CA7.

Figure 6.8a represents the sorption isotherms for the single phase samples (CA2, CA3 and CA7) exhibiting type IV hysteresis loop ranging between 0.5-1.0 (P/P_0) with 6.09, 4.65 and 2.98 m^2/g (respectively) as specific surface area (SSA) [5]. The observed type IV isotherm suggests the presence of mixture of micro- and mesopores on the surface of catalysts. Further, BJH analysis also supports the results with 0.0191, 0.0642 and 0.0104 cm^3/g as pore volume for CA2, CA3 and CA7 (respectively) as shown in Figure 6.8b. The optimized single-phase samples contain less SSA with very small pore volume which might be associated to the larger particle size. As an effect of temperature and holding time, CA2 and CA3 exhibited higher SSA and pore volume due to higher content of evolution of CO/CO_2 during reduction-carburization process as compared to CA7 [6]. At 800 °C, longer holding time of 5.0 h (i.e. sample CA3) can be responsible for the enhanced CO/CO_2 evolution resulting increased pore volume with reduced specific surface area as compared to that of CA2. Here with the help of XRD, Raman, TEM and BET results, the formation of porous NbC-C nanocomposite has been confirmed at relatively low temperatures (700 and 800 °C).

6.7. X-ray photoelectron spectroscopy (XPS):

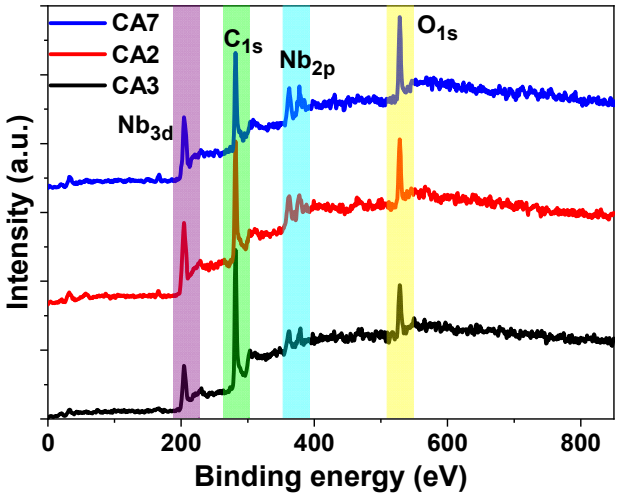

Figure 6.9: XPS survey spectra of CA2, CA3 and CA7 depicting the presence of Nb, C and O on the surface of NPs.

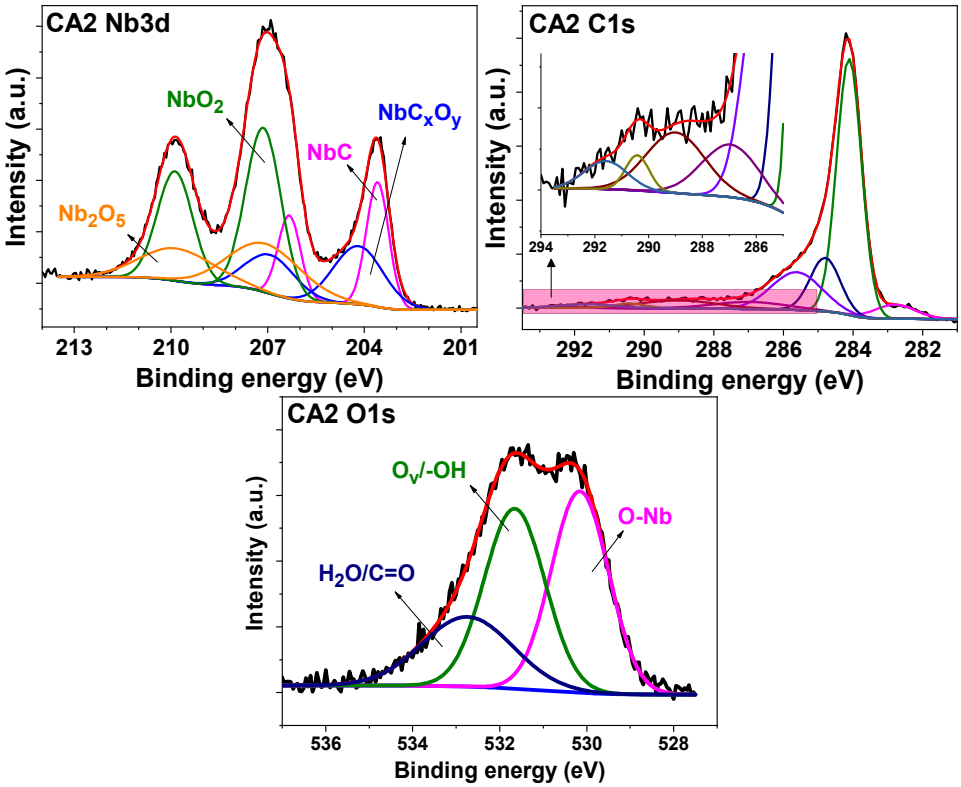

Figure 6.10: HR-XPS spectra of Nb3d, C1s and O1s representing the presence of different functionalities on the surface of CA2.

For the understanding of catalytic response of prepared samples, surface composition becomes very critical to probe the role of individual chemical states of different elements. Figure 6.9 shows the XPS survey spectrum of CA2, CA3 and CA7 confirming the presence of Nb, C and O which are further analyzed through their respective high-resolution spectra as shown in figure 6.10 (representative data) and the respective data is provided in table 6.3.

HR-XPS spectra of Nb3d (figure 6.10) revealed the presence of multiple oxidation states of Nb in the form of NbC, NbC_xO_y, NbO_2 and Nb_2O_5. The presence of peaks associated to oxides at different binding energies (204.1, 207.0 and 207.1 eV) can be related to the presence of oxygen centers in the form of NbC_xO_y or NbO_z inside the nanoparticles as observed in chapter 4. Moreover, it can also be observed that CA2 consists higher volume fraction of NbC and NbC_xO_y as compared to CA3 and CA7 as shown in table 6.4.

Table 6.4: Deconvoluted data of HR-XPS spectra of Nb3d, C1s and O1s of CA2 and CA7.

Group	CA2		CA3		CA7		
	B.E. (eV)	Volume (%)	B.E. (eV)	Volume (%)	B.E. (eV)	Volume (%)	
NbC	203.6, 206.3	18.6	203.7, 206.4	15.5	203.7, 206.4	13.8	[7–9]
NbC_xO_y	204.1, 206.9	19.3	204.5, 207.2	16.1	204.8, 207.5	12.1	
NbO_2	207.0, 209.8	38.3	206.9, 209.7	57.1	207.0, 209.7	56.3	
Nb_2O_5	207.1, 209.9	23.8	207.9, 210.6	11.3	207.5, 210.3	17.8	
NbC	282.7	4.8	283.4	7.2	283.1	6.4	[10,11]
C sp^2	284.1	53.5	284.1	44.6	284.1	48.7	[7,12]
C sp^3	284.8	13.4	284.7	25.8	284.8	20.1	[12,13]
C-OH	285.6	15.8	285.9	7.4	285.8	10.6	[12,13]
C-O	286.9	4.3	286.9	4.9	286.9	4.7	[13,14]
C=O	288.9	5.2	288.7	3.9	288.3	2.9	[12–14]
π-π*	290.4	1.3	290.4	3.3	289.8	3.4	[15]
O=C-O	291.6	1.7	291.8	2.9	291.5	3.2	[14]
O-Nb	530.1	40.1	530.3	32.2	530.0	34.2	[16]
O_v	531.6	37.8	531.6	49.6	531.5	43.5	[16,17]
C=O	532.7	22.1	533.0	18.2	532.7	22.3	[18]

HR-XPS of C1s for both the samples suggested the presence of different carboxylic groups such as C-OH (285.8 eV), C-O (286.9 eV), C=O (288.3 eV) and O=C-O (291.5 eV) along with graphitic carbon (sp^2 hybridized; 284.1 eV). Moreover, the content of sp^2 hybridized carbon is higher for CA2 as compared to CA3 and CA7 which has also been observed in Raman analysis as lower I_D/I_G (0.1360). Further, HR-XPS spectra of O1s for both the samples represent the presence of significant concentration of oxygen defects (531.5 eV) which would support the delayed recombination of charge carriers during irradiation.

6.8. Absorbance and photoluminescence (PL) spectroscopy:

To understand the photocatalytic performance of optimized single-phase samples, optical (absorption and emission) response of these samples becomes critical. Figure 6.11 represents the optical absorbance and emission spectra of CA2, CA3 and CA7. Absorbance (UV-visible) spectra (figure 6.11a) of CA2, CA3 and CA7 describes the significant absorption of visible region while, reduced absorption near 240 nm is associated to the graphitic carbon as graphene [19–21]. Moreover, increased absorption of EM radiation has been observed between 750–450 nm which might be associated to the presence of oxygen

centers as NbC_xO_y as supported by TEM and Raman results [22]. The calculation of optical bandgap using Tauc plot has suggested 1.63, 1.72 and 1.85 eV for CA2, CA3 and CA7, respectively [23].

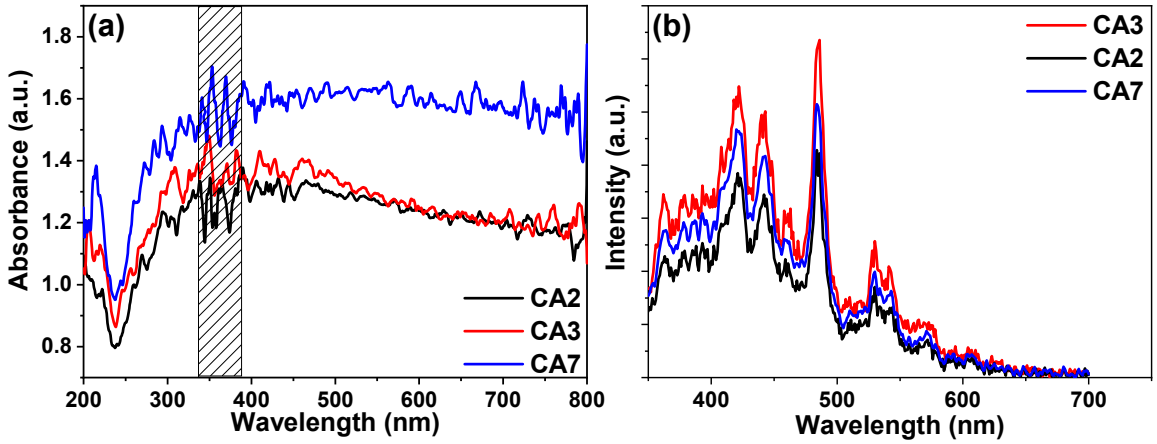

Figure 6.11: (a) UV-visible spectra, Tauc plot (inset); and (b) PL emission spectra (excitation wavelength λ = 340 nm) of CA2, CA3 and CA7.

The photoluminescence (PL) emission spectra (350-800 nm) of these samples was obtained with excitation wavelength λ_{exc} = 340 nm to determine the recombination nature of charge carriers as shown in figure 6.11b. The disordered graphitic carbon (different functions groups and π-π* transitions) and presence of graphene oxide (attachment of oxygen on g-C as obtained from Raman and XPS results) constituted a broad emission up to 650 nm [24,25]. Emission peaks around 500 nm (~435–450, ~490 and ~540 nm) can be attributed to the transfer of electron from carbon to oxygen in GO, due to the shifting of highest occupied molecular orbital (HOMO) downward as opening of band gaps as observed in in figure 6.11a [26,27].

6.9. Photocatalytic study:

To understand the photocatalytic activity of NbC-C nanopowder samples, MB dye (1.0 mg/L) has been taken as model organic compound under household CFL (85 W) illumination. As a result of the establishment of adsorption-desorption equilibrium (30 min stirring in dark chamber), 20.19, 11.23 and 13.81% dye has been adsorbed on the surface of photocatalysts (CA2, CA3 and CA7) respectively. Figure 6.12 represents the relative change in the concentration of MB dye with respect to irradiation time in the presence of CA2, CA3 and CA7. C/C_0 vs. time revealed the discoloration of MB dye to 45.86, 21.72 and 35.55% in the presence of CA2, CA3 and CA7 (respectively) under 8 h of visible exposure. The observed decrement in the concentration of MB dye can be associated to discoloration or photodegradation of MB dye. The rate of photochemical process was determined by pseudo first order kinetics as 0.0733, 0.02938 and 0.0532 h^{-1} (respectively)

with R^2 = 0.99 for all considered samples (figure 6.12b). The better performance was observed with CA2 sample which was examined for 4 continuous cycles with excellent stability as shown in figure 6.13a. It has been observed that there was only 1.68% decrement of photocatalytic activity which might be due to the loss of photocatalyst during the extraction for subsequent cycle.

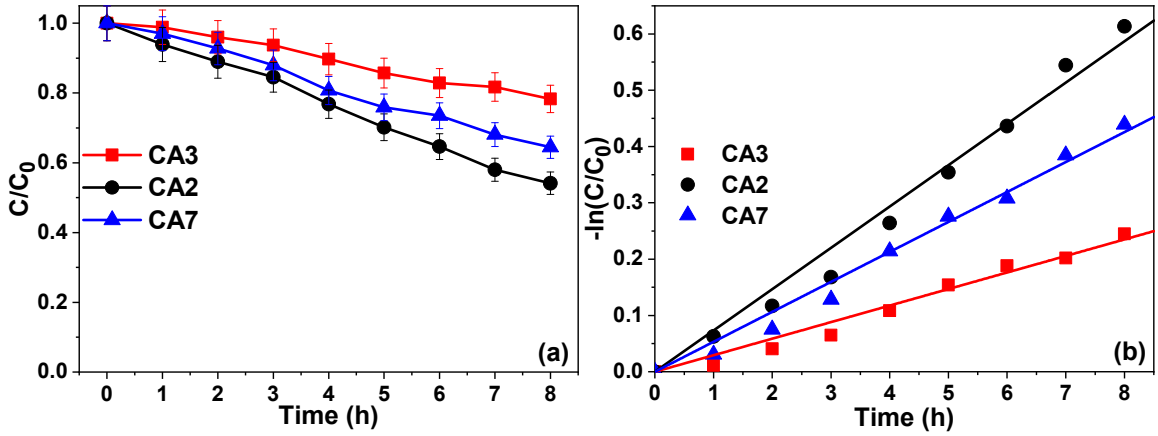

Figure 6.12: Photodegradation of MB dye with the help of CA2, CA3 and CA7. Pseudo first order kinetics of MB dye degradation under household CFL exposure.

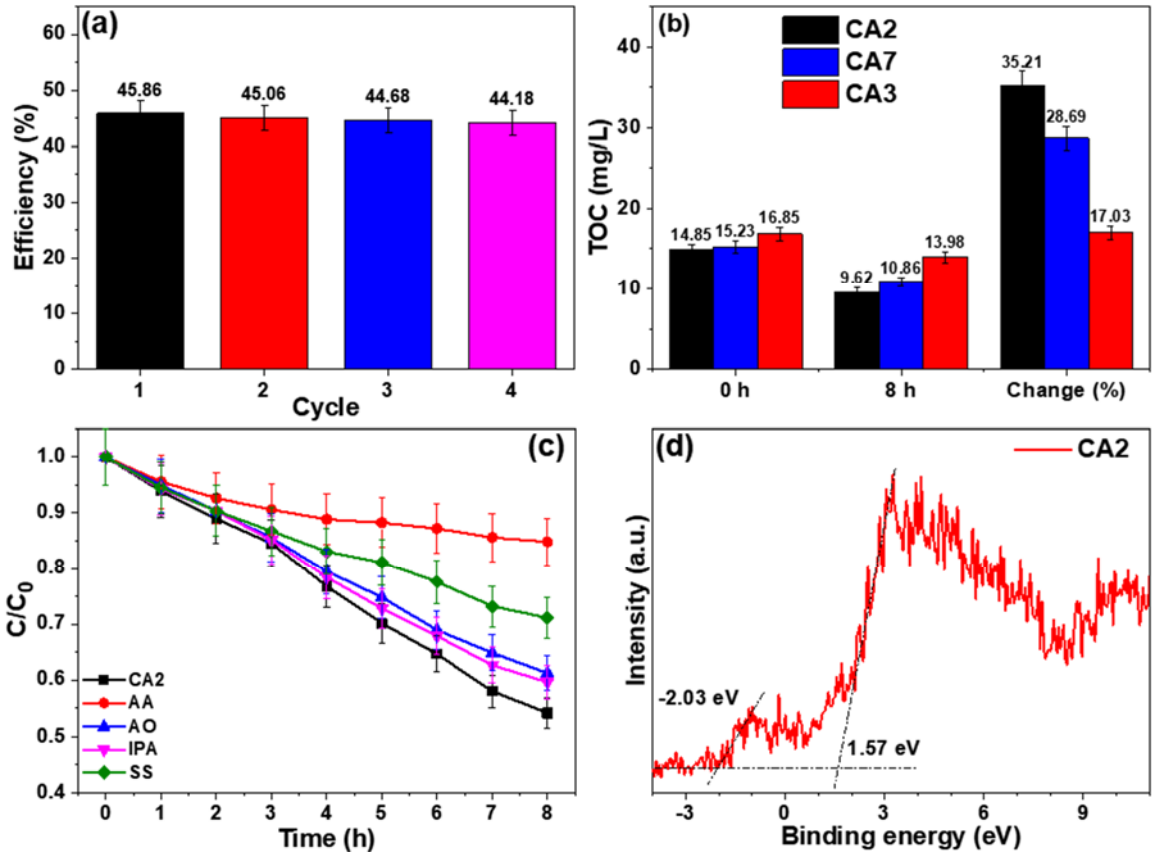

Figure 6.13: (a) Degradation efficiency of CA2 up to 4 continuous cycles; (b) Variation in TOC after the visible exposure of 8 h; (c) Detection of ROS species during the photodegradation of MB dye using CA2; and (d) Valence band spectra of CA2.

Further, the confirmation of decreasing concentration is associated to photodegradation of MB dye, the total organic carbon (TOC) and scavenger test have been carried out. Figure 6.13b represents the TOC value before and after the irradiation in the presence of photocatalysts. The decrement of TOC after the establishment of ads-des equilibrium and 8 h exposure suggested the degradation of MB dye is slightly slower than discoloration of MB molecule. Further, various scavengers were added to the dye solution to understand the photodegradation of MB dye and role of different reactive oxidative species (ROS) in it. Figure 6.13c revealed the involvement of superoxide anion radical ($O_2^{\cdot-}$) as a major oxidizing agent for photo-oxidation of MB dye with CA2 as compared to other ROS species. It is evident from figure 6.13c that the addition of ammonium oxalate (AO) and isopropyl alcohol (IPA) do not affect the photodegradation profile significantly. While, the addition of sodium sulfate (SS) and ascorbic acid (AA) retarded the photodegradation profile suggesting the entrapment of photogenerated e^- and $O_2^{\cdot-}$, respectively.

6.10. Proposed degradation mechanism:

For the establishment of the photodegradation mechanism, it has become necessary to estimate the valance (VBE) and conduction (CBE) band edges of CA2. Figure 6.13d represents the valence band spectra of CA2 providing the presence of dual VBE as 1.57 and -2.03eV (intercept on energy axis of extrapolated curve). With the help of optical absorbance spectrum of CA2 (Figure 6.11a) the position of conduction band edge (CBE) were calculated as -0.06 eV as shown in figure 6.14.

The reduction potential edge of $O_2/O_2^{\cdot-}$ (-0.046 eV vs. NHE) is comparable to the calculated CBE resulting in the generation of super oxide anion radical [28]. Figure 6.14 represents the schematic mechanism for the photodegradation of MB dye with the help of CA2 in which the holes and electron were generated with the illumination of visible light on VBE and CBE, respectively. The detailed photo-chemical reactions involved in the generation of different ROS species can be described as follows:

$$NbC + C + photon \rightarrow NbC + C + h^+ + e^- \quad (6.1)$$
$$O_2^{\cdot} + e^- \rightarrow O_2^{\cdot-} \quad (6.2)$$
$$O_2^{\cdot-} + H_2O \rightarrow OH^{\cdot} + OH^- \quad (6.3)$$
$$OH^- + h^+ \rightarrow OH^{\cdot} \quad (6.4)$$
$$Nb^{3+} \leftrightarrow Nb^{4+} + e^- \quad (6.5)$$
$$Nb^{2+} \leftrightarrow Nb^{3+} + e^- \quad (6.6)$$

It is very well-known fact that NbC has electronic structure similar to noble metals and shows conducting behavior which might be a good support as photocatalyst (charge

transfer medium) to degrade organic pollutants. Here, the synthesized photocatalyst (CA2) exhibits different Nb-O centers as NbC_xO_y and NbO_z (observed in TEM and XPS results) inside the NbC nanoparticles inducing photon absorption ability upon illumination (observed in absorbance spectroscopy). Moreover, Nb is present in multiple oxidation states in the form of NbC, NbC_xO_y and NbO_z which may contribute to scavenge and provide some electrons altering the photochemical reaction rate.

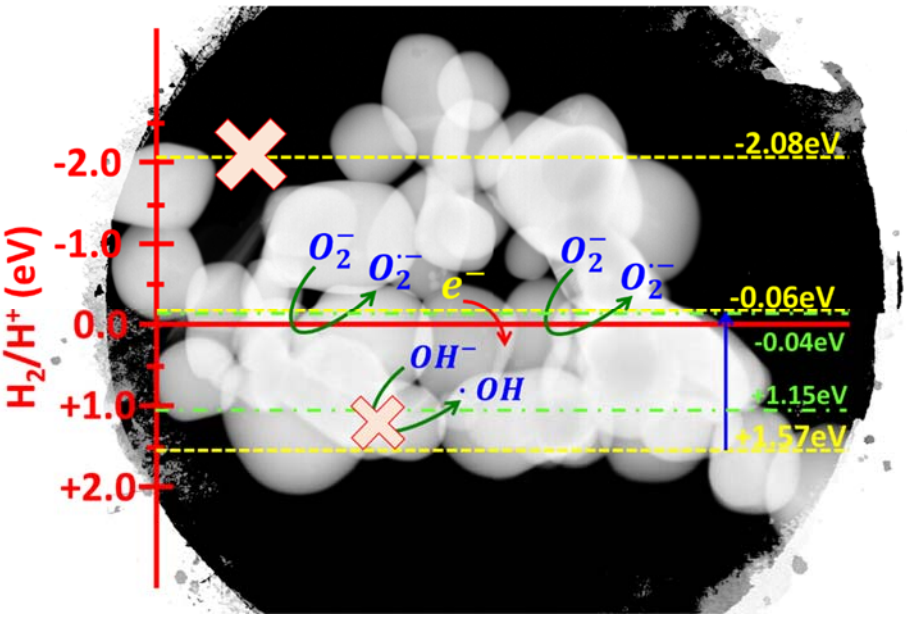

Figure 6.14: Proposed mechanism for the photodegradation of MB dye with the help of CA2 under household CFL lamp.

References:

1 A. Gupta, G. Singla and O. P. Pandey, *Ceram. Int.*, 2016, **42**, 13024–13034.
2 D. N. Miller, A. K. Azad, H. Delpouve, L. Quazuguel, J. Zhou, A. Sinha, P. Wormald and J. T. S. Irvine, *J. Mater. Chem. A*, 2016, **4**, 5730–5736.
3 A. C. Ferrari, *Solid State Commun.*, 2007, **143**, 47–57.
4 J.-B. Wu, M.-L. Lin, X. Cong, H.-N. Liu and P.-H. Tan, *Chem. Soc. Rev.*, 2018, **47**, 1822–1873.
5 M. Thommes, *Chemie Ing. Tech.*, 2010, **82**, 1059–1073.
6 G. Singla, K. Singh and O. P. Pandey, *J. Alloys Compd.*, 2016, **665**, 186–196.
7 J. Halim, K. M. Cook, M. Naquib, P. Eklund, Y. Gogotsi, J. Rosen and M. W. Barsoum, *Appl. Surf. Sci.*, 2016, **362**, 406–417.
8 M. T. Marques, A. M. Ferraria, J. B. Correia, A. M. B. do Rego and R. Vilar, *Mater. Chem. Phys.*, 2008, **109**, 174–180.
9 C. Zhang, M. Beidaghi, M. Naguib, M. R. Lukatskaya, M. Zhao, B. Dyatkin, K. M. Cook, S. J. Kim, B. Eng, X. Xiao, D. Long, W. Qiao, B. Dunn and Y. Gogotsi, *Chem. Mater.*, 2016, **28**, 3937–3943.
10 L. Ramqvist, K. Hamrin, G. Johansson, A. Fahlman and C. Nordling, *J. Phys. Chem. Solids*, 1969, **30**, 1835–1847.
11 J. A. Klug, T. Proslier, J. W. Elam, R. E. Cook, J. M. Hiller, H. Claus, N. G. Becker and M. J. Pellin, *J. Phys. Chem. C*, 2011, **115**, 25063–25071.
12 S. Muralikrishna, K. Sureshkumar, T. S. Varley, D. H. Nagaraju and T. Ramakrishnappa, *Anal. Methods*, 2014, **6**, 8698–8705.
13 F. Zhao, A. Vrajitoarea, Q. Jiang, X. Han, A. Chaudhary, J. O. Welch and R. B. Jackman, *Sci. Rep.*, 2015, **5**, 17–19.
14 H. Yan, C. Tian, L. Sun, B. Wang, L. Wang, J. Yin, A. Wu and H. Fu, *Energy Environmetal Sci.*, 2014, **7**, 1939–1949.
15 D. Chen, H. Feng and J. Li, *Chem. Rev.*, 2012, **112**, 6027–6053.
16 X. Ma, Y. Chen, H. Li, X. Cui and Y. Lin, *Mater. Res. Bull.*, 2015, **66**, 51–58.
17 X. Zhang, J. Qin, Y. Xue, P. Yu, B. Zhang, L. Wang and R. Liu, *Sci. Rep.*, 2014, **4**, 4–11.
18 F. E. Castillejo, D. M. Marulanda, J. J. Olaya and J. E. Alfonso, *Surf. Coatings Technol.*, 2014, **254**, 104–111.
19 M. E. Khan, M. M. Khan and M. H. Cho, *Sci. Rep.*, 2017, **7**, 5928.
20 M. E. Khan, M. M. Khan and M. H. Cho, *New J. Chem.*, 2015, **39**, 8121–8129.
21 X. Wei and M. Chen, *J. Chil. Chem. Soc.*, 2015, **60**, 2988–2997.
22 Z. Weibin, W. Weidong, W. Xueming, C. Xinlu, Y. Dawei, S. Changle, P. Liping, W. Yuying and B. Li, *Surf. Interface Anal.*, 2013, **45**, 1206–1210.
23 M. Mittal, M. Sharma and O. P. Pandey, *Sol. Energy*, 2014, **110**, 386–397.
24 X. Ding, *J. Mater. Chem. C*, 2014, **2**, 3717–3722.
25 Y. Chen, B. Wang, S. Lin, Y. Zhang and X. Wang, *J. Phys. Chem. C*, 2014, **118**, 29981–29989.
26 J. R. Rani, J. Lim, J. Oh, D. Kim, D. Lee, J.-W. Kim, H. S. Shin, J. H. Kim and S. C. Jun, *RSC Adv.*, 2013, **3**, 5926.
27 H. K. Jeong, C. Yang, B. S. Kim and K.-J. Kim, *Europhys. Lett.*, 2010, **92**, 37005.
28 Y. Yang, Y. Guo, F. Liu, X. Yuan, Y. Guo, S. Zhang, W. Guo and M. Huo, *Appl. Catal. B Environ.*, 2013, **142**–**143**, 828–837.

CHAPTER 7 RESULTS & DISCUSSION-IV

Utilization of activated charcoal (Laboratory carbon source)

Overview

Based on previous study presented in chapter 4-6, it has become necessary to probe the synthesis mechanism of NbC-C nanocomposite. For this purpose, activated charcoal, a laboratory reagent has been taken as carbon source to compare the obtained results where carbon sources are different hydrocarbon. Here, also the optimization of synthesis parameters (temperature, time and carbon content) has been carried out and the obtained phase(s) has been confirmed with the help of XRD results. Further, based on XRD results and thermodynamic calculation ($\Delta G_{reaction}$), reduction-carburization of Nb_2O_5 was considered as a base to establish the mechanism to achieve carbon coated NbC nanoparticles.

Optical and photocatalytic response of different samples are also discussed as an effect of composition, lattice distortion, lattice carbon content (x in NbC_x). Further, detailed degradation mechanism has been discussed based on composition (XRD, XPS results) and different photodegradation experiments (scavenger, TOC analysis and PL spectroscopy).

7.1. Introduction

Keeping the fact of the utilization of waste (CFs and PHs) and organic compound (CA) as carbon source (as discussed in previous chapters) for the fabrication of nano NbC, the simplest form of carbon i.e. charcoal, can provide sufficient evidences to establish well-defined mechanism to carburize Nb_2O_5 resulting NbC along with the role of NbC and its partial oxidative composition in its photocatalytic performance. Moreover, the use of activated charcoal (AC) can also support Mg as reducing agent to reduce Nb_2O_5 at relatively lower temperature and activated charcoal is considered as amorphous form of carbon which requires lesser energy to get oxidized as compared to other available organic compounds. Further, figure 7.1 represents the XRD pattern, SEM micrograph and particle size distribution of used activated charcoal. XRD patterns depicts the amorphous nature of charcoal along with small crystallite of graphitic carbon. SEM results indicated the presence of sharp-edged particles with average size ~4.23 µm of activated charcoal. Table 7.1 describe the details of different experimental conditions.

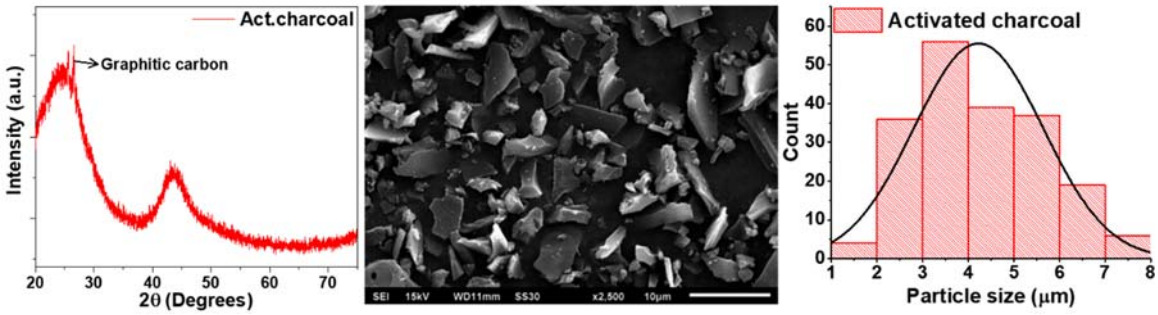

Figure 7.1: XRD, SEM and particle size histogram of activated charcoal used for the synthesis of NbC nanopowder.

Table 7.1: Details of experimental conditions to obtain NbC nanopowder.

Amount (g)			Sample	Temperature (°C)	Holding time (h)
Nb_2O_5	Mg	AC			
1.329	2.0	1.5	AC1	800	10
1.329	2.0	1.5	AC2	700	10
1.329	2.0	1.5	AC3	600	10
1.329	2.0	1.5	AC4	800	5
1.329	2.0	1.5	AC5	800	7
1.329	2.0	1.5	AC6	800	11
1.329	2.0	1.0	AC7	800	10
1.329	2.0	0.5	AC8	800	10

7.2. X-ray diffraction (XRD):

For the synthesis of single-phase carbon coated NbC NPs, synthesis temperatures, holding time and amount of carbon source were optimized on the basis of XRD results

which are shown in figure 7.2. XRD patterns of samples synthesized at 800, 700 and 600 ºC with 10 h holding time are shown in figure 7.2a. The synthesis at 600 ºC resulted in the reduction of Nb_2O_5 to NbO (sample AC3). While, at 700 (AC2) and 800 ºC (AC1), mixtures of (NbC+NbO_2) and NbC were obtained, respectively. The absence of the NbC phase at 600 ºC (figure 7.2a) may be due to the unavailability of enough thermal energy to further reduce and carburize NbO to transform into NbC which can be seen in the case of AC3. Sample AC2 shows the conversion of Nb_2O_5 to NbC with little NbO_2 showing a simultaneous reduction and carburization path. A further increase by 100 ºC (sample AC1) resulted in the complete transformation of Nb_2O_5 to NbC without showing any signature of lower oxides of Nb.

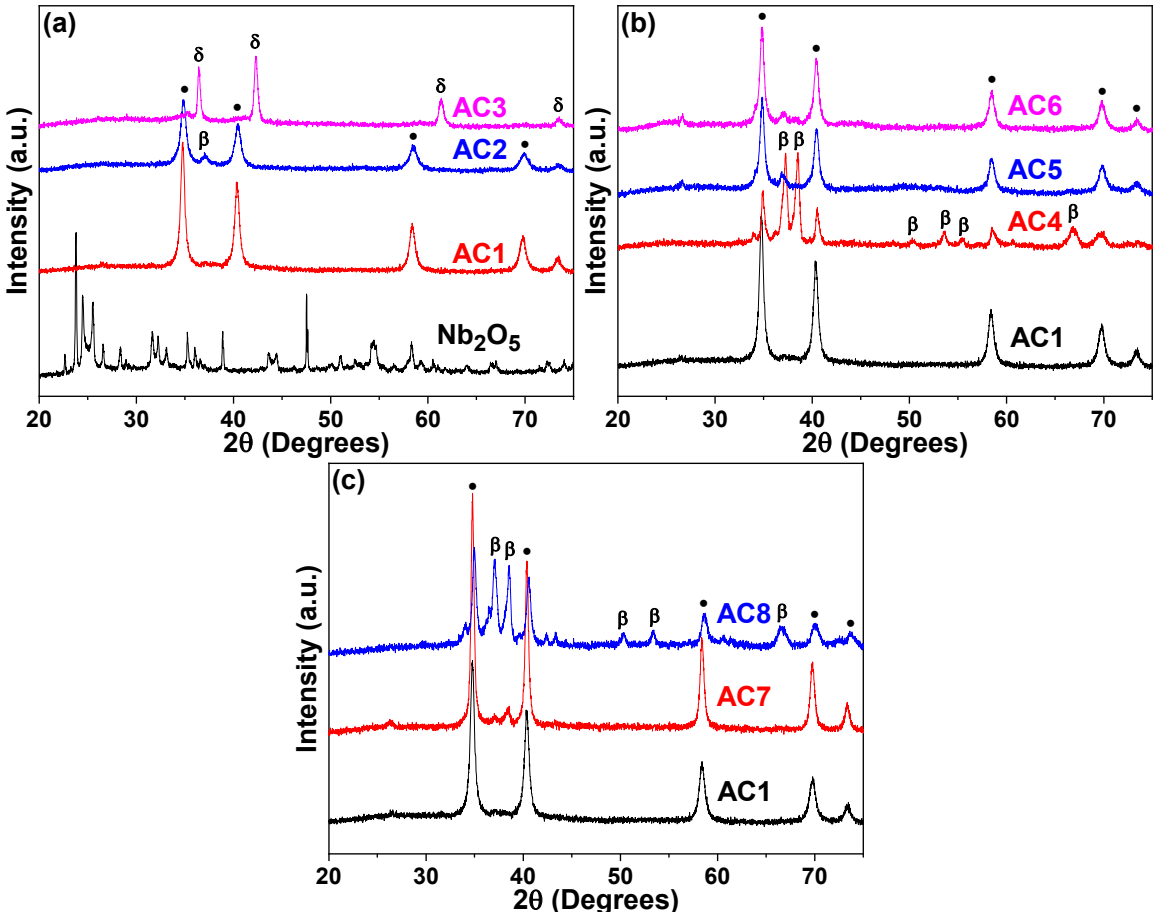

Figure 7.2: XRD diffraction patterns showing the influence of different synthesis parameters; (a) temperatures (600, 700 and 800 °C), (b) holding time (5, 7, 10 and 11 h); and (c) amount of activated charcoal (1.5, 1.0 and 0.5 g) on phase formation. Symbols: • (NbC), α (Nb), β (NbO_2), Δ (Nb_2O_5) and ° (graphitic carbon).

After obtaining single phase NbC at 800 ºC, the holding time has been varied to study the behavior of reduction and carburization of Nb_2O_5 with optimized temperature which is shown in figure 7.2b. AC4 depicted a reduction of Nb_2O_5 to a mixture of NbO_2

and NbC after carburization. AC5 showed contrary results in which carburization exceeded the reduction process as observed by the presence of NbO_2 as a minor phase and NbC as a major phase. In the case of 10 h, complete reduction followed by carburization of Nb_2O_5 was observed in AC1 (figure 7.2b) resulting in single phase NbC. Furthermore, the increment of holding time to 11 h led to decarburization of NbC with the formation of NbO_2. The decarburization of NbC may be caused by a lower CO/CO_2 ratio (CO_2 rich reaction) beyond 10 h at 800 °C [1,2]. While the formation of NbO_2 as a result of decarburization at longer holding (11 h) instead of NbO (as observed in the case of lower temperature) may be attributed to the higher stability of NbO_2 than NbO [3].

7.3. Williamson-Hall (W-H) analysis:

Table 7.2 depicts a comparative study of all the postulates of W-H analysis and Scherrer criteria for all the synthesized NbC samples. The least magnitude of strain in NbC lattice at higher synthesis temperature (AC1) is very obvious due to complete conversion of Nb_2O_5 to NbC, while presence of NbO_2 at 700 °C (AC2) distorts the crystallites which shows higher strain in crystallites. As a function of holding time at 800 ºC, the induced strain tends to decrease as carburization occurs. Figure 7.2b shows that up to 10 h of holding, minor phases are being eliminated (5 h (NbC + NbO_2) to 7 h (NbC + NbO_2) then 10 h (pure NbC)) leading to a large reduction in strain. The diffusion of carbon in the Nb lattice is increased by increasing the holding time which supports the enhancement of lattice parameters by reducing the strain and supporting the attainment of equilibrium positions of Nb and C atoms in the NbC unit cell. Beyond 10h (AC6), decarburization of NbC led to increase the distortion which might be associated to incorporation of oxygen resulting NbO_2.

Table 7.2: Lattice carbon content (x), lattice constant (a) and W-H postulates of various samples using AC.

Sample ID	x	a	USM		USDM			USEDM				Scherrer
		Å	ε, $\times10^{-4}$	t, nm	σ, GPa	ε, $\times10^{-4}$	t, nm	u, $\times10^{-5}$, kJm^{-3}	σ, GPa	ε, $\times10^{-4}$	t, nm	t, nm
AC2	0.874	4.462	19.5	16.7	0.56	13.2	14.8	56.7	0.02	0.4	15.7	10.8
AC1	0.959	4.469	85.1	27.6	2.79	327.4	77.8	1296	0.38	8.9	36.8	18.3
AC4	0.799	4.457	31.8	33.7	1.10	26.2	27.4	185.0	0.05	18.5	31.1	13.6
AC5	0.902	4.464	18.5	25.7	0.54	12.9	22.0	52.6	0.01	0.3	23.8	14.9
AC6	0.904	4.465	30.2	33.7	123.8	1.04	27.8	1.1	0.05	165.8	31.1	14.0

7.4. Transmission electron microscopy (TEM):

TEM micrographs of AC1 are shown in figure 7.3 exhibiting the agglomerated NPs which is attributed to their nano regime. Agglomerated NbC NPs of 10-30 nm are encapsulated in carbon network as shown in figure 7.3a. Figure 7.3b and 7.3c show the

lattice fringes corresponding to (111) and (200) planes having inter-planar spacing of 0.26 nm and 0.22 nm, respectively for NbC. The indistinct interface between the NbC (core) and the amorphous carbon layer is attributed to the solid-state diffusion of carbon as shown in figure 7.3b and 7.3c (marked with dotted lines at the periphery of the particle). Figure 7.3d shows the selected area electron diffraction pattern of the area shown in figure 7.3a, indicating nano crystallinity by concentric diffraction spots corresponding to various atomic planes. Furthermore, a narrow particle size distribution was observed having 12 nm as average particle size of as-synthesized sample as shown in figure 7.4 [4].

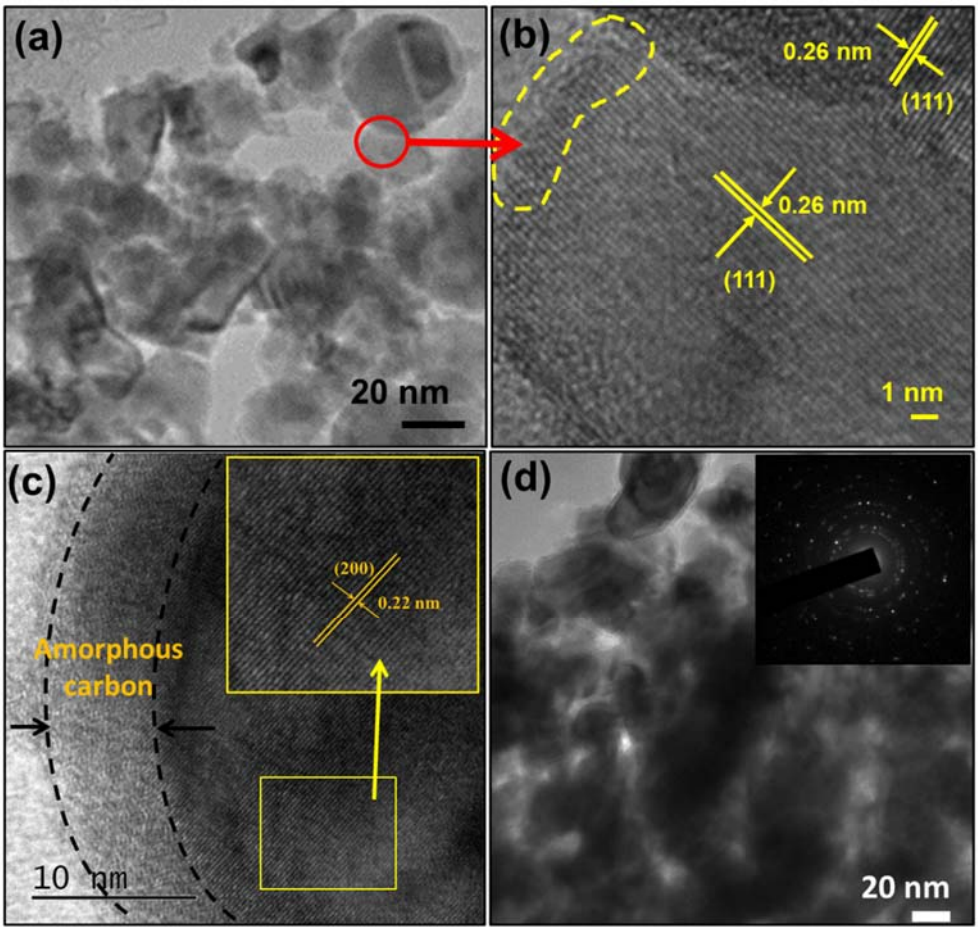

Figure 7.3: (a) TEM micrograph of AC1 showing agglomeration of core shell structure of carbon coated NbC NPs; (b) HR microstructure of marked circle in (a) showing inter-planar spacing of plane (111) of NbC, (c) HR micrograph of NbC NP showing carbon coating (marked with black dotted region) on NbC particle and inset shows the lattice fringes corresponding to (200) plane; (d) Selected area electron diffraction pattern of agglomerated NbC NPs depicting poly-crystallinity.

Further, to observe the distribution of Nb, C and O in the synthesized NbC NPs (AC1), elemental profile was also carried out as shown in figure 7.5 in which distribution of carbon is nearly same as carbon is also present as amorphous network. While,

concentration of oxygen is relatively low throughout the particle confirming the presence of oxygen centers in the NbC nanoparticle resulting NbO_x or NbC_xO_y.

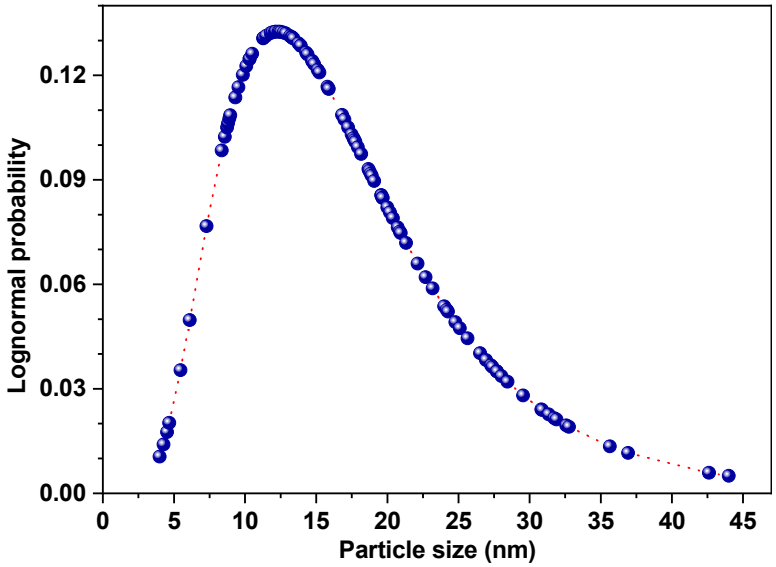

Figure 7.4: Log normal distribution of particles of carbon coated NbC nanoparticles.

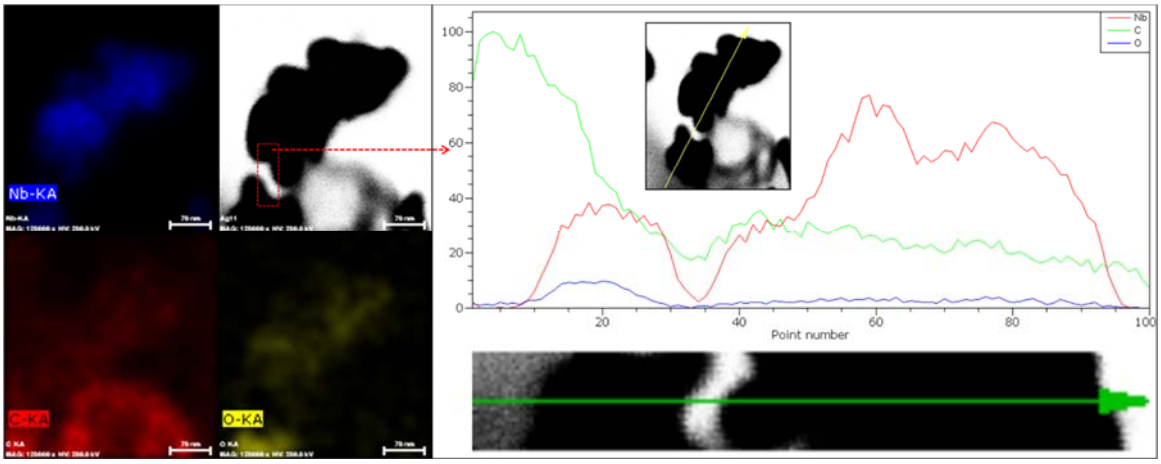

Figure 7.5: Elemental line profile of NbC nanoparticle (AC1) showing the concentration profile (Nb, C and O) across the shown nanoparticles (marked with green arrow). Elemental line profile suggests the homogenous distribution of oxygen inside the NbC nanoparticles while, smaller agglomerate contain higher O content than larger agglomerate.

Elemental line profile (STEM) was also taken to observe the linear distribution of each elements from periphery to core which is also shown in figure 7.5. Extreme left region of line profile shows the higher C content on the left side of nanoparticle which may be associated to the amorphous carbon network. On the nanoparticle region marked by arrow (green colored), increase in the concentration of Nb (red) and C (green) is more as compared to O (blue) confirming the presence of oxygen centers in NbC nanoparticles. Such concentration profile of Nb and O throughout the nanoparticle suggest the presence of multiple oxidation states of Nb corresponding to NbC and NbC_xO_y (NbO_x centers).

7.5. BET analysis:

Surface area analysis: BET specific surface areas (SSA) were calculated from adsorption-desorption curves using N_2 gas for the samples synthesized at 800 °C as shown in figure 7.6. BET analysis suggests the highest SSA of 506 m^2/g with 0.3697 cm^3/g pore volume for AC1 while, the presence of oxide and Nb metal with NbC in other samples induced the reduction in SSA and pore volume as shown in the inset of figure 7.56 also observed by Gupta *et al.* [4]. Such variation of SSA and pore volume of synthesized samples might have occurred due to evolution of CO or CO_2 as a result of in situ reduction and carburization of niobium oxide by encapsulated carbon. Further, pore size distribution suggested the contribution of high surface area and mesopores of as-synthesized samples as shown in figure 7.6.

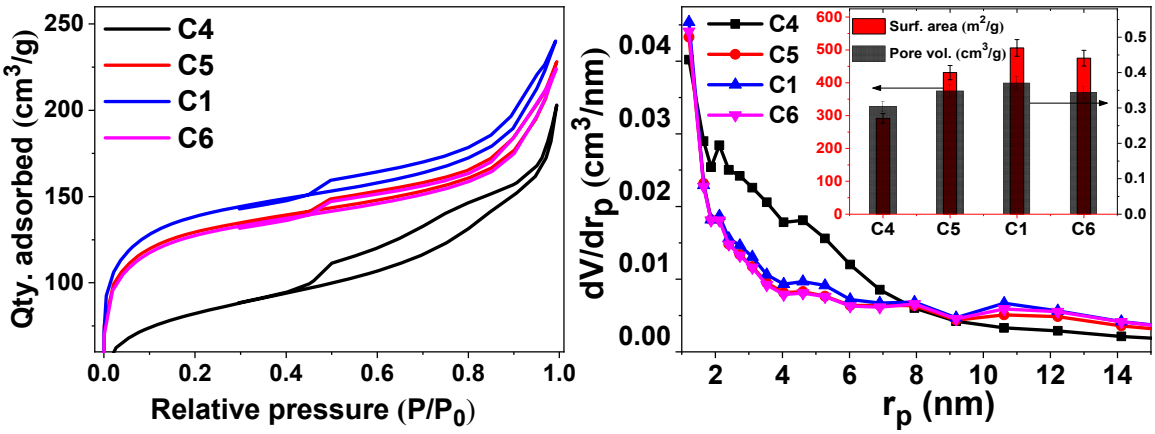

Figure 7.6: BET analysis of all the samples synthesized at 800 °C.

7.6. X-ray photoelectron spectroscopy (XPS):

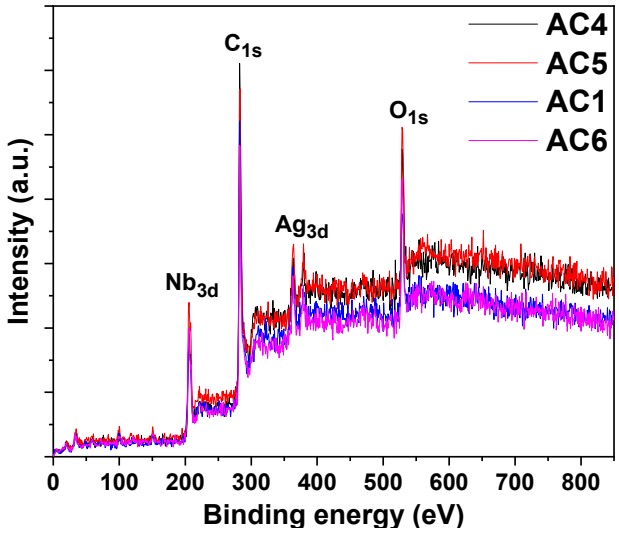

Figure 7.7: XPS survey spectra of all the samples synthesized at 800 °C.

XPS analysis of all the samples synthesized at 800 °C was carried out to understand the surface chemical variations (valence states) that reactants undergo during reduction and

carburization processes. The survey spectrum confirms the presence of Nb, C and O on the surface of as-synthesized samples which is shown in figure 7.7. High resolution XPS (HR-XPS) spectra of Nb3d, C1s and O1s transitions are shown in figure 7.8-7.10 (respectively) in which different chemical states of Nb, C, and O have been illustrated. Peak positions and relative contents of all the elements in various valence states have been listed in table 7.3.

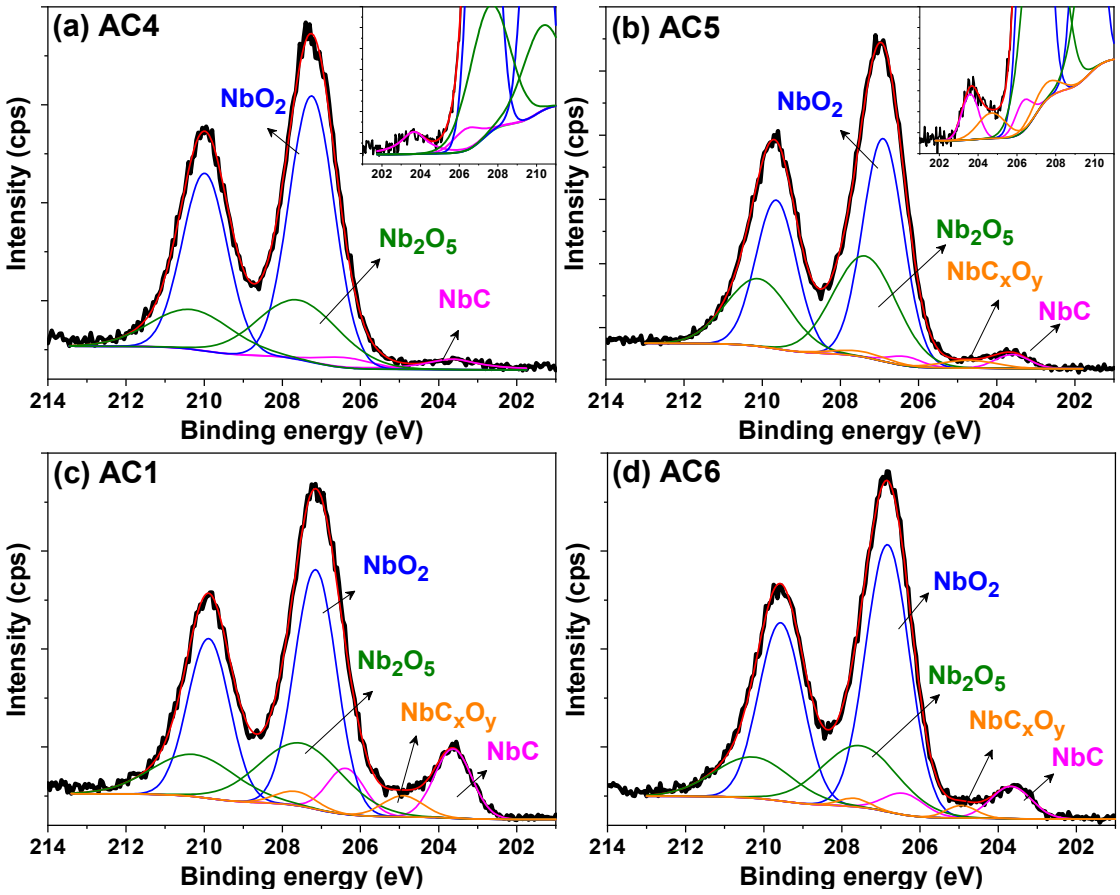

Figure 7.8: HR-XPS spectra of Nb3d for all the samples synthesized at 800 °C (a) AC4; (b) AC5; (c) AC1 and (d) AC6.

Figure 7.8 revealed the presence of multiple oxidation states of Nb associated to different compounds (NbC, NbC_xO_y, NbO_2 and Nb_2O_5) even after obtaining single phase XRD pattern of AC1 as shown in figure 7.2a. Such HR-XPS spectra of single phase NbC (AC1) suggests the generation of different ionic states of Nb during the reduction-carburization process. Variation in the holding time at 800 °C, led to change the chemical composition of samples (suggested by XRD results) which can also be observed in XPS results as shown in figure 7.8b-d. Volume fraction (VF) of different phase present on the surface has also been calculated by deconvoluting the XPS spectrum and listed in table 7.3. Further, the increment in the holding time has led to enhanced carburization up to 10 h as VF of NbC has increased (4.66% to 13.72%) and decreased in AC6 (7.17%) supporting the XRD results. VF of Nb^{4+} (NbO_2) and Nb^{5+} (Nb_2O_5) has increased (AC5; 94.45% and AC6;

90.74%) as the holding time was shifted from 10 h (81.72%). Moreover, binding energy associated to NbC_xO_y (~204.8 eV) was not observed in AC4. HR-XPS data for Nb3d suggest that direct conversion of Nb_2O_5 to NbC involved reduction and carburization simultaneously which was responsible for the multiple transitions of oxidation states of Nb in the lattice as earlier discussed for XRD analyses.

Table 7.3: Results obtained from HR-XPS spectra of Nb3d, C1s and O1s of AC1-AC6.

Group	AC4		AC5		AC1		AC6		
	B.E. (eV)	Volume (%)	B.E. (eV)	Volume (%)	B.E. (eV)	Volume (%)	B.E. (eV)	Volume (%)	
NbC	203.6 206.4	4.66	203.6 206.3	2.90	203.6 206.4	13.72	203.6 206.4	7.17	5–7
NbC_xO_y	-	-	204.7 207.4	2.65	204.9 207.6	4.54	204.9 207.6	2.09	
NbO_2	207.2 209.9	67.84	206.9 209.6	55.32	207.1 209.8	53.44	206.8 209.5	64.58	
Nb_2O_5	207.6 210.3	27.50	207.3 210.1	39.13	207.5 210.2	28.28	207.5 210.3	26.16	
C-Nb	282.8	2.15	282.8	2.91	282.8	3.35	282.7	3.44	7,8
C sp^2	284.4	56.10	284.4	54.10	284.4	59.39	284.4	51.60	5,9
C sp^3	285.0	18.72	285.0	23.57	285.1	18.99	284.9	25.84	9,10
C-OH	286.0	12.99	286.4	4.50	286.3	7.72	286.4	7.80	
COOH	288.2	5.49	288.0	10.22	288.2	5.51	288.3	4.83	
π-π*	290.2	4.57	289.7	4.70	290.1	5.01	290.4	6.49	
Nb_2O_5	530.4	53.79	529.9	42.49	530.2	53.68	529.9	49.48	11
OH/O_v	531.8	25.35	531.3	39.85	531.6	32.23	531.3	24.24	12
H_2O/C=O	532.8	20.87	532.5	17.67	532.8	14.07	532.3	26.28	13

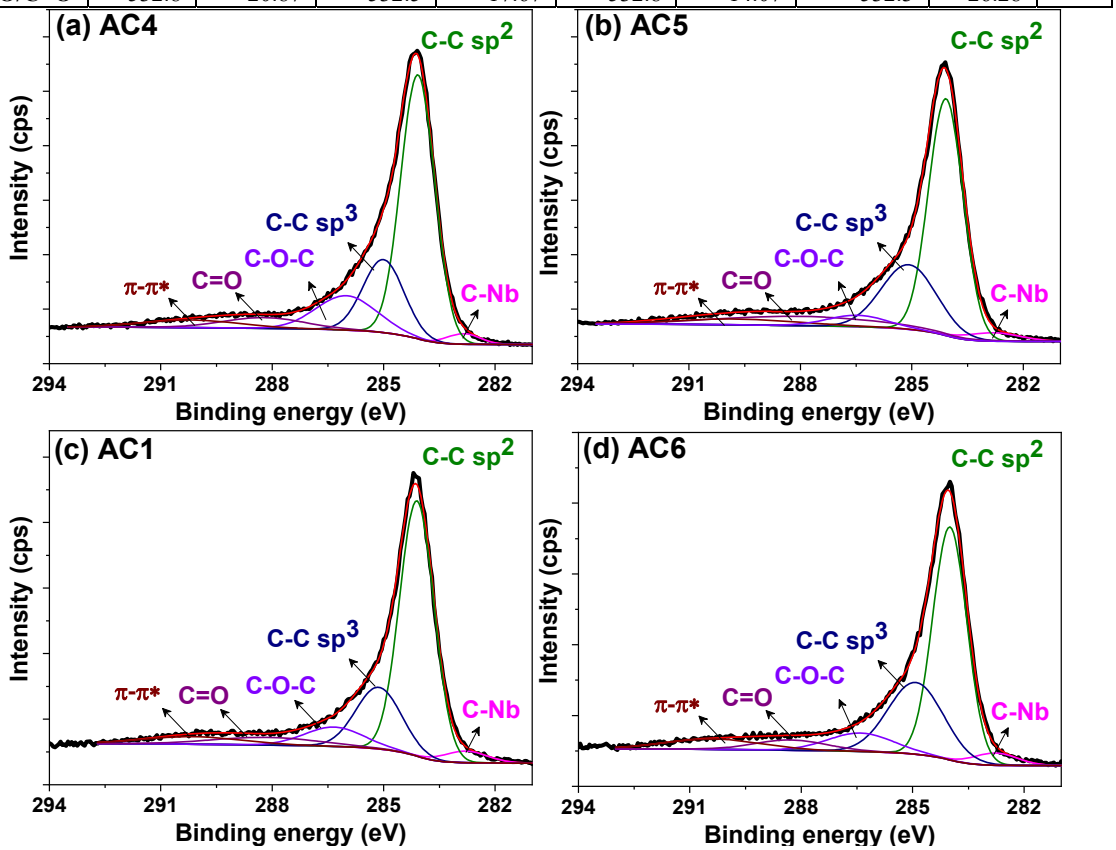

Figure 7.9: HR-XPS spectra of C1s for all the samples synthesized at 800 °C (a) AC4; (b) AC5; (c) AC1 and (d) AC6.

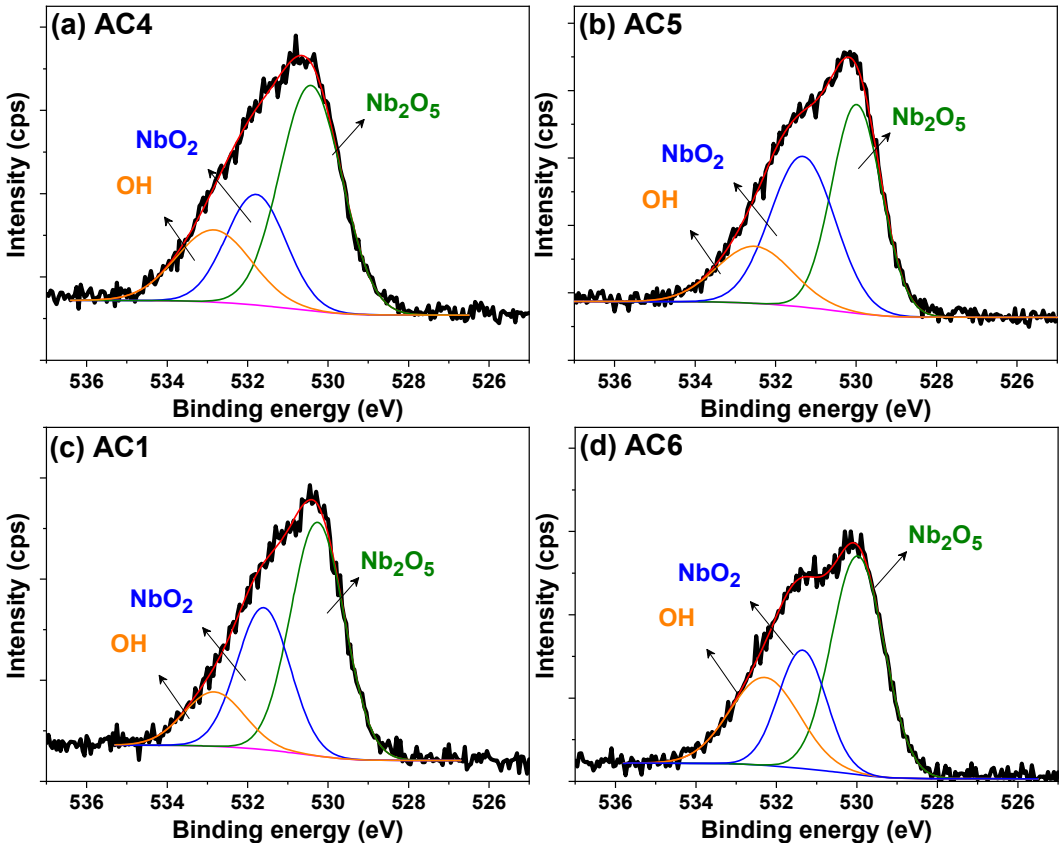

Figure 7.10: HR-XPS spectra of O1s for all the samples synthesized at 800 °C (a) AC4; (b) AC5; (c) AC1 and (d) AC6.

The HR-XPS spectrum of C1s as shown in figure 7.9 revealed the presence of peaks associated with NbC, C-C sp^2 and C-C sp^3 bonds in all the samples at 282.8, 284.4 and 285.1 eV, respectively [5,8–10,14]. Further, peaks observed around 286.4, 288.1 and 290.1 eV might be associated to hydroxyl, carbonyl groups and $\pi \rightarrow \pi^*$ transitions, respectively [9,10]. HR-XPS spectra of O1s (figure 7.10) suggested the presence of oxygen associated to Nb_2O_5 at 530.4 eV. While, the peaks around 531.6 and 532.5 eV may be associated to hydroxyl group/carbonate species/oxygen vacancies (O_v) and adsorbed water/carbonyl (C=O) group, respectively [11,13].

7.7. Synthesis mechanism

Normally NbC is synthesized at >1000 °C [12,15,16] which is higher as compared to the present work. The transition of Nb_2O_5 to NbC at relatively low temperature (800 °C) in a high pressure closed chamber is a temperature driven transition. The mixture of reactants contains Mg and charcoal, which act as reducing agents providing MgO, CO and CO_2 as byproducts. The gaseous byproducts (CO and CO_2) of the reactions lead to increase the pressure inside the autoclave. Various chemical reactions occurring inside the autoclave has been considered and described below:

All the possible chemical reactions are categorized into two categories; (i) reduction and (ii) carburization. Reactions (7.1–7.24) represents the reduction of Nb_2O_5 forming NbO_2, NbO and (NbO_2+NbO) mixture in the presence of reducing agents (Mg and C) and their mixture.

$$Nb_2O_5 + Mg \rightarrow 2NbO_2 + MgO \quad (7.1)$$
$$Nb_2O_5 + C \rightarrow 2NbO_2 + CO \quad (7.2)$$
$$Nb_2O_5 + CO \rightarrow 2NbO_2 + CO_2 \quad (7.3)$$
$$2Nb_2O_5 + C \rightarrow 4NbO_2 + CO_2 \quad (7.4)$$
$$2Nb_2O_5 + C + Mg \rightarrow 4NbO_2 + MgO + CO \quad (7.5)$$
$$3Nb_2O_5 + C + Mg \rightarrow 6NbO_2 + MgO + CO_2 \quad (7.6)$$
$$2Nb_2O_5 + CO + Mg \rightarrow 4NbO_2 + MgO + CO_2 \quad (7.7)$$
$$4Nb_2O_5 + C + CO + Mg \rightarrow 8NbO_2 + MgO + 2CO_2 \quad (7.8)$$
$$Nb_2O_5 + 3Mg \rightarrow 2NbO + 3MgO \quad (7.9)$$
$$Nb_2O_5 + 3C \rightarrow 2NbO + 3CO \quad (7.10)$$
$$Nb_2O_5 + 3CO \rightarrow 2NbO + 3CO_2 \quad (7.11)$$
$$2Nb_2O_5 + 3C \rightarrow 4NbO + 3CO_2 \quad (7.12)$$
$$Nb_2O_5 + C + 2Mg \rightarrow 2NbO + 2MgO + CO \quad (7.13)$$
$$Nb_2O_5 + C + Mg \rightarrow 2NbO + MgO + CO_2 \quad (7.14)$$
$$Nb_2O_5 + CO + 2Mg \rightarrow 2NbO + 2MgO + CO_2 \quad (7.15)$$
$$2Nb_2O_5 + C + 2CO + 2Mg \rightarrow 4NbO + 2MgO + 2CO_2 \quad (7.16)$$
$$Nb_2O_5 + 2Mg \rightarrow NbO_2 + NbO + 2MgO \quad (7.17)$$
$$Nb_2O_5 + 2C \rightarrow NbO_2 + NbO + 2CO \quad (7.18)$$
$$Nb_2O_5 + 2CO \rightarrow NbO_2 + NbO + 2CO_2 \quad (7.19)$$
$$Nb_2O_5 + C \rightarrow NbO_2 + NbO + CO_2 \quad (7.20)$$
$$Nb_2O_5 + C + Mg \rightarrow NbO_2 + NbO + MgO + CO \quad (7.21)$$
$$2Nb_2O_5 + C + Mg \rightarrow 2NbO_2 + 2NbO + 2MgO + CO_2 \quad (7.22)$$
$$Nb_2O_5 + CO + Mg \rightarrow NbO_2 + NbO + MgO + CO_2 \quad (7.23)$$
$$2Nb_2O_5 + C + 2CO + Mg \rightarrow NbO_2 + 3NbO + MgO + 3CO_2 \quad (7.24)$$
$$NbO_2 + C + 2Mg \rightarrow NbC + 2MgO \quad (7.25)$$
$$NbO_2 + 2C + Mg \rightarrow NbC + MgO + CO \quad (7.26)$$
$$2NbO_2 + 3C + 2Mg \rightarrow 2NbC + 2MgO + CO_2 \quad (7.27)$$
$$2NbO_2 + 4C + Mg \rightarrow 2NbC + MgO + CO + CO_2 \quad (7.28)$$
$$NbO_2 + 2CO + 2Mg \rightarrow NbC + 2MgO + CO_2 \quad (7.29)$$
$$NbO_2 + C + CO + Mg \rightarrow NbC + MgO + CO_2 \quad (7.30)$$
$$NbO + C + Mg \rightarrow NbC + MgO \quad (7.31)$$
$$2NbO + 3C + Mg \rightarrow 2NbC + MgO + CO \quad (7.32)$$
$$4NbO + 6C + Mg \rightarrow 4NbC + MgO + CO + CO_2 \quad (7.33)$$
$$NbO + 2CO + Mg \rightarrow NbC + MgO + CO_2 \quad (7.34)$$
$$2NbO + 2C + CO + Mg \rightarrow 2NbC + MgO + CO_2 \quad (7.35)$$
$$3NbO + 4C + Mg \rightarrow 3NbC + MgO + CO_2 \quad (7.36)$$
$$NbO_2 + NbO + 2C + 3Mg \rightarrow 2NbC + 3MgO \quad (7.37)$$
$$NbO_2 + NbO + 3C + 2Mg \rightarrow 2NbC + 2MgO + CO \quad (7.38)$$

$$NbO_2 + NbO + 3C + Mg \rightarrow 2NbC + MgO + CO_2 \quad (7.39)$$

$$NbO_2 + 2NbO + 5C + Mg \rightarrow 3NbC + MgO + CO + CO_2 \quad (7.40)$$

$$NbO_2 + NbO + 4CO + 3Mg \rightarrow 2NbC + 3MgO + 2CO_2 \quad (7.41)$$

$$NbO_2 + NbO + 2C + CO + 2Mg \rightarrow 2NbC + 2MgO + CO_2 \quad (7.42)$$

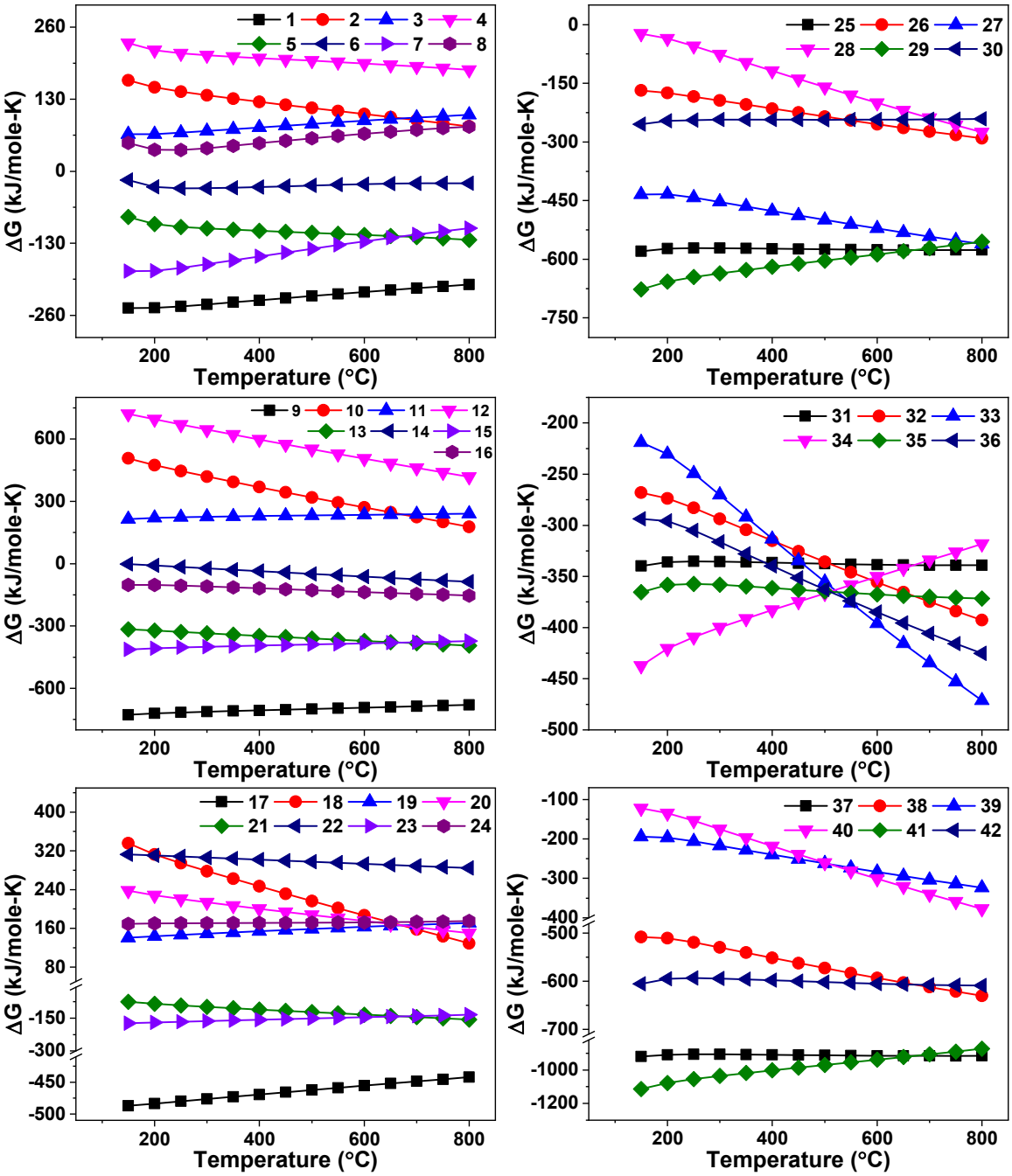

Figure 7.11: Feasibility and non-feasibility of possible reaction paths to form NbC from Nb_2O_5 via multi-step route.

For the reduction and carburization of Nb_2O_5, the values of ΔG at standard pressure corresponding to the above chemical reactions were estimated by

$$\Delta G_T = \Delta H_0 + \int_{T_0}^{T} C_P dT - T\left[\Delta S_0 + \int_{T_0}^{T} \frac{C_P}{T} dT\right], \quad (7.43)$$
$$C_p = \Delta a + \Delta b.\Delta T + \Delta c.\Delta T^{-2}$$

where, (Δa, Δb, Δc), ΔH_0 and ΔS_0 are the difference of the coefficient of heat capacities, enthalpy and entropy at 298 K of products and reactants, respectively. The negative values of Gibbs free energy (ΔG) for the above-mentioned reactions convey the feasibility of the reaction as shown in figure 7.11. All the reduction reactions suggested that Mg (alone) reduced Nb_2O_5 more efficiently to obtain NbO_2, NbO and (NbO_2+NbO) mixture as compared to C and (C+Mg) mixture as represented by reaction (7.1, 7.9, 7.17) in figure 7.11. Further, C and CO (in the presence of Mg) reduced Nb_2O_5 equivalently to obtain similar products as reaction (7.5, 7.13, 7.21) and (7.7, 7.15, 7.23), respectively, which are shown in figure 7.11. Rest of the other reduction reactions are non-feasible due to their positive ΔG suggesting that individually C and CO (in the absence of Mg) are not capable enough to reduce Nb_2O_5.

As a result of reduction reaction, feasibility of the formation of NbO is higher than that of NbO_2 (more negative ΔG of reaction 7.9, 7.17 than 7.1) which is also supported by the XRD pattern of A3. Further, the formation of NbC can be obtained via in-situ reduction carburization of oxide products (NbO_2 and NbO) as Nb metal was not obtained in any of the synthesized sample (as shown in figure 7.2). In the similar pattern, reaction (7.25-7.42) represent the possible chemical reactions for the formation of NbC from NbO_2, NbO and (NbO_2+NbO) mixture, all are feasible with negative ΔG values. Unlike reduction reactions, reduction-carburization of NbO_2 and NbO follow different paths as shown in figure 7.10 by reaction (7.25-7.30) and (7.31-7.36), respectively. While, reduction-carburization of (NbO_2+NbO) mixture is represented by reaction (7.37-7.42) which are more spontaneous than previous chemical reactions (7.25-7.36) with high difference of ΔG values. As single phase NbC was obtained at 800 °C, reduction-carburization reactions follow the following order according to ΔG at 800 °C; 7.37 > 7.41 > 7.38 > 7.42 > 7.25 > 7.27 > 7.29 > 7.33 > 7.36 > 7.32 > 7.40 > 7.35 > 7.31 > 7.39 > 7.34 > 7.26 > 7.28 > 7.30.

Thermodynamically higher feasibility of the formation of NbO_2+NbO mixture is also evidenced in the XRD pattern (figure 7.2a) of AC3 where NbO (major) + NbO_2 (minor) were obtained at 600 °C. This is further converted to NbC (major) + NbO_2 (minor) at 700 °C and NbC at 800 °C. In this sequence, charcoal encapsulated NbO particles which is followed by reduction-carburization reactions. As a result, CO and CO_2 gases are evolved through coated carbon resulting to porous particles. Moreover, the transition ($Nb_2O_5 \rightarrow NbO_2 \rightarrow NbO \rightarrow NbC$) leads to more evolution of gases, which enhances the porosity on the particle surfaces, which is demonstrated in figure 7.12.

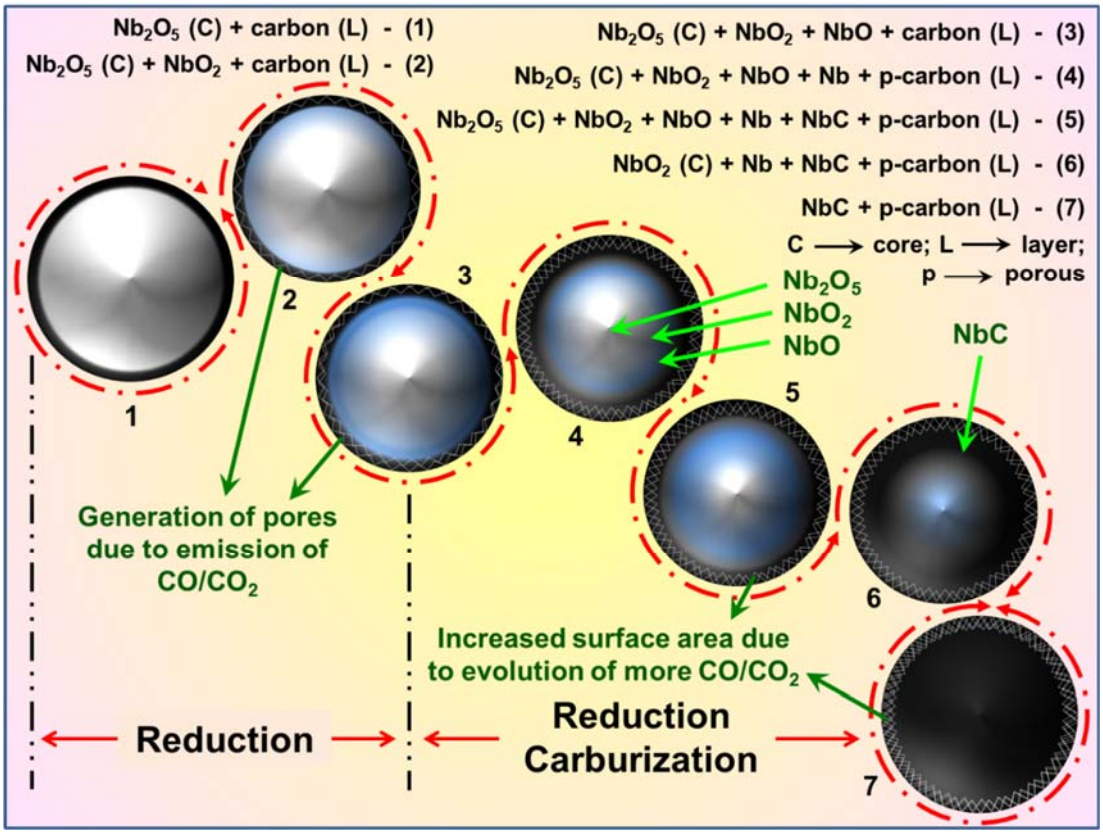

Figure 7.12: Reaction mechanism of the formation of NbC using charcoal as carbon source with Nb_2O_5.

7.8. Raman spectroscopy:

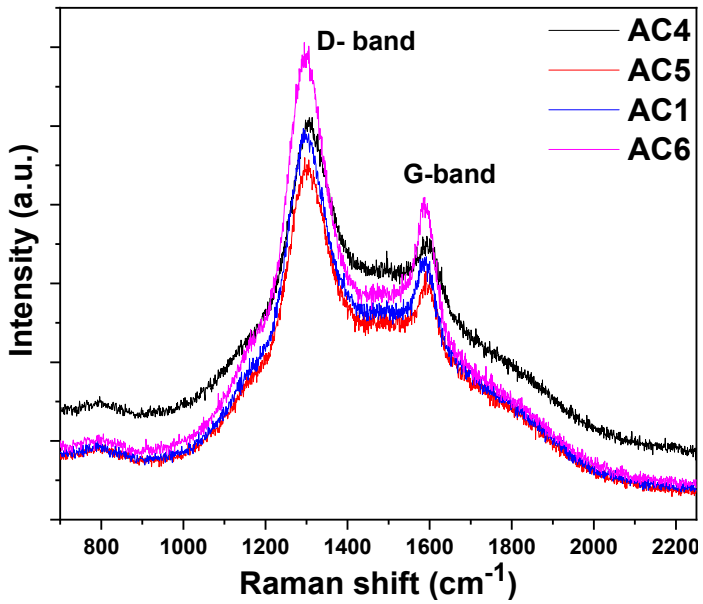

Figure 7.13: Raman spectra depicting the presence of D- and G- band in AC4, AC5, AC1 and AC6.

Raman spectroscopy was used to analyze the nature of carbon in AC1 and AC4. figure 7.13 shows the Raman spectra with two characteristic bands corresponding to disordered (D- band) and graphitic carbon (G- band) near 1282.1 nm^{-1} and 1589.8 nm^{-1}

respectively. Ferrari and Robertson [17] suggested that the disordered scattering and bond stretching of sp^2 carbon atoms contribute to the formation of D- and G- band respectively. The position of the G- band near to 1600 nm^{-1} suggests nano-crystalline graphite. The observed higher intensity of the D- band than the G- band in these samples depicts the amorphous nature of carbon as has also been observed from TEM analysis.

7.9. Absorbance and photoluminescence (PL) spectroscopy:

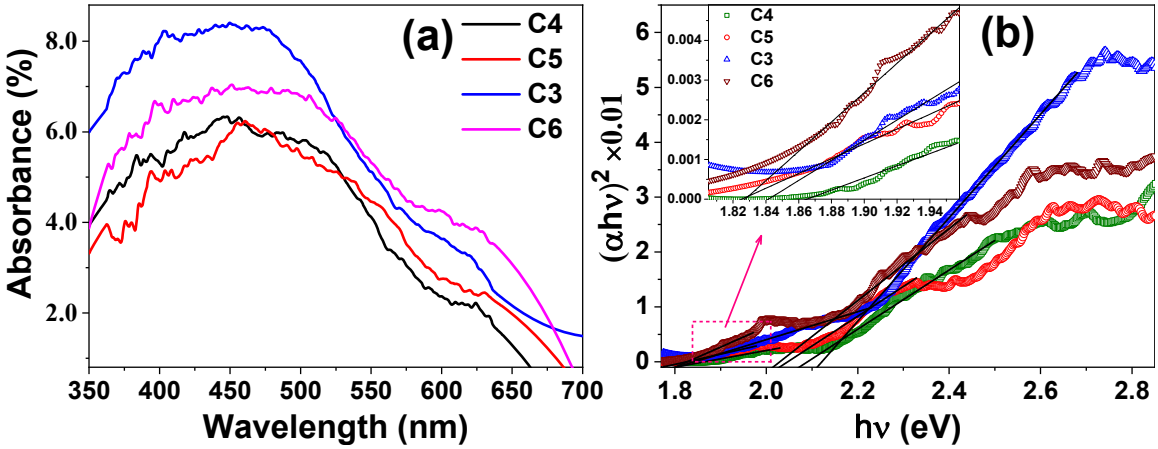

Figure 7.14: (a) UV-visible absorption spectra and (b) Tauc plot depicting dual bandgap corresponding to dual absorbance of all the samples synthesized at 800 °C.

Figure 7.14a shows the UV-visible absorption spectra of all the samples synthesized at 800 °C suggesting broad multiple absorption humps in the visible region, which may be associated with the presence of either oxide centers (NbO_2 and Nb_2O_5) or continuous carbon network (highly disordered graphic carbon) in the nanocomposite powder samples [18–20].

The values of band gap were calculated by extrapolating the linear portion of the $(\alpha h\nu)^2$ vs. hν curve as shown in figure 7.14b. The absorption observed at 600-650 nm and 550 nm might be associated to the presence of disordered carbon [20] and Nb-O centers [19], respectively. Table 7.4 shows the band gaps (~1.8 eV & ~2.1 eV) of as-synthesized samples depicting the absorption in the visible region of the E-M spectrum, which makes them suitable materials for studying their photocatalytic behavior under visible irradiation.

Table 7.4: Band gap of the samples synthesized at 800 °C.

Sample label	Band gap (eV)	
AC4	1.86	2.09
AC5	1.82	2.05
AC1	1.84	2.12
AC6	1.82	2.02

Moreover, to observe the photoemission characteristics of the synthesized samples photoluminescence (PL) spectroscopy was conducted, which is shown in figure 7.15. A

broad emission spectrum in the visible region was observed for all the samples, which is associated with disordered carbon (observed in Raman and XPS analysis) and other functional groups present in the powder samples. Photoemission decreases as the amount of lattice carbon increases and lattice distortion decreases from a holding time of 5 h (AC4) to 10 h (AC1).

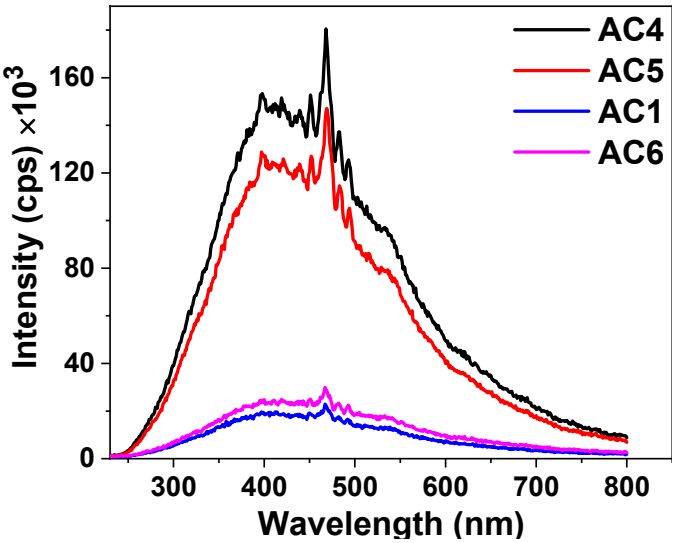

Figure 7.15: Photoluminescence spectra of all the samples synthesized at 800 °C.

For 11 h of holding time (AC6) more intense photoemission is observed as compared to AC1. This is because of the presence of some functional groups, which reduce the efficiency of non-radiative decay. The XPS spectra showed the energy corresponding to $\pi \rightarrow \pi^*$ transition which also promotes the photoluminescence quenching as observed in figure 7.14 which is in good agreement with its volume fraction on the surface of different photo catalysts (AC4 and AC5) [21]. Moreover, the presence of NbC_xO_y on the surface also promotes the photoluminescence quenching.

7.10. Photocatalysis study:

Figure 7.16a represents the adsorption of MB molecule during the establishment of adsorption-desorption equilibrium in which adsorption of dye follows the similar trend as observed in BET surface area analysis. The controlled experiments showed that ~2.8% decolorization of dye (without catalyst) was observed in a dark chamber. Moreover, 3.2% photo bleaching was observed under visible irradiation without photocatalyst which is negligible as shown in figure 7.16b. The experiments under visible irradiation with the as synthesized photo catalysts showed decolorization/degradation as a function of exposure time for the derivatives of MB, respectively as shown in figure 7.16b.

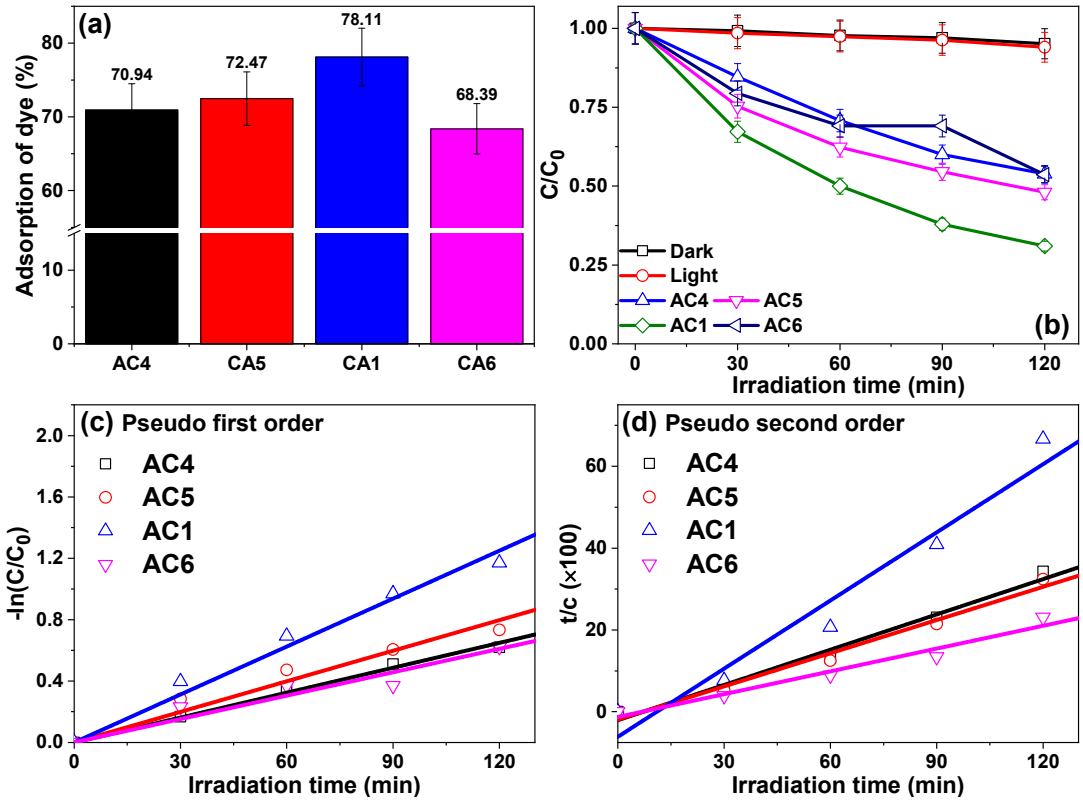

Figure 7.16: (a) Adsorption of MB dye during the establishment of adsorption-desorption equilibrium; (b) Relative change in concentration of MB dye under visible illumination; (c) Pseudo first order kinetics; and (d) Pseudo second order kinetics of MB degradation.

Moreover, it can also be observed that AC1 exhibited 68.9% efficiency under visible illumination for 2.0 h which is quite better than other samples (AC4, AC5 and AC6). The presence of oxides in the samples may affect the generation of excitons and their transfer towards the surface. Sample AC4 shows the least photocatalytic activity while minor content of oxides in AC5 and AC6 resulted in better activity than AC4.

The decolorization/degradation kinetics of photocatalytic reactions were studied with the help of pseudo first and second order law. Plot of '$-\ln(C/C_0)$ vs. t' and 't/C vs. t' represent pseudo first order kinetics (figure 7.16c) and pseudo second order kinetics (figure 7.16d), respectively. The respective reaction rate constants (K_1 and K_2; h^{-1}) and regression coefficients (R^2) have been listed in table 7.5, which illustrated that AC1 has the highest photochemical reaction rate constants (K_1) of 0.6246 h^{-1} following pseudo first order kinetics. Moreover, based on quality of fitting (R^2), it can be suggested that AC1 and AC6 followed pseudo first order kinetics while, AC4 and AC5 followed second order kinetic (table 7.5). Similar trend has also been observed by Yang *et al.* [22] and Younis *et al.* [23] for photoelectron reduction of Cr^{4+} on MoS_2@TiO_2 nanotubes and photodegradation activity of undoped and doped CeO_2 nanocrystals.

Table 7.5: Details of photochemical reaction kinetics of MB dye.

Concentration (mg/L)		Catalyst	Efficiency (%)	Rate constant K (h^{-1})	R^2
Dye	Catalyst				
1.0	20.0	AC4	46.15	0.3246	0.99
1.0	20.0	AC5	51.91	0.3984	0.98
1.0	20.0	AC1	68.96	0.6246	0.99
1.0	20.0	AC6	46.39	0.3048	0.97

The observed diminishing absorption patterns may be associated with the interaction of excitons with different reactive oxygen species (ROS) such as hydroxyl radicals ($OH^{\cdot}$) and superoxide anion radicals ($O_2^{\cdot-}$). With the help of mass spectrometry, it can be illustrated that the decreasing absorption spectra were attributed to the degradation of dye molecules to lighter organic molecules which are shown in figure 7.17 and 7.18 as lower m/z molecules along with the parent molecule.

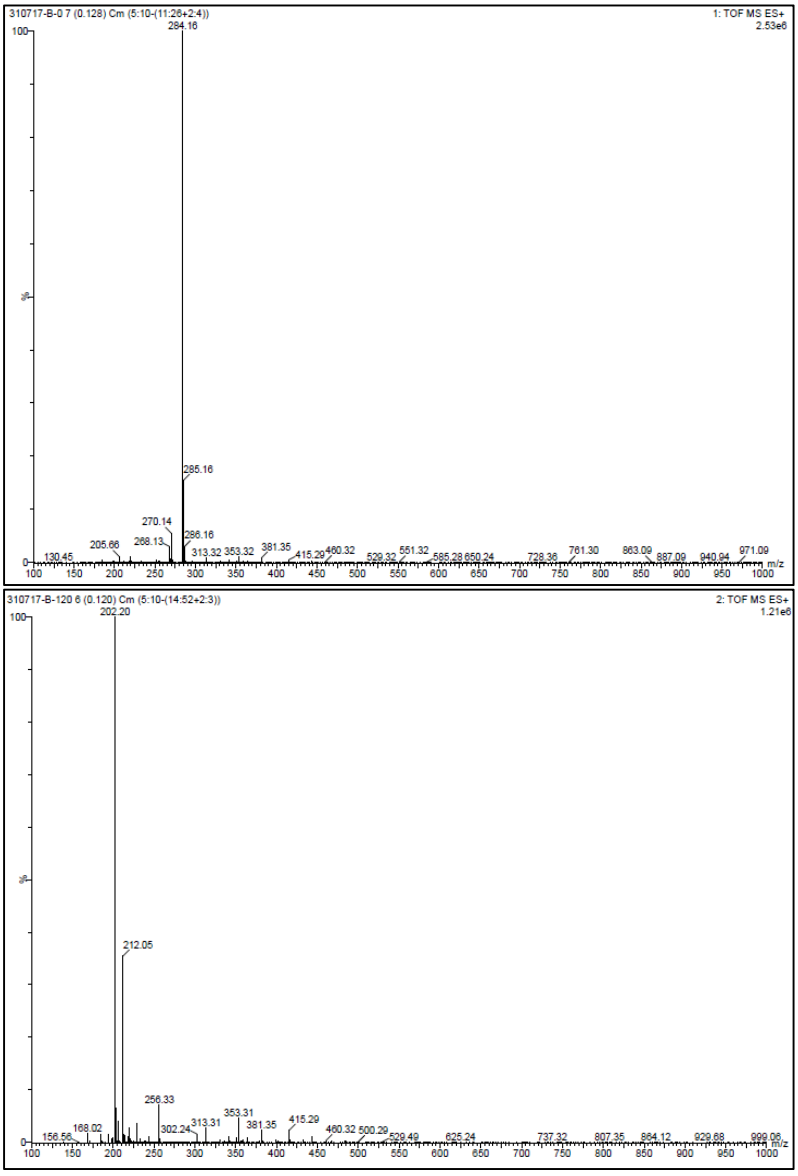

Figure 7.17: Mass spectrometric results of methylene blue (MB) before and after the visible irradiation for 2.0 h using AC1 as photocatalyst.

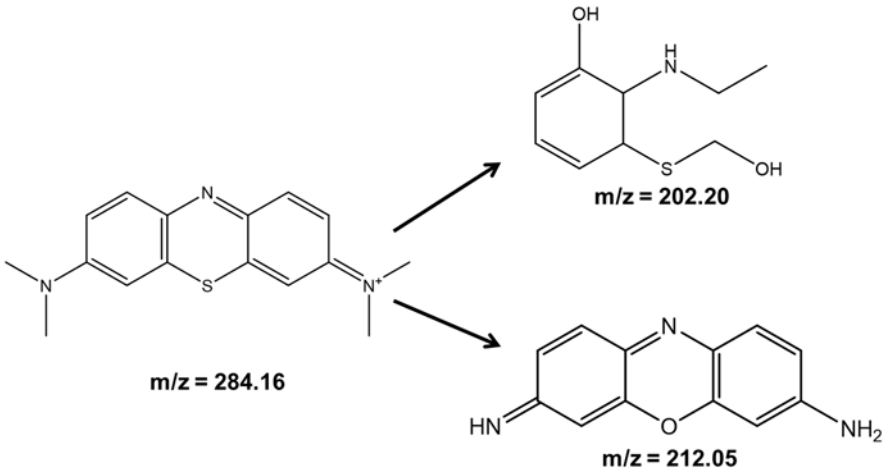

Figure 7.18: Probable degraded products for MB dye after exposer of 120 min.

To ascertain the results obtained from absorption spectra and MS analysis, TOC was carried out to check the decrease of concentration of organic carbon. In association with the MS results, 30.18% reductions were observed for concentrations of organic carbon irradiation in MB dye solution with AC1 after 120 min as shown in figure 7.19a. These results demonstrate the partial degradation of parent dye molecules due to the presence of some organic carbon in the form of aromatic rings which can be asserted that the decolorization (absorption study) rate was faster than the degradation (MS and TOC study) rate of dye molecules.

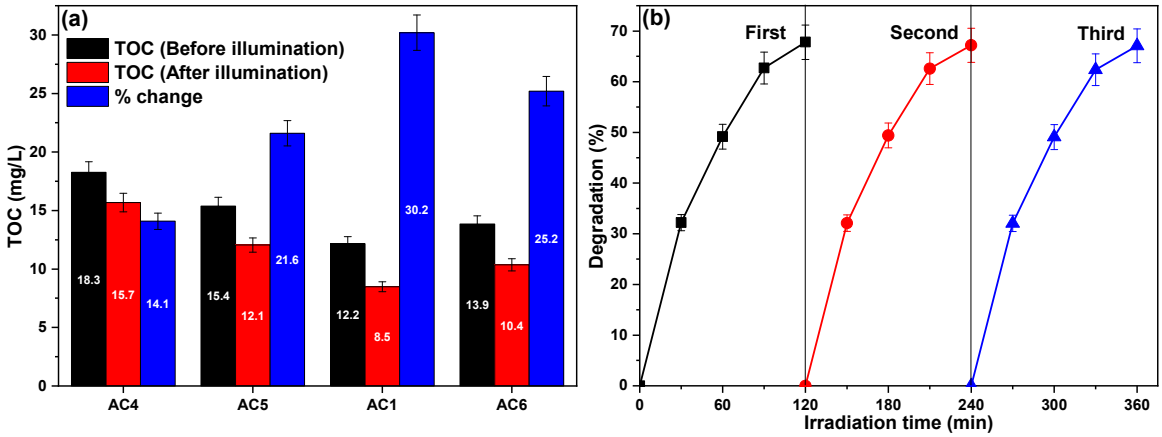

Figure 7.19: (a) Total organic carbon (TOC) of MB dye with AC1 before and after the 120 min visible irradiation; (b) Reusability of AC1 as photocatalyst under visible irradiation.

The photocatalytic activity of the synthesized samples was increased with increasing holding time at 800 °C up to 10 h, which again was decreased at 11 h. As observed from XRD analysis, carbon content in the lattice of NbC has increased from 0.79 (AC4) to 0.959 (AC1) resulting in less distorted crystallites which is further decreased at longer holding time (11 h) with higher distortion as discussed in the W-H analysis.

Moreover, a similar trend was also observed from BET analysis where SSA was increased from 292 m^2/g (AC4) to 506 m^2/g (AC1) and then decreased to 475 m^2/g (AC6). Further, PL spectroscopy data show that recombination decreases with the decreased impurities in the synthesized samples resulting in better degradation of dye with AC1 than other samples. Further, the reusability of the nanocomposite photocatalyst is a significant parameter which maneuvers the practical usefulness of photocatalyst. To observe the reusability and stability of as-prepared C coated NbC NPs, recycle reactions were carried out for the degradation of MB dye over AC1 as shown in figure 7.19b. To observe the recyclability of as prepared photocatalyst, previously used photo catalysts (AC1) were removed from the solution by centrifugation and then reused for the photodegradation of all the dyes with the same concentration of the solution and irradiation intensity. The excellent stability of photocatalyst (AC1) is well-illustrated from the XRD pattern of AC1 after the 3rd cycle of photodegradation reaction as shown in figure 7.20a. These results suggest sufficient stability of the photocatalyst during photodegradation of the dyes and can be reused without significant decrease in performance.

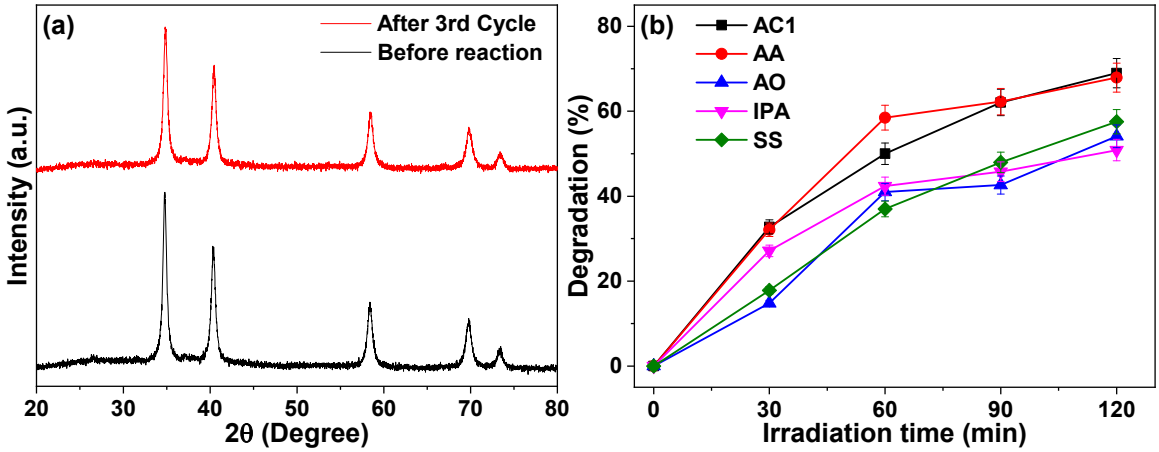

Figure 7.20: (a) XRD pattern of AC1 before and after the photocatalytic reaction; and (b) Effect of various scavengers on the degradation of MB dye with photocatalyst (AC1).

To establish the mechanism responsible for such a good photocatalytic behavior of synthesized photocatalyst, the generation of reactive oxygen species (ROS) has to be confirmed by using e^-, h^+, $OH^{\cdot}$ and O_2^{-} scavengers. As an effect of these scavengers, degradation of MB dye got retarded, which is shown in figure 7.20b. Addition of ascorbic acid (AA) did not alter the photodegradation profile while, all other scavengers (AO, SS and IPA) reduced the efficiency by ~15%. Such decreased efficiency can be associated to the involvement of h^+, e^- and $OH^{\cdot}$ in photochemical reaction.

7.11. Proposed degradation mechanism:

Figure 7.21 illustrates the proposed mechanism responsible for the photocatalytic degradation of MB dye under visible light irradiation. As per the XRD results, it cannot be stated that nanocomposite sample consists of NbC alone, but, presence of O-centers (observed form TEM and XPS analysis) inside the NPs induced the optical active sites generating the charge carriers upon visible exposure. Earlier, Ohgi *et al.* [24] and Ishihara *et al.* [25] also suggested the enhanced generation and transportation of charge carriers by inducing oxygen centers (through partial oxidation) in the carbide nanoparticles. Figure 7.22 shows the valence band XPS spectra of AC1 and AC4 depicting different VB edges of ~1.97 and ~1.71 eV and with the help of optical absorption analysis, the position of the CB can be estimated.

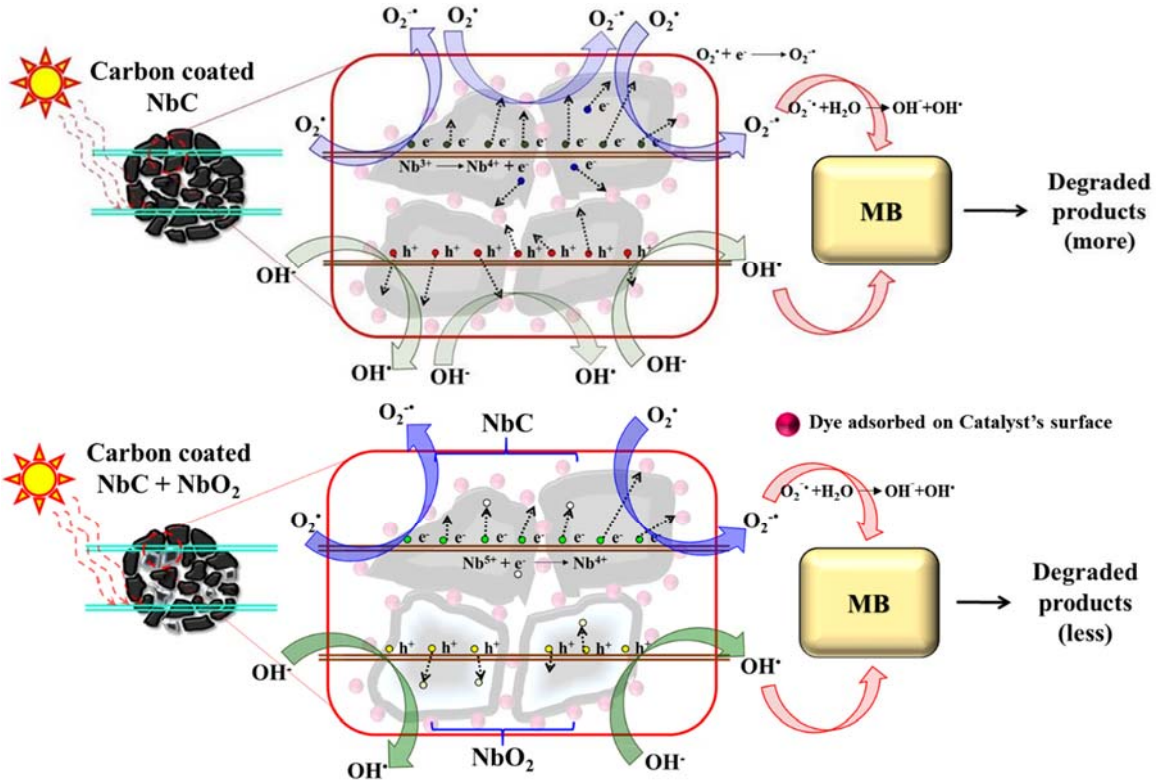

Figure 7.21: Proposed mechanism of photodegradation of MB dye.

The CB edge potential of both the samples (-0.15 eV and -0.38 vs NHE, respectively) are more negative than the standard redox potential of $O_2/O_2^{\cdot-}$ (-0.046 eV vs NHE) to reduce molecular oxygen [26]. Further, VB potential edge of $OH^-/OH^{\cdot}$ (+1.99 eV vs NHE) is lower than VB of photocatalyst [26]. Being metallic in nature, NbC supported the charge transfer towards the surface of NPs where the reaction with the hydroxyl anion and dissolved oxygen in water produces hydroxyl free radicals ($OH^{\cdot}$) and superoxide free radical anions ($O_2^{\cdot-}$), respectively. These reagents are considered as strong oxidizing agents

and thus oxidize the dyes adsorbed on the surface of the NPs. Various reactions, which are responsible for the degradation of dyes and are expressed as follows:

$$NbC + C + h\nu \rightarrow NbC + C + h^+ + e^- \quad (7.44)$$
$$O_2^{\cdot} + e^- \rightarrow O_2^{\cdot -} \quad (7.45)$$
$$O_2^{\cdot -} + H_2O \rightarrow OH^{\cdot} + OH^- \quad (7.46)$$
$$OH^- + h^+ \rightarrow OH^{\cdot} \quad (7.47)$$

For all the samples, degradation efficiency is a function of phase content (NbC, NbC_xO_y and Nb-O), $\pi \rightarrow \pi^*$ transitions and oxygen vacancies present on the surface. Among all of these parameters, the presence of NbC_xO_y and $\pi \rightarrow \pi^*$ governs whole catalytic reaction (as discussed in PL analysis). Moreover, oxygen vacancies promotes the delayed recombination (PL emission peak at 468 nm) which in turn provide more excitons [27]. But excess vacancies can also quench the photocatalytic reaction which might be responsible for the observed reduced photodegradation in AC5 as compared to AC1. While, AC6 possess insufficient vacancies providing lesser degradation efficiency than AC1.

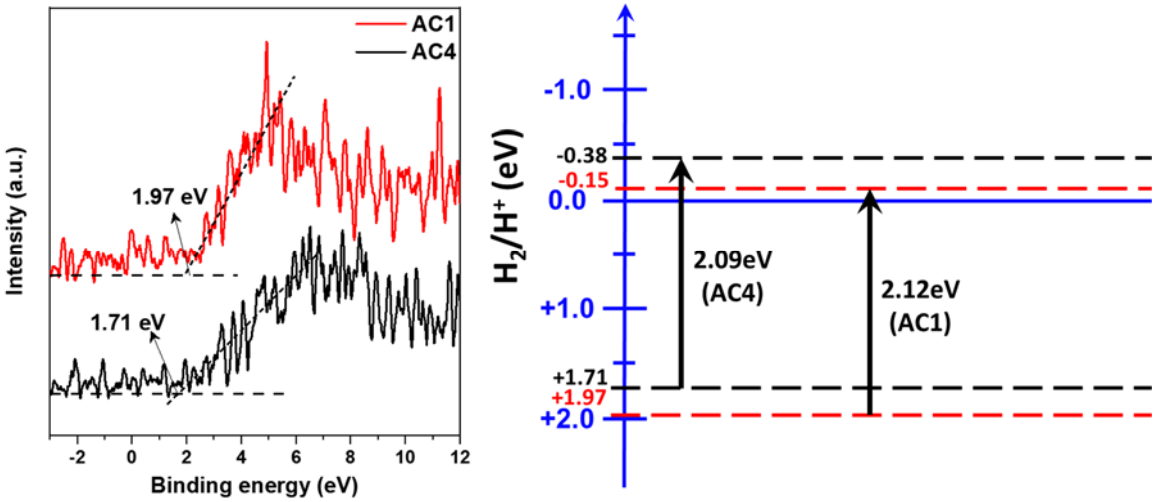

Figure 7.22: Valence band spectra of AC4 and AC1 along with the estimated band structure of synthesized nanocomposite as photocatalyst.

Except for AC1, both AC5 and AC6 contain higher carbonyl (C=O) group, considered as hole scavengers [28,29], which in turn reduce the generation of $OH^{\cdot}$. Since, $OH^{\cdot}$ is a strong oxidizing agent as compared to $O_2^{\cdot -}$, reduction in the generation of $OH^{\cdot}$ retards the photocatalytic degradation efficiency of AC5 and AC6. Furthermore, in AC5 and AC6, Nb exhibits 4+ (NbC_xO_y, NbC, NbO_2) and 5+ (Nb_2O_5) oxidation states in which Nb^{5+} tries to attain a more stable state, i.e. Nb^{4+} by scavenging an electron to retard the photodegradation. Sample AC1 consists of Nb in the 3+ (NbC_xO_y, NbC) and 4+ (NbC_xO_y, NbC, NbO_2) states in which Nb^{3+} will try to achieve Nb^{4+} by ejecting an electron to enhance the degradation efficiency which can be expressed by the following equations:

$$Nb^{5+} + e^{-} \rightarrow Nb^{4+} \quad (7.48)$$

$$Nb^{3+} \rightarrow Nb^{4+} + e^{-} \quad (7.49)$$

As the degradation can be achieved by the transformation of chromophore groups and the generation of energetic electrons in visible light, photocatalysis is thermodynamically and kinetically limited which might cause the partial degradation of MB dye even with the visible range band gap of photo catalysts based on MS and TOC results [30]. With the help of results of detection of ROS species, it can be said that the generation of ROS species is a function of both photocatalyst and dye solution. The degradation of MB dye occurred by the hole, electron, and hydroxyl radical equivalently. Thus, smaller crystallite size, high pore volume and specific surface area, smaller recombination, and fine tuning of bandgaps are considered to be prominent factors for the enhanced photocatalytic properties of single-phase carbon coated NbC NPs.

References:

1 D. S. Venables and M. E. Brown, *Thermochim. Acta*, 1997, **291**, 131–140.
2 G. Singla, K. Singh and O. P. Pandey, *J. Alloys Compd.*, 2016, **665**, 186–196.
3 H. Kwon, W. Kim and J. Kim, *J. Am. Ceram. Soc.*, 2015, **98**, 315–319.
4 A. Gupta, G. Singla and O. P. Pandey, *Ceram. Int.*, 2016, **42**, 13024–13034.
5 J. Halim, K. M. Cook, M. Naquib, P. Eklund, Y. Gogotsi, J. Rosen and M. W. Barsoum, *Appl. Surf. Sci.*, 2016, **362**, 406–417.
6 M. T. Marques, A. M. Ferraria, J. B. Correia, A. M. B. do Rego and R. Vilar, *Mater. Chem. Phys.*, 2008, **109**, 174–180.
7 C. Zhang, M. Beidaghi, M. Naguib, M. R. Lukatskaya, M. Zhao, B. Dyatkin, K. M. Cook, S. J. Kim, B. Eng, X. Xiao, D. Long, W. Qiao, B. Dunn and Y. Gogotsi, *Chem. Mater.*, 2016, **28**, 3937–3943.
8 N. Nedfors, O. Tengstrand, E. Lewin, A. Furlan, P. Eklund, L. Hultman and U. Jansson, *Surf. Coat. Technol.*, 2011, **206**, 354–359.
9 S. Muralikrishna, K. Sureshkumar, T. S. Varley, D. H. Nagaraju and T. Ramakrishnappa, *Anal. Methods*, 2014, **6**, 8698–8705.
10 F. Zhao, A. Vrajitoarea, Q. Jiang, X. Han, A. Chaudhary, J. O. Welch and R. B. Jackman, *Sci. Rep.*, 2015, **5**, 17–19.
11 X. Ma, Y. Chen, H. Li, X. Cui and Y. Lin, *Mater. Res. Bull.*, 2015, **66**, 51–58.
12 X. Zhang, J. Qin, Y. Xue, P. Yu, B. Zhang, L. Wang and R. Liu, *Sci. Rep.*, 2014, **4**, 4–11.
13 F. E. Castillejo, D. M. Marulanda, J. J. Olaya and J. E. Alfonso, *Surf. Coatings Technol.*, 2014, **254**, 104–111.
14 C. Zhang, M. Beidaghi, M. Naguib, M. R. Lukatskaya, M. Q. Zhao, B. Dyatkin, K. M. Cook, S. J. Kim, B. Eng, X. Xiao, D. Long, W. Qiao, B. Dunn and Y. Gogotsi, *Chem. Mater.*, 2016, **28**, 3937–3943.
15 G. Y. Xu, J. B. Li, Y. Huang, W. Y. Yang and Z. P. Xie, *Mater. Sci. Eng. B*, 1999, **60**, 185–188.
16 J. S. Atchison, M. Zeiger, A. Tolosa, L. M. Funke, N. Jäckel and V. Presser, *RSC Adv.*, 2015, **5**, 35683–35692.
17 A. C. Ferrari and J. Robertson, *Phys. Rev. B*, 2000, **61**, 14095–14107.
18 E. Pehlivan, F. Z. Tepehan and G. G. Tepehan, *Sol. Energy Mater. Sol. Cells*, 2005, **87**, 317–322.
19 Z. Weibin, W. Weidong, W. Xueming, C. Xinlu, Y. Dawei, S. Changle, P. Liping, W. Yuying and B. Li, *Surf. Interface Anal.*, 2013, **45**, 1206–1210.
20 P. Yu, X. Wen, Y.-R. Toh, Y.-C. Lee, K.-Y. Huang, S. Huang, S. Shrestha, G. Conibeer and J. Tang, *J. Mater. Chem. C*, 2014, **2**, 2894–2901.
21 Y. Chen, B. Wang, S. Lin, Y. Zhang and X. Wang, *J. Phys. Chem. C*, 2014, **118**, 29981–29989.
22 L. Yang, X. Zheng, M. Liu, S. Luo, Y. Luo and G. Li, *J. Hazard. Mater.*, 2017, **329**, 230–240.
23 A. Younis, D. Chu, Y. V. Kaneti and S. Li, *Nanoscale*, 2016, **8**, 378–387.
24 Y. Ohgi, A. Ishihara, K. Matsuzawa, S. Mitsushima, K. I. Ota, M. Matsumoto and H. Imai, *Electrochim. Acta*, 2012, **68**, 192–197.
25 A. Ishihara, M. Tamura, Y. Ohgi, M. Matsumoto, K. Matsuzawa, S. Mitsushima, H. Imai and K. I. Ota, *J. Phys. Chem. C*, 2013, **117**, 18837–18844.
26 Y. Yang, Y. Guo, F. Liu, X. Yuan, Y. Guo, S. Zhang, W. Guo and M. Huo, *Appl. Catal. B Environ.*, 2013, **142**–**143**, 828–837.
27 M. J. Islam, D. A. Reddy, J. Choi and T. K. Kim, *RSC Adv.*, 2016, **6**, 19341–19350.
28 N. DiCesare and J. R. Lakowicz, *J. Phys. Chem. A*, 2001, **105**, 6834–6840.
29 S. Zheng, Y. Cai and K. E. O'Shea, *J. Photochem. Photobiol. A. Chem.*, 2010, **210**, 61–68.
30 S. Bae, S. Kim, S. Lee and W. Choi, *Catal. Today*, 2014, **224**, 21–28.

CHAPTER 8 CONCLUSIONS & FUTURE SCOPE

Overview

In this chapter, the conclusion drawn from on the basis of work done for the synthesis of NbC-C nanocomposite powder at different experimental conditions using different carbon precursors (smoked cigarette filters, parthenium hysterophorous, cellulose acetate and activated charcoal) is presented. Further, the effect of carbon precursor, lattice strain, lattice carbon (C/Nb) and composition on photocatalytic performance of synthesized samples is summarized. Based on the work done, suggestions for future work is also given.

8.1. Conclusions

Niobium carbide (NbC) is considered as a promising candidate to enhance the toughness of Co-WC cermets, as a thermal barrier coating, corrosion resistive coatings and cutting tools. Apart from these applications, it also exhibits excellent electrocatalytic performance for different fuel cell applications due to excellent chemical stability. Here, the present work explores the photocatalytic behavior of NbC in which photon induced charge carriers generates the ROS reagents resulting oxidation of organic molecules.

In the present work, it has been observed that the performance of synthesized NbC-C nanocomposite as a photocatalyst is a function of particle size, SSA and chemical composition of NbC_x; most importantly in terms of a solid solution of Nb, C and O forming carbon deficient NbC_x and NbC_xO_y/NbO_z defect site inside the NbC lattice. All the above-mentioned parameters depend on the synthesis conditions and the nature of carbon source which was carried out using four different carbon precursors. The major findings as concluded from a series of experiments are presented below:

1. During the optimization of synthesis parameters by using different carbon sources, it has been observed that the larger particles of Nb_2O_5 i.e. ~250 nm were transformed to smaller NbC nanoparticles (10-120 nm) as a result of solid-state reduction carburization reaction among reactants which can also be expressed through following pathway:

$$Nb_2O_5 \rightarrow NbO_2 \rightarrow NbO \rightarrow NbC$$

The above-mentioned chemical phase transformation does not include the formation of metallic Nb and semi-carbide phases (Nb_2C, Nb_4C_3 and Nb_6C_5 etc.). The presence of carbon coating on NbC nanoparticles suggested the temperature and time dependent solid-state diffusion of carbon towards the core of Nb_2O_5 particle resulting NbC (NbC_x, NbC_xO_y and NbO_z) and evolution of oxygen in the form of CO or CO_2 inducing porosity on the surface of the particles.

2. For all the precursors, single phase NbC-C nanocomposite has been obtained at 800 °C with different holding times. In terms of holding time, PH has resulted faster reduction carburization of Nb_2O_5 which did not require the holding time i.e. 0 h whereas the use of CFs suggested the holding time of 20.0 h at 800 °C. Moreover, laboratory grade chemicals (cellulose acetate and activated charcoal) exhibited moderate holding time (2.0 and 10.0 h, respectively) at the same temperature.

3. In this work two different categories of carbon precursors were taken; 1) waste materials (smoked cigarette filters and parthenium hysterophorous well known as carrot

grass) and 2) laboratory grade chemicals (cellulose acetate and activated charcoal). In order to get pure phase, the experimental conditions for each category of carbon source is summarized in table 8.1.

Table 8.1: Comparative data of NbC samples obtained from different carbon precursors.

	Chapter 4	Chapter 5	Chapter 6	Chapter 7
	Cigarette filters	**Parthenium hysterophorous**	**Cellulose acetate**	**Activated charcoal**
Temperature (°C)	800	800	800	800
Holding time (h)	20.0	0.0	2.0	10.0
a (Å)	4.468	4.462	4.466	4.469
x (C/Nb)	0.944	0.881	0.923	0.959
Avg particle size (nm)	120	66	80	12
Strain ($\varepsilon \times 10^{-4}$)	0.84	14.20	2.50	85.10
SSA (m^2/g)	17.70	49.47	6.09	506.00
Pore volume (cm^3/g)	0.092	0.121	0.019	0.369
***NbC content (%)**	14.72	22.90	18.60	13.72
***NbC_xO_y content (%)**	9.99	23.70	19.30	4.54
#I_D/I_G	0.71	0.31	0.13	1.49
Catalyst loading (mg)	60.0	60.0	60.0	20.0
Dye adsorption (%)	54.01	56.70	20.19	78.11
Dye degradation (%)	54.38	100.0	45.86	68.96
Irradiation time (h)	8.0	8.0	8.0	2.0
Rate constant (h^{-1})	0.0905	0.5537	0.0733	0.6246
Detected ROS	$O_2^{\cdot-}$	$O_2^{\cdot-}$	$O_2^{\cdot-}$	$O_2^{\cdot-}$
Recyclability (cycles)	3	4	4	3

**XPS (Nb3d) and #Raman results*

4. Single phase NbC samples (as observed from XRD results) exhibit lattice distortion due to the presence of oxygen centers inside the NbC particles in the form of NbC_xO_y or NbO_z as revealed by the elemental line profile (TEM) and XPS spectroscopy. These oxycarbide (NbC_xO_y) or oxide (NbO_z) centers has also induced optical absorption characteristics in visible region.

5. The Raman spectroscopy revealed the *in-situ* formation of carbon on the surface of carbide as free carbon. The nature of different carbon (amorphous, graphitic etc.) depends on upon the source of carbon taken as precursor. Among all the precursors, activated charcoal induced the formation of higher content of disordered graphic carbon while, smoked cigarette filters and parthenium hysterophorous resulted multilayered graphitic carbon. Further, laboratory grade cellulose acetate resulted in the formation of larger layers of graphite as compared to other carbon precursors.

6. Considering the optical activity under visible region, effect of concentration of dye solution and photocatalyst (single phase NbC-C nanocomposite sample) for the photodegradation of methylene blue dye was optimized to 1.0 mg/l and 60.0 mg/l,

respectively. The preliminary photocatalytic experiments suggested the inverse dependency of the concentration of dye solution due to decreased penetration of light and inter molecular repulsion between dye molecules.

7. As an effect of composition of photocatalyst, single phase NbC with higher content of NbC_xO_y center supported the photocatalytic activity. Moreover, the resultant photocatalytic performance of NbC has also been influenced by the higher specific surface area (compromised with lower content of NbC_xO_y) as observed in the case of activated charcoal. Apart from these factors, the presence of Nb-oxides in the powder sample has also suppressed the photocatalytic performance. Further, the role of free carbon also maneuvered the photocatalytic performance as g-C provides better charge transfer phenomenon while, amorphous carbon induces higher adsorption sites (high specific surface area) for dye molecules.

8. Photocatalytic experiments under household CFL illumination suggested the physisorption (pseudo first order) governing photodegradation of MB dye in which PH derived NbC-C nanocomposite sample exhibited 100% discoloration of dye solution. 83.1% removal of organic carbon (TOC) has been observed suggesting the slower degradation as compared to discoloration. The detection of reactive oxidative species (ROS) revealed the involvement of superoxide anion radical ($O_2^{\cdot -}$) as major oxidizing agent during photodegradation of MB dye. Direct mass spectrometry revealed the partial decomposition of MB dye molecule to lower molecules having m/z ~202.17 suggesting the photodecomposition of MB molecule instead of complete mineralization. Further, the optimized NbC-C nanocomposite sample can be considered as a stable photocatalyst up to 4 continuous cycles without any significant structural modifications.

The use of organic waste (CF and PH) has resulted better photocatalytic behavior of NbC-C nanocomposite samples as compared to those which have been obtained from laboratory grade chemicals.

8.2. Future scope

The present work establishes the utilization of waste materials to develop engineering compound i.e. NbC at relatively low temperature. Here, four different carbon precursors have been used to understand the effect of temperature and holding time on the formation of NbC using single source of Nb and reducing agent. However, other variety of reducing agents (carbonates and zeolites etc.), organic or inorganic wastes (as carbon source) and other Nb precursor can also be used to evolve the structural insights of synthesis

of nano NbC. A systematic work can also be done to determine the exact band diagram (density of states) with proper experimental justification (related to photocatalytic performance) which has numerous theoretical approaches. Apart from photocatalytic degradation of organic pollutants, treatment of some real time pharmaceutical wastes can also be explored along with photocatalytic fuel generation (H_2/O_2 and alcohol production) and CO_2 reduction.